DESIGN AND Characterisation of AlInP Avalanche Photodiodes

JENG SHIUH CHEONG

A thesis submitted for the degree of Doctor of Philosophy

Department of Electronic and Electrical Engineering

The University of Sheffield

June 2016

Table of Contents

ACKNOWLEDGEMENT

First and foremost, I am indebted to Prof. David for giving me the opportunity to undertake the PhD, as well as steering the financial support. Besides his willingness to spend time for countless technical discussions, he has been very supportive in my career development skills during the doctoral studies. I wish to express my gratitude to Dr. Jo Shien Ng and Dr. Chee Hing Tan for their supervision especially at the beginning of my PhD, as well as for providing helpful comments on publications resulting from this work.

I would also like to thank Prof. Graham Rees and Prof. Majeed Hayat for sharing their insights on impact ionisation and solving complex mathematical expressions. I am grateful to Dr. Andrey Krysa and Dr. Faebian Bastiman at the Sheffield III-V National Centre for providing high quality AlInP and AlGaAs wafers respectively. These extremely valuable wafers have made the study of both optical and avalanche properties of these materials feasible. I also would like to thank Dr. Gavin Williams and Dr. Andy Maiden in sharing their expertise in optics, which enabled me to assemble the experimental setup successfully. The help from both the university and Sheffield III-V Centre staff like Paul Haines, Jonathan Milner, Ian Wraith, Ian Lyne, Wayne Frankish, Mick Woodcock, Fahmi Mohammad, Dianne Webster, Saurabh Kumar, Peter Trend, Andrew Brook and Stephen Dorward is deeply appreciated.

I am grateful to Dr. Siok Lan Ong for her patience in showing me the fabrication and experimental procedures, as well as willing to share her expertise and experience even after she left Sheffield. I also wish to thank my colleagues in the group; Dr. Ian Sandall, Dr. Simon Dimler, Dr. Siew Li Tan, Dr. Pin Jern Ker, Dr. Abdul Rahman Mohmad, Dr. Rajeev Gomes, Dr. James Green, Dr. Robert Richard, Dr. Christopher Hunter, Dr. Shiyu Xie, Dr. JingJing Xie, Dr. Xinxin Zhou, Dr. Xiao Meng, Akeel Auckloo, Danuta Mendes, Benjamin White, Zhize Zhou, Liang Qiao, Faezah Harun and Aina Baharuddin for valuable and enjoyable discussions. Special thanks go to my buddies Shengji Tee and Jiashen Teh who travelled with me frequently during my stay in the UK.

Finally, I am especially thankful to my family for their constant support throughout my PhD studies.

LIST OF PUBLICATIONS

Journal publications

1. **J. S. Cheong**, J. S. L. Ong, J. S. Ng, A. B. Krysa, and J. P. R. David, "$Al_{0.52}In_{0.48}P$ SAM-APD as a Blue-Green Detector," *Selected Topics in Quantum Electronics, IEEE Journal of*, vol. 20, pp. 142, 201.

2. **J. S. Cheong**, J. S. Ng, A. B. Krysa, J. S. L. Ong, and J. P. R. David, "Determination of absorption coefficients in AlInP lattice matched to GaAs," *Journal of Physics D: Applied Physics*, vol. 48, pp. 405101, 2015

3. **J. S. Cheong**, M. M. Hayat, Z. Xinxin, and J. P. R. David, "Relating the Experimental Ionization Coefficients in Semiconductors to the Nonlocal Ionization Coefficients," *Electron Devices, IEEE Transactions on*, vol. 62, pp. 1946, 2015.

4. L. Qiao, **J. S. Cheong**, J. S. L. Ong, J. S. Ng, A. B. Krysa, J. E. Green, *et al.*, "Avalanche Noise in $Al_{0.52}In_{0.48}P$ Diodes," *Photonics Technology Letters, IEEE,* vol. 28, pp. 481, 2016.

5. A. Auckloo, **J. S. Cheong**, X. Meng, C. H. Tan, J. S. Ng, A. B. Krysa, *et al.*, "$Al_{0.52}In_{0.48}P$ avalanche photodiodes for soft X-ray spectroscopy," *Journal of Instrumentation,* vol. 11, pp. P03021, 2016.

6. **J. S. Cheong.**, A. N. Baharuddin, J. S. Ng, A. B. Krysa., and J. P. R. David, "Determination of absorption coefficients in AlGaInP lattice matched to GaAs," (Submitted)

7. **J. S. Cheong**; J. P. R. David., "The effect of electric field gradient on avalanche multiplication and noise," (In preparation)

Conference papers

1. **J. S. Cheong**, J. S. L. Ong, J. S. Ng, A. B. Krysa, F. Bastiman, and J. P. R. David, "Design of high sensitivity detector for underwater wireless communication," Proc. SPIE, Emerging Technologies in Security and Defence, vol. 8899, 2013.

2. **J. S. Cheong,** A. Auckloo, J. S. Ng, A. B. Krysa, and J. P. R. David. "A high sensitivity detector for underwater wireless communication," Proc. SPIE, Unmanned/Unattended Sensors and Sensor Networks, vol. 9647, 2015.

Conference proceedings

1. **J. S. Cheong**, J. S. L. Ong, J. S. Ng, A. B. Krysa, and J. P. R. David, "$Al_{0.52}In_{0.48}P$ avalanche photodiodes for underwater wireless communication," Semiconductor and Integrated Optoelectronics, Cardiff, 2013.

2. **J. S. Cheong**, J. S. L. Ong, J. S. Ng, A. B. Krysa, and J. P. R. David, "III-V based detectors for underwater communication, " UK Semiconductors, Sheffield, 2014.

3. **J. S. Cheong**, J. S. L. Ong, J. S. Ng, A. B. Krysa, and J. P. R. David, "Narrow-band detector for underwater communication system," IEEE Photononics Conference, San Diego, 2014.

4. **J. S. Cheong**, A. N. Baharuddin, J. S. L. Ong, J. S. Ng, A. B. Krysa, and J. P. R. David, "Absorption coefficients in $Al_{0.52}In_{0.48}P$," Semiconductor and Integrated Optoelectronics, Cardiff, 2015.

5. L. Qiao, **J. S. Cheong**, J. S. L. Ong, J. S. Ng, A. B. Krysa, J. E. Green, and J. P. R. David, "Noise performance of $Al_{0.52}In_{0.48}P$ avalanche photodiodes," Semiconductor and Integrated Optoelectronics, Cardiff, 2015.

6. **J. S. Cheong**, L. Qiao, A. N. Baharuddin, J. S. Ng, A. B. Krysa, and J. P. R. David, "$Al_{0.52}In_{0.48}P$ photodetector for underwater communication systems," Asia Communications and Photonics Conference, Hong Kong, 2015.

7. A. N. Baharuddin, **J. S. Cheong**, J. S. Ng, A. B. Krysa, and J. P. R. David, "Narrow spectral response $(Al_xGa_{1-x})_{0.52}In_{0.48}P$ visible photodiodes," Semiconductor and Integrated Optoelectronics, Cardiff, 2016.

ABSTRACT

The aim of this work is to design a highly sensitive AlInP APD operating at ~ 480 nm for underwater wireless communication systems. Visible light is potentially an alternative to acoustic waves since it can propagate through seawater without much attenuation over short distances while having a high bandwidth. The optical properties of AlInP were studied by measuring the spectral response of AlInP PINs with various cladding and depletion thicknesses. In addition to the minority carrier diffusion lengths, absorption coefficients over a wide dynamic range from 10^6 to 10^0 cm^{-1} were extracted from these samples. The ternary alloy narrow spectral full-width-half-maximum (FWHM) of 22 nm was found to be independent of bias voltages.

The absence of enabled ionisation coefficients and threshold energies has prevented the modelling of excess noise in a wide range of semiconductors in thin submicron devices. A simple correlation was found to relate the device-independent and enabled ionisation coefficients, while the threshold energies are shown can be extracted from the multiplication curve without the necessity of performing the avalanche noise measurement as suggested by the literature. The relationship between these ionisation coefficients hold true for a wide range of III-V and group IV semiconductors.

These optical and avalanche parameters are then used to design a (Separate-Absorption-Multiplication) SAM-APD which the cladding and absorption region thicknesses are tailored to yield the optimum quantum efficiency. A thin avalanche region is desired to give low operational voltage and avalanche noise. Characterisation results of these devices showed the dark current prior to breakdown was < 20 pA at 99.99 % of the breakdown voltage. Under 480 nm illumination, the responsivity was 18 A/W with a gain of ~ 160 at -65.9 V. The measured excess noise corresponds to McIntyre's *k* of 0.3 and this agrees well with the modelled results. The excess noise, however potentially can give *k* of 0.1, as demonstrated in the PINs. The AlInP APD showed distinguishable photocurrent signal under the presence of strong background light of 1 kW m^{-2} due to the intrinsically narrow spectral FWHM of 22 nm.

GLOSSARY

a	: Lattice constant
A	: Area
APD	: Avalanche photodiode
AUV	: Autonomous underwater vehicle
B	: Bandwidth
c	: speed of light
C_j	: Junction capacitance
C	: Capacitance
D	: Laser spot diameter
$D_e(D_h)$	: Electron (hole) diffusion coefficient
$d_e(d_h)$	: Electron (hole) dead-space
E	: Energy
E_g	: Bandgap
E_Γ	: Energy gap between the lowest point of Γ valley and the highest point of valence band
E_X	: Energy gap between the lowest point of X valley and the highest point of valence band
E_L	: Energy gap between the lowest point of L valley and the highest point of valence band
E_{ind} (E_{dir})	: Direct (indirect) energy gap
E_{ii}	: Ionisation threshold energy
E_{phonon}	: Phonon energy
E_{th}	: Threshold energy
E_{the} (E_{thh})	: Electron (hole) threshold energy
F	: Avalanche excess noise
FWHM	: Full width half maxumum
F_e (F_h)	: Avalanche excess noise due to electron (hole)
g	: Density of state
h	: Plank constant
$\hbar$	: Reduced plank constant
$h_e(x\|x_0)$	: Ionisation probability of an electron created at x_0
$h_h(x\|x_0)$	: Ionisation probability of a hole created at x_0
I	: Current
I_{dr}	: Drift current
I_0	: Saturation current
I_{ph}	: Photo-current
I_{tunn}	: Tunnelling current
J	: Current density
k_m	: Momentum
K	: Extinction coefficient
k (k_{eff})	: McIntyre (effective) ionisation coefficients ratio
k_b	: Boltzmann constant
LIA	: Lock-in amplifier
L_e (L_h)	: Minority electron (hole) diffusion length
l	: Ionisation path length
m	: Orders of diffraction
m_0	: Electron mass
m_e (m_h)	: Electron (hole) effective mass

M : Multiplication
M_e (M_h) : Multiplication induced by electron (hole)
N : Number of trials
N_a : Acceptor doping concentration
N_d : Donor doping concentration
N_i : Unintentional doping concentration
n : Refractive index
n_0 : Ideality factor
n_e (n_p) : Electron (hole) concentration
n_i : Intrinsic carrier concentration
PIN : *p-i-n* diode
PMT : Photomultiplier tube
PDF : Probability density function
q : electron charge
r : Random number
r_d : Diode effective resistance
R_s : Series resistance
R_{sh} : Shunt resistance
R : Reflectivity
SAM : Separate absorption multiplication
SMC : Simple monte carlo
SNR : Signal to noise ratio
T : Temperature
TIA : Transimpedence amplifier
V : Voltage
V_a : Applied voltage
V_{bi} : Built-in voltage
V_{bd} : Breakdown voltage
w : Depletion width
x_d (x_a) : Depletion width to n^+ (p^+) cladding
Z : Phonon occupation number
α (β) : McIntyre's electron (hole) ionisation coefficients
α_{device} (β_{device}) : Device-width dependent electron (hole) ionisation coefficients
α' (β') : Device-width independent electron (hole) ionisation coefficients
α_{MC} (β_{MC}) : Monte Carlo's electron (hole) ionisation coefficients
α^* (β^*) : Effective electron (hole) ionisation coefficients
α_s (β_s) : Spatial electron (hole) ionisation coefficient
λ : Wavelength
γ : Absorption coefficient
η : Quantum efficiency
ρ : Resistivity
μ : Reduced effective mass
μ_e (μ_h) : Electron (hole) mobility
τ_{eff} : Effective carriers generation rate
$\hbar\omega$: Photon energy
ζ : Electric field
j : Incident light intensity

Chapter 1 INTRODUCTION

1.1 Motivation

Underwater communication plays a significant role in various applications. Underwater Acoustic Sensor Networks [1] consisting of onshore bases, satellites, surface stations, buoys and underwater sensors as illustrated in Figure 1.1 have been installed for environmental monitoring, underwater explorations, disaster prevention, assisted navigation, 3-D ocean sampling and tactical surveillance. Autonomous Underwater Vehicles (AUVs) are frequently employed to enhance the capabilities of these systems. High bandwidth is necessary to control the AUVs, to establish communication between the divers and surface platform, and send useful visual data to both parties in real time [2].

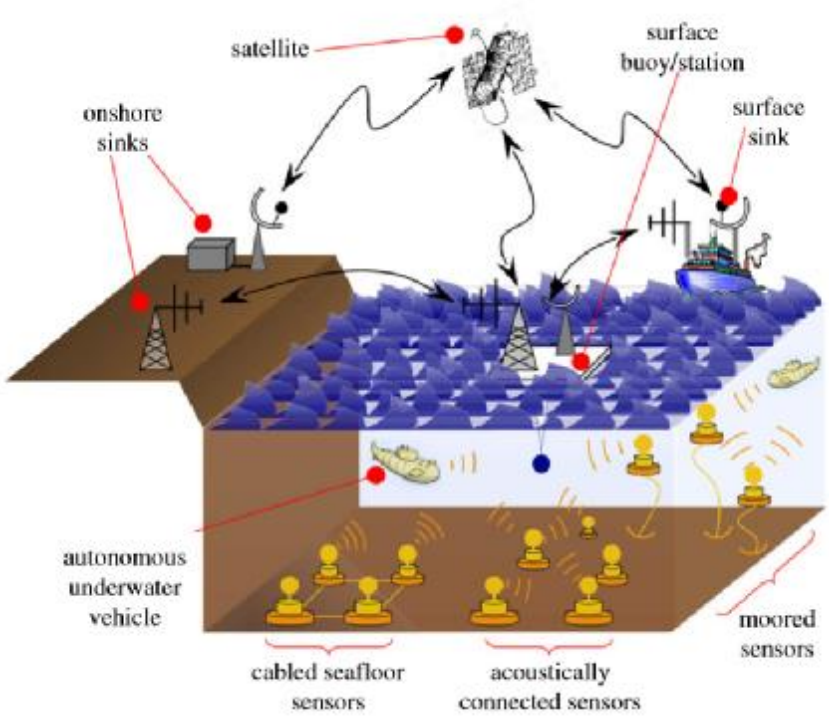

Figure 1.1 *Visualised underwater networks connected to air and land [2]*

Despite the rapid advancement in wireless communication on land, underwater wireless communication lags far behind for several reasons. Seawater, with its high conductivity not only severely attenuates radio waves, it also limits the data transmission range to within 10 metres [3]. Huge antennae that are employed in radio communication systems

are also impractical for underwater networks. Although acoustic waves can comfortably cover a wide range of several kilometres, data rates are limited to only hundreds of kbps [4] as shown in Figure 1.2. Acoustic waves also suffer from multipath propagations especially in swallow waters [2] resulting in inter-symbol interference where the signals arriving at the receiver at different times may result in the masking of subsequent bits. Furthermore, the surrounding man-made noise such as shipping activities and ambient noise due to seismic activities, ocean currents etc. can prevent successful retrieval of the signals [2]. To overcome these problems, complicated algorithms were introduced to improve the reliability of the systems [5]. However, these measures do not allow real-time communication. Optical communication can provide a much higher bandwidth of around 100 Mbps over a moderate range of 100 m [6] and thus, appears to be a better option than the traditional underwater acoustic communication that are used in such applications.

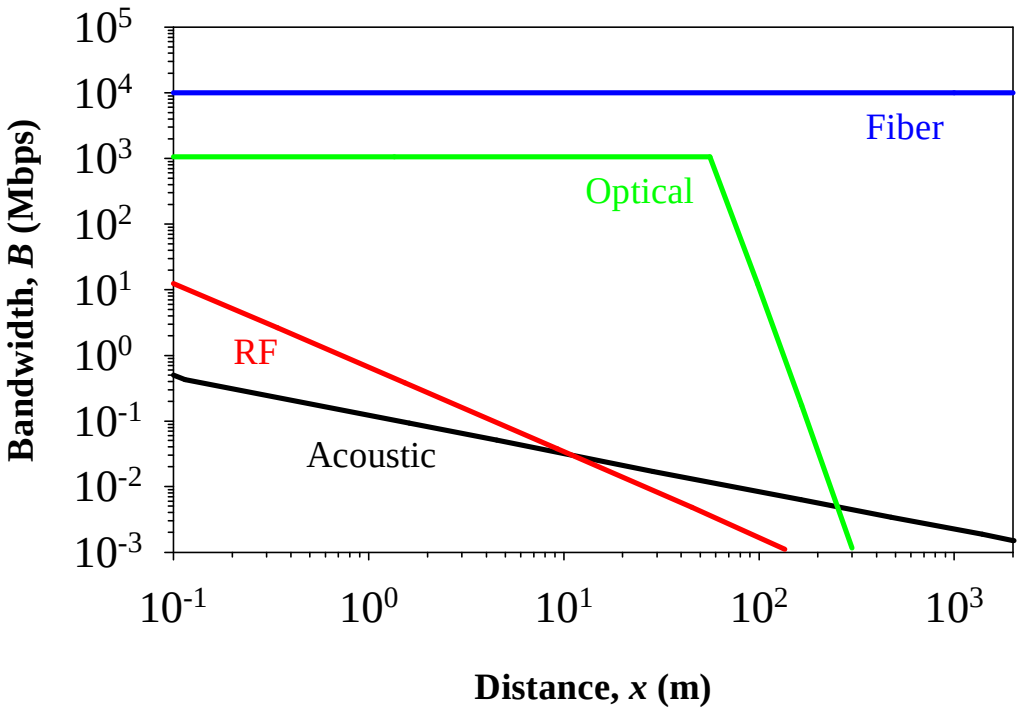

Figure 1.2 *The bandwidth attained by using different channels underwater [4]*

Transmission of a broad spectrum of electromagnetic (EM) waves in seawater was studied and visible light shows the least attenuation [7] while ultraviolet, infrared and microwave regime are severely attenuated [8, 9] primarily due to molecular absorption [10]. Jerlov [7] categorized offshore seawaters (Type I, II and III) and coastal seawaters (Type 1, 3, 5, 7, 9) by the level of turbidity as shown in Figure 1.3. Turbidity is caused

by suspended particles in the water, such as sediment which attenuates the light by scattering it (Mie scattering [11]). The scattering coefficient generally is proportional to the square of the diameter of the particles [11]. Plankton, which contain chlorophyll in their cells have peak absorption at 450 nm and 680 nm wavelengths and therefore result in low transmittance in these wavelengths in coastal waters [12]. Generally, all offshore seawaters have a good transmittance at ~ 480 nm with low attenuation ranging from –0.1 dB/m to –3.5 dB/m and therefore such wavelengths appear to be the most suitable channel for data transmission. Light sources such as LEDs and lasers operating at these wavelengths are also now commercially available [13].

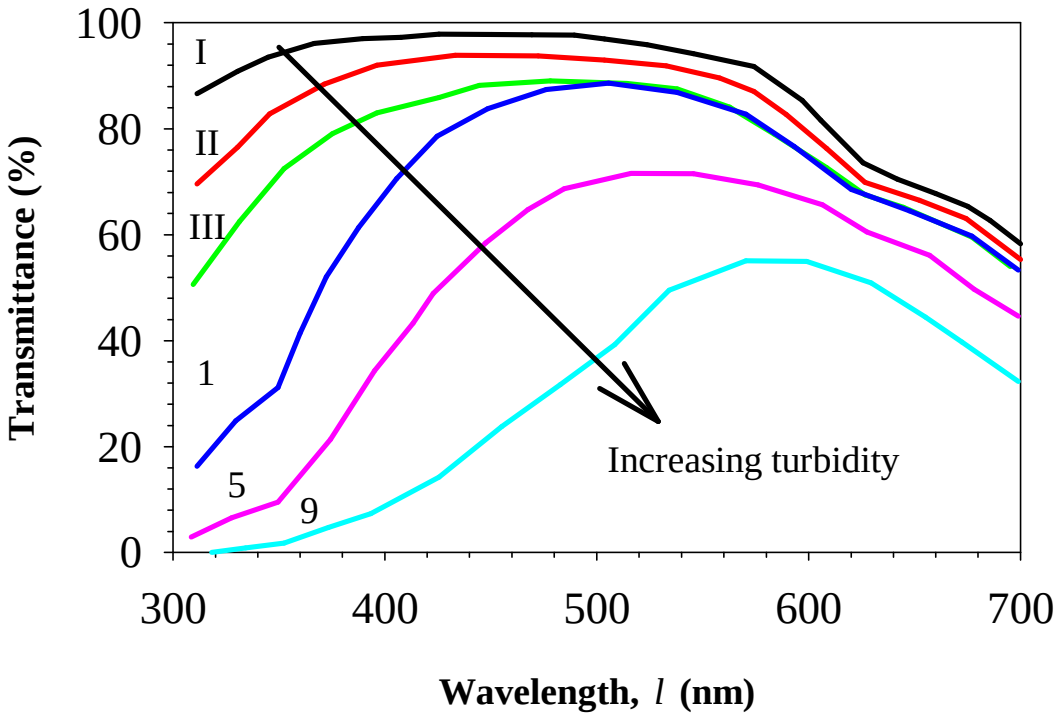

Figure 1.3 *Transmittance of visible wavelength lights for different types of seawater [7]*.

Apart from underwater communication, a detector which has a peak response at 480 nm may have other uses such as the detecting the presence of gamma rays when it is coupled with a Bismuth Germanate (BGO) crystal. This high-efficiency scintillation material has a maximum emission at 480 nm [14] after absorbing high energy (up to 30 MeV [15]) gamma rays as shown in Figure 1.4. It is currently used extensively in wide range of applications in high energy physics, nuclear physics, space physics and especially in oil and gas industries, where gamma ray detectors are used to detect the hydrocarbon (carbon and hydrogen) nuclei [16] due to the interaction of neutron. Due to the adverse environment in these applications, a photodetector must be able to withstand

high temperature of ~ 150 ºC without losing its sensitivity and suffer catastrophic failures. There has been interest growing interest recently in replacing the conventional photomultiplier tube with a solid-state avalanche photodiode [17] as the latter proves superiority over the former in having longer operating lifetime at elevated temperatures and better immunity to shock and vibration. The details of these photodetectors will be discussed later in section 1.2.

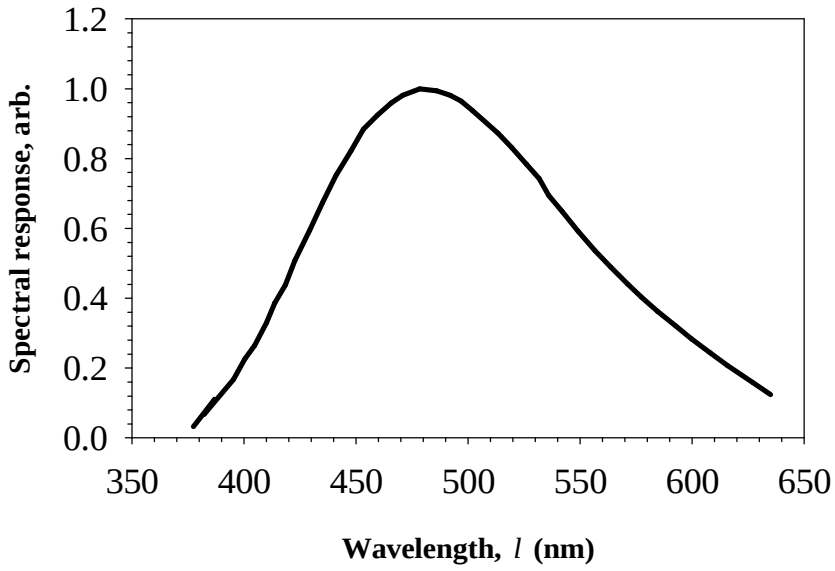

Figure 1.4 *Scintillation emission spectrum of a Bismuth Germate crystal [14]*

1.2 Photodetector requirements

Photodetectors are essential components in receivers of all types of optical communications, where they convert optical signals to electrical signals. Inevitably, the signal strength deteriorates while travelling through the medium and therefore the system performance is largely depending on the quality of the signal received by the detectors. Improvement on photodetectors' performance increases the system reliability. Fewer repeaters are required in the system and the installation cost can be reduced. Performance of a photodetector is determined by the following criteria;

1. Quantum efficiency, η

   Quantum efficiency (η) in photodetectors, ideally, should be unity, i.e. a photon give rise to an electron-hole pair, for a given wavelength shorter than the material cut-off wavelength. Photon absorption in semiconductors is governed by absorption

coefficient, γ (inverse of mean length of photons absorbed) and therefore it is preferably to have a reasonably high γ in order to obtain a high η.

2. Internal gain

Internal gain is preferred as this enables detection of smaller number of photons due to a higher generation of electron-hole pairs per photon, leading to a higher responsivity and signal-to-noise ratio.

3. Narrow spectral response

Unlike in closed fibre systems, sensitivity of detectors in free-space communication systems is susceptible to the background light. The spectral full-width-half-maximum should be as narrow as possible such that the detector only responds to the transmitted signal.

4. Response speed

The detector response speed is crucial as this determines the communication systems bandwidth. The response speed is generally limited by the parasitic RC or transit time of carriers in a photodetector.

5. Device noise

Noise may hinder information retrieval from a signal so should be kept as low as possible. The signal-to-noise ratio (SNR) can be written as [18]

$$SNR = \frac{P_{opt}}{N_s + N_{amp}}, \tag{1.1}$$

where P_{opt}, N_s and N_{amp} are the signal power, shot noise and amplifier noise respectively. P_{opt} is governed by η of the photodetector, whereas N_s and N_{amp} are shot noise originated from the photodetector and noise introduced by the external amplifier circuit respectively. Shot noise in photodetectors is mainly contributed by dark current or background radiation. Shot noise due to optical power may become dominant in low optical power conditions as the light source power fluctuates.

6. Low power consumption

Some applications may require detectors to be operated in remote areas where main power lines are not accessible. The system thus, must operate under minimal power consumption in order to extend the battery lifespan. Photovoltaic or low voltage operation detectors are preferred in these circumstances.

7. Device ruggedness

Harsh environmental conditions such as shock, vibration and high ambient temperature may have effects on the detector performance and lifespan. These may limit the operational conditions of the detectors.

The popular choices of photodetectors are photoconductor, Photomultiplier Tube (PMT), phototransistor and photodiode (PD). Photoconductors are slabs of intrinsic semiconductors, with ohmic contacts in both terminals. High photocurrent gain of ~10^6 [19] can be obtained by selecting semiconductor materials with dissimilar electron and hole mobility, however at the expense of the response speed due to the transit time of the slower carrier. Despite the low cost and simple structure of the photoconductors, the long response time, typically tens of milliseconds [20, 21], is the main drawback in high-speed applications. Improving the response time is possible by reducing the length of the semiconductor slabs, but this decreases the dark resistance. Lower dark resistance causes more current to flow and thus, increases the power consumption of photoconductors.

PMTs operate on the basis of the photoelectric effect. An electron can be promoted from valence band to vacuum level by an energetic photon and subsequently multiplied by dynodes and then collected by the anode. The main advantage of PMTs over PDs is the PMTs' very high gain, typically between 10^5-10^8 [22], decent response speed and large effective area . PMTs are hence the primary choice when intensity of the light is extremely weak and typical PDs are unable to generate significant photocurrent. This results in a poor SNR. Therefore, PMTs are suitable for photon counting applications and are widely used in many fields, especially in spectroscopy. PMTs however have several disadvantages; transformers which supply a high voltage of more than 1 kV are required to power up the dynodes for secondary electron emission in PMTs. In addition, PMTs are fragile as the vacuum tubes are made of glass and extreme care of handling is necessary. Besides having lower quantum efficiency (~ 30 % or less) compared to PDs, the performance of PMTs are susceptible to magnetic field, temperature, humidity and mechanical stress, making them unsuitable to operate in harsh environmental conditions.

As photocathode and dynodes are composed of materials which have low work functions, dark current increases twice as much when temperature goes up by 10 ºC [22]. PMTs also show a noticeable degradation in sensitivity and lifespan when ambient temperature increased beyond 90 ºC [22]. The linearity of PMTs with illumination intensity is limited to a dynamic range of 10^4, whereas PDs offer a higher value of 10^6. Furthermore, the complex structure of PMTs makes them large and expensive.

The structure of a phototransistor is the same as that of a bipolar transistor and the photocurrent is generated by optically injecting minority carriers into the base and subsequently being amplified by the transistor gain. The responsivity is high in these devices where 10^5 - 10^7A/W has been reported [23, 24]. However, the main drawback of phototransistors is the slow response speed due to the slow discharge of minority carriers in the base. Similar to PMTs, phototransistors suffer from a low dynamic range.

Typical PIN diodes are epitaxially grown on lattice matched substrates, with ohmic contacts formed at both of the terminals. However, unlike PMTs, typical PDs are cheaper, have near-unity quantum efficiency [25], can be operated in photovoltaic mode, are insensitive to magnetic fields and are small in size. The bandwidth of PDs is typically around hundreds of MHz to several GHz [26]. The response speed is primarily limited by the junction capacitance and parasitic resistance across the device, apart from the drift and diffusion speed of the carriers in the depletion width and cladding regions respectively [26, 27]. Capacitance of PDs may be reduced by having smaller radii devices and thicker depletion width, however at the expense of lower quantum efficiency. For high speed operation in GHz regime, the depletion width must be optimised to reduce the carrier transit time [26, 27].

The poor sensitivity of PDs can be compensated by avalanche gain in avalanche photodiodes (APDs), where the photocurrent is amplified internally and results in high SNR provided the avalanche excess noise is low. Unlike other gain mechanisms in phototransistors, photoconductors and PMTs, the ionisation process in APDs is a stochastic process and therefore each carrier experiences different multiplications. This results in excess noise in the photocurrent. The SNR ratio is now expressed as [18]

$$SNR = \frac{P_{opt}}{FN_s + N_{amp}/M^2} \tag{1.2}$$

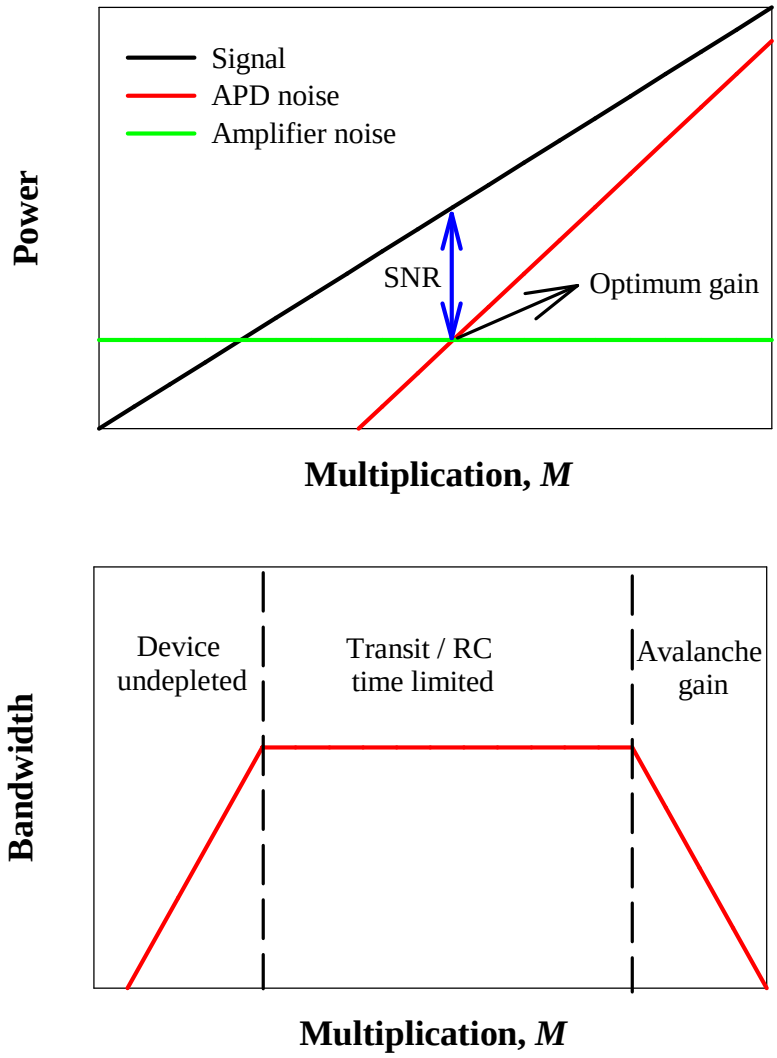

Figure 1.5 *The SNR (top) and bandwidth (bottom)of an optical receiver system with a function of avalanche gain.*

where M and F are avalanche gain and its corresponding excess noise factor respectively. As illustrated in Figure 1.5, the SNR increases initially with gain up to an optimum point where F becomes the dominant noise in the receiver system.

A high multiplication value may however deteriorate the bandwidth of APDs. Similar to SNR, the bandwidth initially improves with gain due to widening of the depletion region which gives a lower capacitance. The bandwidth saturates after the APDs fully punch-through and it is limited by the RC, or the transit time of carriers in the depletion width. Thereafter, the bandwidth deteriorates with increasing gain as shown in Figure 1.5. The worst APD bandwidth at a given multiplication and depletion width is attained when the electron ionisation rate is the same as holes' [28], as the multiplication process

relies heavily on the generation of secondary carriers' feedback which increases the transit time of carriers significantly .

Due to the recent advances in their performance where high bandwidth, high gain and low avalanche noise are achievable [29-33], APDs are more widely employed as detectors in various fields such as imaging, medical engineering and telecommunication compared to other detectors. The following discussions will be focused on APDs.

1.3 Competing material

As discussed in the previous section, photodetectors must be able to respond well at ~ 480 nm and therefore any semiconductors with band-gap narrower than 2.58 eV can be used for such applications. Commercially available photodiodes such as InGaAs [34] and Ge [35] with bandgaps of ~ 0.75 eV have poor η of < 10% despite having strong absorption at such wavelengths (γ > 3 ×10^5 cm^{-1}) [36, 37]. This is because carrier generation occurs at the surface of the semiconductor, where carrier loss due to recombination process is likely. GaP is an indirect bandgap material with band gap of 2.76 eV [38] and therefore γ is low at ~ 10^3 cm^{-1} [37] which gives a poor η [39]. III-nitrides have been proven an excellent material system for optoelectronic devices such as LEDs [40] and lasers [41] due to the bandgap tunability of InGaN from 0.7 to 3.4 eV, and has moderately high γ of ~ 10^4 cm^{-1} with 18 % indium composition [42].

Silicon is the most attractive solution as it covers a wavelength of 480 nm comfortably with γ of 10^4 cm^{-1} [43] as well. Due to its mature technology, sufficiently thick high purity silicon can be grown and hence blue enhanced silicon detectors have near unity η while having extremely low dark current density of 5 nA cm^{-2} [1]. Higher sensitivity can be achieved by silicon APDs due to high multiplication of > 100, with low avalanche excess noise and high bandwidth of ~ 1 GHz [44].

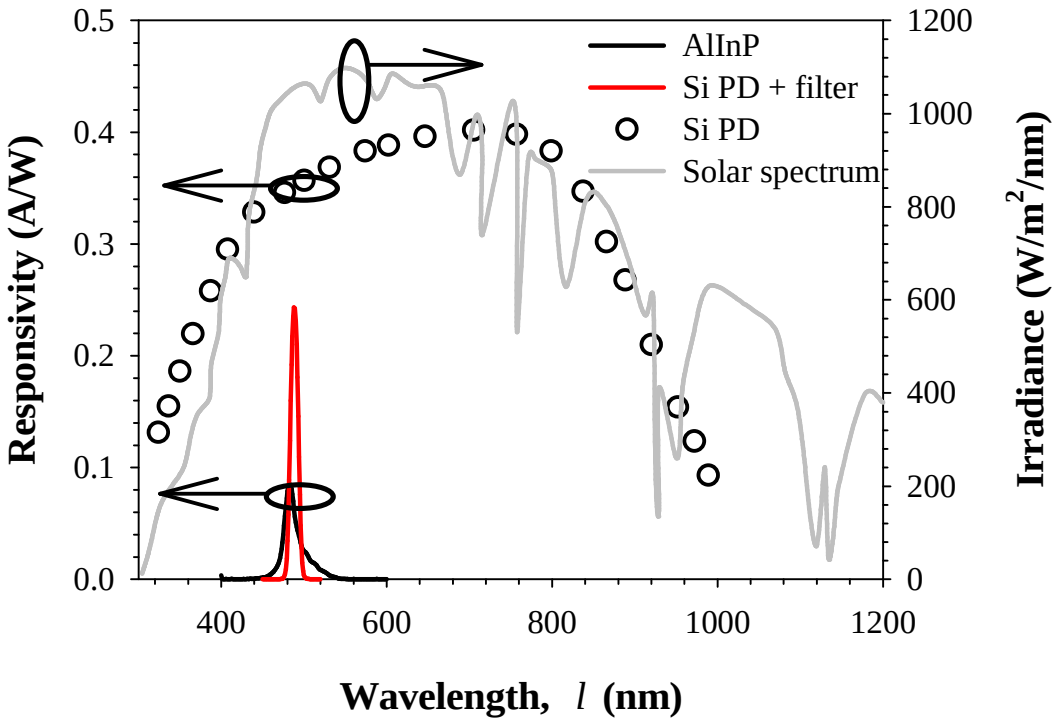

Figure 1.6 *Responsivity vs. wavelength in a 1.0 µm AlInP PIN (red), blue enhanced Si commercial photodiode with and without colour filters (black line and circles respectively) at device punch-through voltage. Also shown AM 1.5 solar spectrum (grey line) [45].*

Despite having these advantages, Si broad spectral response from visible to near-infrared regime shown in Figure 1.6 is detrimental to the SNR, as mentioned in section 1.2, due to the presence of ambient light which is primarily due to sunlight, and this may saturate the detector [46]. Therefore, a narrow full-width-half-maximum (FWHM) band-pass filter has to be used, which is usually made from Fabry-Perot filter comprises of large number of alternating dielectric stacks with distinct refractive index which their thicknesses are $\lambda/4$ where λ is the central wavelength. However, these filters are designed for normal incidence operation and the central wavelength shifts to shorter wavelengths with incident light angle deviating from normal which results in a reduced detector responsivity.

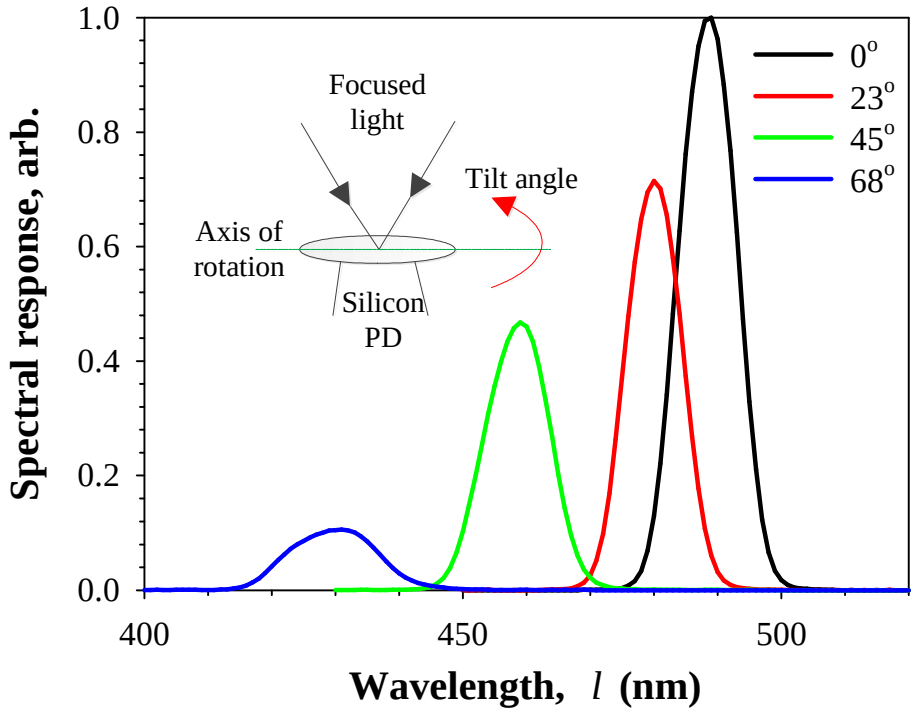

Figure 1.7 *The peak response wavelength of the silicon photodiode was blue-shifted 58 nm away from the desired central wavelength of 488 nm, with FWHM widened from 10 nm to 17 nm as the tilt angle increased from 0 to 68º. Inset shows the configuration of the experimental setup where the detector was tilted at various angles.*

To demonstrate this effect, a Thorlabs band-pass filter that has a central wavelength of 488 nm with a full-width-half-maximum (FWHM) of 10 nm was introduced before the light was focused on a commercial Si photodiode which has a response shown in Figure 1.6. The detector was initially normal to the incident light angle (0º) and thereafter tilted at various angles (23º, 45º and 68º) and the results are illustrated in Figure 1.7. This shows that a band-pass filter is not suitable for underwater applications as a small change in the incident beam angle may drastically reduce the responsivity of the detector.

III-V compound semiconductors are able to detect a wavelength of ~ 480 nm with not only a good responsivity but also can have a narrow spectral response. Without using any filters, an $Al_{0.8}Ga_{0.2}As$ homo-junction PIN can has a FWHM of 47 nm with a peak response at 487 nm [47]. A $Ga_{0.51}In_{0.49}P$-$Al_{0.52}In_{0.48}P$ PIN photovoltaic detector can provide a peak response at 480 nm with 0.17 A/W responsivity and 45 nm FWHM at room temperature [48]. More recently, despite having a simple structure, an $Al_{0.52}In_{0.48}P$ (hereafter AlInP) homo-junction PIN grown on lattice-matched GaAs substrate exhibited a much narrower FWHM of 22 nm [49] with similar peak response shown in

Figure 1.6. The spectral response and FWHM of the detector are unaffected by the incident light angle [50]. Furthermore, despite having an un-optimised fabrication process, dark currents obtained in AlInP detectors at avalanche gain of 100 are comparable to that of commercial Si photodiodes and other wide band-gap semiconductors such as GaN [51, 52], SiC [53, 54] and GaP [39] as illustrated in Figure 1.8.

AlInP PINs showed an almost temperature-independent breakdown voltage with a small temperature coefficient of 15 mV/K [55] even in the thick 1.0 µm PIN. These features indicate that AlInP gain at a given bias voltage is relatively insensitive to temperature compared to that a silicon APD, which typically has a value of > 500 mV/K.

AlInP can therefore potentially be an alternative to silicon as a high sensitivity detector for underwater applications primarily due to its inherently much narrower spectral FWHM, its lower dark current density and small breakdown voltage temperature coefficient. The operating voltage of the APDs can be optimised as will be discussed in Chapter 6.

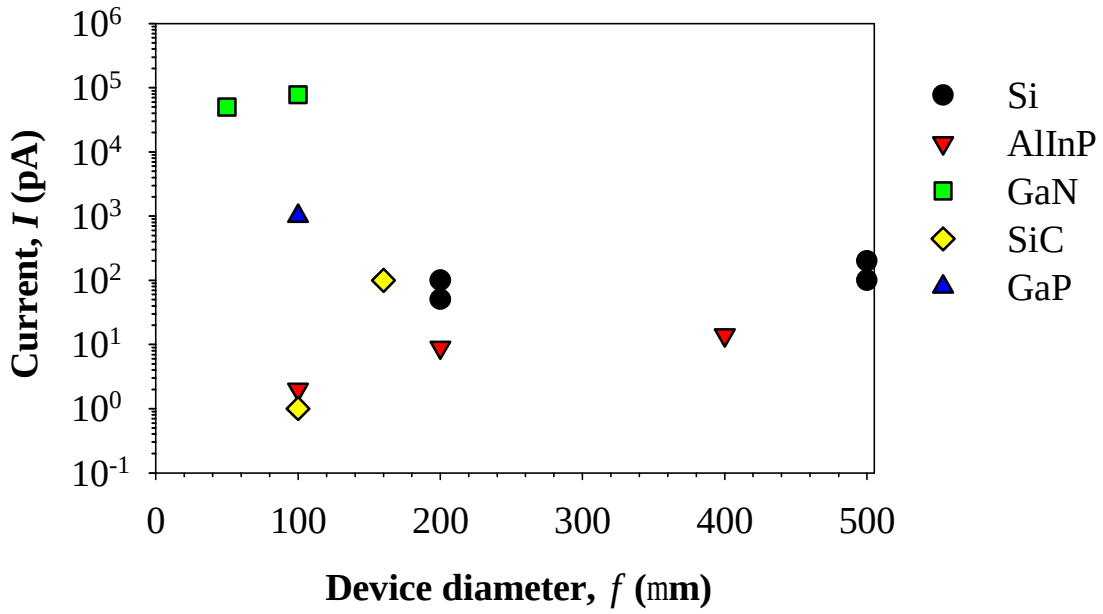

Figure 1.8 *Dark current measured in AlInP and several materials APDs at an avalanche gain of 100.*

1.4 Thesis Description

First, an overview of photodiodes and APDs is introduced in Chapter 2. Important features of APDs such as dark current, light absorption and impact ionisation mechanism are discussed.

Chapter 3 describes different characterisation techniques used in the work such as current voltage (*I-V*), capacitance voltage (*C-V*), photocurrent and photo-multiplication measurements. To understand the absorption and avalanche characteristic in AlInP, several measurements were performed on the PINs initially.

Detailed photocurrent measurements were conducted on several AlInP PINs with various p^+ cladding and intrinsic region thicknesses and the absorption characteristics were determined from these layers in Chapter 4.

To accurately predict the excess noise in AlInP, good knowledge of effective ionisation coefficients is required, which unfortunately is unavailable in the literature. A detail background study reveals that either local or effective ionisation coefficient is published in most III-V and group IV semiconductor materials. It is therefore useful to relate these ionisation coefficients so that these parameters can be used interchangeably in different avalanche models. The derivation details are discussed in Chapter 5. Previous literatures suggest avalanche excess noise measurements are needed to deduce these parameters, which is shown otherwise in this chapter, by knowing the onset of multiplication in various *w*'s in a given semiconductor precisely.

Subsequently, an AlInP homo-junction SAM-APD was designed to give the optimised operating voltage, spectral response, avalanche multiplication and the corresponding avalanche noise in Chapter 6. It is shown the behaviour of the APD is similar to the PINs counterpart and therefore the simulated results agree well with the experimental data. Modelling results showed that the SAM-APD noise performance could be similar to that of commercial Si APD by reducing the width of the avalanche width. Furthermore, the SAM-APD sensitivity is shown relatively better compared to that of commercial silicon APD under the presence of strong ambient light of 1 kW m^{-2}.

Chapter 7 concludes the thesis and highlights the key results achieved, along with a list of suggestions for future work.

Chapter 2 BACKGROUND

2.1 Dark current

The standard diode current density-voltage (J_T-V) equation is given by [56]

$$J_T = J_0\left[\exp\left(\frac{qV}{n_0 kT}\right)-1\right] \tag{2.1}$$

where J_0, q, n_0, k_b and T are the saturation current density, electron charge, ideality factor, Boltzmann constant and temperature respectively. The ideality factor indicates how closely the diode behaviour follows the ideal diode equation (n_0 = 1). This parameter varies between 1 and 2, depending on whether the current is dominated by diffusion or generation-recombination mechanism respectively. Ideality factor may be greater than 2 if two or more diodes are connected in series, probably due to the rectifying contacts [57].

The total current density measured in a diode, J_T is contributed by both the bulk current, I_{bulk} and the surface of the mesa diode, I_{sh} given as,

$$J_T = \frac{I_{bulk}}{A_{bulk}} + \frac{I_{sh}}{A_{sh}} \tag{2.2}$$

The degree of contribution due to these components can be assessed by scaling the current to their respective bulk and surface area, A_{bulk} and A_{sh} respectively. The effective resistance of a diode, r_d at a given bias voltage can be obtained by dividing equation (2.2) by ΔV to give

$$\frac{1}{r_d A} = \frac{1}{r_{bulk} A_{bulk}} + \frac{1}{r_{sh} A_{sh}} \tag{2.3}$$

where $r_d A$ is the effective resistance area product.

The bulk resistance, r_{bulk} is mainly contributed by the resistivity of the semiconductor, r_d expressed by

$$\frac{1}{r_d} = n_e q \mu_e + n_p q \mu_h \tag{2.4}$$

where n_e and n_p are the electron and hole concentrations in the p^+ and n^+ claddings while μ_e and μ_h are the mobility of electron and hole respectively.

Figure 2.1 shows the DC model of a *p-n* junction. At low forward bias voltages (less than the diode built-in voltage), *J-V* is dominated by the bulk characteristic and therefore the measured current obeys equation (2.1). This assumes that R_{sh} is sufficiently large, i.e. ~ 10^{12} Ω and thus the surface leakage current is negligible. By plotting log *J* vs *V*, I_0 is obtained by extrapolating the curve to the y-intercept while n_0 is treated as a fitting parameter to give good agreement with the gradient of the measured curve. As the current increases exponentially with forward bias voltage in a diode, r_d is much lower than the parasitic resistance, R_s, i.e. $r_d < R_s << R_{sh}$ and this therefore allows the extraction of R_s.

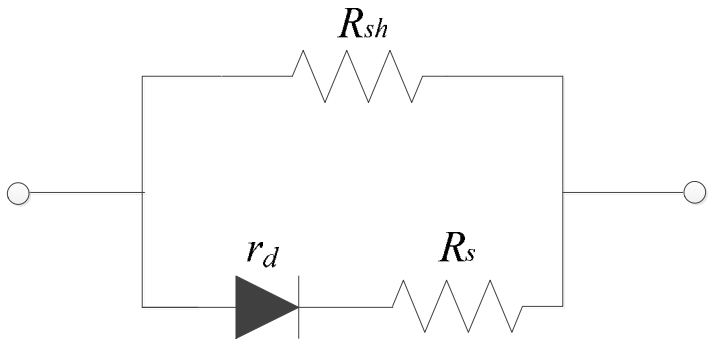

Figure 2.1 *DC model of p-n diode*

In the reverse bias regime, the theoretically lowest dark current is J_0 which is related to the carrier diffusion lengths as [56],

$$J_0 = \frac{qD_h n_i^2}{L_h N_D} + \frac{qD_e n_i^2}{L_e N_A} \tag{2.5}$$

where n_i, $D_e(D_h)$, $L_e(L_h)$ and $N_D(N_A)$ are the semiconductor intrinsic carrier concentration, electron (hole) diffusion coefficients, electron (hole) diffusion lengths and donor (acceptor) concentration respectively. However, the measured reverse leakage current is usually higher than J_0 due to several non-ideal factors of a diode. This is particularly true for large band-gap materials where dark current of potentially $< 10^{-12}$ A even in the largest devices (radius of 210 μm) in this work due to very low J_0,

which is beyond the source-measure-unit (SMU) measurement capability. Also, due to un-optimised etching, surface leakage current may dominate the measured current, i.e. $r_d >> R_{sh}$. Another mechanism which could contribute to a high leakage current is Shockley-Read-Hall generation-recombination current, $I_{G\text{-}R}$ due to energy states in the forbidden gap created by the defects [58] and is given by [59]

$$J_{G-R} = \frac{qn_i w}{2t_{eff}}\left[\exp\left(-\frac{qV}{2k_b T}\right)\right] \tag{2.6}$$

where q, W and τ_{eff} are electron charge, depletion width and effective carrier generation rate respectively, assuming that the defect centre is $E_g/2$, which yields the highest recombination rate. In high reverse bias voltages, tunnelling mechanism may dominate the bulk dark current. Considering that the work here is on an indirect wide band-gap semiconductor, the tunnelling current should be negligibly small even up to the breakdown voltage (< 0.5 μA cm^{-2}).

2.2 Absorption of Light

Besides thermal excitation, carriers are introduced to the conduction band via absorption of light, provided the photon has energy higher than the bandgap of the semiconductor material. The photon energy, E is related to its wavelength by

$$E = \frac{hc}{l} \tag{2.7}$$

where h is planck's constant, c is the speed of light, 3×10^8 m s^{-1} and λ is the photon's wavelength. A photodetector cut-off wavelength refers to the longest detectable wavelength, where the photon has the minimal amount of energy to promote an electron from the valence band to conduction band.

Absorption of light in photodetectors is governed by the absorption coefficient, γ of a given semiconductor material. Given a photodetector under monochromatic wavelength illumination, the number of photons being absorbed is proportional to the concentration of photons at dx. The intensity of light, φ when travelling through a semiconductor with a thickness x can be described as

$$\frac{dj}{dx} = -gj\,(x) \tag{2.8}$$

Solving equation (2.8) yields

$$j = j_0 \exp(-gx) \tag{2.9}$$

where the average distance travelled by photons before being absorbed is $1/\gamma$, i.e. the distance corresponds to $1/e$ of the initial intensity. A larger γ indicates more photons are absorbed nearer to the surface of semiconductor.

An ideal photodiode should instantly absorb all photons which have energy higher than its bandgap energy ($\gamma \rightarrow \infty$) and vice versa, be transparent to photons that have energy less than the bandgap ($\gamma = 0$). However, the promotion of an electron from the valence band is only possible when there is an available state in the conduction band, i.e. an electron-hole pair cannot be generated if the energy of photon is not sufficient to promote an electron to the next available state in the conduction band. Therefore, γ varies as a function of wavelength. Since the joint density of states, ***g(E)*** increases with energy level given as [60],

$$g(E) = \frac{1}{2p^2}\left(\frac{2m^*}{\mathbf{h}^2}\right)^{\frac{3}{2}} E^{\frac{1}{2}} \tag{2.10}$$

the absorption coefficient can be expressed as [61],

$$\begin{aligned} g &\propto \left(\mathbf{h}w - E_g\right)^{\frac{1}{2}} \quad , \mathbf{h}w \geq E_g \\ g &= 0 \qquad\qquad \mathbf{h}w < E_g \end{aligned} \tag{2.11}$$

which is proportional to $g(E)$. By plotting γ^2 versus E, the bandgap of the material at the x-intercept can be determined. Nevertheless, equation (2.11) is only valid for direct-bandgap materials, which the conduction band lowest point is aligned with the highest point of the valence band at Γ. For indirect bandgap materials, the relationship of photons absorption to the band-gap is [61],

$$g \propto \left(\mathbf{h}w - E_g \,\mathbf{m}\, \mathbf{h}\Omega\right)^2 \quad ,\mathbf{h}w \geq E_g \qquad (2.12)$$
$$g = 0 \qquad \mathbf{h}w < E_g$$

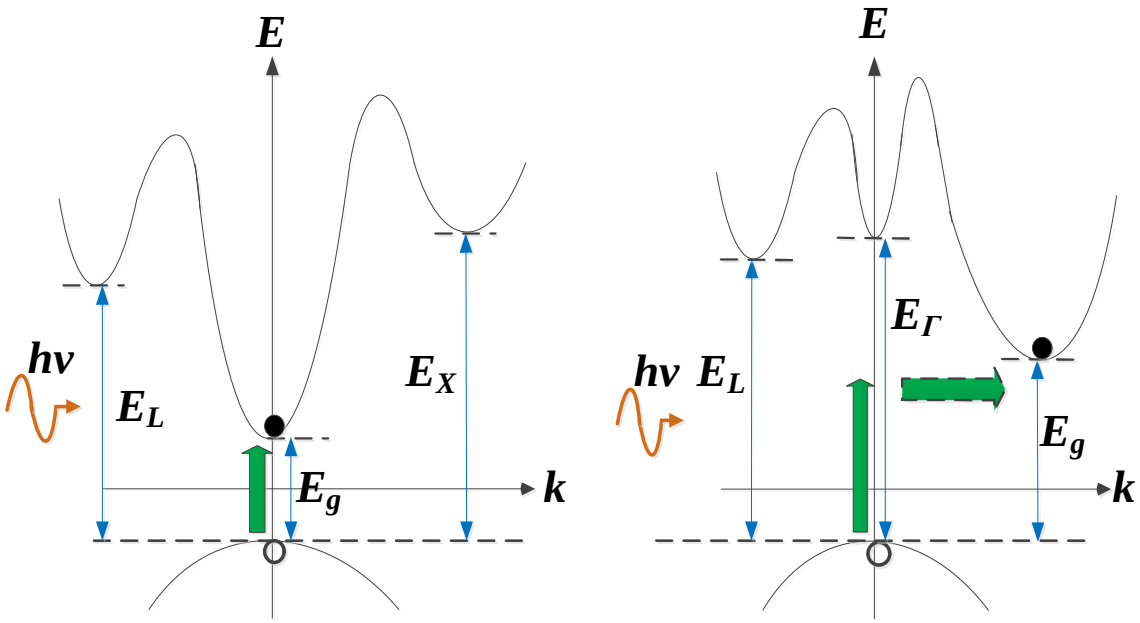

Figure 2.2 *E-k diagram of a direct (Left) and indirect (right) semiconductor*

where $\mathbf{m}\,\hbar\Omega$ is the phonon absorption and emission. The indirect gap is determined by the *x*-intercept in the $\gamma^{0.5}$ versus *E* plot. Photons that have energy less than the Γ point energy gap are expected to be very weakly absorbed by the indirect bandgap since the absorption process requires the assistance of phonons to change the momentum, as shown in Figure 2.2. Consequently, the band-edge absorption in indirect bandgap materials is a stronger function of temperature where the cut-off wavelength blue-shifts with lower temperature as the average phonon number reduces (an extreme case would be at 0 K where the cut-off wavelength corresponds to E_Γ of the material), and vice versa with higher temperature. Conversely, direct bandgap materials are able to generate electron-hole pairs without the aid of phonons and therefore the probability of photons being absorbed is much higher.

Figure 2.3 shows the absorption coefficient, plotted as a function of wavelength measured in some well-known semiconductors. Direct band-gap semiconductors such as GaAs [62] and InP [37, 63] have much sharper absorption profiles at their respective bandgap compared to the indirect band-gap semiconductors like Ge [37, 64] and Si [65]. The direct absorption at Γ contributes to the relatively steeper increase in the absorption in germanium for wavelengths shorter than 1.7 µm. Similar behaviour can be found in

silicon at wavelengths shorter than 440 nm. The absorption coefficient thereafter "saturates" at even shorter wavelengths due to the limited number of states in the conduction band and this can be found in GaAs, Si and Ge shown in Figure 2.3.

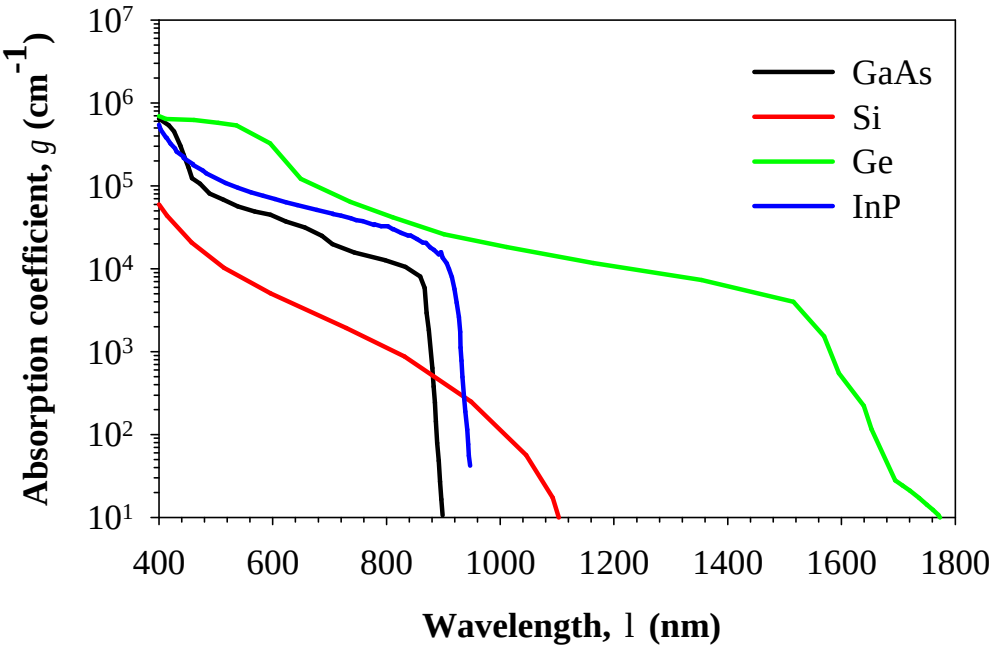

Figure 2.3 *Absorption coefficient of several semiconductor materials at 300 K.*

The absorption characteristic in a semiconductor can be modulated by the presence of an electric field and this has strong effects in direct band-gap materials near the cut-off wavelength. The electro-absorption in semiconductor was initially studied by Franz [66] and Keldysh [67] which has two effects;

a. The absorption of photons beyond the cut-off wavelength are due to the tunnelling of electrons into the conduction band and the absorption coefficient decreases exponentially as a function of photon energy

b. The oscillating effect in the absorption coefficient above the band-edge

The Franz-Keldysh (*F-K*) effect has been found in various semiconductor materials [68, 69] where the photocurrent response can be extended to longer wavelengths. Assuming a uniform electric field profile, the absorption coefficients (in cm^{-1}) as a function of photon energy, $\hbar\omega$ (in eV) and electric field strength, ζ (in V cm^{-1}) was formulated by Callaway [70] and Tharmalingam [71] to consider the effects of electro-absorption as discussed above as

$$g(l,z) = 1\times10^{4}\left(\frac{1+(m_v/m_0)^{-1}}{n}\right)\left(\frac{2m}{m_0}\right)^{\frac{4}{3}} z^{\frac{1}{3}}\int_b^x |Ai(z)|^2 dz \qquad (2.13)$$

where m_0, m_v, E_g, n and $\mu(=[1/m_e+1/m_v]^{-1})$ are electron mass, hole effective mass, band-gap, refractive index and reduced effective mass respectively. The integral of the Airey function, $Ai(z)$ in (2.13) can be written as

$$\int_b^x |Ai(z)|^2 dz = \left(\left|\frac{dAi(z)}{dz}\right|_b\right)^2 - c|Ai(z)|^2 \qquad (2.14)$$

where χ is expressed as

$$c = 1.1\times10^{5}(E_g - \mathbf{h}w)\left(\frac{2m}{m}\right)^{\frac{1}{3}} E^{-\frac{2}{3}}, \qquad (2.15)$$

Figure 2.4 shows the calculated the absorption coefficients of GaAs as a function of electric field strength, assuming E_g = 1.42 eV, where the photocurrent spectrum can be extended to λ > 1.0 μm at high electric fields.

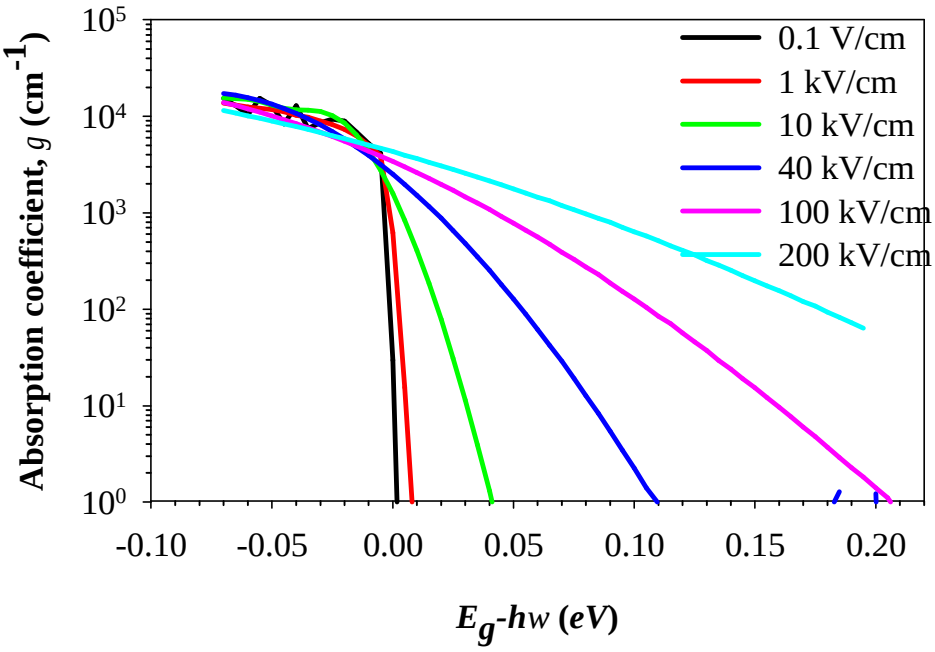

Figure 2.4 *Calculated absorption coefficient in GaAs at various electric fields using equation (2.13).*

2.3 Quantum efficiency in photodiodes

Ideal photodiodes have unity η but it is very challenging to achieve this in practical devices without the presence of internal gain due to surface recombination, minority carrier recombination and reflectivity at the semiconductor-air interfaces.

Carriers recombination at the semiconductor surface is due to the deep trap recombination causes by dangling bonds [72], deformation of crystal lattice arrangement periodicity [73] and multiple phonon emissions [74]. Thus, carriers are more likely to undergo non-radiative recombination at the surface of semiconductor rather than diffusing towards the depletion region. The surface recombination effect is more pronounced at shorter wavelengths with γ^{-1} only several tens of nm and therefore the excited carriers are unlikely to contribute to the photocurrent. As a result, photodiodes usually have "short" cut-off wavelengths with the responsivity approaching 0 AW^{-1}. Surface recombination can be addressed by passivation to reduce the number of surface states [75]. An alternative method is to create a "barrier" in the band diagram at the semiconductor-air interface to prevent the carriers diffusing to the surface and this can be achieved by introducing a heterojunction interface [76] or heavily doped surface [77].

Minority carriers generated more than the average diffusion length away from the depletion region are more likely to recombine and thus, have no contribution to the photocurrent. The diffusion length mainly depends on the crystal quality (associated with trap-assisted recombination) [78], doping concentration [79], temperature [79] and band structure (whether the semiconductor is a direct or indirect material) [80]. The semiconductor-air interface will also reflect light and reduce the quantum efficiency further, however, this can be improved by having an anti-reflection coating on the optical window. Thus, it is preferable that photons are absorbed in the depletion region as this utilises the electric field to reduce the probability of recombination by sweeping the holes and electrons in the opposite direction.

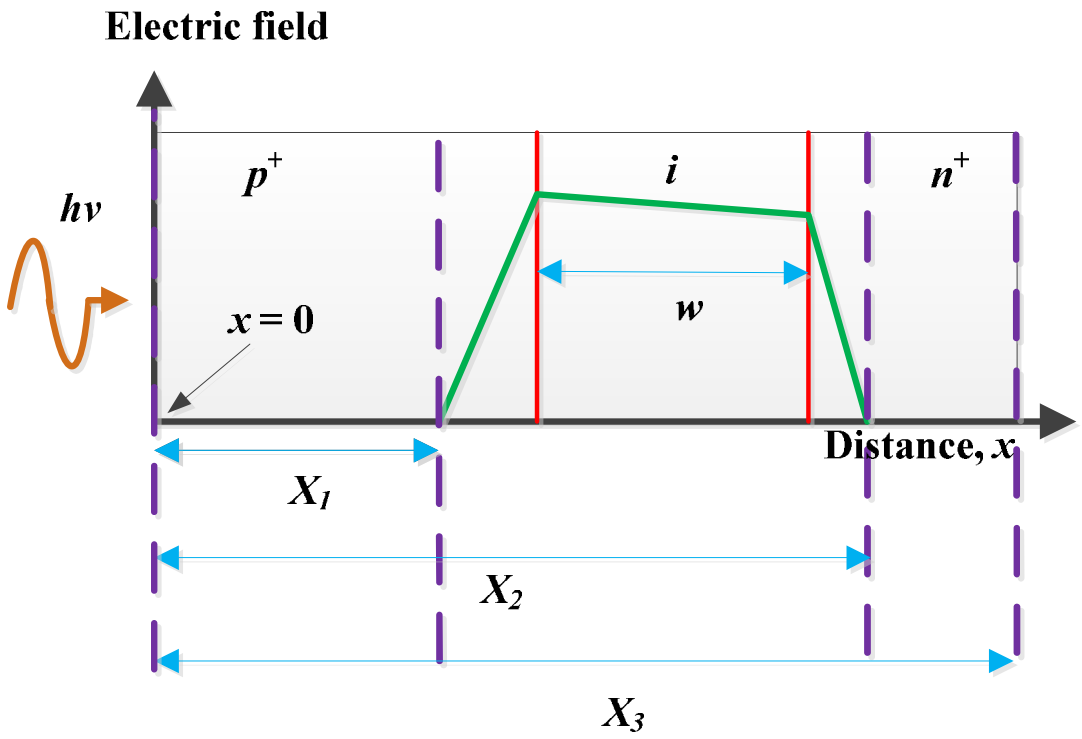

Figure 2.5 *Electric field profile of a PIN diode. The red line is the electric field profile of an ideal PIN whereas the blue line is a non-ideal PIN, assuming the intrinsic region is n-doped.*

The description above can be expressed analytically in the quantum efficiency model, which is derived from current-continuity equation. A brief on the model is as follow. EHPs created in the depletion region are assumed to be collected with 100% efficiency as they are swept away by the electric field. Therefore, η due to the intrinsic region strongly depends on the absorption coefficient only. Considering that monochromatic light is injected from the *p*-cladding of a PIN diode as shown in Figure 2.5, the generation rate of EHPs generated due to photons absorption at position x can be expressed as,

$$G_e(x) = \begin{cases} 0 & , \quad x < 0 \\ \varphi_o \gamma \exp(-\gamma x), & x \geq 0 \end{cases} \tag{2.16}$$

where φ_o is the number of photons injected per unit area from the *p*-cladding. The photocurrent, J_{dr} can be calculated by integrating equation (2.16) with lower and upper limits of X_1 and X_2 [81].

$$J_{dr} = -q \int_{X_1}^{X_2} \varphi_o \gamma \exp(-\gamma x) = q\varphi_o e^{-\gamma X_1}[1 - e^{-\gamma(X_2 - X_1)}] \tag{2.17}$$

The η calculation is based on equation (2.17),

$$\eta_2 = \frac{J_{dr}}{q\varphi_o} = e^{-\gamma X_1}[1 - e^{-\gamma(X_2 - X_1)}] \tag{2.18}$$

As there are carriers excited in the p and n-cladding, EHPs generated outside the depletion region can contribute to the photocurrent through diffusion. The photocurrent density due to electrons, J_n can be obtained by using the one dimensional diffusion equation, taking surface recombination into account as in [81],

$$J_n = \left[\frac{q\varphi_o \gamma L_e}{\gamma^2 {L_e}^2 - 1}\right]\left[\frac{\frac{S_e L_e}{D_e} + \gamma L_e - \exp(-\gamma X_1)\left(\frac{S_e L_e}{D_e}\cosh\frac{X_1}{L_e} + \sinh\frac{X_1}{L_e}\right)}{\frac{S_e L_e}{D_e}\sin\frac{X_1}{L_e} + \cosh\frac{X_1}{L_e}} - \gamma L_e \exp(-\gamma X_1)\right] \tag{2.19}$$

where L_n is the minority electron diffusion length, S_e is surface recombination velocity of the p-cladding surface, D_e is the electron diffusion coefficient which can be related to L_e by $L_e = \sqrt{D_e \tau_e}$ where τ_e is the minority electron lifetime.

η due to electrons created in the p-cladding is [81]

$$\eta_1 = \frac{J_n}{q\varphi_o} = \left[\frac{\gamma L_e}{\gamma^2 {L_e}^2 - 1}\right]\left[\frac{\frac{S_e L_e}{D_e} + \gamma L_e - \exp(-\gamma X_1)\left(\frac{S_e L_e}{D_e}\cosh\frac{X_1}{L_e} + \sinh\frac{X_1}{L_e}\right)}{\frac{S_e L_e}{D_e}\sin\frac{X_1}{L_e} + \cosh\frac{X_1}{L_e}} - \gamma L_e \exp(-\gamma X_1)\right] \tag{2.20}$$

Similarly, for photocurrent due to holes created in the n-cladding, J_p [81]

$$J_p = \left[\frac{q\varphi_o \gamma L_h}{\gamma^2 {L_h}^2 - 1}\right] \exp[-\gamma(X_3 - X_2)] \left[[\gamma L_h - \frac{\frac{S_h L_h}{D_h}[\cosh\frac{X_3}{L_h} - \exp(-\gamma X_3)] + +\sinh\frac{X_3}{L_h} + \gamma L_h \exp(-\gamma X_3)}{\frac{S_h L_h}{D_h}\sinh\frac{X_3}{L_h} + \cosh\frac{X_3}{L_h}}] \right] \quad (2.21)$$

η due to generated holes in the *n*-cladding can be expressed as [81],

$$\eta_3 = \frac{J_p}{q\varphi_o} = \left[\frac{\gamma L_h}{\gamma^2 {L_h}^2 - 1}\right] \exp[-\gamma(X_3 - X_2)] \left[[\gamma L_h - \frac{\frac{S_h L_h}{D_h}[\cosh\frac{X_3}{L_h} - \exp(-\gamma X_3)] + +\sinh\frac{X_3}{L_h} + \gamma L_h \exp(-\gamma X_3)}{\frac{S_h L_h}{D_h}\sinh\frac{X_3}{L_h} + \cosh\frac{X_3}{L_h}} \right] \quad (2.22)$$

where L_h is the minority hole diffusion length, S_h is the surface recombination velocity in the *n*-cladding surface and D_h is the diffusion coefficient of holes.

The internal η of a PIN diode, η_i is the summation of η_1, η_2 and η_3 while the external η takes the reflectivity, R of semiconductor surface into consideration such that

$$\eta = (1 - R)\eta_i = (1 - R)(\eta_1 + \eta_2 + \eta_3) \quad (2.23)$$

2.4 Optical constant characterisation

The operation of optoelectronic devices such as lasers, solar cells, and waveguides critically depends on the materials optical constants, such as refractive indices, dielectric constants, extinction coefficients and absorption coefficients, where these parameters vary with wavelength, temperature and electric field. The knowledge of these optical parameters in a material is helpful to design and optimise the performance of these devices. Transmission and ellipsometry measurements are two methods used to extract these properties reliably. The following sections will discuss the principle of the measurements, as well as their advantages and disadvantages.

2.4.1 Transmission measurement

Early absorption measurements on Ge and Si were demonstrated by several workers [64, 65, 82-84] where transmission of these materials was determined by illuminating the samples using a monochromatic light with intensity a_0 and subsequently the transmitted light intensity, a_T is measured by a detector. The measurement was repeated for several thicknesses, x to ensure the deduced γ is consistent.

However, multiple reflections occur when a beam of light travels through mediums of distinctive refractive indexes (assuming the absence of absorption). As the thickness of a sample is comparable to the wavelengths used, it can result in Fabry-Perot oscillations due to the constructive and destructive interference of light. Therefore, equation (2.9) no longer holds true. To account for this, the absorption coefficient, γ was deduced using [85]

$$\frac{a_T}{a_0} = \frac{\left[(1-R)^2 + 4R\sin^2 y\right]\exp(-gx)}{1-R^2\exp(-2gx)} \tag{2.24}$$

where $y = \tan^{-1}[2K/(n^2 + K^2 - 1)]$, and R, n and k_e are reflectivity, refractive index and extinction coefficient of a material respectively. To determine R accurately, the sample is illuminated with light with wavelengths longer than the material cut-off wavelength such that $\gamma \rightarrow 0$ and therefore equation (2.24) simplifies into $a_T/a_0 = (1 - R)/(1 + R)$. As R is approximately the same at the absorption band edge, γ can be determined. To ensure the calculated R reflects the true characteristic from the measured material, the samples are polished to remove any oxide layer and to ensure a smooth surface profile. Such measurement are quite accurate at the absorption band edge up to $\gamma \sim 10^3$ cm^{-1} with ~ 20 % error [64] and this enables accurate band gap estimation as shown by Macfarlane and Roberts [64, 65] using equations (2.11) and (2.12).

The transmission measurement, however is increasingly inaccurate when the material is highly absorbing, i.e. $\gamma > 10^3$ cm^{-1} as a_T in equation (2.24) approaches 0. Therefore, the signal strength might below the sensitivity of the detector or the measuring equipment. Thus, the only way to obtain γ of $> 10^3$ cm^{-1} reliably is to grow thin film samples with thicknesses of a few microns.

Nevertheless, the drawback in thin film measurements is that the film must be grown on a transparent substrate, and even if that is possible, the beam reflection between the

boundaries of each material complicates the calculation [84]. Furthermore, most III-V alloy semiconductors are grown on opaque substrates, i.e. the grown epilayer bandgap is larger than that of substrate, and therefore transmission measurement cannot be done unless the substrate is completely removed.

2.4.2 Ellipsometry measurement

Another alternative of obtaining γ is via ellipsometry measurements, which was initially proposed by Drude [89] and later was demonstrated by Ingersoll and Littleton [90]. Ellipsometry measurements can extract refractive index and extinction coefficient of a sample (n and K respectively) using the fact that the polarization of light is altered from linear to elliptical, or vice versa when it is reflected off a surface. γ thereafter can be calculated from

$$g = \frac{4pK}{l} \tag{2.25}$$

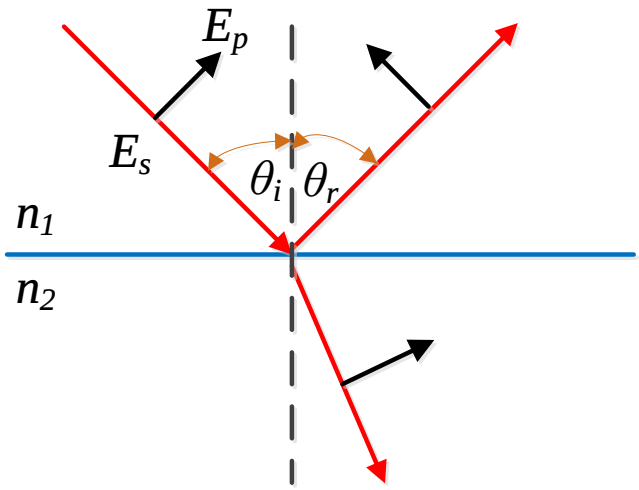

Figure 2.6 *A light travels from medium 1 to 2 with an incident angle of q_i which its electric field component is comprises of two perpendicular s and p vector.*

A brief description of ellipsometry theory is as follows. Electromagnetic waves are comprised of two components; electric and magnetic field. The electric field component is defined as the polarized light and can be further decomposed to two vectors; *s* and *p* vectors which is perpendicular and parallel to the plane of incident light (E_s and E_p respectively) as shown in Figure 2.6. Say we have light with an incident angle q_i and such that both *s* and *p* vectors are in phase with each other. The sum of *s* and *p*

components ($\sqrt{s^2 + p^2}$) gives amplitude which oscillates back and forth in time and therefore the light is said to be linearly polarized. Upon hitting the surface of medium 2, a fraction of light is reflected with an angle $q_r = q_i$ due to the law of reflection while the rest is refracted according to Snell's law. Generally both *p* and *s* components experience different reflectance and phase change and thus this alters the linearly polarized light to elliptical. The ellipsometer thereafter measures the amplitude and phase difference due to *p* and *s* vectors and relates the components reflection coefficients to the complex refraction indices ($n^* = n + iK$) of the sample via Fresnel's equations. There is a critical angle (Brewster's angle, q_b) however, where the reflected light is composed of purely *s* component and the relationship of the angle with the refractive indices of two mediums is given as

$$q_b = \tan^{-1}\left(\frac{n_2}{n_1}\right) \tag{2.26}$$

There are several techniques in conducting the experiment. However, only null ellipsometry, which is the traditional methodology to obtain the optical constants, will be described here. The experimental setup consists of a sequence of an unpolarised monochromatic light source, polarizer, compensator, sample and analyser (which is also a linear polarizer). The polarizer converts the light into linearly polarised light and thereafter the compensator retards the phase angle of the two perpendicular vector of the electric field component by π/4 to give an elliptical polarization. When $q_i = q_b$, the reflected beam is linearly polarised. By adjusting the azimuth angle of the polarizer (ψ) and analyser (*P*), the minimum intensity of light reaches the detector is achieved. The complex reflectance ratio, r_p/r_s is related to these parameters via

$$\frac{r_p}{r_s} = \tan(y)\exp(i\Delta) \tag{2.27}$$

where Δ (= 2*P* + π/2) is the phase difference in *p* and *s* vector. The complex refractive index, n_2 is then given as

(2.28)

$$n_2^* = \frac{\left[\sqrt{1-4\sin^2(q_1)\tan(y)\exp(i\Delta)+2\tan(y)\exp(i\Delta)+\tan^2(y)\exp(i\Delta)}\right]\sin(q_1)}{\cos(q_1)[1+\tan(y)\exp(i\Delta)]}$$

assuming the first medium is air.

Ellipsometry is more accurate than the transmission measurement as the former is a relative measurement to obtain r_p/r_s rather than measuring the absolute reflected intensity. From the phase difference in *s* and *p* vector, film thickness can be obtained down to sub-nanometre of accuracy theoretically, assuming the film composition is homogeneous, eg. free of contamination during deposition and the oxide layer can be neglected and has a smooth surface.

However, a spectral measurement requires a long time in order to obtain a pair of ψ and *P* for each wavelength. Therefore, such measurement method was only widely used after a century it was proposed where measurements can be conducted via a computer. Another disadvantage of such measurement is the difficulty of calculating γ is increasing for $\gamma < 10^4$ cm^{-1}. The reliability of the measurement primarily depends on the surface quality of the semiconductors and it was shown that the optical constants at the absorption band edge can vary considerably due to surface roughness and native oxide [91]. The precision of the measurement boils down to the accuracy in determining Δ which gives *K*, the imaginary component of *n** shown in equation (2.28). A standard deviation of as low as $\pm 0.02^o$ in Δ at 500 nm [92] gives a significant impact on γ with uncertainty of ± 500 cm^{-1} using equation (2.25). This is therefore transmission measurement is still preferable in estimating γ at low values of absorption.

2.5 Overview of Impact Ionisation

Impact ionisation is commonly observed in a diode when the electric field is sufficiently high where carriers are able to gain sufficient energy to promote another electron from valence to conduction band after collision with the lattice. Early works were demonstrated by McKay and McAfee [93] who showed photocurrent enhancement in Si and Ge *p-n* junction at near breakdown voltage, which behaved similarly to gases in the pre-breakdown region.

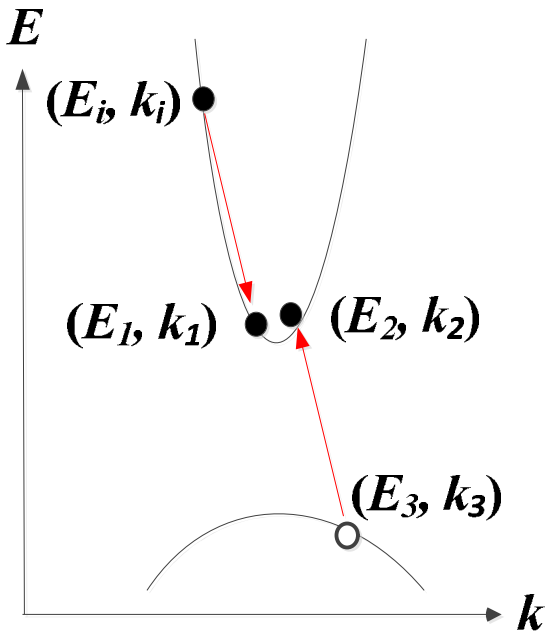

Figure 2.7 *E-k diagram during electron-initiated impact ionisation. Initial energy and momentum are labelled as i and the final states are labelled as 1, 2 and 3*

Figure 2.7 shows an ionisation process of a highly excited electron in the conduction band, with energy E_i and momentum k_i. After the collision, part of the energy is transferred to excite an electron from the valence to conduction band and therefore creates a hole in the valence band. The initial electron consequently loses energy and descends to a lower energy state, E_1 with momentum k_1 due to the conservation of momentum. While the primary and the secondary carriers are in the high field region, they may continue to impact ionise to create more electron-hole pairs and this process results in avalanche multiplication as illustrated in Figure 2.8.

To determine the carriers ionisation rates, threshold energy, E_{th} which is the minimum energy required to impact ionise have to be accurately known. From Figure 2.7, E_{th} should be larger than the bandgap since all particles have finite energy and momentum after ionisation process. Assuming both conduction and valence band are simple two parabolic bands as illustrated in Figure 2.7, Anderson and Crowell [94] showed that $E_{th} = 3/2\ E_g$ (shown in Appendix E) if electron and hole share the same mass and travelling at the same velocity. There were several attempts to calculate E_{th} based on a more realistic band structures [95-97]. Unfortunately, these approximations do not apply to all semiconductors as real band structures are very complex, resulting in an orientation-dependent E_{th} [98, 99]. Furthermore, the interaction of carriers with phonons causes the carriers ionising probability as a function of energy to increase gradually from zero and therefore a softer E_{th} [100, 101] is obtained.

Monte Carlo approaches therefore apparently give the most accurate results as the model simulates the carrier transport in a semiconductor by introducing a realistic band structure and phonon scattering mechanisms. Nevertheless, it has been shown by several authors that E_{th} can be treated as an adjustable parameter using an empirical expression

$$d = \frac{E_{th}}{z} \tag{2.29}$$

assuming ζ is constant, where d and ζ are the distance of a carrier must travel before it can impact ionise and electric field respectively [102, 103].

2.6 Impact Ionisation Models

One of the earliest impact ionisation models [93] was derived based on the Townsend theory, which describes the electron multiplication in gases prior to breakdown. Carrier ionisation rate, α_c, i.e. the average ionisation length is simply given by

$$a_c = \frac{1}{w}\frac{M-1}{M} \tag{2.30}$$

assuming ζ is constant, where M and w are multiplication and depletion width thickness respectively assuming equal rate of ionisation in electron and hole.

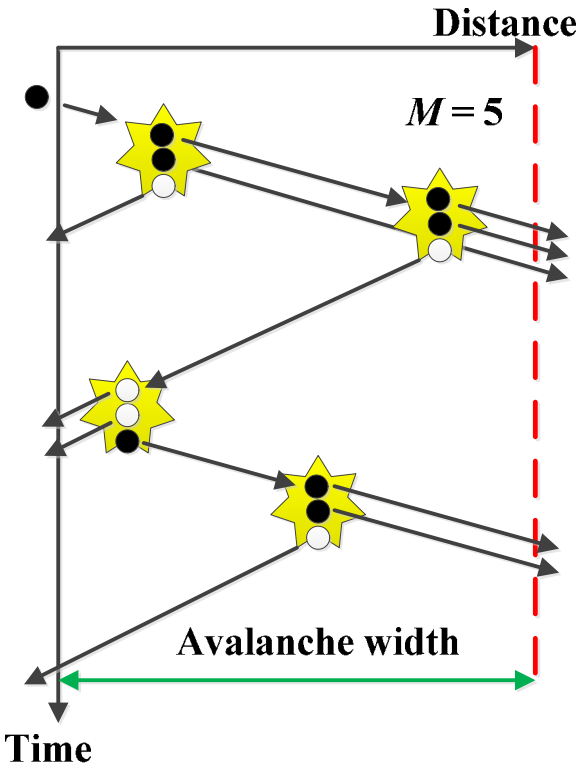

Figure 2.8 *Multiplication process initialized by an electron. Electrons are swept to +x direction while holes drift to –x direction.* $M_e = 5$.

In reality, electron and hole ionisation rates, α and β can be significantly different in several semiconductor materials. A more comprehensive model was formulated by McIntyre [104] where multiplication can be calculated for an arbitrary electric field in terms of α and β respectively, which is solely dependent on the electric field as

$$M(x) = \frac{\exp\left[-\int_x^w a(x') - b(x')dx'\right]}{1 - \int_0^w a(x')\exp\left[-\int_{x'}^w a(x'') - b(x'')dx''\right]dx'} \tag{2.31}$$

where x is the injection position of carriers within 0 to w with electron and hole travelling in $-x$ and $+x$ direction respectively as illustrated in Figure 2.8. These carriers were assumed to have ionisation probability density functions (PDF) expressed as perfect exponential function as shown in Figure 2.9.

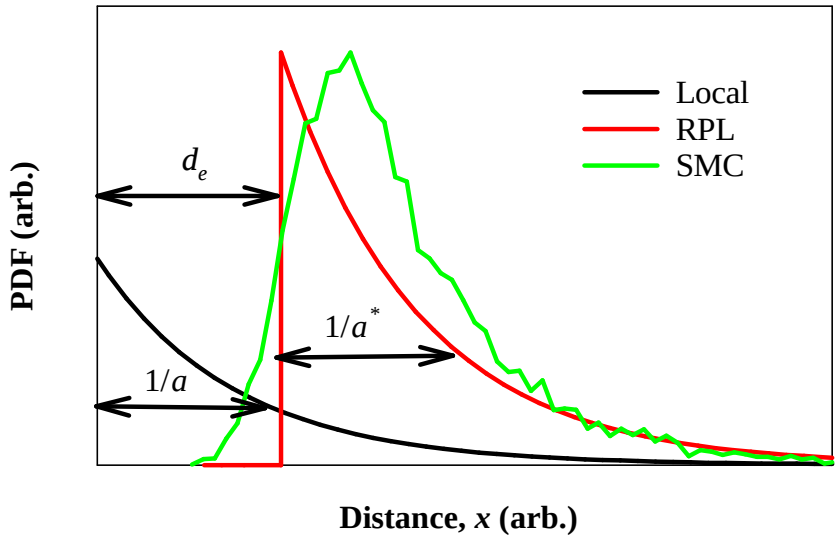

Figure 2.9 *The probability density functions (PDFs) assumed in McIntyre's local model and DSMT model, shown in black and red lines respectively. The PDF calculated from the simple Monte Carlo model is shown in green line.*

In a perfect PIN where the electric field is constant throughout w, equation (2.31) can be simplified to

$$M_e = \frac{1}{1-\frac{a}{b-a}\left[\exp\left(w(b-a)w\right)-1\right]} \tag{2.32}$$

$$M_h = \frac{1}{1-\frac{b}{a-b}\left[\exp\left(w(a-b)w\right)-1\right]}$$

assuming pure electron and hole initiated multiplication (M_e and $\underline{M_h}$) by injecting the carriers at $x = w$ and $x = 0$ respectively.

Later, Stillman and Wolfe [105] showed α and β can be expressed analytically in terms of M_e, M_h and w as

$$a = \frac{1}{w}\left(\frac{M_e - 1}{M_e - M_h}\right)\ln\left(\frac{M_e}{M_h}\right) \qquad b = \frac{1}{w}\left(\frac{M_h - 1}{M_e - M_h}\right)\ln\left(\frac{M_e}{M_h}\right) \tag{2.33}$$

In one extreme case where $\alpha=\beta$, equation (2.30) can be obtained whereas by setting β = 0 gives

$$a = \frac{1}{w}\ln(M_e) \tag{2.34}$$

by rearranging equation (2.31). However, equation (2.33) is valid for perfect PINs only and erroneous data may result when there is significant depletions into the doped cladding layers, especially in the thin PINs with w < 0.1 µm where a more complicated solution proposed by Grant [106] to extract α and β as a function of electric field is necessary.

Due to the randomness in the multiplication behaviour, each carrier may experience different multiplication and therefore there is a fluctuation in avalanche gain around the mean multiplication value. This is undesired as another noise source is being introduced to the external circuit, which will limit the maximum useful gain that can be obtained by an APD.

McIntyre formulated a noise theory [104] to determine the excess noise factor F_e (F_h) associated with M_e (M_h) as

$$F = kM + (1-k)\left(1-\frac{1}{M}\right) \tag{2.35}$$

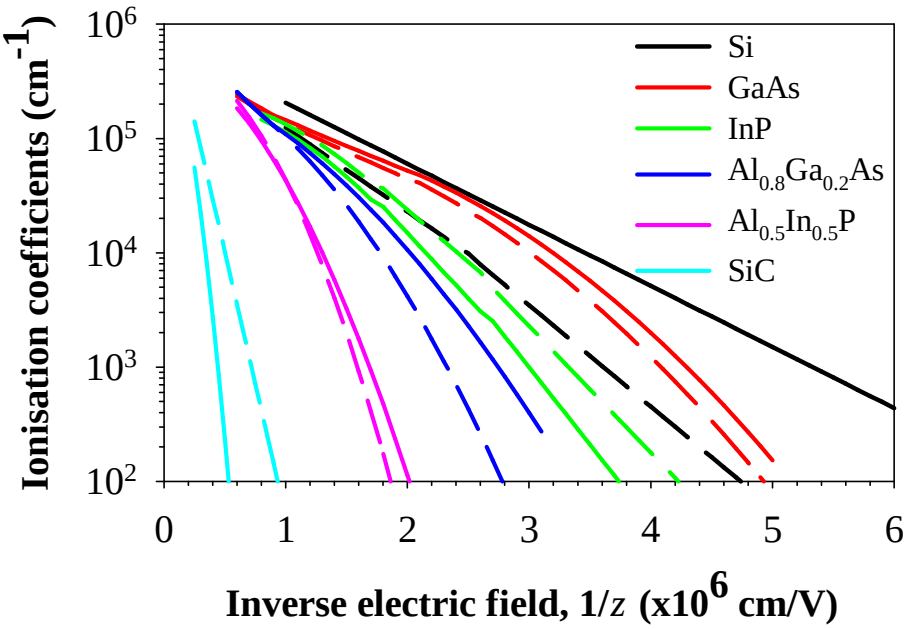

Figure 2.10 *Ionisation coefficients, α and β shown as solid and dashed lines respectively measured in several semiconductors [107-112] as a function of electric field.*

where k is the ionisation ratio given by β/α and α/β associated with M_e and M_h, respectively. From equation (2.35), it is apparent that k is solely dependent on the

electric field, and is an inherent property of a semiconductor material. The excess noise decreases as k approaches 0, with the carrier type more likely to ionise initiating the multiplication. It is empirically found that k decreases with electric field in most semiconductor materials as shown in Figure 2.10 where k of 0.1 can be obtained at a field of 250 kV/cm in Si. To achieve low excess noise, it is therefore desirable to have a thick avalanche region.

However, this local model is highly simplified as it assumes that the impact ionisation probability depends only on the local ionisation coefficients where the carrier is. Assuming a perfect PIN where the electric field is constant, the spatial ionisation coefficient, α_s (β_s) is constant throughout the structure, w as shown in Figure 2.11, i.e. α_s ($0 < x < w$) = α and β_s ($0 < x < w$) = α. Realistically, it may be necessary for a carrier to travel a certain distance in an electric-field to gain sufficient energy before it can ionise, i.e., the dead-space distance, d_e (d_h). Early measurements of impact-ionisation coefficients were undertaken on thick bulk-like structures, where the dead-spaces are small relative to the device dimensions and in which case equations (2.31) and (2.35) are accurate. As device dimensions decrease, the dead spaces result in device-dependent measured ionisation coefficients, α_{device} (β_{device}), which increasingly deviate from the local values of α (β) as the avalanching width of a device reduces, particularly at low electric fields [106, 113, 114], i.e. α_{device} (β_{device}) depends strongly on the width of the high-field region.

One simplistic yet convenient method for determining the multiplication (or avalanche gain) in such structures is by changing the limits to the integral in equation (2.31) [106, 114, 115] to account for the dead space while using device-independent ionisation coefficients, α' (β'), which are only functions of the electric-field. In this "modified" local model, carriers injected into the high field region are assumed "cold", i.e. they have zero kinetic energy and therefore there is no immediate ionisation possible. After the carriers travel their respective dead spaces, d_e (d_h), they are assumed to achieve equilibrium, i.e. to have ionisation coefficients of α' (β') and remained constant throughout the structure as shown in Figure 2.11. The spatial ionisation coefficient, α_s (β_s) can be expressed as

$$\begin{aligned} a_s(x) &= 0 \quad 0 \le x < d_e \\ a_s(x) &= a' \quad d_e < x < w \end{aligned} \tag{2.36a}$$

(2.36b)

$$b_s(x) = 0 \quad w - d_h < x < w_e$$
$$b_s(x) = b' \quad 0 < x < w - d_h$$

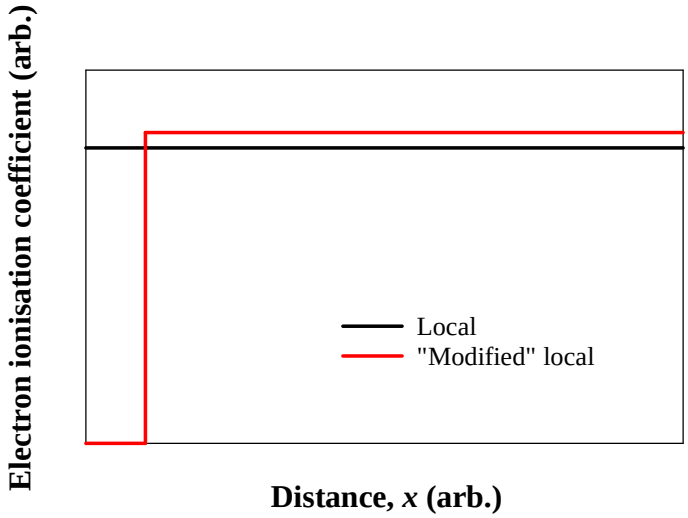

Figure 2.11 *Spatial ionisation coefficients in local and "modified" local model shown in black and red lines respectively.*

The quantities α' (β') are available for many semiconductor materials in the literature and have often been obtained by correcting α_{device} (β_{device}), to account for the effect of the dead space on the multiplication. A simplified form of the comprehensive treatment by Okuto *et. al*. [94], was suggested by Bulman *et. al*. [113] as

$$1 - \frac{1}{M_e} = \exp\left[\int_0^{d_e} b'(x)dx\right] \int_{d_e}^{w} a'(x') \exp\left[-\int_{d_e}^{x} a'(x') - b'(x')dx'\right] dx \tag{2.37}$$

A similar equation can be obtained for M_h by interchanging α' and d_e with β' and d_h respectively. Using a first order approximation, i.e. $\exp(x) \approx 1 + x$, M_e (M_h) can be written in terms of α' (β') as

$$1 - \frac{1}{M_e} \approx -a'(d_e - w)(1 + b'd_e)$$
$$1 - \frac{1}{M_h} \approx -b'(d_h - w)(1 + a'd_h) \tag{2.38}$$

where α' (β') can be solved iteratively. While multiplication characteristics obtained in this manner work quite well over a range of electric-fields and device dimensions down to 0.1µm [110, 116], this technique does not allow accurate prediction of the excess

noise when dead-space effects are important [117, 118]. Instead, the avalanche noise reduces with device dimension (β/α approaches 1 as those devices breakdown fields are > 600 kV/cm) [117, 118]), which is against the McIntyre prediction.

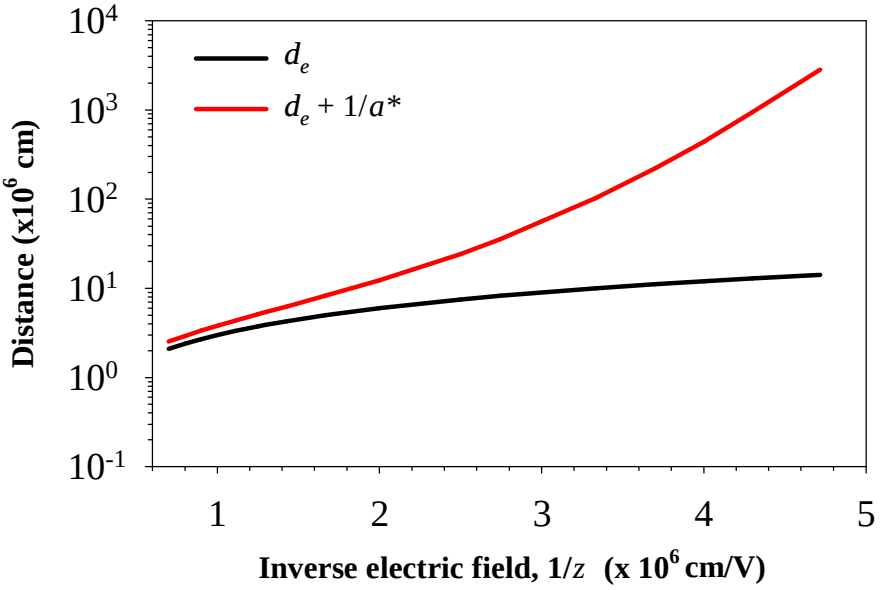

Figure 2.12 *The mean ionising length of an electron in GaAs and its corresponding dead space plotted as red and black lines respectively.*

A comprehensive study of the effect of dead space on the avalanche excess noise was demonstrated by Ong et. al. [119] using a Monte Carlo model where the carriers dead spaces and mean ionising lengths at different electric fields were compared. At a relatively low electric field, the mean ionising length is much longer than the carrier dead space as shown in Figure 2.12 and therefore the local model predicted noise is valid. However, as the device dimension shrinks and the electric field strength required to achieve a given gain increases, the carriers' mean ionising length reduces quickly and is comparable to its dead space. This results in a more deterministic ionisation which leads to a lower excess noise. By extrapolating the mean ionising distance to higher fields in Figure 2.12 leads to an extreme case where a carrier can impact ionise immediately right after it travels the dead space. This resembles the ionisation process in a photomultiplier tube where noiseless avalanche multiplication, i.e. $F = 1$ can be achieved.

2.6.1 Recurrence model

One of the first models to successfully predict the excess noise and multiplication in devices with thin sub-micron avalanche widths was developed by

Hayat et al. [120], which the model is based on branching process [121]. The dead-space multiplication theory (DSMT) is capable of calculating the multiplication and excess noise of PIN devices down to avalanche widths of 0.1 μm [122, 123].

Consider an APD with an avalanche width, w with electric field pointing from right to left as shown in Figure 2.8. Assuming an electron-hole pair is injected at position x_0 and ionise at x, the electron and hole ionisation PDF with the presence of dead space, $h_e(x|\,x_0)$ and $h_h(x|\,x_0)$ respectively are given by,

$$h_e(x \mid x_0) = \begin{cases} 0 & , x - x_0 \le d_e \\ a^* \exp\left[-a^*\left(x - x_0 - d_e\right)\right] & , x - x_0 > d_e \end{cases} \tag{2.39}$$

and

$$h_h(x \mid x_0) = \begin{cases} 0 & , x_0 - x \le d_h \\ b^* \exp\left[-b^*\left(x_0 - x - d_h\right)\right] & , x_0 - x > d_h \end{cases} \tag{2.40}$$

where d_e and d_h, are electron and hole dead spaces related to the electric field, ζ shown in equation (2.29) while α^* and β^* are electron and hole enabled ionisation coefficients, which is the ionisation coefficients after the carriers travelled their respective dead spaces. The PDF used in the DSMT model is similar to that of McIntyre's local model, which is a displaced exponential decay function as shown in Figure 2.9. It should be stressed that these parameters are dissimilar compared to α's and β's mentioned above, and will be discussed in detail later in Chapter 4. $z(x_0)$ and $y(x_0)$ are the average number of electrons and holes generated and can be expressed as

$$z(x_0) = \left[1 - \int_{x_0}^{w} h_e(x \mid x_0)dx\right] + \int_{x_0}^{w} \left[2z(x) + y(x)\right] h_e(x \mid x_0)dx \tag{2.41}$$

and

$$y(x_0) = \left[1 - \int_{0}^{x_0} h_h(x \mid x_0)dx\right] + \int_{0}^{x_0} \left[2y(x) + z(x)\right] h_h(x \mid x_0)dx \tag{2.42}$$

Equation (2.41) has two components where the first term accounts for the probability that the electron does not impact ionise at all from x_0 to the end of depletion width while

the second term describes the electron with a ionising PDF, $h_e(x|\ x_0)$ to ionise another electron-hole pair (and therefore the term $2z(x) + y(x)$ in the equation). A similar expression applies for holes as shown in equation (2.42). These equations can be solved numerically and the mean multiplication, M is expressed as

$$M(x_0) = \frac{z(x_0) + y(x_0)}{2} \tag{2.43}$$

The excess noise factor, F is given by

$$F = \frac{< M^2 >}{< M >^2} \tag{2.44}$$

which can be written as

$$F(x_0) = \frac{z_2(x_0) + 2z(x_0)y(x_0) + y_2(x_0)}{\left(z(x_0) + y(x_0)\right)^2} \tag{2.45}$$

where the second moment of $z(x_0)$ and $y(x_0)$, $z^2(x_0)$ and $y^2(x_0)$ are expressed as

$$z_2(x_0) = \left[1 - \int_{x_0}^{w} h_e(x \mid x_0)dx\right] + \int_{x_0}^{w} \left[4z^2(x) + y^2(x) + 4z(x)y(x)\right] h_e(x \mid x_0)dx \tag{2.46}$$

and

$$y_2(x_0) = \left[1 - \int_{0}^{x_0} h_h(x \mid x_0)dx\right] + \int_{0}^{x_0} \left[4y^2(x) + z^2(x) + 4z(x)y(x)\right] h_h(x \mid x_0)dx \tag{2.47}$$

2.6.2 Random Path Length (RPL) model

An alternative way to calculate multiplication and excess noise with the presence of dead space is the RPL model. Essentially, RPL and DSMT models are equivalent as both models use the same expressions for the carriers PDF as shown in equation (2.39) and (2.40), however the former calculate the multiplication and noise via a numerical iteration while the latter uses a Monte Carlo method. As shown in Figure 2.13, indistinguishable multiplication and excess noise are obtained in a 1.0 μm Si PIN simulated from RPL and DSMT model by using the same ionisation coefficients [108] and threshold energies [124]. The random path length (RPL) model was developed by Ong *et al*. [122] and they demonstrated both multiplication and excess noise can be predicted in PINs successfully down to w = 0.05 μm.

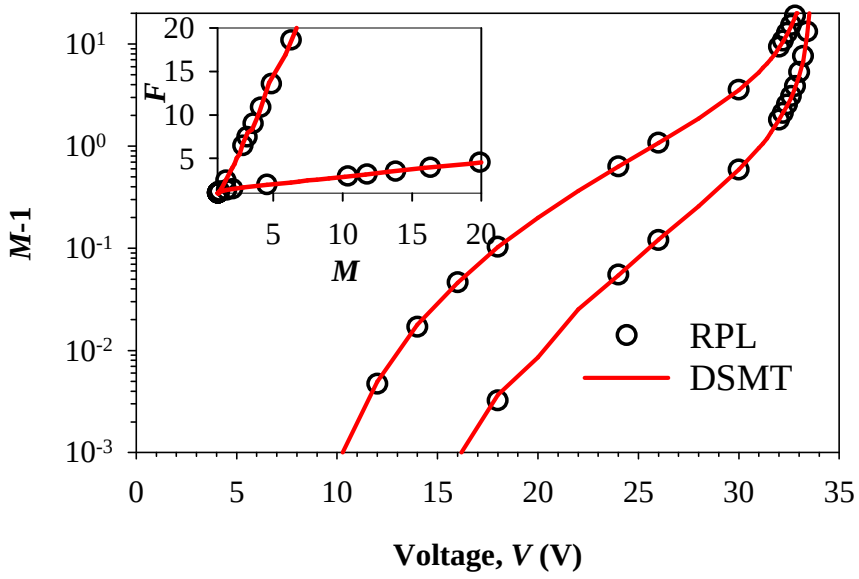

Figure 2.13 *Simulated multiplication (M-1) of a Si 1.0 µm PIN obtained from RPL (○) and DSMT (line). Also shown the calculated noise (F) in the inset.*

Assuming an electron is injected at position x_0, the probability to ionise within x, $P_e(x_0<y<x|\, x_0)$ can be computed by integrating the PDF from $x_0 + d_e$ to x to give,

$$P_e(x_0 < y < x \mid x_0) = \begin{cases} 0 & , x - x_0 \le d_e \\ 1 - \exp\left[-a^*(x - d_e)\right] & , x - x_0 > d_e \end{cases} \tag{2.48}$$

The survival probability, $S_e(x_0<y<x \mid x_0)$ is simply the probability that the electron does not impact ionise up to position x and is given by,

$$S_e(x_0 < y < x \mid x_0) = 1 - P_e(x \mid x_0) = \begin{cases} 1 & , x - x_0 \le d_e \\ \exp\left[-a^*(x - d_e)\right] & , x - x_0 > d_e \end{cases} \tag{2.49}$$

$S_e(x_0<y<x \mid x_0)$ can be denoted as a variable r, a uniformly distributed random number which has a value from 0 to 1. Rearranging equation (2.49) yields

$$x = d_e - \frac{\ln(r)}{a^*} \tag{2.50}$$

where x is the distance an electron travels before it impact ionises.

By replacing d_e, h_e, P_e, S_e and α^* to d_h, h_h, P_h, S_h and β^*, similar arguments in equation (2.48)-(2.50) can be obtained for holes.

Consider an electron injected in the depletion width, w with a constant electric field at x = 0 as illustrated in Figure 2.8. A pseudo-random-number generator (PRNG) is used to

generate a random number, r to determine the ionising length of the primary electron and these numbers are independent of each other. The program keeps track of the position of electrons and holes where they impact ionise until all carriers exit w completely. To obtain a reliable result with an error < 1 %, the simulation is repeated for N trial until the results converge as shown in Figure 2.14. The mean multiplication, $M(x_0)$ is written as

$$M(x_0) = \frac{M_1 + M_2 + M_3 + ... + M_{n^{th}}}{N} = \sum_{N=1}^{N} M_N \tag{2.51}$$

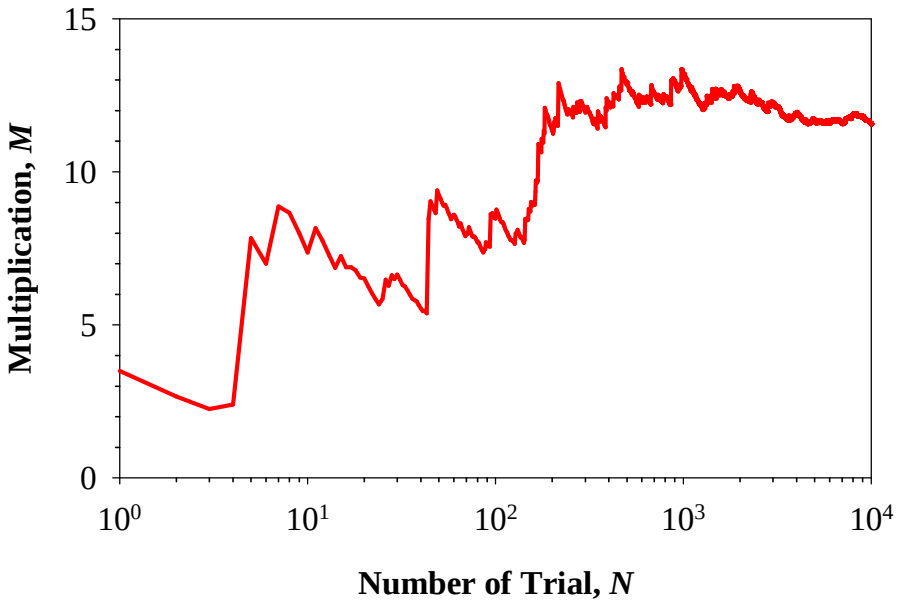

Figure 2.14 *Simulation of RPL model of multiplication factor versus number of trials. Consistent gain of 11.7 can be roughly achieved after 5000 trials are performed.*

Excess noise, F can be calculated using

$$F(x_0) = \frac{1}{NM^2(x_0)} \sum_{N=1}^{N} M_N{}^2 \tag{2.52}$$

2.6.3 Simple Monte Carlo (SMC) model

Several Full Band Monte Carlo (FBMC) models [102, 125-127] were demonstrated to accurately predict the carriers transport properties, i.e. saturation velocities and energies as a function of doping densities, temperature and electric field strength. This allows an accurate simulation of the bandwidth [128], multiplication and noise in a simple or

complex APD structure [119, 129] and even the breakdown probability in a single photon avalanche detector [130]. The success of the model is due to its ability to simulate realistically the carriers transport by including several scattering processes such as acoustic, optical and polar optical phonon scattering. However, this requires a good knowledge of the band structure as well as inter and intra valley (*Γ*, *X* and *L*) scattering rates, which is the main drawback of the model as these parameters are usually available only in well-established semiconductor materials like Si, GaAs and InP.

Plimmer *et al.* [131] demonstrated that by assuming two parabolic bands which represent the valence and conduction bands similar to Figure 2.7, the simple Monte Carlo (SMC) model simulated electron and hole ionisation PDFs can be similar to those obtained from the FBMC model and therefore successfully reproduce the multiplication and noise down to w = 0.025 μm in GaAs. While using a small number of input parameters, the model was proven to work in other semiconductors such as Si and InAlAs over a wide electric field range [132, 133] and it is not as computationally intensive as the FBMC model. However, due to the over-simplified band structure, the SMC model is not capable of simulating carrier energies and velocities, or determining the contribution of different valleys to carriers' ionisation.

The SMC model description [131] is summarised as follows. A carrier is launched into the high-field region and accelerate ballistically for a certain amount of time, i.e. free flight time, t before it collides with a phonon. The scattering mechanisms could be phonon-absorption, emission or impact ionisation and their respective scattering rates are Γ_{ab}, Γ_{em}, and Γ_{ii}. Both Γ_{ab}, Γ_{em} vary with carrier energy, E given as

$$\Gamma_{ab}(E) = \frac{Z}{l(2Z+1)}\sqrt{\frac{2(E+\hbar w)}{m^*}} \tag{2.53}$$

and

$$\Gamma_{em}(E) = \frac{Z+1}{l(2Z+1)}\sqrt{\frac{2(E-\hbar w)}{m^*}} \tag{2.54}$$

where m^*, Z, λ and $\hbar\omega$ are carriers effective masses, phonon occupational number expressed as $Z=[\exp(\hbar\omega/k_bT) - 1]^{-1}$, mean free path of phonon scattering and average phonon energy respectively.

Impact ionisation is allowed to occur when a carrier's energy exceeds the ionisation threshold energy, E_{th}. The model adopts the formulation similar to that of Keldysh [134] to determine the ionisation rate, shown as

$$\Gamma_{ii}(E) = C_{it}\left(\frac{E - E_{th}}{E_{th}}\right)^{g} \tag{2.55}$$

where C_{ii} is an adjustable parameter while γ is the softness factor in the ionisation rate. The PDF of the carrier free flight time, $P(t)$ determines t to encounter a scattering event and this is given by

$$P(t) = \Gamma_{tot}(E(t))\exp\left(-\int_0^t \Gamma_{tot}(E(t))dt\right) \tag{2.56}$$

where Γ_{tot} is the sum of Γ_{ab}, Γ_{em} and Γ_{ii}. To simplify the complexity in integrating equation (2.56) without changing the distribution probability of the free flight time, an artificial self-scattering mechanism, Γ_{ss} is introduced [135]. The values of $\Gamma_{ss}(E)$ are chosen in such a way that the sum of these scattering rates, $\Gamma_0(E) = \Gamma_{tot}(E) + \Gamma_{ss}(E)$. Equation (2.56) can now be rewritten as

$$P(t) = \Gamma_0 \exp\left(-\int_0^t \Gamma_0 dt\right). \tag{2.57}$$

The free flight time is determined by integrating equation (2.57) with a limit from 0 to t and after rearranging the equation gives

$$t = \frac{-\ln(r)}{\Gamma_0}. \tag{2.58}$$

where r is the probability of the carrier collision obtained from a random number generator, which is uniformly distributed between 0 to 1. The carrier position (z_{new}, z_{old}) and the corresponding wave vector (k_z^{new}, k_z^{old}) prior to and after the free-flight are given as

$$z_{new} = z_{old} + \frac{\hbar k_z^{old} t}{m^*} + \frac{qFt^2}{2m^*}. \tag{2.59}$$

and

$$k_z^{new} = k_z^{old} + \frac{qFt}{\mathbf{h}}. \tag{2.60}$$

while the resultant carrier energy, E_{new} is

$$E_{new} = \frac{\mathbf{h}^2}{2m^*}\left[(k_x^{old})^2 + (k_y^{old})^2 + (k_z^{new})^2\right] \tag{2.61}$$

where k_x and ky are the wave vectors which are vector components perpendicular to the direction of the field.

After the free-flight, the carrier is scattered and another random number, r_2 is generated (uniformly distributed from 0 to 1) to determine the p^{th} (p = 1, 2, 3, 4) scattering mechanism which satisfies the condition

$$\frac{\sum_{i=1}^{p-1}\Gamma_i(E)}{\Gamma_0} < r_2 < \frac{\sum_{i=1}^{p}\Gamma_i(E)}{\Gamma_0}. \tag{2.62}$$

as illustrated Figure 2.15.

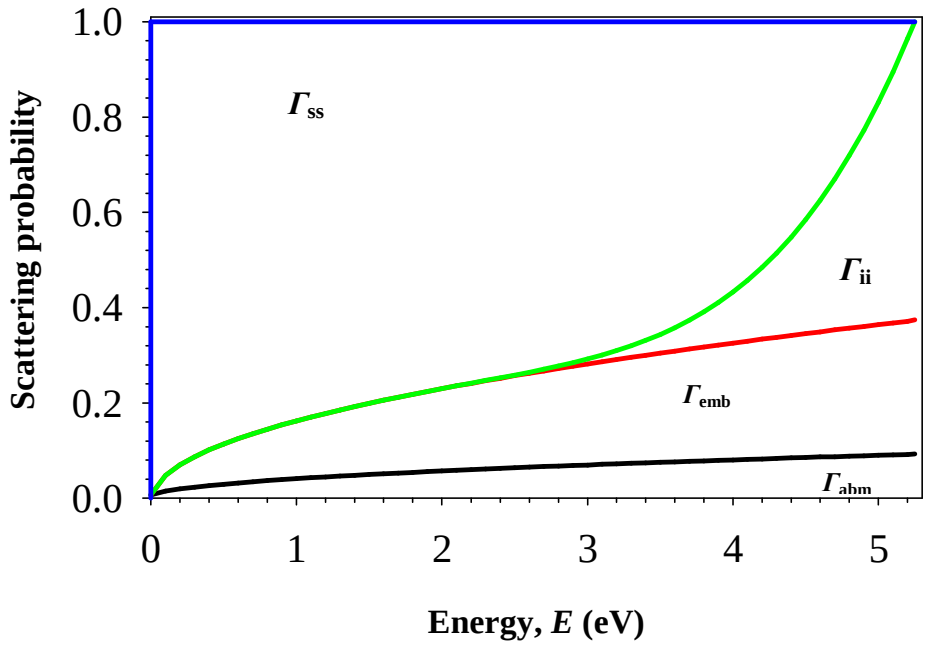

Figure 2.15 *Scattering probability in a typical semiconductor where scattering mechanisms, n = 1 to 4 are Γ_{ab}, Γ_{em}, Γ_{ii} and Γ_{ss} respectively.*

After a scattering event (except self-scattering mechanism where a carrier retains its previous energy and wave vector), the carrier energy is updated accordingly (i.e. $E_{new} = E_{old} - \hbar w$ in phonon emission while $E_{new} = E_{old} + \hbar w$ in phonon absorption) and the wave vectors (k_x^{new}, k_y^{new}, k_z^{new}) are recalculated to determine the carrier's new

momentum. Using E_{new}, the magnitude of the wave vectors, k_{xyz}^2 (= $k_x^2 + k_y^2 + k_z^2 = k_{xy}^2 + k_z^2$) is computed from equation (2.61). Subsequently, k_{xyz} is resolved to k_{xy} and k_z vector at a certain angle, q as

$$(k_{xyz}^{new}\cos q)^2 + (k_{xyz}^{new}\sin q)^2 = k_{xyz}^{new^2} \tag{2.63}$$

where $\cos^2 q = 2r_3 - 1$. The parameter r_3 is a random number uniformly distributed between 0 and 1 while $\sin^2 q$ can be computed from trigonometry as $\cos^2 q + \sin^2 q = 1$. In an impact ionisation event, the carrier excess energy (after subtracting E_{th}) is assumed to be divided equally among the three carriers. The new carriers' wave vector is randomised again using equation (2.63). The model uses equation (2.58)-(2.63) to track carriers and compute both M and F in a similar method as the RPL model.

Note that the periodicity of the employed pseudo-random number generator must be greater than the call frequency of random numbers (~ 10^9) to ensure the random numbers are truly randomly distributed.

The model can then be used to calculate the carriers' PDFs and mean ionisation length, $1/\alpha_{MC}$ ($1/\beta_{MC}$), by logging each trial ionisation length. An example of a PDF calculated by SMC is shown in Figure 2.9. Again, the Monte Carlo PDF is a more realistic approximation compared to that of recurrence/RPL due to the consideration of soft threshold energy, as discussed in section 2.5. Nevertheless, such PDF can be approximated by a perfect exponential decay using equation (2.39) shown in Figure 2.9 with good accuracy of computed multiplication and excess noise in the recurrence/RPL model. The details can be found in Chapter 5.

The summary of α's (β's) used in this chapter, namely α (β), α_{device} (β_{device}), α' (β'), α^* (β^*), α_{MC} (β_{MC}), α_s (β_s) can be found in Appendix B.

Chapter 3 EXPERIMENTAL TECHNIQUES

3.1 Introduction

This chapter describes the experiment techniques used to perform measurements on devices in this work at room temperature. These characterisations are crucial to interpret the absorption and avalanche behaviours accurately. The current-voltage (*I*-*V*) measurements were carried out to obtain the dark current in devices up to the breakdown voltages while capacitance voltage (*C*-*V*) measurements determine the thicknesses and background doping levels of the depletion regions, as well as the doping densities in the cladding layers. Photocurrent measurements reveal the spectral responses of devices, at a given bias voltage. The photo-multiplication measurements were performed by illuminating these devices using monochromatic light and the resulting photocurrent was measured as a function of bias voltage.

3.2 Electrical Characterisation

3.2.1 Dark Current Voltage (I-V) Measurement

An HP4140B pico-ammeter or Keithley 236/237/238 Source Measurement Unit (SMU) was used to source voltages and subsequently measure the dark current of the device under test (DUT) via the control of PCs through a GPIB cable. Specifications of SMUs are tabulated as follow.

Table 3.1 *Applied voltage, measured current range and resolution of SMUs. Keithley 236/237/2*

Manufacturer	Hewlett-Packard	Keithley Instruments		
Model number	HP4140B	236	237	238
Applied voltage range (V)	0.00 to ±100.0	0 to ±110.00	0 to ±1100.0	0 to ±110.00
Measured current range (*I*)	1 fA to ±10 mA	0.01 pA to ±100.000 mA	0.01 pA to ±100.000 mA	0.01 pA to ±1.0001 A

All SMUs are able to provide the voltages required since the breakdown voltages of all samples measured are lower than 100.0 V. Considering the samples studied in this work are wide bandgap materials, very low reverse dark currents of subpico-amps prior to device breakdown is expected. However, several factors may result in extraneous current generated within the system which masks the results of the measurement. Depending on the quality of the interconnecting coaxial cables, the potential difference between the core and the outer shield could result in a significant leakage current of a few nano-amps. Stray capacitance of the cables, C_c may cause a charging current, I_c during current-voltage sweeping, which is given by

$$I_c = C_c \frac{dV}{dt}. \tag{3.1}$$

Frictional and mechanical stress due to vibration and bending of the cables could also lead to triboelectric and piezoelectric effects respectively. Dirty surfaces and probe tips may introduce charge to the system when a bias is applied while a ground loop results in a current flow between nominal ground points. As the devices in this work are sensitive to visible light, the presence of ambient light can contribute to the photocurrent.

To prevent the complications mentioned, high resistance BNC cables of > 1 TΩ were used, cables length were kept at the minimum, the setup was vibration-free with a probe station and SMUs share a common ground, probe needles and glass slides were cleaned with IPA solution and the devices were shielded from light before measurements were performed. The open circuit noise floor level of the setup (this was done by connecting one of the terminals to the glass slide while leaving another probe hanging) was less than ±10 pA as shown in Figure 3.1 up to 70 V.

The connecting cables were kept as short as possible with lengths less than a metre each and therefore the parasitic resistance are negligible.

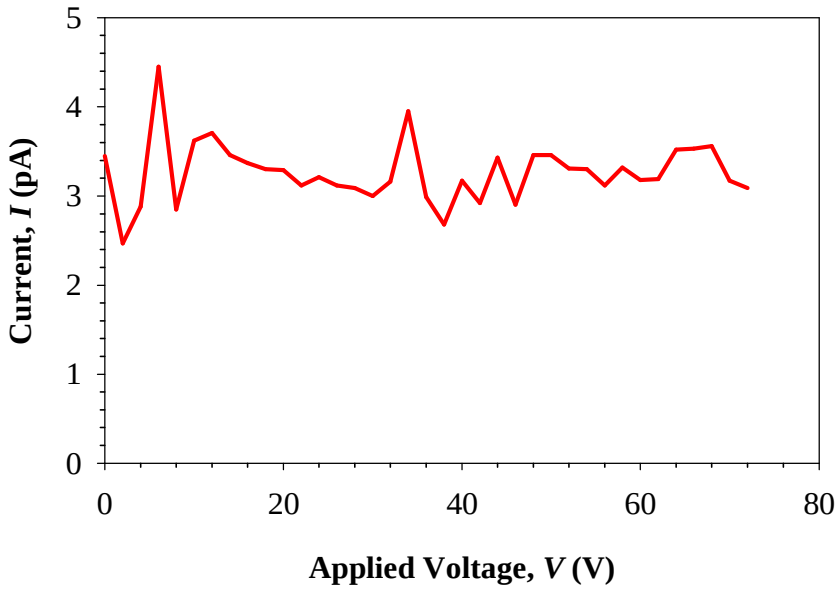

Figure 3.1 *Measured stray current in picoammeter HP-4140B*

3.2.2 Capacitance Voltage (C-V) Measurement

C-V measurements were performed to obtain the capacitance, built-in voltage and doping profile of a DUT. The DUT was biased by a DC voltage together with a small AC signal using HP 4275A LCR meter as shown in Figure 3.2.

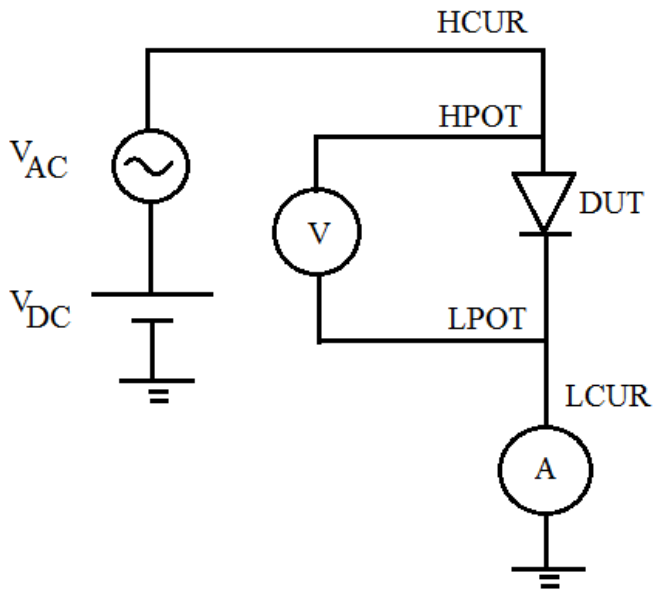

Figure 3.2 *Schematic of C-V measurement. HCUR. HPOT, LPOT, LCUR are high current, high potential, low potential, low current respectively.*

The capacitance of a DUT, *C* can be calculated by

$$C = \frac{I_a}{2pfV_a}. \tag{3.2}$$

where I_a, V_a and f are AC current, AC voltage across DUT and test frequency respectively.

The specifications of the LCR meter are as follow.

Table 3.2 *Specifications of HP4275A*

DC voltage	0 to ±100 V, maximum step resolution of 1 mV
AC signal	1 mV to 1 V
Frequency options	10 kHz, 20 kHz, 40 kHz, 100 kHz, 200 kHz, 400 kHz, 1 MHz, 2 MHz, 4 MHz, 10 MHz
Circuit mode	Series or parallel
Measured Capacitance (C)	1 fF to 100.00 μF

The applied AC signal must be sufficiently large to be measured accurately by the AC voltmeter and ammeter. Alternatively, a high test frequency can be applied to lower the reactance of the capacitor. The AC signal amplitude however, should be negligible compared to the DC voltage supply to measure the capacitance more accurately for a given DC bias voltage.

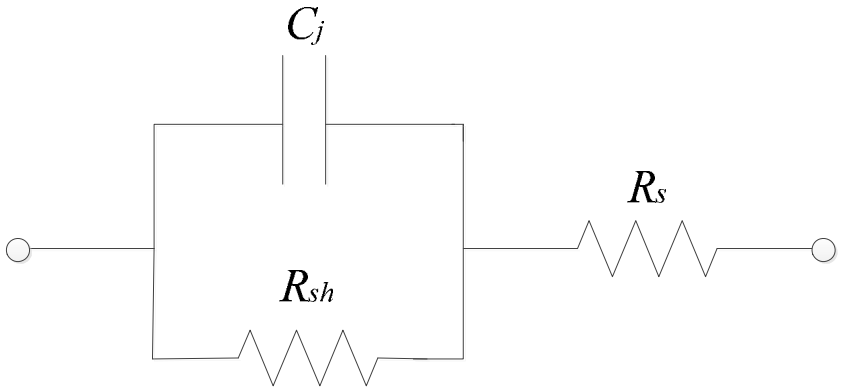

Figure 3.3 *AC model of p-n diode*

The LCR meter measures the effective impedance across the DUT. Therefore, choosing the right equivalent circuit model (series or parallel model) is crucial for a good

estimation of diode capacitance. AC model of a reverse-biased diode is shown in Figure 3.3.

In this work, the capacitance reactance is much higher than the series resistance and is negligible compared to the shunt resistance. Therefore, either series or parallel model can be used as the difference using these models is minimal. In an ideal capacitor, voltage lags current by 90º. However, the phase angle can deviate from 90º when the DUT leakage current is high due to a low shunt resistance. This problem can be addressed by increasing the test frequency and therefore reducing its reactance. Typically, DUTs were tested with an AC signal of ~ 0.05 V at a frequency of 1 MHz. Devices with different radii were probed to make sure good agreement in the capacitances per unit area.

The depletion width, w can be obtained from the measured junction capacitance of the diode, C_j using

$$C_j = \frac{eA}{d} \tag{3.3}$$

where A is the cross section area of the diode.

The capacitance reduces with increasing reverse bias voltage due to a wider depletion width and this relationship can be expressed as

$$C_j = \sqrt{\frac{qeN_a}{2V_T}} \tag{3.4}$$

assuming a one sided p-n^+ diode with an abrupt junction. Rearranging equation (3.4) yields

$$\frac{1}{C_j^{\,2}} = \frac{2}{qeN_a} V_T = \frac{2}{qeN_a}(V_{bi} - V_a) \tag{3.5}$$

A linear graph can be obtained by plotting $1/C_j^2$ versus V_a and the built-in voltage, V_{bi} is the x-axis intercept. All diodes in this work were not one-sided junction and therefore extraction of V_{bi} from equation (3.5) is not valid. Nevertheless, the depletion in the diodes can be reduced to that of a one-sided junction by forward-biasing these diodes

slightly and this enables the estimation of V_{bi} as illustrated in Figure 3.4. Assuming that both p^+ and n^+ claddings are heavily doped such that their Fermi levels are the same as that of valence and conduction bands respectively, the theoretical maximum built-in voltage is the band-gap of the semiconductor material. In all AlInP diodes, V_{bi} was found to be 2.0 V and this is a reasonable value compared to the band-gap of AlInP obtained experimentally [136, 137].

By differentiating equation (3.5),

$$\frac{d\left(\frac{1}{C_j^{\,2}}\right)}{dV} = -\frac{2}{qeN_a} \tag{3.6}$$

the doping concentrations in the un-doped and cladding region can be calculated.

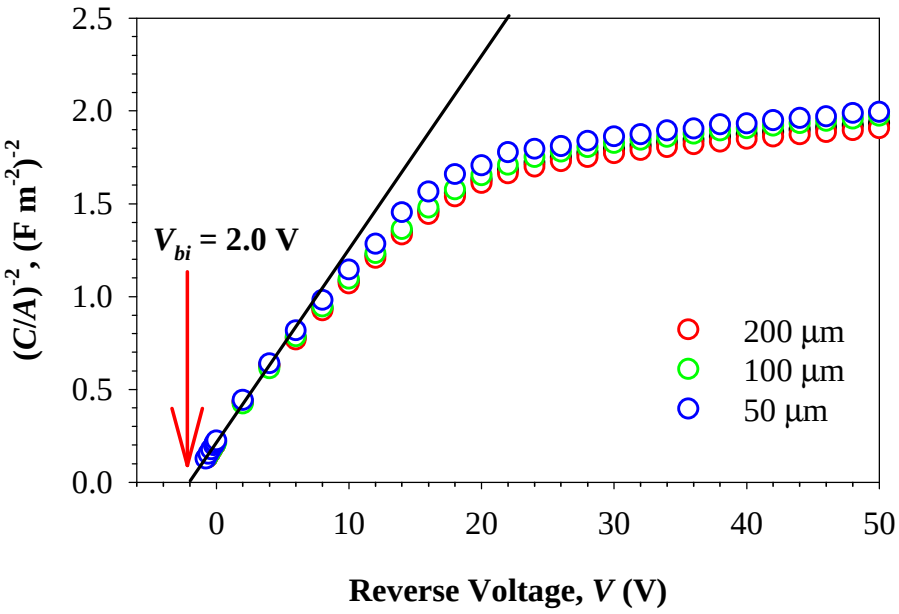

Figure 3.4 $\frac{1}{C_j^{\,2}}$ *vs. bias voltage obtained from the C-V measurement in an AlInP PIN with device radii of 200, 100 and 50 µm.*

The analytical expressions to calculate the capacitance in a complex *p-p-p-p-n* structure is shown in Appendix A, assuming the doping density in each layer is uniform. The model is used to model the *C-V* in all devices used in this work.

3.3 Photocurrent Measurement

The photo-response of a photodiode is measured by using a setup which comprises a Horiba Scientific iHR320 monochromator, Keithley 236/237 SMU, Standford Research SR830 lock-in amplifier (LIA), chopper and desktop computer with data acquisition module (DAM) installed.

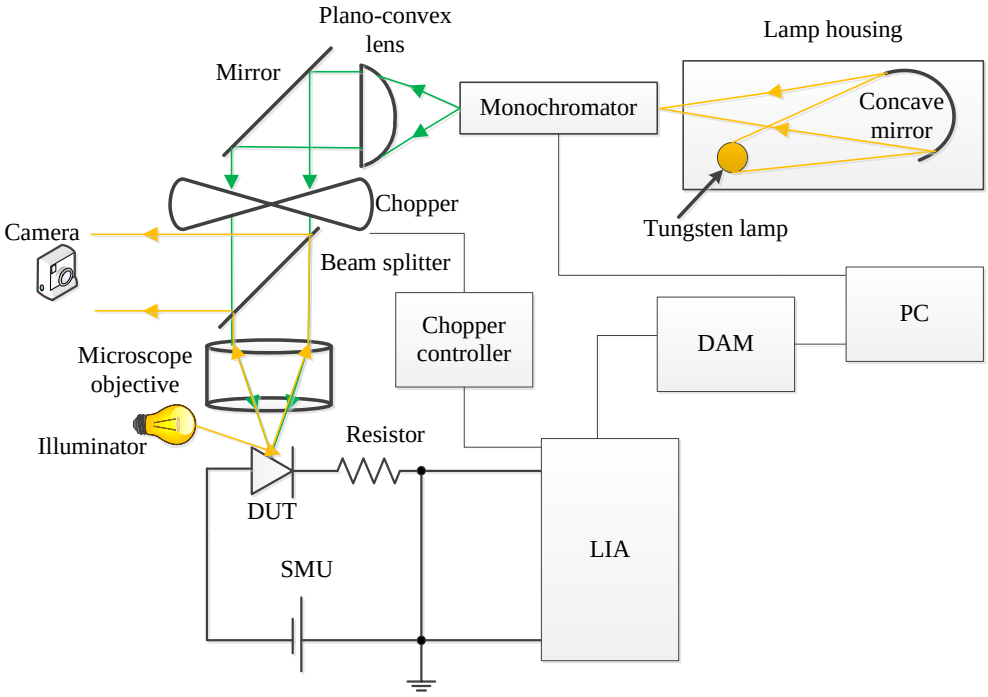

Figure 3.5 *Schematic diagram of experimental setup for photocurrent AC measurement*

As illustrated in Figure 3.5, the monochromatic light is chopped to modulate the optical signal. The frequency of chopper can be of any frequencies less than the cut-off frequency of the device or the cables, whichever that gives a lower value. Frequencies at the multiples of 50 Hz, however are not recommended to avoid interference by the line frequency. The beam is subsequently focused on the optical window of the DUT by a microscope objective and the resultant photocurrent is measured by a LIA through the voltage drop of the resistor. The voltage output of the LIA, V_{LIA} is given by

$$V_{LIA} = \frac{\text{Reading of LIA}}{\text{Sensitivity of LIA}} \times 10V \,. \tag{3.7}$$

where it is digitised by the DAM and subsequently read by the PC.

In this work, a 100 Watt tungsten bulb is used as the light source. Although the light intensity varies with wavelength due to its blackbody response and the grating

response, , it still has a relatively smooth spectrum in the visible light regime. As all optics involved in the setup such as lenses, mirrors and grating have different transmissions or efficiencies, the output power across the wavelength of interest is measured using a commercial PD.

As the tungsten bulb is not a point source, the focused spot size appeared to be large, ~ 1 mm × 2 mm. The area of illumination hence, is much larger than the optical window of DUTs, i.e. only a fraction of the incident beam power is illuminating the mesa optical window. The Hamamatsu PD S5973-02 [138] is chosen as the commercial photodiode to calculate the responsivity of the DUTs as its photosensitive area (radius of 200 μm) is similar to the largest devices in this work. Furthermore, the commercial photodiode has a near unity responsivity from 400 to 600 nm and this allows accurate estimation of the power for a given wavelength. The optical power on DUTs, however is less than that falling on the commercial device due to the large metal contacts. The incident power on the DUT was determined by scaling the incident power obtained from the commercial photodiode proportionally with area, assuming the power density is uniform across the optical window. The photosensitive area of our 210 μm radii devices was determined to be ~ 63 % of that of a commercial photodiode. The area was estimated by printing a magnified image of a 210 μm radius device on a gridded graph paper.

3.3.1 Monochromator

The iHR320 monochromator is a Czerny-Turner monochromator, as shown in Figure 3.6. First, polychromatic light is focused at the entrance slit via a concave mirror which is installed in the lamp housing. The light is then collimated by the concave mirror and refracted by the grating to split the polychromatic light into individual wavelengths. The monochromatic light is brought into focus again using a concave mirror. Selecting a wavelength on the PC rotates the angle, θ of the grating such that the intended wavelength is focused at the exit slit of monochromator. To ensure the maximum throughput, the F-number of the tungsten lamp housing and the collimating lens must match the same F number as the monochromator.

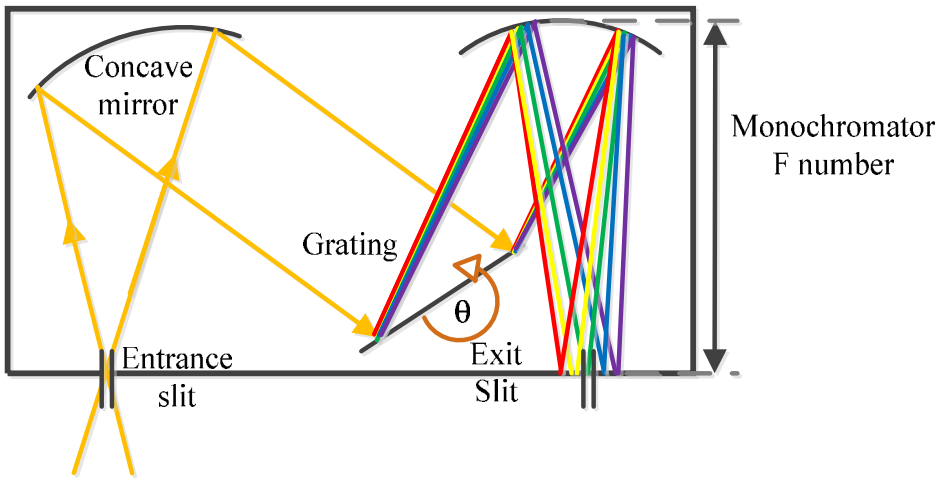

Figure 3.6 *Diagram of a Czerny-Turner monochromator*

The diffraction grating that is commonly used in monochromators is a reflective diffraction grating where it splits the collimated polychromatic light to constituent spectral colours via interference, unlike the prism which utilises the refractive principle to achieve the same purpose. The advantage of a reflective grating is to have a high throughput in ultraviolet and infrared regime whereas these wavelengths are absorbed in the prism. A blazed holographic grating surface is manufactured with grooves which are saw-tooth shaped in structure with a periodic distance, *d*. Gratings are rated by groove density, number of grooves per unit length, for instance, 1200 g/mm grating. The grating equation is given as,

$$ml = d(\sin q_i + \sin q_r) \tag{3.8}$$

where θ_i and θ_r are the incident angle and reflective angle respectively while m is the diffraction order. A typical monochromator usually uses the first order (m=1) to give the highest throughput for a specific wavelength. From equation ((3.8), the grating acts like a mirror at zeroth order (m = 0) where white light is reflected and therefore $\theta_i = \theta_r$. Due to the presence of higher-order light (m > 1), the DUT may detect wavelengths of λ/m other than the desired wavelength, λ and therefore a high-pass colour filter is required to avoid anomalous results.

Blaze wavelength is the wavelength that achieves the highest efficiency at a given diffraction order and blaze angle. Generally, the usable wavelengths of grating are from a factor of 2/3 to 3/2 of the blaze wavelength, or named as (2/3, 3/2) rule in order to operate the grating at reasonable efficiency.

The angular dispersion of a grating, $\frac{dq}{dl}$ can be expressed as,

$$\frac{dq}{dl} = \frac{mN_g}{\cos q}. \tag{3.9}$$

where m, N_g, θ are diffraction order, groove density and diffraction angle respectively. High dispersion with a smaller change of wavelength improves resolution and can be achieved by either using a higher groove density, diffraction order or having a higher diffraction angle.

Linear dispersion is the product of angular dispersion and focal length, f of the concave mirror such that

$$\frac{dl}{dq} = \frac{\cos q}{fmN_g}. \tag{3.10}$$

Thus, the band-pass, *BP* of the exit slit is the product of the entrance or exit slits width, w_s and reciprocal of the linear dispersion.

$$BP = \frac{w_s \cos q}{fmN_g}. \tag{3.11}$$

BP is defined as the FWHM of the light spectrum at the exiting slit and is the feature that determines the performance of a monochromator. Increasing the focal length of the concave mirror or reducing the exit slit size width increases resolution but lowers the light intensity. Resolution and light power should be optimized to observe the photoresponse of a PD in fine wavelength steps while the LIA is still able to read the photocurrent signal.

In this work, 1800 grooves/mm grating blazes at 400 nm was used since the DUTs peak response is at ~ 480 nm. As both entrance and exit slits are set to be 2 mm, the grating has a linear dispersion of 1.67 nm/mm at 500 nm, thus yields BP_{500nm} of ~ 3.4 nm.

3.3.2 Phase Sensitive Technique

Although the best devices used in this work exhibited low dark currents (tens of pico-amps) even up to the breakdown voltage, some gave considerable large dark currents of sub nano-amps contributed by a low shunt resistance due to the device etching. Such high dark currents were comparable or higher than the photocurrent especially at the

absorption band-edge where the responsivities at these wavelengths were very low. A weak signal with frequency within the operating bandwidth of an amplifier can be amplified. Unfortunately, noise is amplified as well. The SNR can be worse if the bandwidth is broad as the noise increases as the square-root function of the bandwidth.

A LIA is capable of amplifying an AC photocurrent signal and suppressing the noise level simultaneously. Generally, a reference frequency, f is necessary for every lock-in measurement to generate a reference sine wave which is $V_{ref}\sin(w_{ref}t+q_{ref})$ where $\omega = 2\pi f$. The sine wave is then multiplied with the input signal, $V_a\sin(w_at+q_a)$ to yield [139]

$$\begin{aligned} V_t &= V_aV_{ref}\sin(w_at+q_a)\sin(w_{ref}t+q_{ref}) \\ &= \frac{1}{2}V_aV_{ref}\cos[(w_a-w_{ref})t+q_a-q_{ref}]-\frac{1}{2}V_aV_{ref}\cos[(w_a+w_{ref})t+q_a+q_{ref}] \end{aligned} \tag{3.12}$$

Since $w_a = w_{ref}$, equation (3.12) is simplified to [139]

$$V_t = \frac{1}{2}V_aV_{ref}\cos(q_a-q_{ref})-\frac{1}{2}V_aV_{ref}\cos[2w_at+q_a+q_{ref}] \tag{3.13}$$

The multiplied signal is passed through a low-pass filter (LPF) which eliminates the AC term in equation (3.13). As the LIA $V_{ref} = \sqrt{2}$ V, equation (3.13) becomes [139]

$$V_t = \frac{\sqrt{2}}{2}V_a\cos(q_a-q_{ref}) \tag{3.14}$$

In the photocurrent measurement, the LIA reference frequency is provided by the chopper frequency controller shown in Figure 3.5 and the input signal is a square wave. Since the LIA takes the first component of square wave (which is $\frac{2V_a}{p}$), equation (3.14) is now,

$$V_t = \frac{\sqrt{2}}{p}V_a \tag{3.15}$$

after synchronizing the phase of input and reference signal. V_t is the value which appears on the LIA display.

Because the LIA has a reference frequency, a narrow bandwidth LPF can be designed and successfully reduces the noise without attenuating the desired signal. Hence, the SNR increases and signal extraction from noise is possible. The LIA is required whenever the dark current generated by the photodiode itself is comparable to photocurrent.

Inevitably, there is some noise at the output of the LIA due to the LPF bandwidth. A longer time constant, t will reduce the noise by narrowing the bandwidth of the LPF and therefore results in a more stable and reliable reading of the LIA. However, this requires a longer measurement time apart from masking the real changes in input signal. Hence, the time constant should be chosen such that the reading of LIA is reasonably stable (fluctuates < 5 % of the mean value) to keep the measurement uncertainty low. Since the LPF has a rise time, the integration time of the PC was set to be $3t$ so that the LIA output signal reaches 95 % of the final value.

The voltage drop across resistor can be increased by using a higher resistor value to obtain a stable reading, provided it is negligible to the voltage drop across DUT. However, the reading of the LIA can be reduced significantly when the chosen resistor is comparable to the input impedance of the LIA, which is 10 MΩ.

3.4 Photo-multiplication measurement

There are two types of light sources; one provides a wide range of wavelengths, for instance, Hamamatsu L2174 xenon bulb has a continuous broad spectrum from 185 nm to 2000 nm. In order to obtain a monochromatic light, a light bulb is coupled with a monochromator. Despite the convenience of having light of any wavelength within the bulb spectrum, monochromator output light power is much lower than that of a laser at a comparable wavelength. Additionally, as the bulb is not an ideal point source, it is difficult to focus the light into a small spot.

A laser has relatively high power at its operating wavelength and therefore the signal-to-noise ratio increases and the resultant photocurrent can be measured easily as a function of bias voltage. Furthermore, due to the minimal divergence from the laser beam, a good spot can be easily obtained using some simple lenses. As the laser spot is much smaller than the optical window, the photodiode responsivity can be conveniently calculated using a power meter. The smallest diameter of a focused laser beam spot, D with a Gaussian intensity profile is diffraction limited and is given by,

$$D = \frac{4 l f M_l^{\,2}}{p D_0} \tag{3.16}$$

where λ, f, M_l^2 and D_0 are the wavelength of the laser beam, focal length of the plano-convex lens, laser mode factor and the input diameter of the laser beam. The spot diameter is defined by the distance where the intensity of the beam reduces to$1/e^2$ of the maximum intensity.

The simplest way to focus a laser beam is to use a short local length lens, i.e. a 2 mm diameter beam from a 633 nm laser requires lens which has f=0.05 mm in order to focus the beam down to 10 µm according to equation (3.16). However, such a short f increases the difficulty in beam alignment and device probing. Therefore, it is better to expand D_0 using a beam expander before the beam is brought into focus. The magnification factor, M_l of a beam expander is given by $\frac{f_2}{f_1}$ where f_2 and f_1 are the focal lengths of the second and the first lenses as illustrated in Figure 3.7.

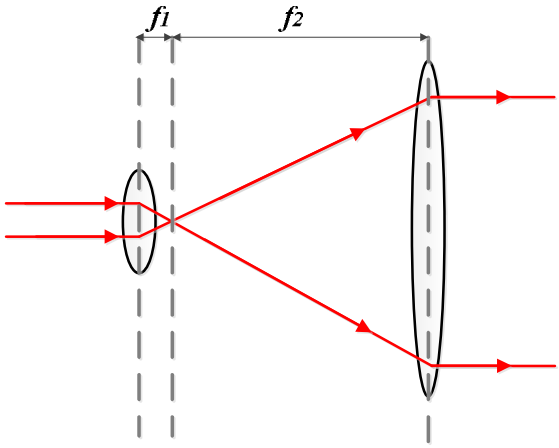

Figure 3.7 *Optical diagram of a beam expander*

In this work, a Melles-Griot 2074-M-A03 He-Cd 442 nm laser which has a D_0 = 2.1 mm was used as the light source to obtain pure-electron initiated multiplication. The laser was then expanded to 21 mm using a Thorlabs BE10M-A beam expander and brought to a focus using a simple 1.5 inch diameter plano convex lens with a f of 200 mm. The lens diameter was chosen to be larger than the beam diameter to avoid spherical aberration, which results in a larger laser spot. The lens were mounted on a linear translation stage to conveniently focus the light to D ~ 25 µm. Using the setup as shown in Figure 3.8, the DUT can be imaged and aligned with the laser beam

simultaneously with a Thorlabs BS013 beam splitter. The camera was mounted on a magnification system which has an illumination port for a better image quality.

Neutral density filters were added before the measurement to determine the spot diameter to avoid saturating the camera. Photocurrent as a function of bias voltage was measured using these filters to ensure the linearity of the photocurrent with respect of light intensity. The deviation from the linearity could be due to a) heating effects which may change the bandgap of the DUT, b) space-charge effects which reduces the electric field strength and therefore affect the multiplication factor and c) series resistance which reduces the voltage drop across the junction at high photocurrent. As the laser spot is smaller even than the smallest radii devices, the measured photocurrent is independent of device size. The measurements were repeated on smaller radii devices to ensure good consistency of gain and responsivity.

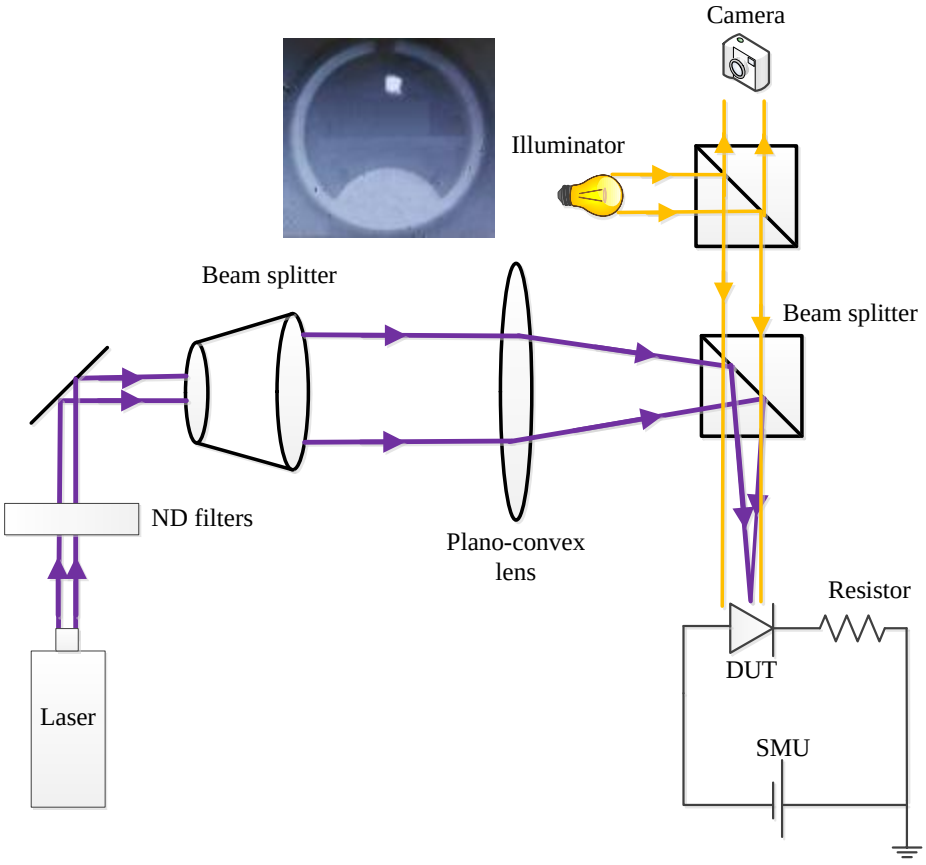

Figure 3.8 *Schematic diagram of experimental setup for photo-multiplication measurement. The image is a 200 µm radius device with 442 nm laser spot attenuated using ND3 filter.*

A fine laser spot allows a 2-D photocurrent scan to be performed by focusing the beam at various positions on the top cladding layers to check the gain uniformity of an APD at a given bias voltage as shown later in Figure 6.5. Using this technique, edge

breakdown can be easily observed around the device perimeter, indicated by sharp peaks illustrated in Figure 6.5b where the gains in these areas are exceptionally high due to field crowding [53].

3.5 Measurement uncertainties

Uncertainty propagation analysis usually is required to understand the sensitivity of variables in a function, where these variables are usually obtained from measurements where the uncertainties may vary. Given uncorrelated variables A, B and C with their respective uncertainties, δA, δB and δC in an equation $f = AB/C$, then the total uncertainty, δ_f is

$$\frac{d_f}{f} = \sqrt{\left(\frac{d_A}{A}\right)^2 + \left(\frac{d_B}{B}\right)^2 + \left(\frac{d_C}{C}\right)^2}\,. \tag{3.17}$$

For example, the uncertainty in depletion width of a circular mesa diode determined from C-V measurement is calculated as below, with variables C, ϵ and A of 10 pF±0.1, 11.25±0.56 and 200μm±2 respectively. Equation (3.3) was first rewritten into $d = \varepsilon\pi r^2/C$ and d was found to be 1.25 μm. Variables $\delta A/A$, $\delta B/B$ and $\delta C/C$ in (2.63) are now equated as

$$\frac{d_A}{A} = \frac{0.56}{11.25} \quad \frac{d_B}{B} = \frac{2(2)}{200} \quad \frac{d_C}{C} = \frac{0.1}{10}\,. \tag{3.18}$$

according to error propagation rule. δd can be computed by applying (2.63) to be ~5% of d, i.e. d = 1.25 μm ± 0.07.

The measured responsivity uncertainty was calculated using a similar calculation method as above and was determined to be ± 10%, primarily due to uncertainties in the resistor values (± 5%), lock-in amplifier readings (± 5%) and the active area of optical window (± 2%).

Chapter 4 ABSORPTION COEFFICIENTS IN AlInP

4.1 Introduction

The ternary alloy AlInP has received great attention recently for various optoelectronic applications. Being the widest bandgap III-V semiconductor material which can be grown lattice-matched to GaAs, AlInP is used in various devices such as multi-junction solar cells [140], visible lasers [141], multi-quantum barrier lasers [142] and laser diodes [143]. More recently, it has been used for demonstrating a narrow band high sensitivity photodiode [48] and avalanche photodiode [144] working at ~ 480 nm. In several of these devices, to optimize their performance requires an accurate knowledge of the material absorption coefficient, γ as a function of wavelength near the optical band-edge.

Although Kato et al. [91] showed that the optical properties of AlInP over a broad wavelength range of 225-1033 nm can be deduced from ellipsometry measurements, the noise around the fundamental absorption in the dielectric spectra results in unreliable absorption coefficients in the wavelength range of 440 – 550 nm where $\gamma < 10^5$ cm^{-1} as discussed in section 2.4.

A broad range of absorption coefficients from 10^6 down to 10 cm^{-1} is usually obtained by merging the data from both transmission and ellipsometry measurements [43, 145, 146]. However, such data has not been reported for AlInP. In this paper, we show that γ can be determined accurately over a wide dynamic range in a wavelength range of 380 – 550 nm via spectral response measurements on a series of PIN and NIP diodes. The absorption coefficients obtained may be used to optimise the design of AlInP APDs, which will be discussed in depth in the following chapter.

4.2 Absorption coefficient characterisation

Transmission measurements, as discussed in section 2.4 are hard to perform on AlInP epilayers, which are grown lattice matched to GaAs substrate and therefore opaque to the wavelengths of interest. As an ellipsometric method is inaccurate for low absorption values, photocurrent measurement could be an attractive alternative.

However, there are several aspects to consider in estimating γ accurately. While AlInP absorbance is low, multiple reflections at the GaAs and AlInP interface could occur and

the resultant photocurrent might be higher than expected. A simple reflectance calculation was carried out at the AlInP band edge absorption of 550 nm using

$$R = \frac{(n_2 - n_1)^2 + k_2^{\,2}}{(n_2 + n_1)^2 + k_2^{\,2}} \tag{4.1}$$

where n_1, n_2 and k_2 are refractive index of AlInP, refractive index of GaAs and extinction coefficient of GaAs, given as 3.1 [147], 4.1 [148] and 0.37 [148] respectively. It was found that R is ~ 2 % and therefore multiple reflections between GaAs and AlInP are negligible.

Another concern in low absorbance measurements is the diffusion of optically excited carriers in GaAs substrate to AlInP epilayers. Watanabe and Ohba [149] showed that GaAs-AlInP has a Type I conduction and valence band offset of 0.31 and 0.62 eV and therefore such barrier prevents the minority carriers created in GaAs diffusing to AlInP PIN, while allowing the majority carrier to flow across the heterojunction interface. Therefore, it can be assumed that the measured photocurrent is purely contributed by AlInP epilayers only.

After ruling out these complications, the resulted photocurrent in all devices can be analytically expressed in quantum efficiency model, as discussed in section 2.3. This allows the extraction of γ from the photocurrent measurement.

4.3 Sensitivity analysis

Similar to other experimental techniques, the accuracy of the photocurrent measurement in deducing γ is ultimately limited at short wavelengths where photons are absorbed very near to the surface of the epilayer, where any oxide of the epilayer may exhibit different optical properties to the bulk. In addition to that, it requires knowledge of other material parameters such as the minority carrier diffusion lengths, surface recombination velocities and carriers mobilities in advance, which may not be available in the literature for new alloys such as AlInP. It can be shown however that, these unknowns can be obtained using a first-order approximation without jeopardizing the precision of γ.

To weight the importance of the parameters as mentioned in the previous paragraph, a well-studied III-V material, $Al_{0.8}Ga_{0.2}As$ is used as it is an indirect semiconductor with a band-gap of 2.09 eV [150], similar to that of AlInP [136]. Absorption coefficient of

$Al_{0.8}Ga_{0.2}As$ in [148] was used to simulate a series of spectral responses of a PIN structure shown in Figure 4.1 with a 1.0 µm thickness in p^+, *i*, and n^+ layers by varying one parameter, i.e. either L_e (L_h), S_e (S_h) or μ_e (μ_h) at a time while the others are kept constant. The default values used are from the literature; L_e (L_h) = 0.25 (0.1) µm [151], S_e (=S_h) = 10^7 cm/s [152] and μ_e (μ_h) = 200 (20) cm^2/v.s [153] while these parameters are varied as tabulated below. The simulation results are shown in Figure 4.2.

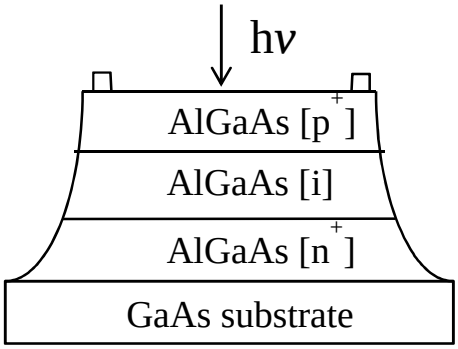

Figure 4.1 *The test structure of $Al_{0.8}Ga_{0.2}As$ to model the spectral responses in Figure 4.2.*

Table 4.1 Several test conditions used in sensitivity analysis where a parameter was varied at a time while the others were set at their default values

Test	**Parameter to vary**	**Test values**				
T1	L_e (µm)	0.1	0.25	0.3	0.5	1.0
T2	L_h (µm)	0.05	0.1	0.2	0.5	1.0
T3	$S_e = S_h$ ($cm\ s^{-1}$)	10^0	10^3	10^6	10^9	10^{12}
T4	μ_e (cm^2/v.s)	10^0	10^1	10^2	10^3	5×10^3
T5	μ_h (cm^2/v.s)	10^0	10^1	10^2	10^3	5×10^3

As most of the absorption occurs in the top first two layers (p^+ and *i* region), minority holes have insignificant contribution to the overall photocurrent and thus increasing L_h only improves η by a tiny fraction in the longer wavelengths. The hole parameters, S_h and μ_h are therefore not shown. Conversely, η dramatically changes especially in the shorter wavelengths by varying L_e and S_e due to the increasing collection efficiency in the p^+ layer. Minority electron mobility, μ_e determines the diffusion speed of electron and consequently may have an impact on device efficiency. Nevertheless, an untreated semiconductor surface usually has high surface recombination ($S_e \sim 10^7$ cm/s) due to the defect states, severely limiting the diffusion of electrons near the surface to the intrinsic

region. This explains why η remains similar regardless of μ_e values < 5000 cm^2/v.s in Figure 4.2.

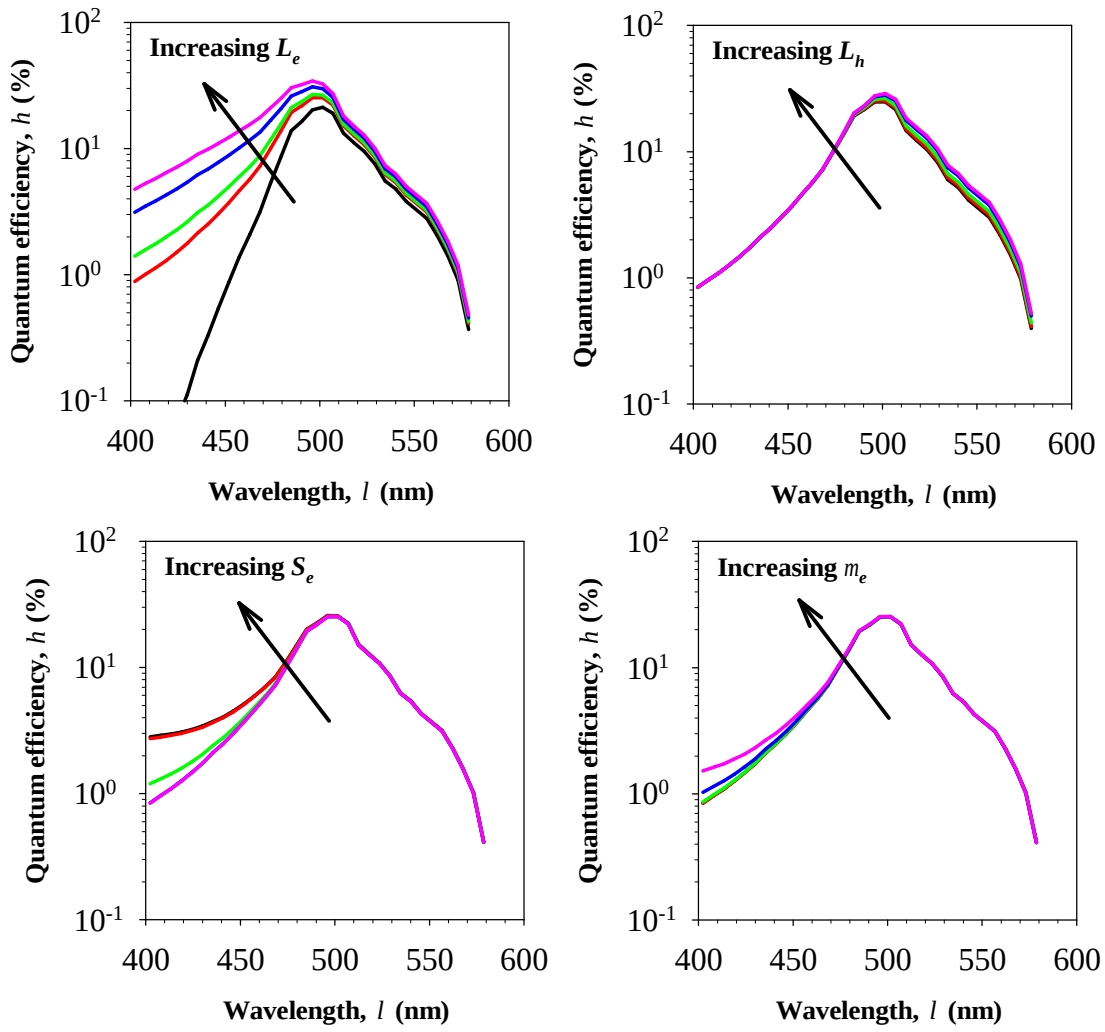

Figure 4.2 *The spectral responses of $Al_{0.8}Ga_{0.2}As$ by varying one of the parameters L_e (L_h), S_e (S_h) or μ_e (μ_h) at a time while the rest are fixed at constant values similar to the published results.*

Thereby, the parameters which are crucial to calculate γ are L_e and S_e only, and thus this simplifies the analysis. Another important observation from Figure 4.2 is that the longer wavelengths responses, λ > 520 nm gives < 30% difference at the extreme values of L_e and S_e. Such an error is similar to that of transmission measurements [64] and thus allows $\gamma < 10^4$ cm^{-1} to be estimated reliably even if there is some degree of uncertainty in L_e and S_e, provided X_1, X_2 and X_3 can be known accurately from the *C-V* data. The accuracy in measuring photocurrents at the absorption band-edge nevertheless will be limited by the capability of the measurement equipment.

4.4 Device Growth, Fabrication and Characterisation

The growth was done at the University of Sheffield, EPSRC National Centre for III-V Technologies. Three AlInP PINs (P1, P2-1 and P3-1) and one NIP homo-junction diode (N1-1) with nominal intrinsic layer thickness, w of 1.0, 0.8, and 0.2 μm as shown in Table 4.2 were grown by low pressure (150 Torr) metalorganic-vapor phase epitaxy (MOVPE) in a horizontal flow reactor at 680-730 ºC on n^+ (p^+) GaAs substrates, which have an off-cut angle of 10º towards [111A] plane to minimize copper-platinum (Cu-Pt) ordering [154]. The epilayers were capped with ~50 nm of heavily doped GaAs to ensure a good ohmic contact. The source materials for the epitaxial growth were trimethylaluminium, trimethylgallium, trimethylindium, phosphine and arsine. Diethylzinc and disilane were used as p and n-type dopant respectively. The growth rate of AlInP and GaAs were 2.7 μm/hr.

X-ray diffraction was performed by the grower in order to reveal the lattice mismatch of AlInP and GaAs substrates in these structures. A monochromatic, collimated X-ray beam with wavelength, λ of 0.154 nm corresponding to a Cu-α emission line was incident upon these crystalline structures at an angle, q and the lattice constant, a can be easily obtained via the following expression

$$m l = 2a\sin q \tag{4.2}$$

where m is a positive integer. The data were normalised to the GaAs peak as shown in Figure 4.3, which could be easily identified by GaAs Bragg angle of ~ 33.03°. There are two major peaks due to the AlInP, contributed by the intrinsic and p^+ layers, both showing compressive strain with respect to to GaAs where the latter of which was less compressively strained than the former due to zinc dopants [155]. The peak separations, $\Delta\omega$ between GaAs and these AlInP intrinsic layers were used to estimate the aluminium compositions in these samples. The lattice constants of these samples were found by subtracting the Bragg angle of GaAs (q = 33.025º) with Δq . Using a linear interpolation in a between InP and AlP, the aluminium composition in these AlInP samples was determined to be 52.0-52.7%, which is close to the nominal composition in order to be lattice matched to GaAs. The resulting strains therefore, are minimal, being between 2 - 6 $\times 10^{-4}$, obtained using $\frac{a_{AlInP} - a_{GaAs}}{a_{GaAs}}$.

The FWHM of the peaks that are associated with AlInP layers obtained from the XRD are ~ 45 arcsec and it is comparable to ~ 30 arcsec simulated by BEDE (now known as RADS X-ray software), indicating the samples crystal quality were reasonably well.

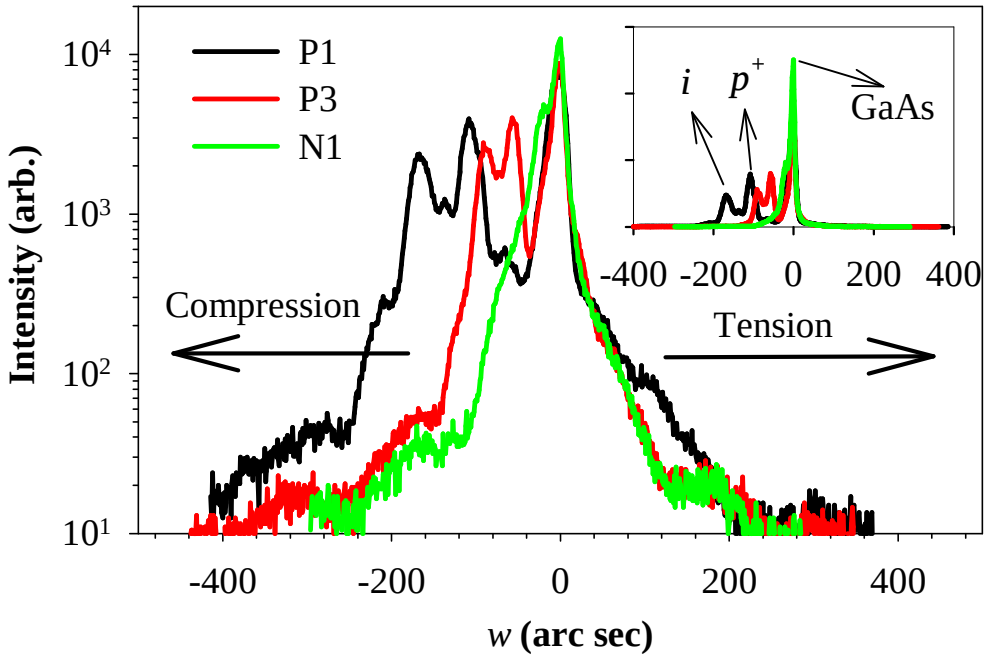

Figure 4.3 *X-ray results obtained from P1, P3 and N1. The structural details can be found in Table 4.2. Inset showed the same results with y-axis plotted in linear scale.*

To ensure that the incident light is absorbed by only the AlInP, the GaAs cap of the optical window is etched off in the devices as shown in Figure 4.7 using a selective wet chemical etchant which consists of H_2SO_4:H_2O_2 and H_2O mixture at a ratio of 1:8:80 [156].

Table 4.2 *Extracted device parameters of AlInP diodes*

Layer	**p^+ (n^+) thickness (µm)**	***w* (µm)**	**N_p (x10^{17} cm^{-3})**	**N_n (x10^{17} cm^{-3})**	**N_i (x10^{15} cm^{-3})**
P1	1.00	0.97	4.0	20	2
P2-1	1.00	1.12	4.0	10	15
P2-2	0.47				
P2-3	0.23				

P3-1	1.00	0.25	4.3	20	16
P3-2	0.26				
N1-1	1.00	0.81	2.5	20	2
N1-2	0.42				
N1-3	0.27				

The central top 1.0 μm AlInP claddings in some devices of P2-1 were further thinned using Reactive-Ion etching (RIE) to give p^+ cladding thicknesses of 0.2 – 0.5 μm ± 0.07, namely P2-2 and P2-3, as tabulated in Table 4.2. As P2-2 and P2-3 were fabricated from P2-1, the doping densities in the claddings and w are identical. Similar process was performed on P3-1 and N1-1 to give P3-2, N1-2 and N1-3. Finally, the samples underwent the standard photolithography techniques after the contacts metallisation and mesa diodes of 35 – 210 μm radii were formed using universal etchant, CH_3COOH: HBr: $K_2Cr_3O_7$ with ratio of 1:1:1. However, etchants such as the universal 1:1:1 is not perfectly isotropic and therefore results in bevel edges as shown in Figure 4.4. Hence, photons can be injected at both the optical window and sidewall of a diode simultaneously when the spot size of the light is larger than the device area. Relatively long-wavelength light has negligible effect on the spectral response of the diode as these photons are less likely to be absorbed in the diode. On the contrary, short-wavelength photons are absorbed strongly once they are injected into the exposed intrinsic region, resulting in a significantly higher photocurrent due to a higher QE compared to those which are injected at the top p^+-cladding.

These anomalous photocurrents can have major impact on determining the multiplication and absorption coefficient in AlInP and therefore it is necessary to avoid sidewall illumination from the light source by deposit a thin layer of metal around the mesa edges. This was done by first spinning and patterning the SU-8 photoresist (with a thickness of ~ 4 μm) which planarises the structure. Samples were then underwent standard photolithography process to passivate 200 nm of gold on the SU-8 as shown in Figure 4.5. Gold was chosen as the passivation layer rather than aluminium as the former is chemically more inert than the latter. The details of fabrication steps of AlInP PINs can be found in Appendix F.

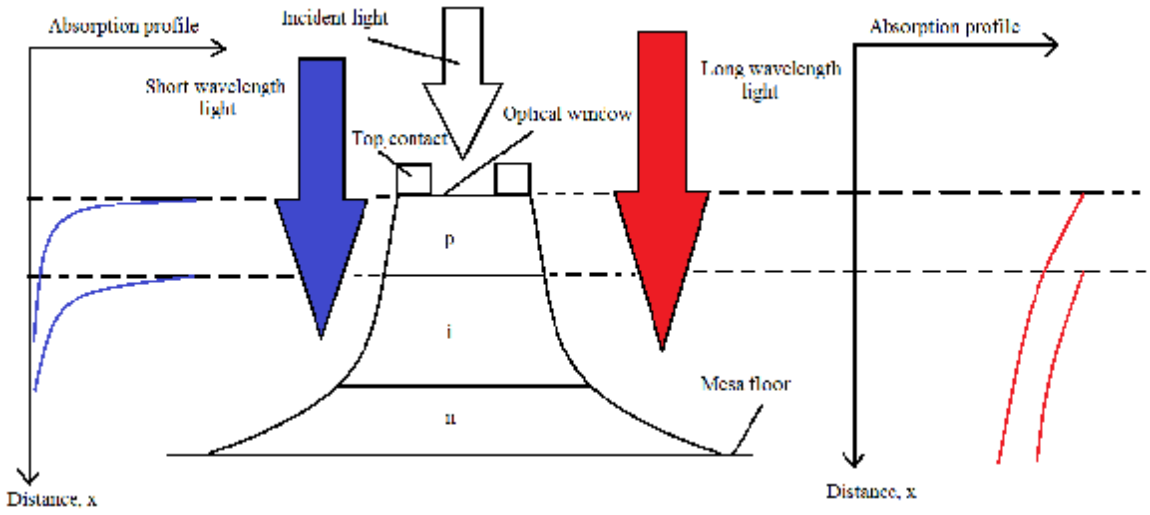

Figure 4.4 *Side view of a mesa p-i-n diode together with absorption profile of short wavelength (blue) and long wavelength (red) incident light which are injected at the optical window and sidewall of diode.*

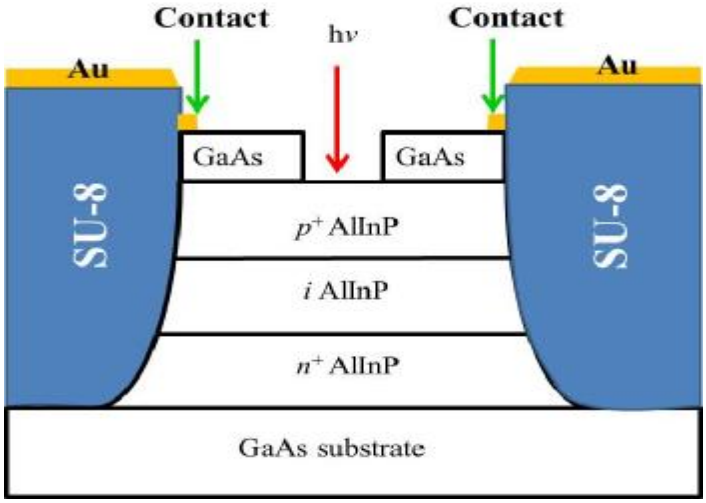

Figure 4.5 *A cross-section of AlInP diodes after SU-8 passivation and metallisation.*

4.4.1 Capacitance-Voltage Measurement

Capacitance-voltage (*C-V*) measurements were performed on the mesa diodes to determine *w* and the doping densities in the p^+-*i*-n^+ layers (N_p, N_i and N_n respectively). Several of these unprocessed samples were sent to Loughborough Surface Analysis for Secondary Ions Mass spectroscopy (SIMs) measurements to corroborate these parameters, as well as obtaining thicknesses of the cladding p^+ (n^+) layers. This measurement was carried out by first bombarding the surface of the sample with

energetic Cs^+ particle of 10 keV energy, over an area of ~20 µm. The sputtered particles formed secondary ions which were then separated by their mass to charge ratio using a mass spectrometer. The resulting signal intensities (in counts per second) in these terminals were plotted against the bombardment time. By using a Dektak 6M profilometer, the crater depth was measured to translate the graph to intensity vs. depth. To determine the doping concentrations accurately, the instrument was first calibrated with samples of known composition. To distinguish between GaAs and AlInP, concentrations of arsenic and phosphorus were measured while zinc and silicon concentrations correspond to the dopants in the AlInP of p^+ and n^+ claddings respectively, as illustrated in Figure 4.6.

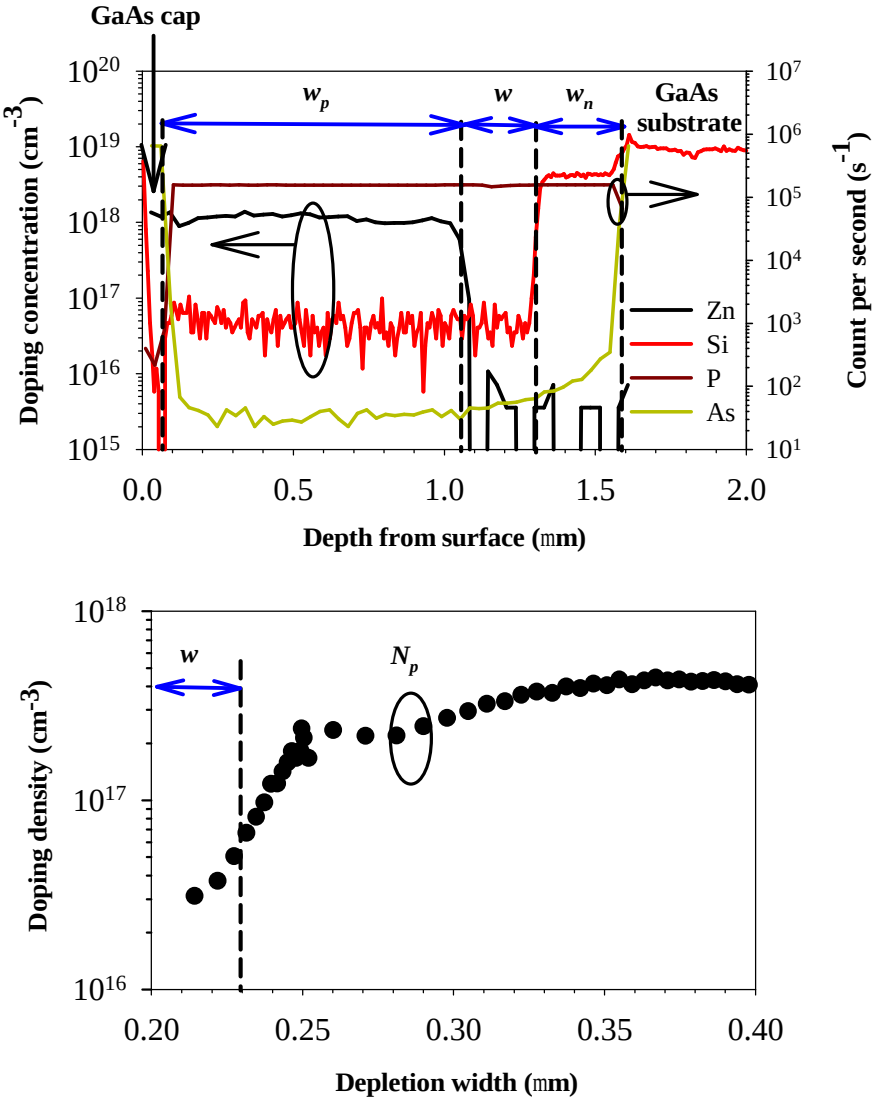

Figure 4.6 *Doping concentrations obtained from SIMs (top) and C-V measurements (bottom)from sample P3-1.*

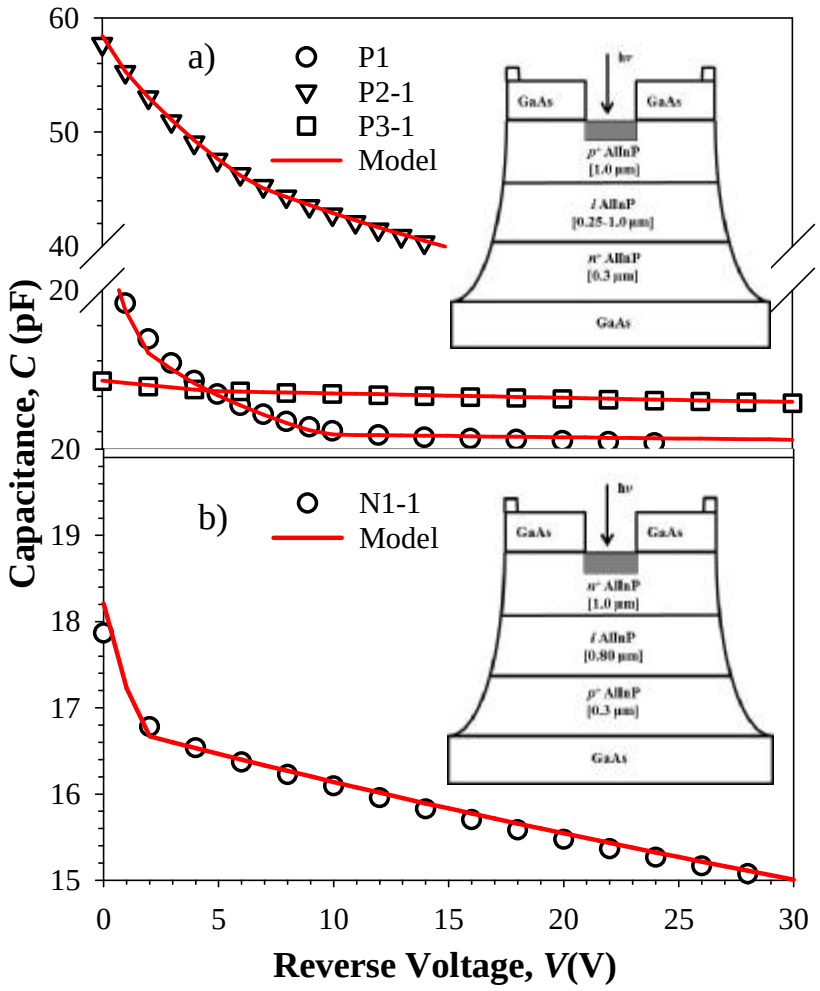

Figure 4.7 *Measured (symbols) and modelled (lines) capacitance of the a) PINs (P1, P2-1 and P3-1 as ○, □ and ▽ respectively) and b) N1-1. Also shown in the inset is the schematic diagram of the device structures, with RIE-etched area shaded in grey.*

Although results from both *C-V* and SIMS measurements agree on the values of *w* as shown in Figure 4.6 where data of P3-1 was shown only, the p^+ claddings doping densities estimated from *C-V* and SIMs were estimated to be 3-4×10^{17} and 1×10^{18} cm^{-3} respectively. *C-V* gives more accurate measurements than SIMs as the former measures the electrically activated dopants while the latter measures the total dopants concentration in a sample. The discrepancy in the results suggests that not all dopants are ionised and one possible reason may be due to background oxygen contamination [158] and the solubility of the zinc dopants in AlInP [159]. Conversely, it was reported that high carrier concentration of >10^{18} cm^{-3} can be achieved using Si-dopant [158]. Assuming the doping densities in the n^+ and p^+ regions are 1-2×10^{18} and 2-5×10^{17} cm^{-3} respectively as shown in Table I the results obtained from *C-V* modelling (with a dielectric constant of 11.2, interpolated from InP [160] and AlP [161] values), showed

good agreement with the experimental data as shown in Figure 4.7. The details of the model can be found in Appendix A.

4.4.2 Current-Voltage Measurement

Current-voltage (*I-V*) measurements were conducted in forward and reverse bias condition on P1 to P3 where the largest size devices (f = 420 µm) were measured as shown in Figure 4.8.

All devices showed good forward bias *I-V*s and the current densities from different device radii in each of the samples agree (not shown). From the *I-V* fitting using the Shockley-Read Hall equation as stated in equation (2.1), the parasitic resistance and saturation current in the largest devices are found to be ~ 32 Ω and < 10^{-20} A respectively. These devices showed similar characteristic (except P1 where the curve shifted to the left) regardless of their depletion widths. This difference appears to be significant but the shift in the curve only corresponds to a ΔV of ~0.08 V, primarily due to a minor discrepancy in E_g, which is suggested by the XRD curves in Figure 4.3. To show the correlation between E_g and forward I-V characteristic, GaInP and GaP PINs were measured, which have bandgaps of 1.9 eV [136] and 2.26 eV [162] respectively. The structure details are shown in Table 4.3. As illustrated in Figure 4.8, ΔV agree qualitatively with ΔE_g in these materials.

Table 4.3 *Nominal device parameters of GaP and GalInP diodes*

Material	**p^+ (n^+) thickness (µm)**	***w* (µm)**
GaInP	1.0 (0.3)	1.0
GaP	0.5 (0.5)	2.0

In the reverse bias *I-V*, the breakdown voltages in these devices agree qualitatively with *w* obtained from the *C-V*. Due to low dark leakage current in all devices (< 0.1 nA up to 95% of the breakdown voltage), the current in smaller devices was immeasurable due to limitation by the instrument. Therefore, only the results of the largest size devices are shown. The dark currents shown in Figure 4.8 however, are much higher than the saturation current. This is primarily contributed by the shunt resistance due to mesa sidewall leakage and therefore results in inconsistent dark currents in these devices. Considering the similarity of band structure (Γ and X energy gaps) in AlGaAs [150] and AlInP [136], the electric field corresponds to a tunnelling current of ~ 1 nA in a 200 µm

radius device is ~1.4 MV/cm [110]. This explains there is no evidence of tunnelling current (limited by the measurement setup) in the largest size devices of all samples up to an electric field of 1 MV/cm.

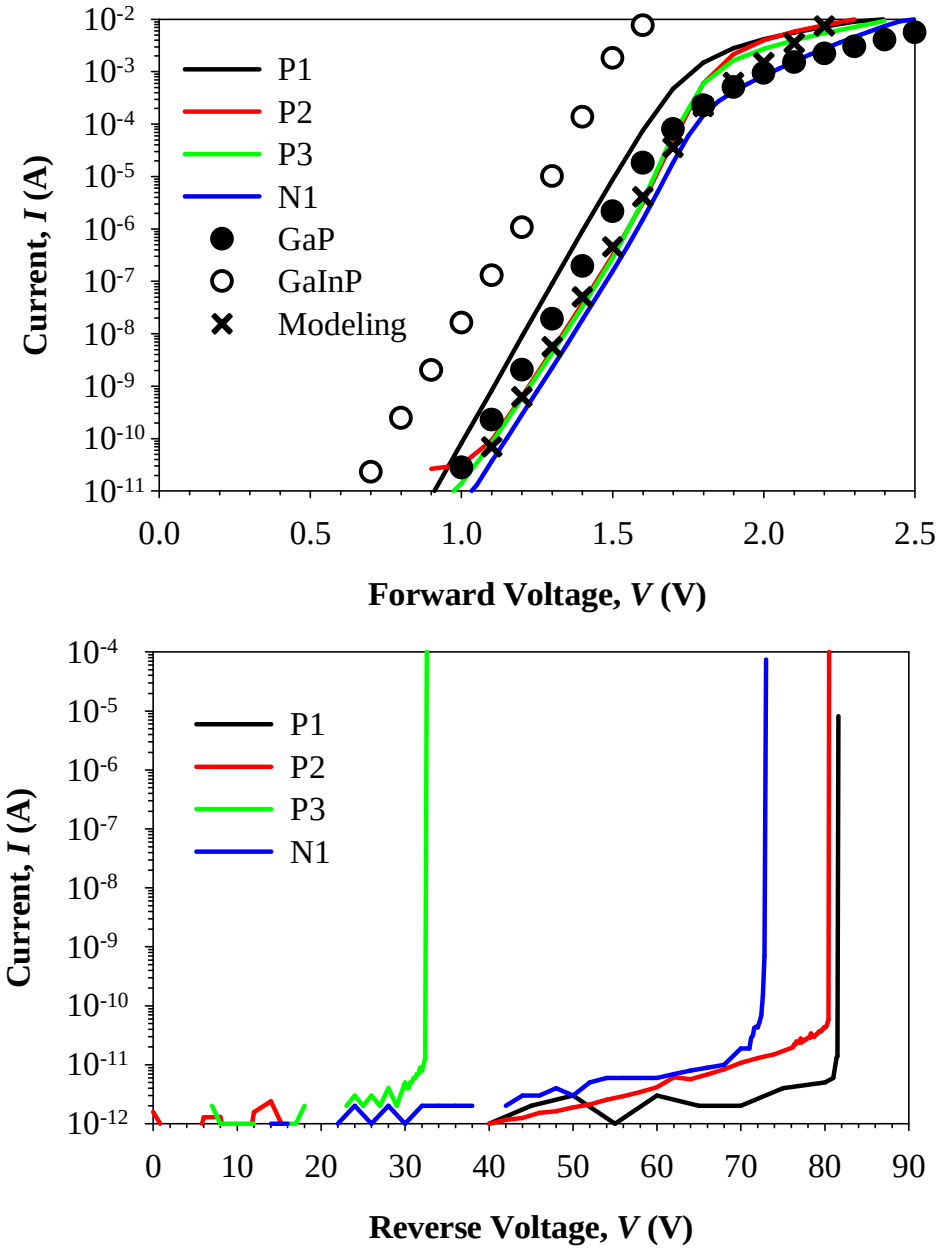

Figure 4.8 *Forward (top) and reverse bias (bottom) I-V measured in P1, P2, P3 and N1 with* f = 420 µm *shown as black, red, green and blue lines respectively. Also shown are the forward I-V results from GaInP and GaP and the modelled result.*

4.4.3 Photocurrent Measurement

A 100 W tungsten halogen bulb and a grating monochromator which has a resolution of ± 1.5 nm were used to measure the spectral responses of the 210 µm radii devices as

shown in Figure 4.11. Since the dark current at low bias voltages is extremely low in these devices [111] as shown in Figure 4.8, very small photocurrents (~10 pA) around the cut-off wavelength regime where the absorption is expected to be very weak, can still be measured accurately. The results were confirmed using phase sensitive technique where the light signal was mechanically modulated at 180 Hz and the photocurrent was measured using a lock-in amplifier. The quantum efficiencies, η of the devices illustrated in Figure 4.11 were deduced from a calibrated Si photodiode and were confirmed using a 442 nm He-Cd laser, where the laser beam was focused to a ~20 µm diameter spot on the device optical windows.

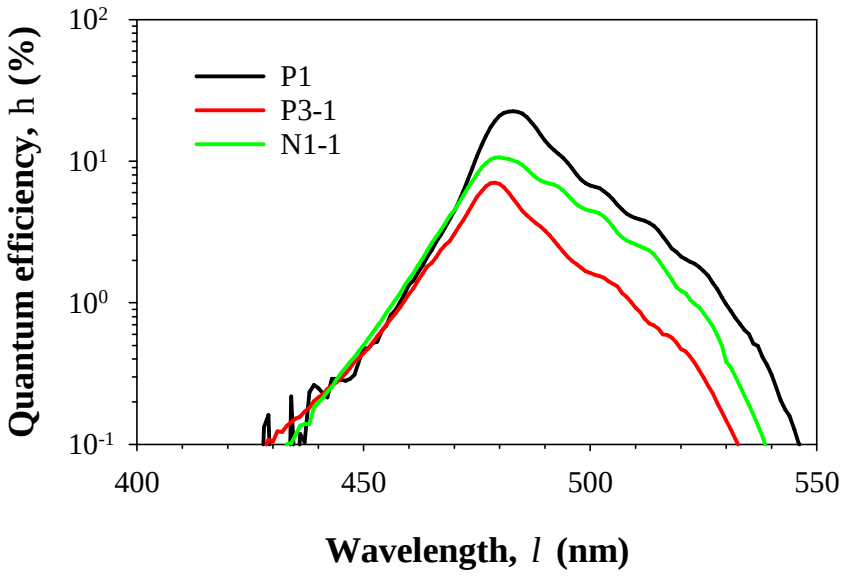

Figure 4.9 *Quantum efficiency measured in P1, P3-1 and N1-1 shown as black, red and green lines respectively.*

The parameters L_e (L_h) in PINs (NIPs) can be independently obtained by measuring the change in responsivity under illumination of 442 nm as a function of reverse bias voltage before the onset of avalanche multiplication. This measurement was performed on those samples with a 1.0 µm thick top cladding (i.e. P1, P2-1, P3-1 and N1-1) since > 99.9% of the photons are absorbed in the top cladding layer and therefore the photocurrent contribution due to the intrinsic region and bottom cladding layer can be neglected. Experimental results measured in P1, P3-1 and N1-1 illustrated in Figure 4.10 shows the photocurrents due to 442 nm illumination in these samples are very similar regardless of *w*.

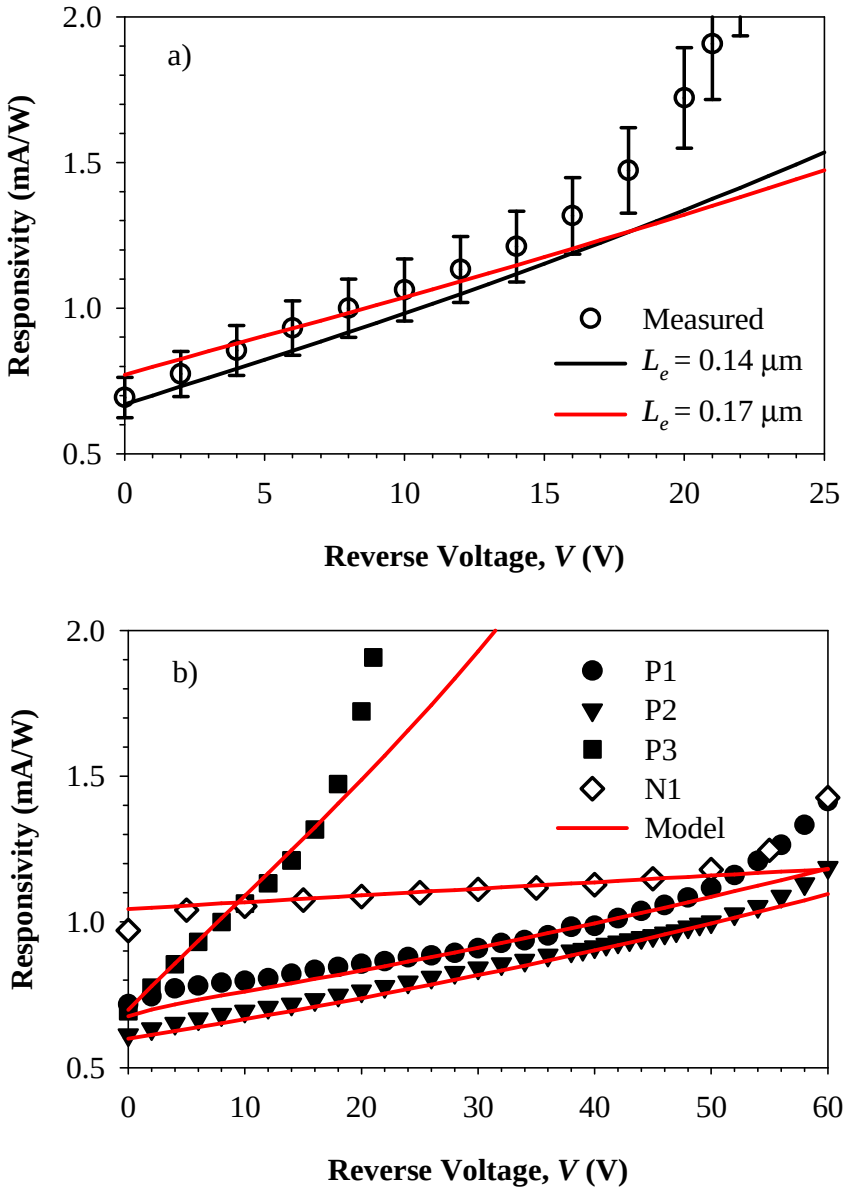

Figure 4.10 *a) Responsivity as a function of bias voltage under illumination using 442 nm, with ± 10 % uncertainty (symbols) measured in P3. The modelled results using equation* (2.20) *assuming* L_e *= 0.14 and 0.17 µm are shown by black and red lines respectively b) Similar measurements on P1, P2, P3 and N1 (symbols) with the modelled results using* L_e *= 0.155 µm ± 0.015 µm and* L_h *= 0.170 µm ± 0.015 µm*

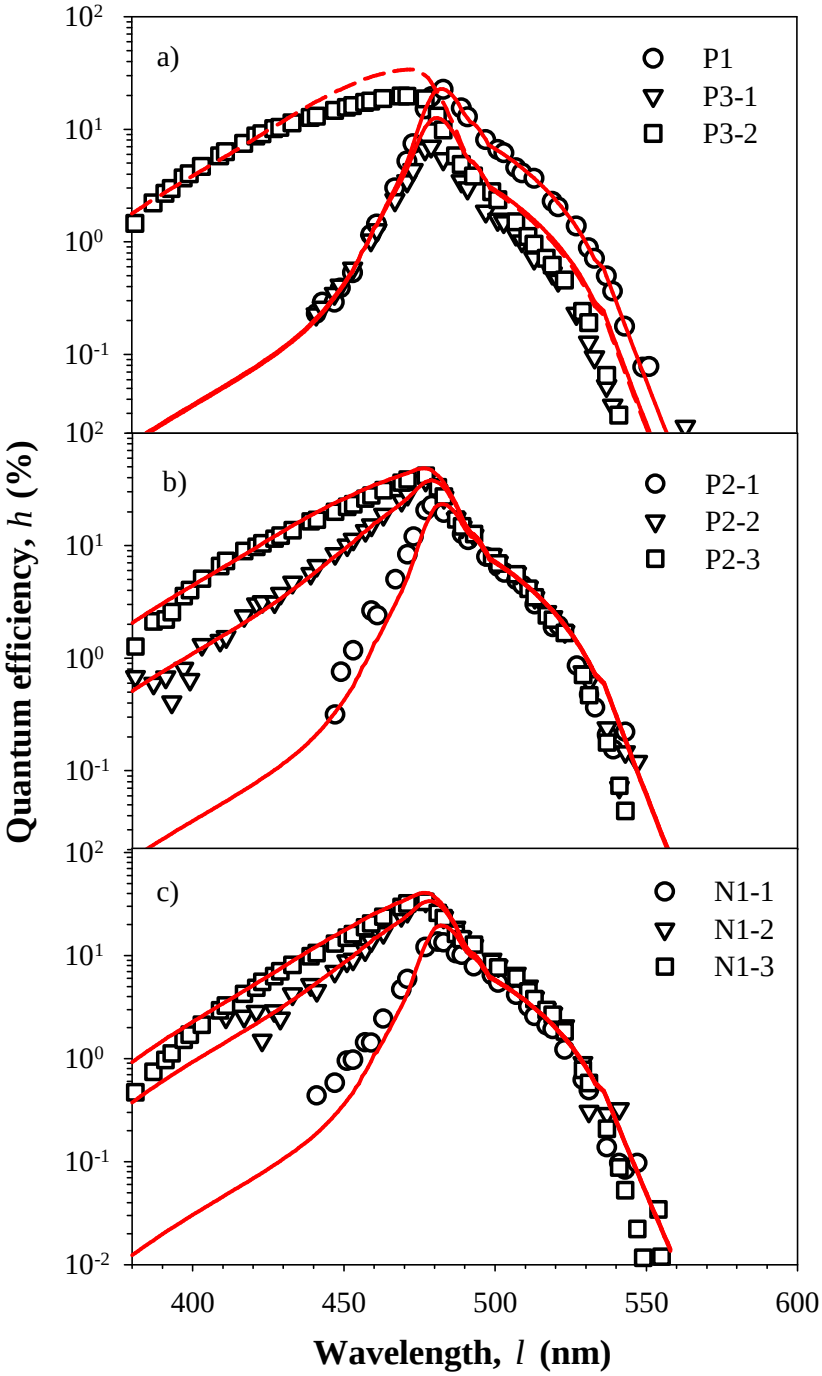

Figure 4.11 *Experimentally obtained η (symbols) from a) P1, P3-1 and P3-2 shown as ○, ▽ and □ respectively. b) P2-1 and P2-2 and P2-3 shown as ○, ▽ and □ respectively. c) N1-1 and N1-2 and N1-3 shown as ○, ▽ and □ respectively. Simulated results are shown by the lines.*

The increasing photocurrent due to 442 nm illumination with applied bias voltage is therefore due to the depletion into the top cladding layer only and therefore enables us to estimate the minority carrier diffusion length using equation (2.20) in a similar manner as [114]. Measurement uncertainties in photocurrent and *C-V* must be taken into account before diffusion lengths can be measured reliably, as discussed in section 3.5.

Errors of ± 10% and ± 2% in the modelled p^+ cladding doping density and its corresponding thickness were introduced due to the resolution obtained in the *C-V* modelling and the SIMs result respectively. An error of ± 10% was introduced to accommodate for experimental error in obtaining a value for γ of 1.1×10^5 at 442 nm [91] as well. The possible combinations of these variables were simulated to obtain the smallest and largest possible L_e where the simulated results are within the responsivity measurement error prior to the onset of avalanche multiplication. Using a μ_e of 160 cm s^{-1} [163] and R of 32.1% at AlInP-air interface using equation (4.1) (n_{442nm} = 3.57 [147]), the value of L_e determined from P3-1 was 0.155 µm ± 0.015 µm, and this value is consistent across all samples as illustrated in Figure 4.10.

Due to the short L_e, the modelled results showed insignificant change when surface recombination velocities (assuming $S_e = S_h$) were increased from their nominal values of 1×10^7 cm s^{-1} [152]. Again, such S_e (S_h) was assumed for an untreated semiconductor surface. Such Similar measurement was done on N1-1 giving L_h of 0.170 µm ± 0.015, using μ_h of 10 cm s^{-1} [163].

After determining the parameters (L_e, L_h, μ_e, μ_h, S_e, S_h) in equation (2.18), (2.20) and (2.22), γ can be solved numerically by fitting the modelled η to the experimental results. Again, the surface reflectivity, R as a function of wavelength was calculated using equation (4.1) where n was taken from [147]. The parameters used are summarised in Table 4.4. Values of γ shown in Figure 4.12 extracted from P1, P2-1, P3-1 and N1-1 are in close agreement, assuming L_e and L_h of 0.155 and 0.170 µm respectively. This suggests that the measured γ is independent of the doping type for the levels used in this work, in agreement with those reported in other semiconductors [62, 164].

Table 4.4 *Parameters used to model the external quantum efficiency curves of AlInP*

Parameters	**Value**
Electron (hole) diffusion length, L_e (L_h)	0.155 (0.170) µm
Electron (hole) mobility, μ_e (μ_h)	160 (10) cm s^{-1}
Surface recombination velocity ($S_e = S_h$)	1×10^7 cm s^{-1}
Reflectivity, R	32.1 %

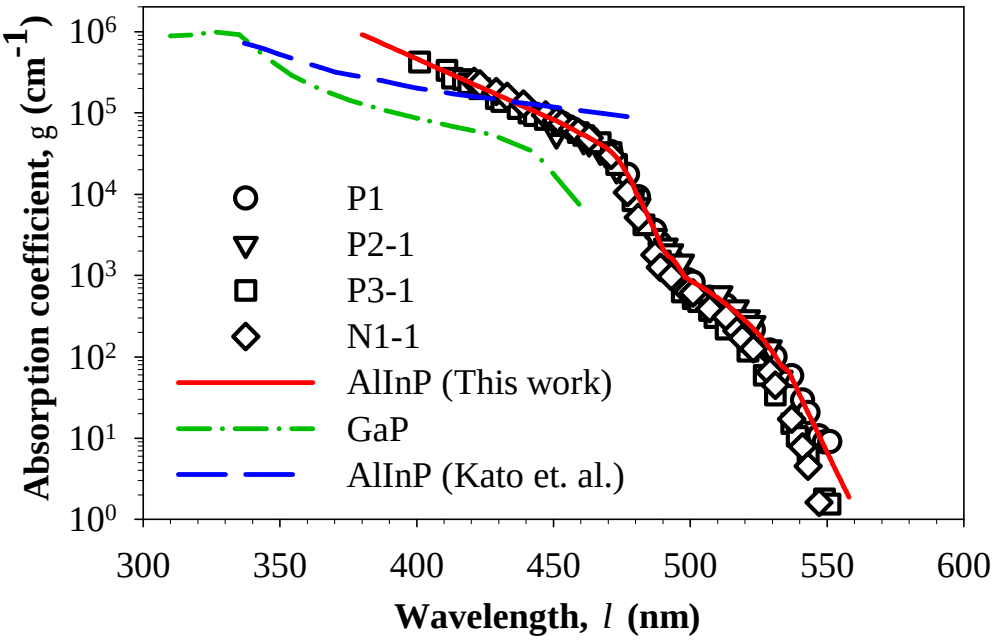

Figure 4.12 *Absorption coefficient, γ obtained from P1, P2-1, P3-1 and N1-1 as ○, ▽, □, and ♢ respectively. The highest achievable γ for a given wavelength (solid line) was taken as the bulk value. The published AlInP [91] and GaP [12] data are shown as dashed and dashed-dot lines respectively.*

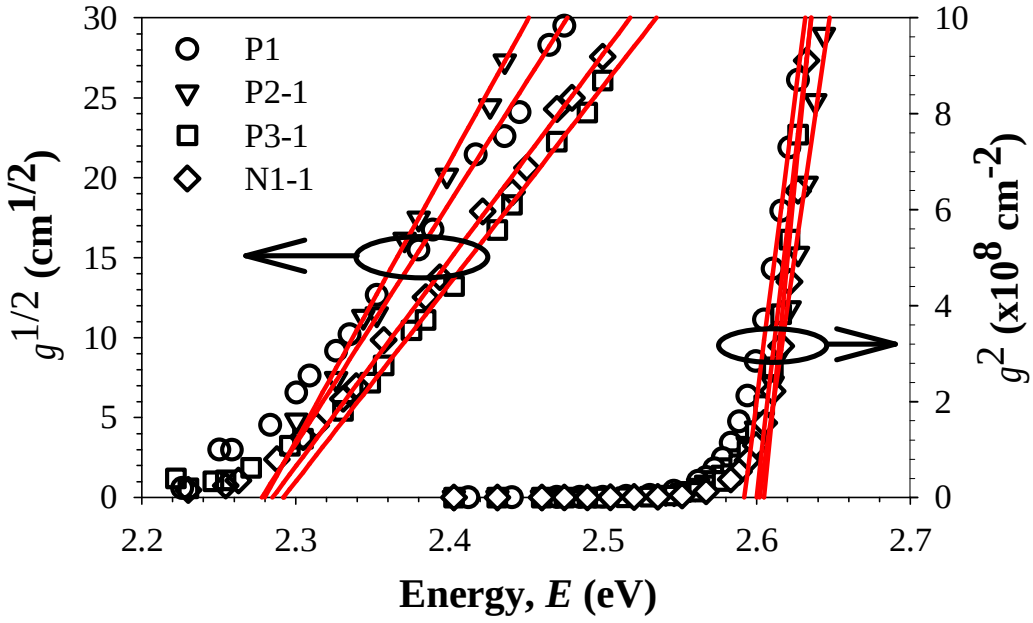

Figure 4.13 *Experimentally obtained root (left) and square (right) of absorption coefficient obtained from P1, P2-1, P3-1 and N1-1 at 0 V shown as ○. ▽,□ and ♢ respectively. The fittings are shown as lines to extract the indirect (left) and direct energy gaps (right).*

AlInP is an indirect-gap semiconductor (the direct-indirect crossover point is at 44 % Al [137]) and to understand the behaviour of γ with wavelength, we need to determine the energy gaps. To extract the band-gap of AlInP, $\gamma^{½}$ versus photon energy extracted from P1, P2-1, P3-1 and N1 at 0 V is plotted as shown in Figure 4.13. These data can be fitted by straight lines and by extrapolating these to the *x*-intercept, E_g which corresponds to the *X*-valley can be determined. By averaging the values obtained in these samples, E_g was found to be 2.289 ± 0.006 eV. The direct gap, E_Γ was estimated to be 2.597 ± 0.008 eV using similar method by plotting γ^2 versus photon energy. The band diagram of AlInP is shown in Figure 4.14. The minor discrepancies are primarily due to slight variation in the aluminium composition (52.0-52.7%) between samples while nominally still lattice-matched to GaAs. These results are comparable to those obtained from photoluminescence or cathodoluminescence spectroscopy [136, 137] which give E_g and E_Γ of 2.26 – 2.33 eV and 2.50 – 2.60 eV respectively for disordered material (reported 4 K data was converted to 300 K data by subtracting 80 meV).

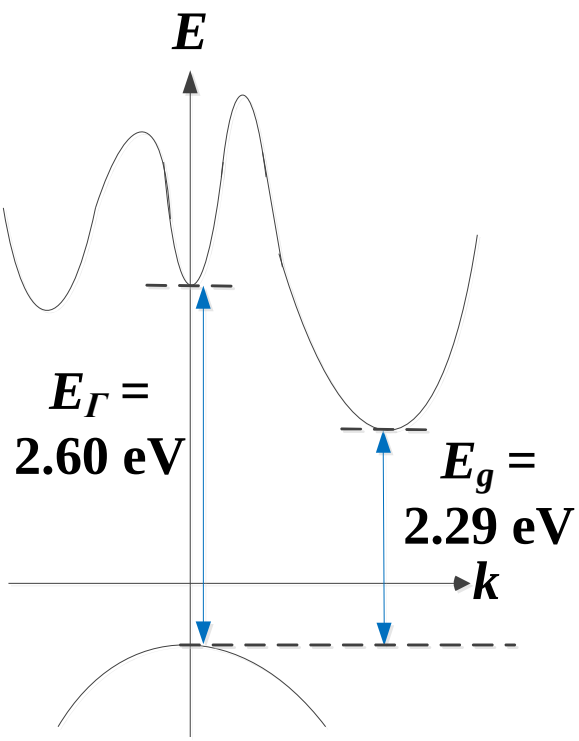

Figure 4.14 *Band diagram of AlInP*

The discrepancy between the measured γ and those reported by Kato et al. [91] are clearly shown in Figure 4.12, The γ determined here decreases rapidly at 470 nm and relatively more gradually at 495 nm, and this can be attributed to the absorption processes in the Γ and *X* valleys respectively. For comparison, the absorption behaviour of GaP [37], also an indirect band-gap semiconductor, is also shown in Figure 4.12 and

is seen to be similar to our data but blue shifted by about ~ 30 nm due to the larger E_{Γ} of GaP, reported as 2.757 eV [38].

The γ from Figure 4.12 for AlInP was used to reproduce the η in P1-1, P2-1, P3-1 and N1-1 as illustrated in Figure 4.7. Good agreement over 3 orders of magnitude can be seen in these samples. Although the peak response wavelength agrees well, η obtained from the experimental data is slightly lower than the modelled results in P3-1, most probably due to the presence of surface roughness or a surface oxide layer which is ignored in the simulations.

The same η measurements were performed on the RIE-etched devices. As RIE is known to roughen the surface of semiconductor and degrade the optical performance [165], no attempt was made to extract γ from these results. Instead, γ was extrapolated from 400 nm to 380 nm as shown in Figure 4.12 to simulate the η obtained from these devices. The modelled results in Figure 4.7 showed surprisingly good fit to the experimental data, especially in the P2 samples. The surface roughness and damage depth of ~ 100 nm after RIE etching [165] may explain the discrepancies found in the P3 and N1 samples in Figure 4.7 where the surface optical transmission and minority carriers diffusion length may have been reduced.

4.5 Bias-dependent spectral response

Spectral responses of GaAs APDs were shown extendable to near 1000 nm at high electric fields near breakdown voltage, well beyond the cut-off wavelength of ~873 nm [166]. Such extended response is undesired for narrow-band detectors as this increases the spectral full-width-half-maximum (FWHM). To investigate the Franz-Keldysh effects as described in section 2.2, spectral measurements were performed on the thickest available 1 μm AlInP PIN (P1), where the electro-absorption effect is expected to be most significant, up to near breakdown voltage (V = 0, 10, 20, 50, 70, 75 V). For clarity, only spectral responses of 0, 50, 70 and 75 V are shown only in Figure 4.15.

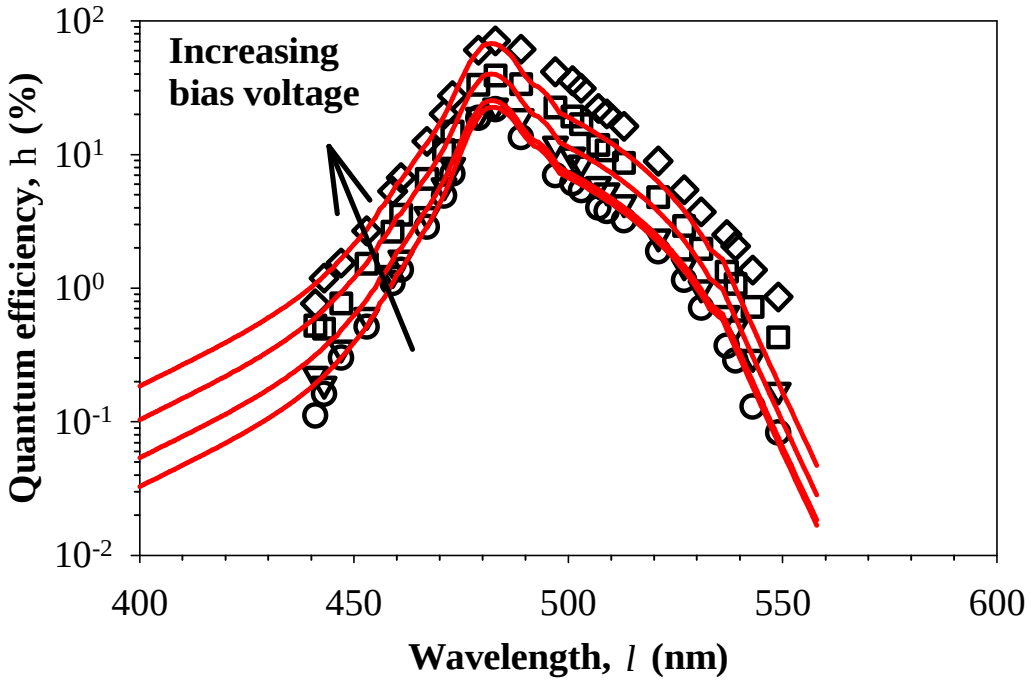

Figure 4.15 *Measured η in P1 at bias voltages of 0, -50, -70 and -75V (*○, ▽, □ and ◇ *respectively). The modelled η (lines) at these respective bias voltages include the effects of avalanche multiplication?.*

However, avalanche multiplication occurs in the higher bias voltages and in order to observe the electro-absorption, an accurate estimation of avalanche gain is required. Considering the avalanche width in this device is relatively thick and therefore any dead-space effect is minimal, a local model can be used to compute the gain. This was done by first constructing the electric-field profile of P1 using doping densities in *p*, *i* and *n* layers as shown in Table 4.2.

Due to different absorption profiles across the wavelength range of interest (400 – 600 nm), the multiplication gain can vary, depending on where the carriers initiating the avalanche process are created. Using the absorption coefficient as shown in Figure 4.12, the photocurrent contribution due to p^+ and n^+ cladding layers as well as the high-field region (which corresponds to pure electron, pure hole and mixed injection, M_e, M_h and M_{mix} respectively) was determined as discussed in section 2.3. The mean multiplication, $\overline{M}$ for a given wavelength can be written as

$$\overline{M} = \frac{h_1 M_e + h_3 M_h + h_2 M_{mix}}{h_1 + h_2 + h_3} \tag{4.3}$$

The parameters M_e, M_h and M_{mix} can be calculated by substituting 0, w and x respectively to (2.31) where x is determined by a random number generator, r which uniformly distributed from 0 to 1, expressed as

$$x = \frac{-\ln(r)}{g} - w_1 \tag{4.4}$$

The multiplication gains resulting from injecting carriers in various x positions in the depletion width were averaged over at least 10,000 trials to give a reliable M_{mix}.

The model was verified under strong ($\gamma = 10^6\ cm^{-1}$) and weak absorption ($\gamma = 10^1\ cm^{-1}$) in a 1.0 μm perfect PIN with a 1.0 μm p^+ cladding, which gives a pure and mixed carrier injection. The absorption profiles calculated from these γ's are shown in Figure 4.16. For the case of a low $\gamma \sim 10^1\ cm^{-1}$, it was assumed the carriers are created uniformly across the depletion width.

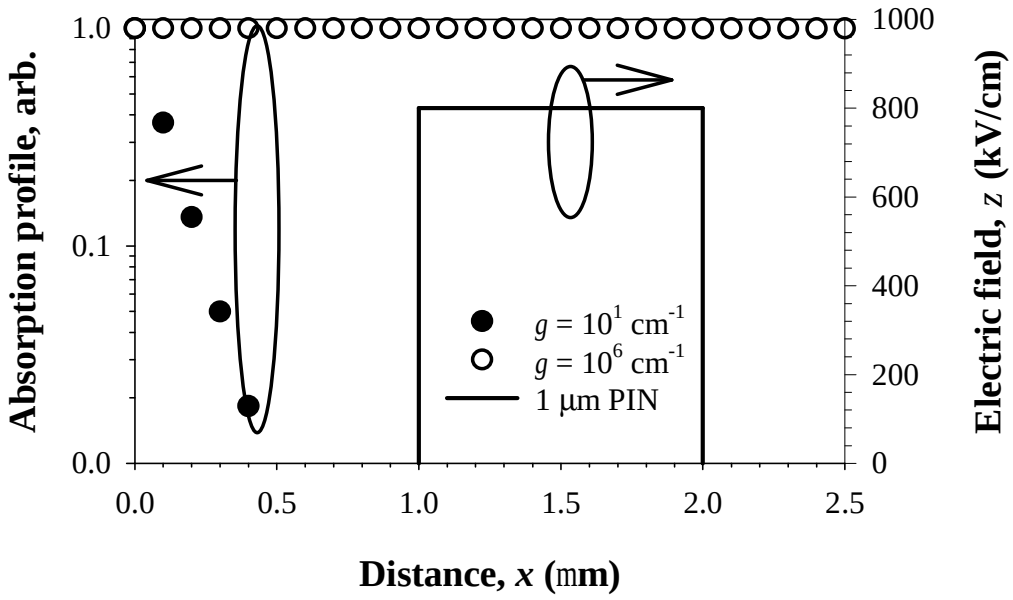

Figure 4.16 *The absorption profiles with γ of 10^6 and $10^1\ cm^{-1}$ shown as ● and ○ respectively in a 1.0 μm PIN, which has an electric field profile shown as —* .

The simulations were done by setting the ionisation coefficient ratio, k (= β/α) to be 1, 0.5, 0.1 and 0, with the minority carriers parameters remaining the same as mentioned in the previous section. The simulation results were then compared to those obtained from the recursive model (setting the carriers dead spaces to 0). The averaged multiplication gains, $\overline{M}$ due to carrier pair injection at $x = 0$ to w were calculated from.

$\overline{M} = \frac{\sum_{x=0}^{w} M(x)}{N}$ where N is the number of bins introduced in *w*. The results illustrated in Figure 4.16 showed excellent agreement in these models from *k* of 0 to 1.

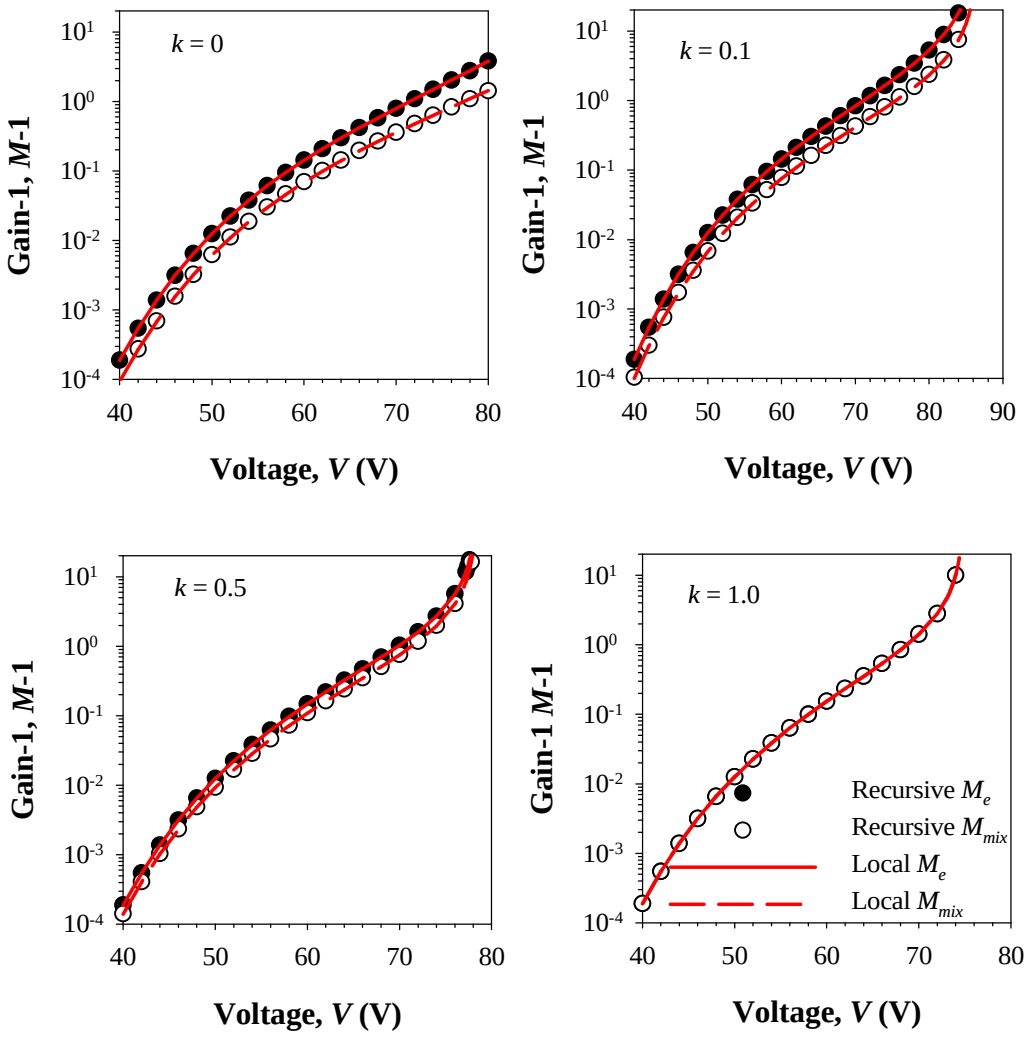

Figure 4.17 *The simulated M-1 vs V obtained by incorporating the local and quantum efficiency model with various k ratio between 0 and 1, where the avalanche process initiated by single carrier type due to strong absorption ($\gamma = 10^6$ cm^{-1}), and mixed carrier type due to weak absorption ($\gamma = 10^1$ cm^{-1}) shown as solid and dashed lines respectively. Also shown the corresponding recursive simulation results as ● and ○.*

The constructed model was then used to simulate the spectral responses of P1 as shown in Figure 4.15. The measured η at the longer wavelengths > 480 nm are noticeably higher than the simulated results due to the *F-K* effect. Nevertheless, both measurement and simulation results agree well in the shorter wavelengths as most of the photons were created in the cladding, where the absorption is not enhanced by the electric field.

The absorption coefficients at high bias voltages may be extracted after the effect of avalanche multiplication was factored out, as shown in Figure 4.18. An additional absorption of ~ 50% was found at electric field of 800 kV/cm in AlInP. The *F-K* effect, however occurs predominantly in the Γ valley and therefore the results are not as pronounced as in GaAs, which is a direct band gap semiconductor.

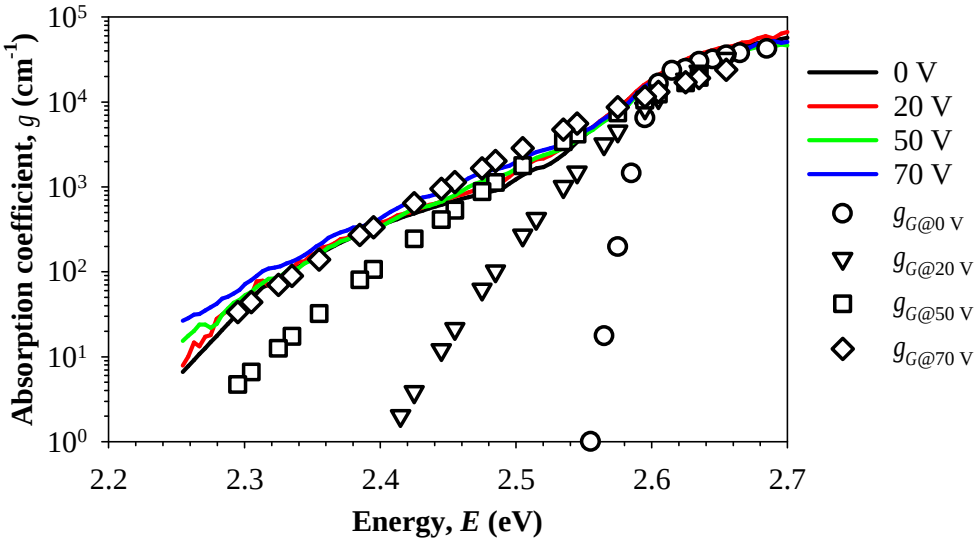

Figure 4.18 *Absorption coefficients extracted from P1 at bias voltages of 0, -20, -50 and -70 V shown as black, red, green and blue solid lines. The simulated absorption coefficients due to the Γ-valley as a function of bias voltage were obtained from F-K simulation shown as ○, ▽, □ and ◇ respectively.*

To understand the electro-absorption in an indirect semiconductor like AlInP, *F-K* simulation was performed using equation (2.13), with both m_e* and m_h* assumed as 0.15, obtained from interpolation between AlP and InP [167, 168]. The reduced effective mass, μ of 0.075 was obtained using $\mu^{-1} = m_e^{*-1} + m_h^{*-1}$. The band gap, E_g was taken to be 2.59 eV, corresponding to the direct gap of AlInP. The electric field at a given bias voltage was calculated assuming the structure P1 is a perfect PIN. The simulated absorption coefficients illustrated in Figure 4.18 are contributed by Γ-valley only. However, the modelled and measured absorptions agree well for photon energies > 2.55 eV as the Γ-valley begins to dominate the absorption process.

As the direct gap absorption is negligible near the band-edge (E < 2.55 eV) in AlInP at low bias voltages of 0 and -10 V, the extracted absorption coefficients at these bias voltages are indistinguishable in Figure 4.18. Nevertheless, as the bias voltage increases, the absorption contribution from the Γ-valley becomes comparable to that from the *X*-

valley and therefore an enhanced absorption can be observed from -45 V to the diode breakdown voltage.

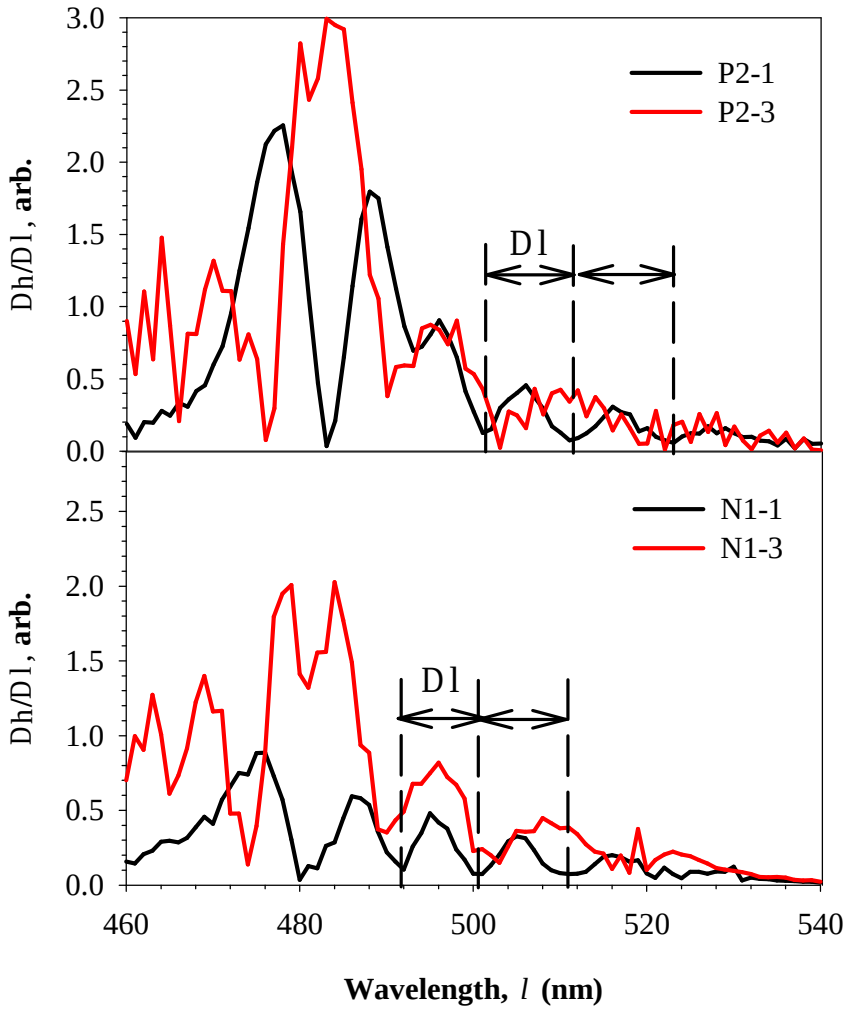

Figure 4.19 $\Delta\eta/\Delta\lambda$ *obtained in P2s and N1s. Arrows show the* $\Delta\lambda$ *in both P2-1 and N1-1.*

F-K oscillation, however, is not found in the measured absorption coefficients corresponding to photon energies larger than the direct gap of AlInP, which is most probably due to the resolution of the measurement setup. In contrast, oscillations at low energies corresponding to wavelengths longer than ~ 480 nm is found in all samples. The results obtained in P1s and N1s are plotted as $\Delta\eta/\Delta\lambda$ to emphasis the oscillation effect as shown in Figure 4.19. The $\Delta\lambda$ between the peaks (or valleys) are consistent between 10-12 nm (48 – 58 meV) even in those samples where the p^+ cladding was etched down to ~ 0.2 μm (P2-3 and N1-3). The Fabry-Perot effect therefore, is not the primary reason for these oscillations, where the $\Delta\lambda$ is sensitive to the cavity thickness which consists of AlInP *p*, *i* and *n* layers. Similar effects in the spectral response

however, have been reported for indirect band-gap semiconductors like Si and Ge; these effects were associated with transverse optical (TO), traverse acoustic (TA), longitudinal optical (LO) and longitudinal acoustical (LA) phonons where carrier promotion to the conduction band involves emission and absorption of phonons [69]. It is believed that the measured value is primarily due to LA, which is the dominant phonon in assisting the absorption process that involves a transition of Γ to X energy-gap [169]. LA was determined as 24 – 29 meV (= $\Delta\lambda/2$ [69]) and such value is similar to $Ga_xIn_{1-x}P$ (15.5 – 32 meV when x is varied between 0 and 1 respectively [169]).

The absorption beyond the theoretical bandgap is commonly found in other material systems such as Si [170] and GaAs [171], and is known as Urbach tailing [172], which can be described by

$$g(E) = g_g \exp\left[\left(E - E_g\right)/E_0\right] \tag{4.5}$$

where γ_g is the γ value at the band gap. E_0 is a parameter which is composed of the temperature dependence component due to phonons interactions and structural disorder respectively. By extracting E_g and the corresponding γ_g in Figure 4.13, E_0 is found to be 17-25 meV. The calculated E_0 appears to be very similar to that of LA phonon, which could play an important role in the absorption process at long wavelengths [173].

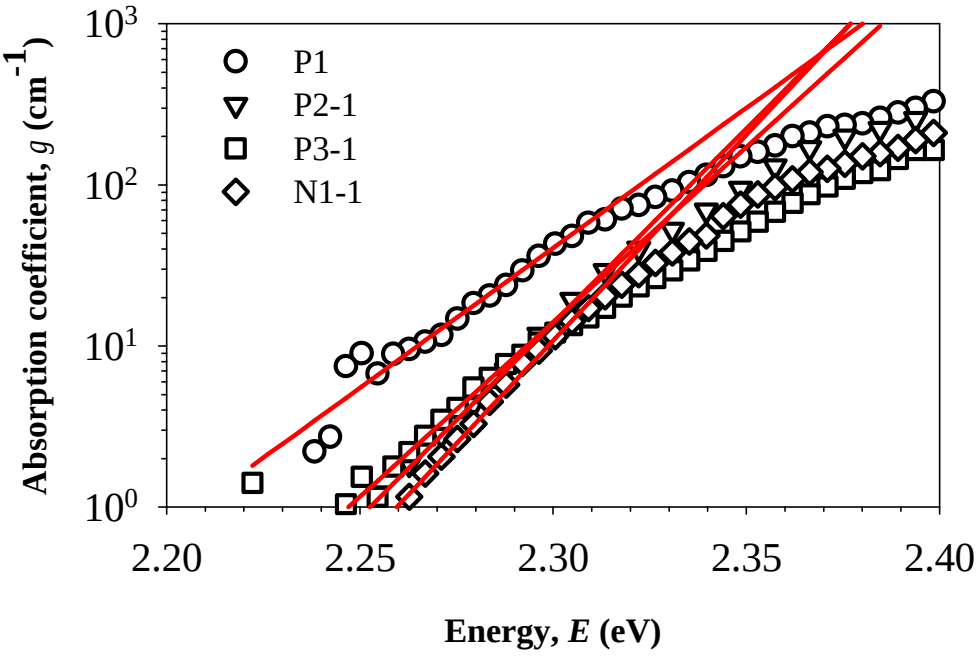

Figure 4.20 *The measured absorption coefficients in P1, P2-1, P3-1 and N1-1 shown as* ○. ▽,□ *and* ♢ *respectively. The lines are plotted using (4.5) to extract* E_0.

4.6 Conclusion

A detailed and systematic study of the absorption behaviour in AlInP was performed on PINs with top cladding and i-region thicknesses ranging from 1 µm down to 0.2 µm. Photocurrent in these devices were scanned for uniformity to ensure that the measurements reflect the bulk values, while the deduced responsivity was confirmed using a laser. The absorption coefficient in AlInP over a wide dynamic range was determined accurately via spectral response measurements and bias dependent photocurrent scans, and it was found to be consistent across all samples. The calculated absorption coefficient was later used to determine the energies of the direct Γ and X valleys in AlInP. The Franz Keldysh effect which primarily contributes to the spectral FWHM widening was investigated by incorporating quantum efficiency and McIntyre's multiplication models into the photoresponse model. Due to a relatively higher absorption contribution in the X-valley, the F-K electro-absorption effect is negligible and the spectral FWHMs are similar at high gain.

Chapter 5 DETERMINATION OF IMPACT IONISATION COEFFICIENTS

5.1 Introduction

Avalanche photodiodes (APDs) are widely employed in optical systems, particularly where low-light detection is necessary due to their superior sensitivity compared to PIN photodiodes. While a high avalanche gain is desirable, the excess noise factor due to the stochastic nature of impact ionisation eventually limits the sensitivity of APDs. It is therefore important to have a model to predict the multiplication and excess noise of these devices in order to optimize their performance and this in turn requires accurate knowledge of the impact ionisation behaviour of the carriers.

As discussed in section 2.5, the local model fails to predict the low multiplication values and the excess noise due to the neglect of the dead space. One of the first models to successfully predict the excess noise and multiplication in devices with thin sub-micron avalanche widths was developed by Hayat et al. [120] who numerically solved a set of two coupled recurrence equations, which incorporate the carriers ionisation probability density function (PDF) with the presence of dead space as shown in section 2.6. Their dead-space multiplication theory (DSMT) is capable of calculating the multiplication and excess noise of PIN devices down to avalanche widths of 0.05 μm [122, 174].

However, the accuracy of the DSMT model depends critically on an accurate knowledge of the ionisation probability density function (PDF). The ionisation PDF requires knowledge of d_e (d_h), related simply to the electron (hole) ionisation threshold energy E_{the} (E_{thh}) and the electric-field, ζ as $E_{the} = \frac{d_e}{z}$ (assuming a uniform field), and on the ionisation coefficients of carriers after travelling the dead space. The latter is also referred to as the enabled ionisation coefficients, α^* (β^*). (Estimates for the quantity E_{the} (E_{thh}) can be obtained from the literature or from the band structure; these can be used in the DSMT as a starting point.) However, despite the availability of α' (β') for many semiconductors including AlInP [111], these coefficients are not applicable to the DSMT model as there is no simple relationship relating experimentally determined α' (β') and α^* (β^*). Historically, obtaining α^* (β^*) and E_{the} (E_{thh}) has required the experimental values of M_e (M_h) and F_e (F_h) in a series of different thicknesses PIN

devices and a fitting procedure using the DSMT model [174]. While this procedure works, it requires the accurate generation of considerable new noise data in many materials.

In this chapter, α^* (β^*) is showed can be approximated from experimentally determined α' (β') using a simple equation provided that a reasonably accurate knowledge of E_{the} (E_{thh}) exists without the need for any excess-noise data. The parameter α' (β') is determined from multiplication measurements on PINs with a uniform electric field as they simplify the subsequent discussions. These estimates of α^* (β^*) can, in turn, be used in the DSMT models to generate the multiplication and excess noise in PIN devices as thin as 0.05 μm. They can also be used to predict the breakdown probability and breakdown voltage [123, 175], as well as the statistical characteristics of the time response of the APD [176, 177].

Definitions of α's (β's) used in this chapter, i.e. α (β), α_{device} (β_{device}), α' (β'), α^* (β^*), α_{MC} (β_{MC}), α_s (β_s) are summarised in Appendix B.

5.2 Model

In the DSMT model, the electron ionisation PDF, $h_e(x)$ is described as a perfect exponential function after the carrier traverses the dead-space distance, d_e [120] as mentioned in equation (2.39) where the corresponding mean ionising path length, x_e is $d_e + 1/\alpha^*$. However, the mean ionisation path length between successive electron ionisations, x_{se} is different from x_e because as each time an electron ionises, an secondary electron is launched alongside the primary electron and they are both set forth to initiate the subsequent ionisations independently from each other after they traverse their individual dead spaces. To calculate x_{se}, we must first consider the electron survival probability, $S_e(x)$, where an electron travels a distance x without impact ionising as shown in equation (2.49).

Once an electron impact ionises and therefore gives rise to an additional electron-hole pair, both the primary electrons, which starts afresh, and the secondary electron are then assigned with survival probabilities S_{e1} and S_{e2}, respectively. The joint survival probability, $S_T(x)$ for the primary and secondary electrons, according to which both electrons travel a distance x without impact ionising is the product of $S_{e1}(x)$ and $S_{e2}(x)$, namely,

$$S_T(x) = S_{e1}(x)S_{e1}(x) = \begin{cases} 1 & , x \le d_e \\ \exp\left[-2a^*(x-d_e)\right] & , x > d_e \end{cases} \quad (5.1)$$

The ionising PDF for the electron pair, $h_T(x)$, can be obtained by differentiating 1- $S_T(x)$, which gives

$$h_{T1}(z) = \begin{cases} 0 & , x \le d_e \\ 2a^*\exp\left[-2a^*(x-d_e)\right] & , x > d_e \end{cases} \quad (5.2)$$

Interestingly, the mean here, x_{se}, is $(1/2\alpha^*) + d_e$. A similar derivation can be repeated in the case of the local model framework where $d_e = 0$ and

$$h_{T2}(z) = 2a'\exp\left[-2a'x\right] \quad , x > 0 \quad (5.3)$$

is obtained with a mean of $x_{se} = 1/(2\alpha')$. The relationship between α^* (β^*) and α' (β') can now be found by equating the mean ionising lengths from the DSMT and local model when they are compared at the same electric field in identical PIN structures as they should yield the same multiplication value. This gives

$$a' = \frac{1}{\frac{1}{a^*} + 2d_e} \quad (5.4)$$

Note that α' (β') given by equation (5.4) is not the same as $1/x_e$ as it is derived from $1/x_{se}$. This accounts for why there is $2d_e$ rather than just d_e in the denominator of equation (5.4). The rate β' can be expressed in similar manner by replacing $h_e(x)$, α^*, d_e, x_{se}, and $S_e(x)$ respectively with $h_h(x)$, β^*, d_h, x_{sh} and $S_h(x)$.

An alternative (more complicated and less intuitive) way to arrive at equation (5.4) is as follows. In an earlier paper, Spinelli and Lacaita [178] attempted to solve the DSMT model to extract the multiplication analytically. This technique involved differentiating the DSMT recurrence equations and then further simplifying them using a perturbation

method, which is reasonably accurate for small dead-space to device-width ratios, d/w. The quantity M_e (M_h) obtained is then expressed in terms of α^* (β^*) in the presence of dead space as follows [178]:

$$M(w) = M_e = \frac{\exp(ad_h)}{1 - \int_{d_e}^{w-d_h} a \exp\left[-\int_{x}^{w-d_h}(a-b)dx'\right]dx} \tag{5.5}$$

$$M(0) = M_h = \frac{\exp(bd_e)}{1 - \int_{d_e}^{w-d_h} a \exp\left[-\int_{x}^{w-d_h}(a-b)dx'\right]dx} \tag{5.6}$$

where

$$a = a^* \frac{1 + 2b^* d_h + b^* d_e}{1 + 2a^* d_e + 2b^* d_h + 3a^* b^* d_e d_h} \tag{5.7}$$

$$b = b^* \frac{1 + 2a^* d_h + a^* d_e}{1 + 2a^* d_e + 2b^* d_h + 3a^* b^* d_e d_h} \tag{5.8}$$

The local rate α and β from equation (5.5) to (5.8) are valid for $d_e \leq x \leq w\text{-}d_h$ as defined in [178]. From equation (5.5), it is possible to equate the multiplication obtained from solving the recurrence equations (after the perturbation approximation) and the multiplication obtained from the local model (where no dead-space is assumed) for a given w in order to relate α^* to α_{device}. The parameter α_{device} is normally extracted from experiments and therefore includes the effect of the dead space. This is the rate used in the local model which results in multiplication that is equivalent to that obtained from the DSMT model. For simplicity, assuming a perfect PIN structure where $M_e = M_h$ and $F_e = F_h$, i.e., $\alpha = \beta$, equation (2.31) reduces to

$$M(w) = M_e = \frac{1}{1 - a_{device} w} \tag{5.9}$$

Similarly, assuming $d_e = d_h$ and $\alpha^* = \beta^*$, equation (5.5) simplifies to

$$M(w) = M_e \approx \frac{1+\left(d_e + \frac{1}{a^*}\right)^{-1} d_e}{1-\left(d_e + \frac{1}{a^*}\right)^{-1}(w-2d_e)}. \tag{5.10}$$

By equating the gain expressions in equation (5.9) and (5.10), we obtain

$$a_{device} \approx \frac{1-\frac{d_e}{w}}{\frac{1}{a^*}+2d_e}. \tag{5.11}$$

The denominator of this expression is identical to that in equation (5.4) but the effect of the device-dependent α_{device} (β_{device}) is accounted for qualitatively by the d/w term in the numerator. Similar derivations were used in another simple extreme case where β^*, d_h in equation (5.5) and β in equation (2.31) are set to 0. These simplified multiplication expressions are equated to each other and equation (5.11) is once again obtained. It is therefore concluded that equation (5.11) is independent of β^* and d_h.

This first-order approximation becomes increasingly inaccurate in thin devices with high gains due to the large d/w ratio; the approximation is therefore not a good way for determining the multiplication as pointed out in [178]. However, if the asymptotes of α_{device} for devices with different widths (at high field) are considered, i.e., when d/w becomes negligible, then equation (5.11) approaches equation (5.4). The derivation details can be found in Appendix C. This means that the enabled (non-local) ionisation coefficient, α^* (β^*) can be extracted from the asymptotes of a family of the experimental coefficients, a_{device}. For each device width, the asymptote can be found when the electric field is high, or equivalently when the multiplication is high.

To verify the validity of equation (5.11), we have used a simple Monte-Carlo (SMC) model to generate the associated multiplication and noise characteristics in an idealized series of PINs. Several authors showed that such a model agrees well with experimental gain and noise for several semiconductor materials even with w thinner than 0.1 μm [131-133]. Using the input parameters from Plimmer *et al.* [131], multiplication (M_e and M_h) and noise (F_e and F_h) of GaAs perfect PIN devices with w of 0.05, 0.1, 0.2, 0.5, and 1.0 μm were simulated using the SMC model. Details of the SMC model have been

reported previously in [131]. This SMC data was compared against the multiplication and noise data obtained from the random-path-length (RPL) model [122], which utilizes the randomly generated ionisation path lengths according to the ionising PDF given by equation (2.39). The RPL technique essentially gives identical results to the DSMT technique [120], as shown in [179]. The results are described in the next section.

5.3 Results

The parameters α_{device} (β_{device}) were determined from M_e and M_h simulated from the SMC model using equation (2.33). The device-independent ionisation coefficient α' (β') was parameterized using the highest value of α_{device} (β_{device}) at a given electric field, which was extracted from multiplication of different thicknesses PINs as illustrated in Figure 5.1 to give the device-independent ionisation coefficient. The results are tabulated in Table I. These values are similar compared to those in [107] but they cover a wider electric-field range. For clarity, α_{device} (β_{device}) for only 0.05, 0.1, and 1.0 μm PINs are shown.

The SMC model can also generate the ionising PDF at a given electric field by logging the ionising length between two successive ionising events, i.e., x_e, as shown in Figure 5.3, which gives the mean electron ionising length, $1/\alpha_{MC}$. This can be done for primary ionising carriers, injected with just thermal energy and for those secondary ionising carriers which can start with significant residual energy [119]. This resulted in a slight difference in ionising PDF between the primary and secondary ionising carriers shown in Figure 5.2, where the latter has a higher probability to impact ionise after travelling a distance, $\underline{x}$.

The PDF at the same electric field (600 kV/cm) is approximated in the DSMT model in Figure 5.3 using equation (2.39), which comprises d_e followed by an exponential function which has a mean of $1/\alpha^*$. The dead space d_e was defined as the distance where the rising edge of the PDF reached 50% of its peak value [103]; therefore, E_{the} (E_{thh}) for secondary ionising carriers was calculated as 3.0 (3.3) eV using equation (2.29) as illustrated in the inset of Figure 5.1 while the initial carrier threshold energies, E_{the} (E_{thh}) determined from the SMC model was about 15% higher than those for the secondary carriers at 3.5(3.8) eV. (Using the secondary carrier threshold energy for the primary injected carrier will result in a slight overestimation of the low multiplication values in devices but it will not change the breakdown voltage appreciably.)

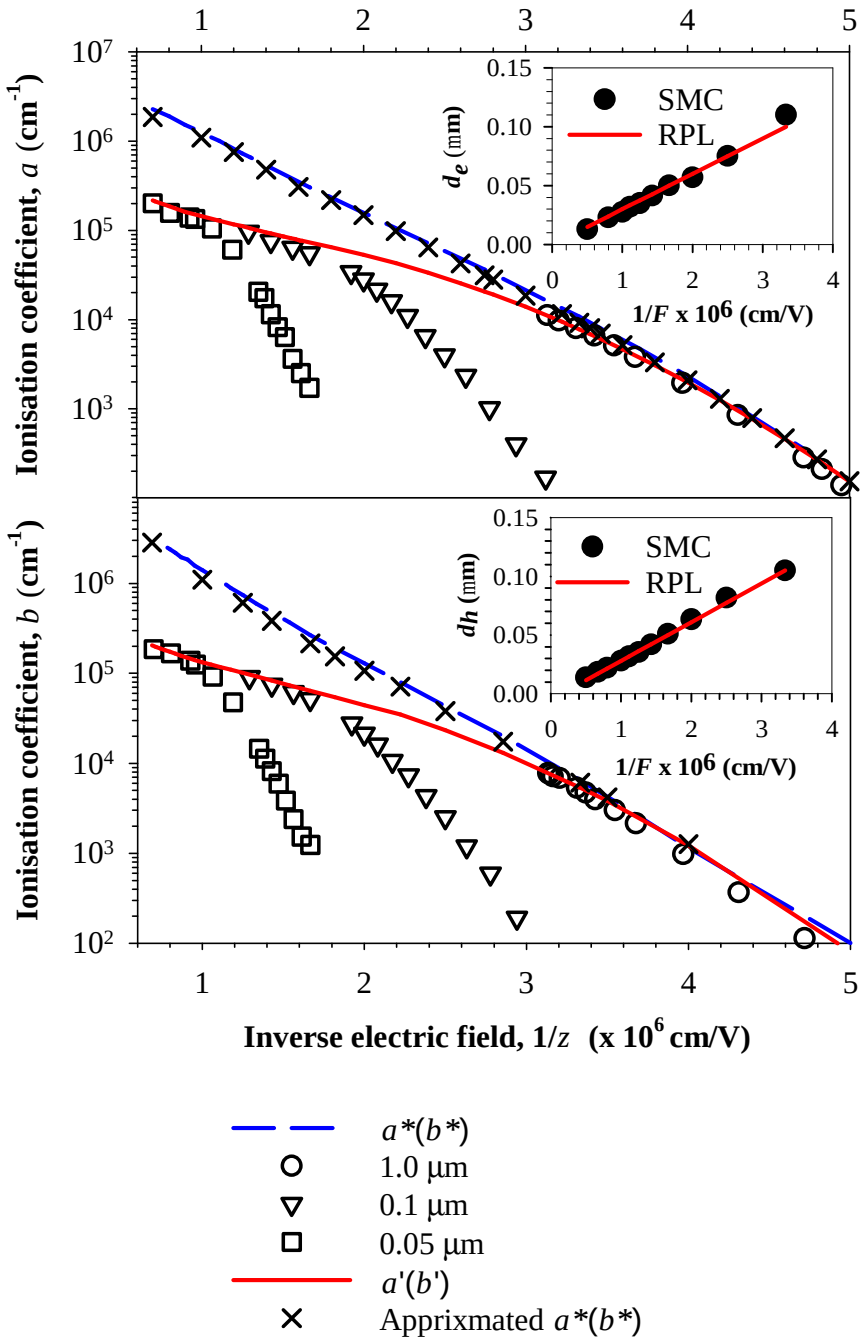

Figure 5.1 α_{device} (β_{device}) *of 0.05, 0.1, and 1.0µm PINs calculated from equation (2.33) denoted as* □, ▽, *and* ○, *respectively. Parameterized* α' (β'), $\alpha^*(\beta^*)$ *determined from equation (5.4) and (5.12) are shown as solid, medium-dash lines, and* ×, *respectively. Inset shows fittings (lines) of carriers dead-space using equation (2.29) with those obtained from the SMC simulations (circles).*

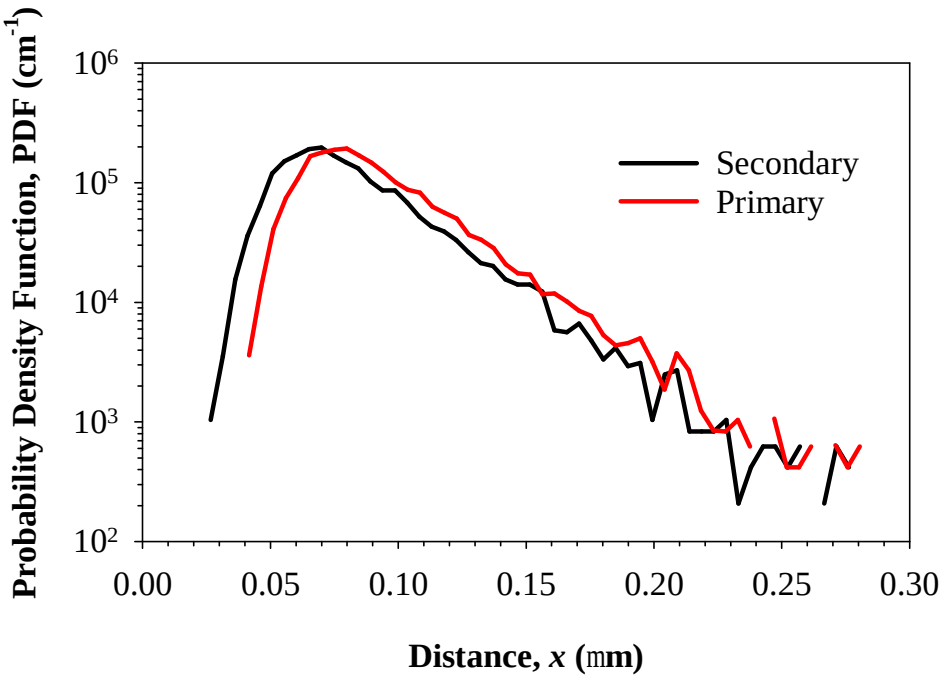

Figure 5.2 *The ionisation PDF of primary and secondary carriers at 600 kV/cm shown as black and red lines respectively.*

The enabled ionisation coefficient α^* (β^*) can then be determined from α_{MC} (β_{MC}) using

$$\frac{1}{a_{MC}} = d_e + \frac{1}{a^*} \tag{5.12}$$

and this is plotted as a function of electric field for secondary ionising carriers in Figure 5.1.

The ionising PDF associated with α' is also shown in Figure 5.3 where the peak is significantly lower than those from the SMC and DSMT models as this assumes that secondary carriers have no dead space and therefore are allowed to ionise immediately after they are created.

Using equation (5.4) with E_{the} (E_{thh}) of 3.0 (3.3) eV on α' (β') shows that excellent agreement to the α^* (β^*), which were determined from the SMC simulations, can be achieved over a wide range of electric fields from 200 kV/cm to 1.4 MV/cm as shown in Figure 5.1. Again, these values can be used as input parameters to the DSMT model to generate multiplication and excess noise. By using the appropriate E_{the} (E_{thh}) for primary and secondary carriers, the calculated DSMT-based multiplication characteristics agree well with those obtained from the SMC simulations even for a 0.05 µm thick PIN over several orders of magnitude as shown in Figure 5.4.

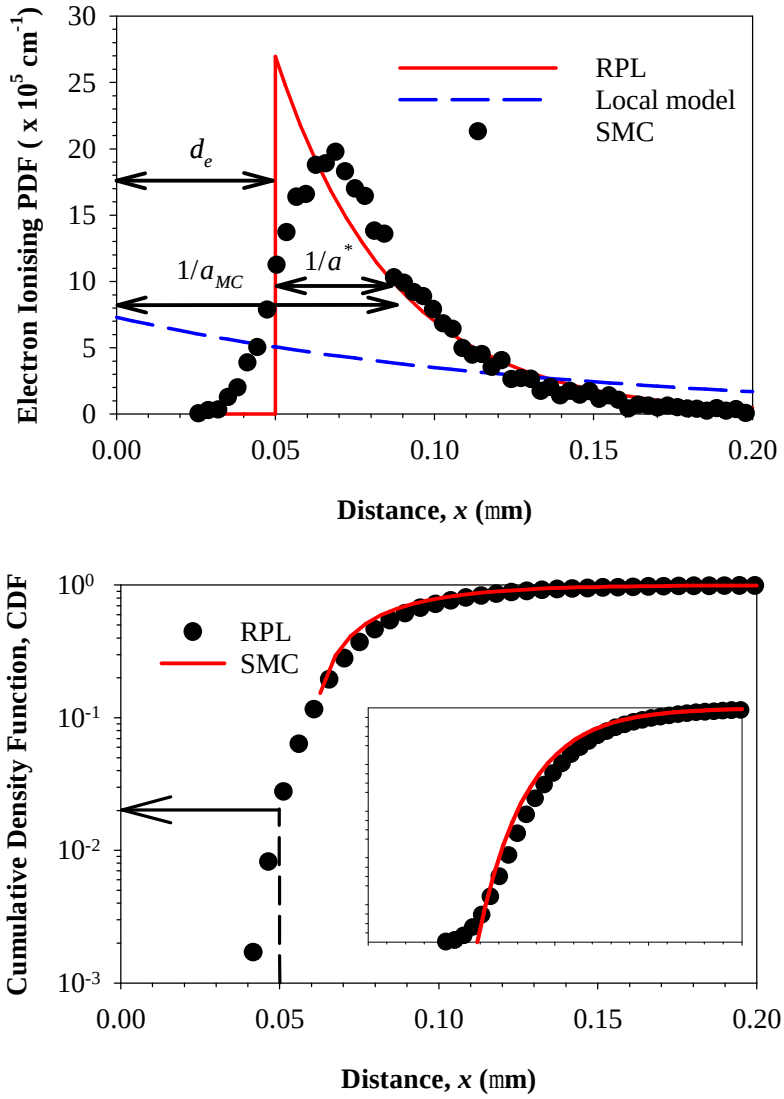

Figure 5.3 *Top: The electron ionising PDF of GaAs at 600 kV/cm obtained from the SMC simulations (●). The mean ionising length ($x_e=1/\alpha_{MC}$) and dead space (d_e) were determined to calculate α^* using equation (2.29) to generate the PDF (solid line). Also shown is α' obtained using equation (5.4) as dashed lines. Bottom: The cumulative density function (CDF) obtained from the SMC and RPL simulations shown as symbols and line respectively.*

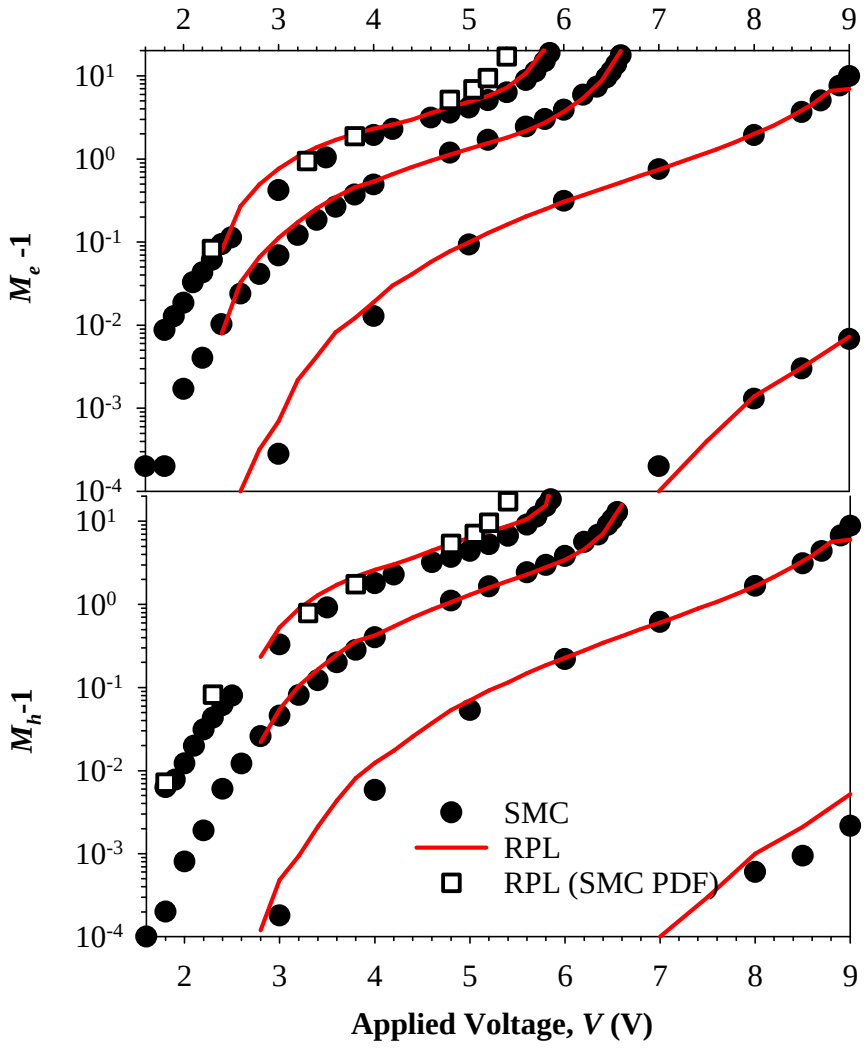

Figure 5.4 *M_e-1 and M_h-1 curves of PINs with w of 0.05, 0.1, 0.2, and 0.5 µm (from left to right) simulated by the RPL (solid line) and SMC model (●). For clarity, the multiplication of 1.0 µm PIN is not shown. Also shown RPL simulated results using the PDFs obtained from the SMC model as* □.

Furthermore, excess noise factors calculated from the DSMT recurrence model showed reasonable agreement with those obtained from the SMC simulations down to 0.1 µm PIN as shown in Figure 5.5. As the device width shrinks further to 0.05 µm, the DSMT model underestimates both F_e (F_h) and shows no multiplication at low electric-fields because of the hard dead-space assumption. In reality, the ionising PDF is not accurately presented by equation (2.39) even at relatively low field of 600 kV/cm as illustrated in Figure 5.3 where it initially rises to the peak value gradually due to the "soft" dead space and thereafter decays exponentially. To emphasise on the softness factor, the CDF simulated in both SMC and RPL at 600 kV/cm is plotted in both linear and logarithmic scale as shown in Figure 5.3. Although a good agreement can be achieved in these models in linear scale, SMC model shows a non-zero value of CDF

after a traverse distance of < 0.05 μm where electron has a probability to ionise, unlike that of RPL model. Using SMC's simulated CDF, 0.05 μm PIN gives multiplication value of ~1.03 at such electric field (or an applied voltage of 1.8 V) which agrees to the result in Figure 5.4.

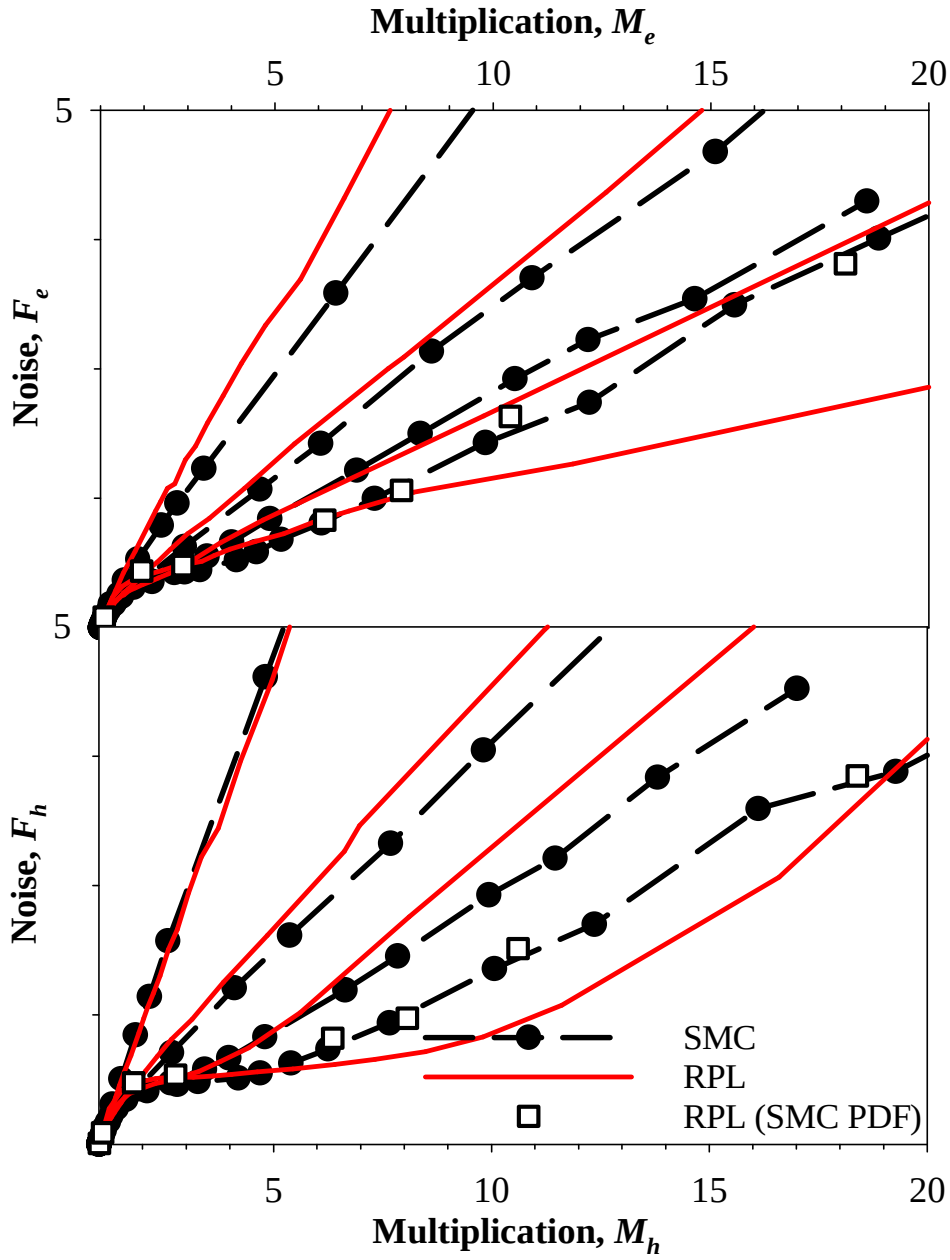

Figure 5.5 *Excess noise of PINs with w of 0.05, 0.1, 0.2, and 1.0 μm (from top to bottom) due to pure electron and hole injection, F_e and F_h respectively simulated by the RPL (solid lines) and SMC model (symbols with dashed lines). Also shown RPL simulated results using the PDFs obtained from the SMC model as* □.

Considering the simplicity of equation (5.4) in estimating α^* (β^*), simulated results of multiplication and excess noise factor from the DSMT model for a wide range of semiconductor materials like Si [124], InP [180], SiC [181], $Al_{0.6}Ga_{0.4}As$ [182],

$Al_{0.8}Ga_{0.2}As$ [183], $In_{0.52}Al_{0.48}As$ [184] and $Ga_{0.52}In_{0.48}P$ [185] agree surprisingly well with the experimental data, provided good knowledge of α' (β') and their corresponding E_{the} (E_{thh}) exists, as shown in Table I. The results can be found in Appendix D.

The "effective" threshold energy in the DSMT model is the mean energy carriers attain before impact ionisation, and as such it differs from other definitions in the literature [94, 97, 186]. The threshold energy E_{the} (E_{thh}) can be obtained from excess-noise measurements. In the absence of the experimental data such as in $Al_{0.8}Ga_{0.2}As$ and AlInP, the parameters can be be estimated from low values of multiplication in devices with the avalanche width, w < 0.5 µm where the effects of the dead space become important. The primary carrier ionisation coefficient is relatively low at the onset of multiplication where on average not every carrier gives rise to another electron hole pairs before leaving the avalanche width, i.e. M < 2. The measured multiplication thus, is mostly due to the primary carrier with minimal feedback carriers and this allows extraction of the threshold energy.

To obtain both E_{the} (E_{thh}), they were used as fitting parameters in RPL model to generate M_e-1 (M_h-1) to match to those obtained from a 0.1 µm GaAs PIN simulated by SMC model, as illustrated in Figure 5.6. The parameter α* (β*) was then adjusted accordingly to the varying E_{the} (E_{thh}) as shown in equation (5.4) before multiplications were computed using RPL model. The lower limit of E_{the} (E_{thh}) were set as 1.42 as this is the band gap of GaAs. Using E_{the} = 3 eV, low values of M_e-1 obtained from RPL fit best with those obtained from SMC model and this is independent of E_{thh} value. By varying E_{thh} to 3 eV, breakdown voltages M_e-1 simulated in both models agree well. The fitting procedure was repeated on M_h-1 data and both E_{the} and E_{thh} were found to be ~ 3 eV.

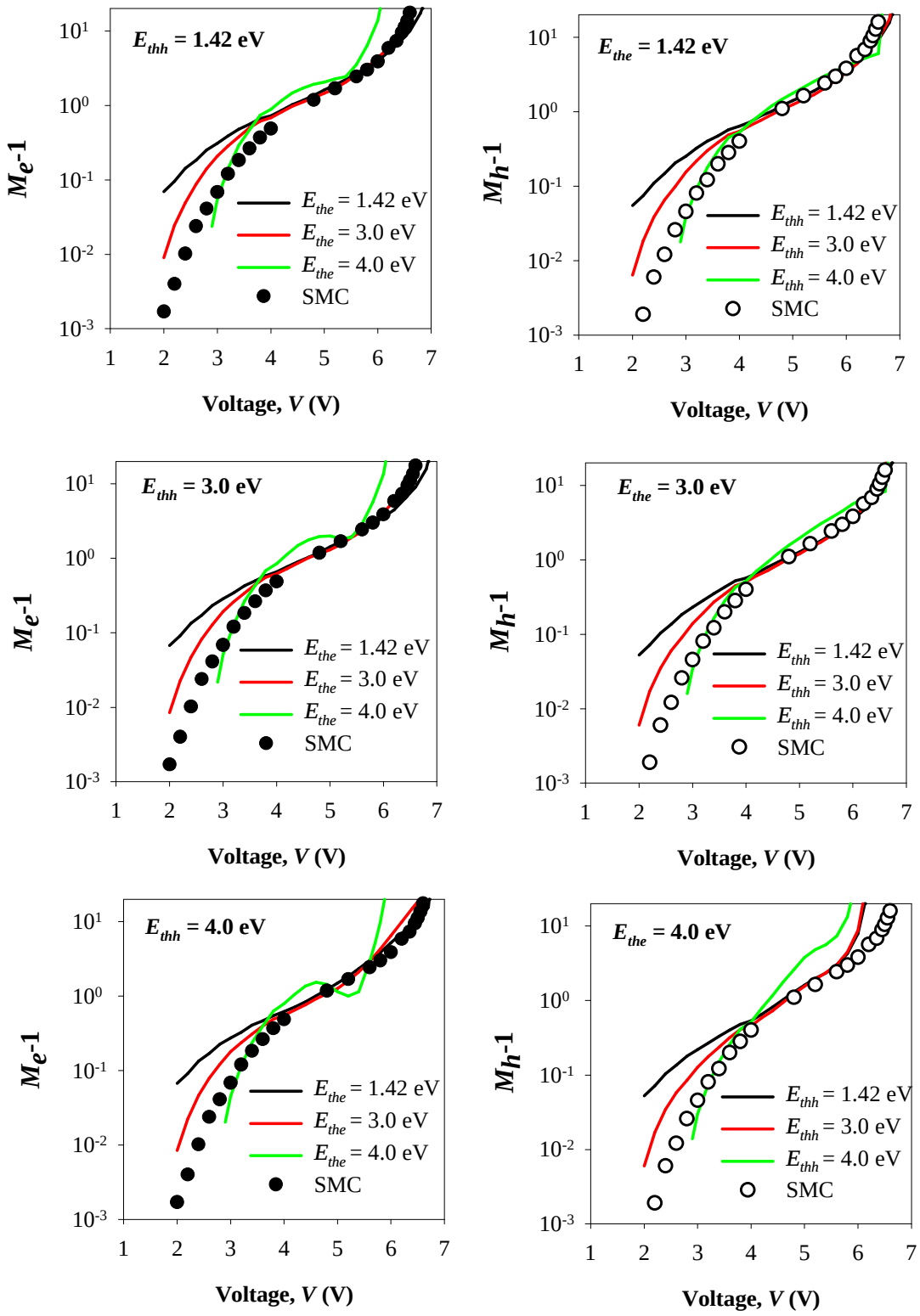

Figure 5.6 *M_e-1 (M_h-1) simulated in 0.1 µm PIN using SMC model shown as ● and ○ respectively. By fixing E_{thh} (E_{the}) values, M_e-1 (M_h-1) was simulated using E_{the} (E_{thh}) = 1.42, 3.0 and 4.0 eV shown as black, red and green lines.*

Table 5.1 *α' (β') of group IV and III-V semiconductors expressed as α' (β') = Aexp[-(B/ζ)^c] where ζ is electric field. The ionisation coefficients that were found to have a wider electric field range than the previous reports are marked as *. The threshold energies shown are for secondary ionising carriers.*

Material	Electric field range (kV/cm)	Coefficient Type	A ($\times 10^5$ cm^{-1})	B ($\times 10^5$ V cm^{-1})	C	E_{the} (eV)	E_{thh} (eV)
Si [108]	175-400	α'	7.03	12.3	1.00	1.8 [124]	2.4[124]
		β'	15.8	20.4	1.00		
	400-800*	α'	7.03	12.3	1.00		
		β'	6.71	16.9	1.00		
GaAs [107]	150-900	α'	2.28	677	1.51	3.0 [107]	3.3
		β'	2.24	715	1.55		
GaAs (this work)	150-500	α'	1.45	5.00	2.10	3.0	3.3
		β'	1.55	5.50	2.00		
	500-1110	α'	4.70	12.0	0.90		
		β'	4.00	11.0	1.00		
	1110-1400	α'	6.39	16.0	0.90		
		β'	5.92	15.5	0.95		
InP [109]	240-380	α'	112	31.1	1.00	2.8 [180]	3.0 [180]
		β'	47.9	25.5	1.00		
	380-560	α'	29.3	26.4	1.00		
		β'	16.2	21.1	1.00		
	560-1250*	α'	2.32	8.46	2.00		
		β'	2.48	7.89	2.00		

SiC	1000-4000	α'	7.00	70.0	1.66	12.0 [181]	8.0 [181]
		β'	19.0	103	1.01		
$Al_{0.6}Ga_{0.4}As$ [107]	330-1100	α'	2.95	11.6	1.44	3.4 [182]	3.6 [182]
		β'	3.11	12.1	1.43		
$Al_{0.8}Ga_{0.2}As$ [110]	328-1110	α'	3.18	10.4	1.67	3.2 [183]	2.3 [183]
		β'	3.55	11.2	1.85		
	1110-1540	α'	38.4	102	0.55		
		β'	38.4	102	0.55		
$In_{0.52}Al_{0.48}As$ [187]	220-980	α'	2.20	8.90	1.71	3.2 [184]	3.5 [184]
		β'	2.95	11.5	1.71		
$Ga_{0.52}In_{0.48}P$ [188]	357-1700	α'	4.57	14.1	1.73	4.1 [185]	4.1 [185]
		β'	4.73	14.3	1.65		
$Al_{0.52}In_{0.48}P$ [111]	400-1300*	α'	4.93	16.5	1.78	4.6	4.6
		β'	5.29	15.9	1.98		

5.4 Discussions

Equation (5.4) can be derived analytically when $\beta^*=0$ and $\beta^*=\alpha^*$ ($k^*=0$ and $k^*=1$) but the derivation is not straightforward for intermediate values of k^* ($=\beta^*/\alpha^*$). Therefore, it is best to demonstrate the validity of the equation numerically. The multiplications for a series of PINs with w of 0.05, 0.1, 0.2, 0.5, 1.0 µm were simulated using RPL model where the test conditions are $\beta^*=\alpha^*$, $\beta^*=0.5\alpha^*$ and $\beta^*=0$ ($k^*=1$, 0.5 and 0 respectively). The parameter α_{device} was extracted using equation (2.33) and this was shown in Figure 5.7. α_{device} for a given w has approximately the same value irrespective of β^*, and therefore equation (5.4) holds true as an approximation for k^* values between 0 and 1.

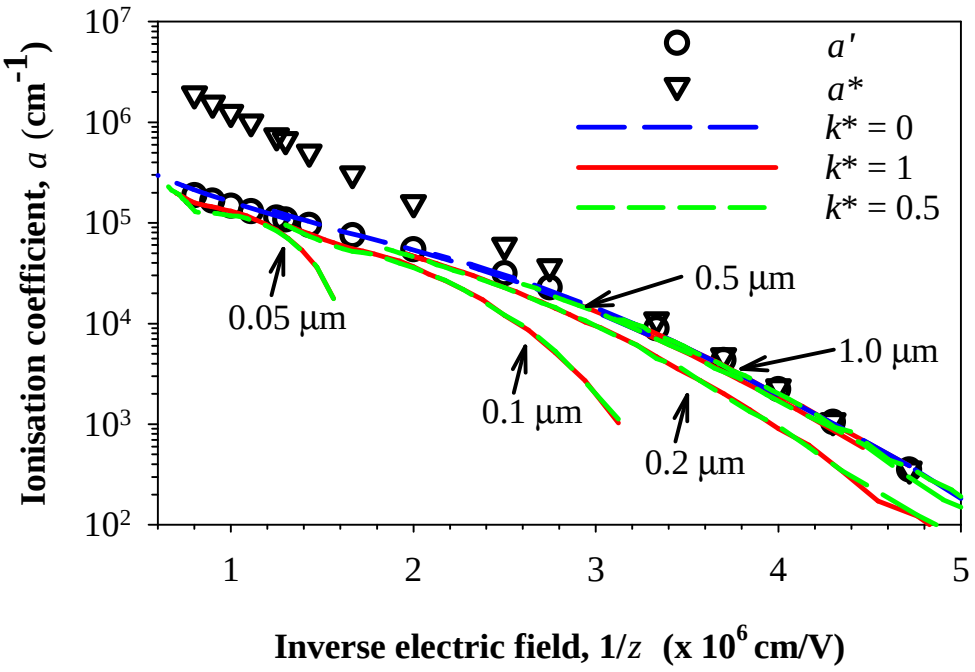

Figure 5.7 *α_{device} of 0.05, 0.1, and 1.0µm PINs calculated from equation (2.33) which corresponds to k* of 0, 0.5 and 1.0 shown as blue, green and red lines. The parameter α* and α' obtained from equation (5.4) are shown as ▽, and ○ respectively.*

From both equations (5.4) and (5.11), the correlation between $\alpha^*(\beta^*)$, $\alpha'(\beta')$ and α_{local} (β_{local}) are shown mathematically by incorporating the carriers dead spaces. The dead spaces appear to supress the ionisation rates in the primary and secondary ionising carriers, indicated by the numerator and denominator of equation (5.11). The effects of the dead space can be visualised better in spatial ionisation coefficient, α_s (β_s) and this will be discussed as follows. The notations used below such as $\alpha^*(\beta^*)$, $\alpha'(\beta')$, α_{local} (β_{local}), d_e (d_h) and ζ shall remain the same.

To simplify the argument, these parameters were set; $\beta^* = 0$, $\alpha^* = 3 \times 10^6$ cm^{-1}, ζ = 300kV/cm and d_e = 3 eV. The multiplication value in a perfect PIN was simulated and α_{local} was obtained using $\alpha_{local} = \ln(M_e)/w$. Sufficient mesh points of 100 were introduced to the structure to log the carriers ionisation positions. These were used later to calculate α_s using

$$a_s(x) = \frac{1}{N}\frac{dn}{dx} \tag{5.13}$$

where N is the number of electrons which entering dx while dn is the frequency of ionisation events due to these electrons.

To separate the dead space effects in primary and the subsequent carriers, several tests were conducted on a 1 µm PIN, except for C5 which the simulation was done on a 0.5 µm PIN. The summarised test conditions are shown in Table 5.2.

Table 5.2 *Different test conditions by varying the threshold energies in the primary and secondary carriers simulated in 1.0 µm (C1-C4) and 0.5 µm PINs (C5)*

Tests	**Tests condition**	**Gain**	α_{device} **(× 10^4 cm^{-1})**
C1	Primary carriers and the secondary carriers are both subjected to threshold energies of 0 eV (local model)	20.07	3.00
C2	Primary carriers and the secondary carriers are subjected to threshold energies of 3 and 0 eV respectively.	14.89	2.70
C3	Primary carriers and the secondary carriers are subjected to threshold energies of 0 and 3 eV respectively.	7.19	1.97
C4	Primary carriers and the secondary carriers are both subjected to threshold energies of 3 eV (RPL model)	5.94	1.78
C5	Primary carriers and the secondary carriers are both subjected to threshold energies of 3 eV (RPL model)	2.24	1.61

All multiplication gains, α_{device} and α_s for each test conditions were obtained in a similar manner as mentioned above. The results are shown in Figure 5.8.

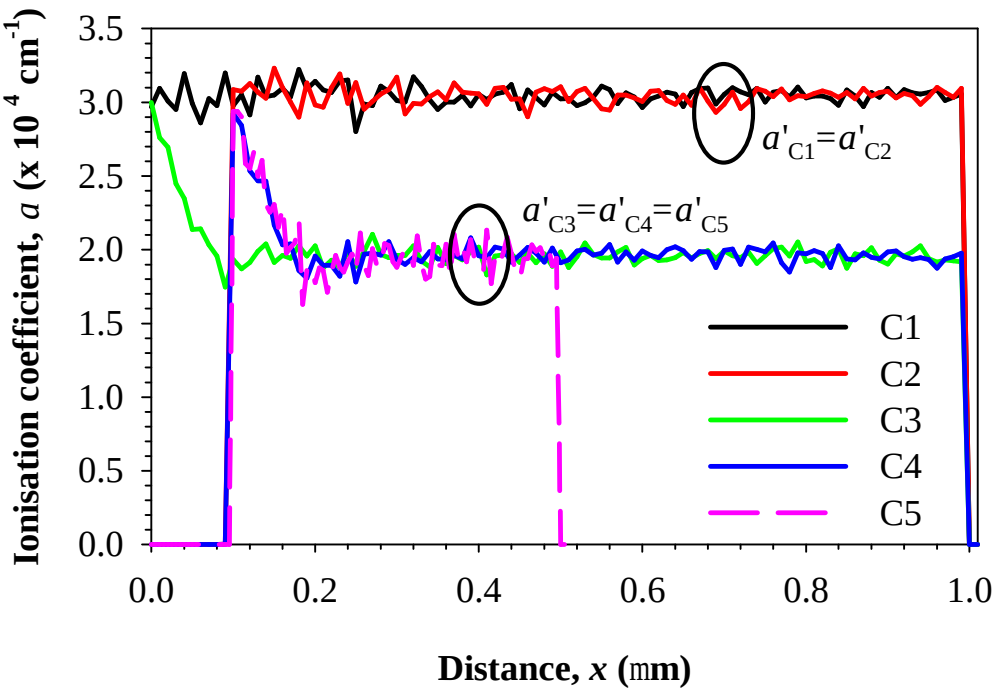

Figure 5.8 *Calculated α_{local} and α_s showed as solid and dashed red lines respectively at electric field 300 kV/cm assuming α^* and d_e of 3×10^4 cm^{-1} and 3.0 eV respectively.*

Test C1 resembles the typical local model where the dead space is assumed negligible in a device and therefore a constant α_s is obtained throughout the structure as illustrated in Figure 5.8. Because there is no dead space effect, $\alpha' = \alpha_s\ (0 < x < w) = \alpha^*$. As the primary carrier has an ionisation threshold in C2, there is no probability for electron to ionise initially due to the dead space, i.e. $\alpha_s\ (x < d_e) = 0$ and thereafter the ionisation coefficient is equal to α^*, i.e. $\alpha_s\ (x > d_e) = \alpha^*$. As the primary electron only initiates the ionisation after $d > 0.1$ µm, the effective w is 0.9 µm instead of 1.0 µm and this explains why $\alpha_{device\_C2} = 0.9(\alpha_{device\_C1})$.

From Figure 5.8, it is also apparent that $\alpha_s\ (x > d_e)$ is only dependent on the secondary carrier threshold energy and not the primary carriers'. This is because α_s is the instantaneous ionisation rate experienced by electrons at a given position, i.e. $\alpha_{s\_C1}\ (x > d_e) = \alpha_{s\_C2}\ (x > d_e)$ and $\alpha_{s\_C3}\ (x > d_e) = \alpha_{s\_C4}\ (x > d_e)$. The spatial ionisation coefficient, α_s is also independent of device width as $\alpha_{s\_C3}\ (x > d_e) = \alpha_{s\_C4}\ (x > d_e) = \alpha_{s\_C5}\ (x > d_e)$ and therefore such value can be associated to α', which is a device-independent parameter. Equation (5.4) can then later be applied to retrieve α^* from α'.

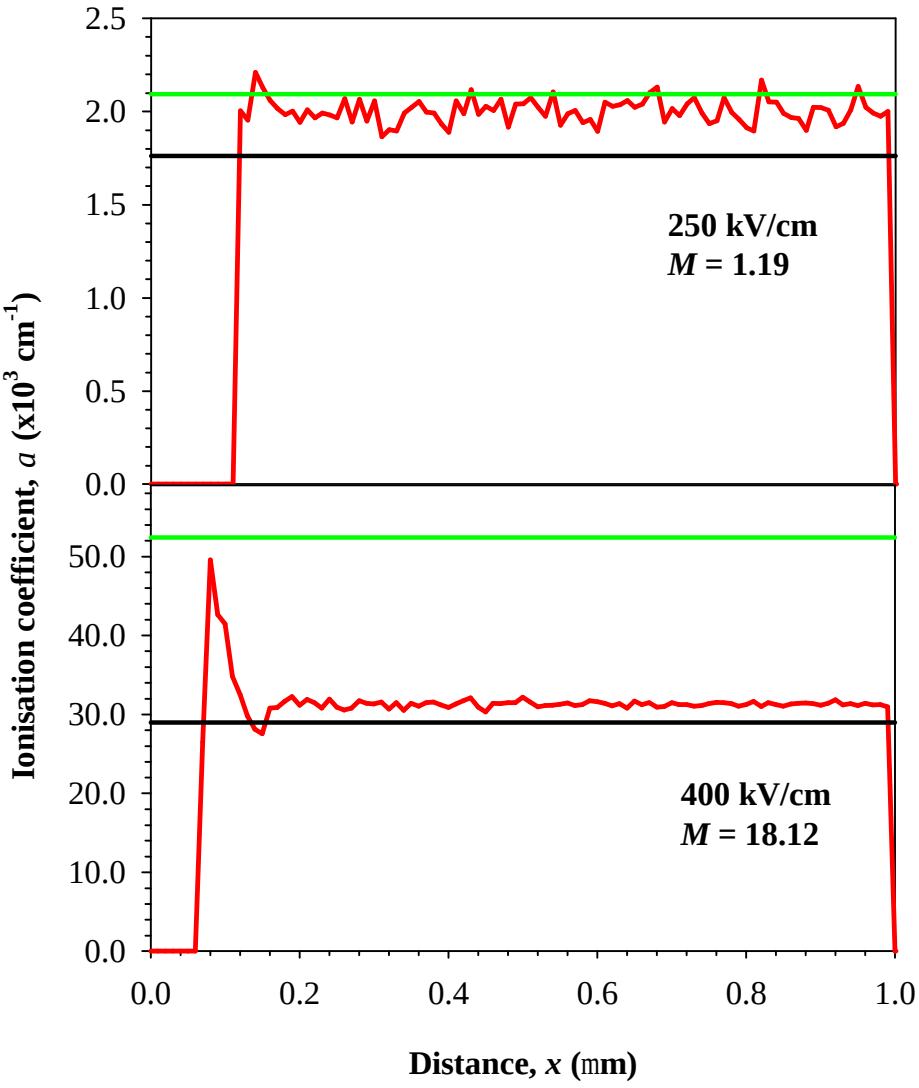

Figure 5.9 α_{local}, α_s, *and* α^* *showed as black, red and green lines respectively at electric fields of 250 and 400 kV/cm shown at the top and bottom of the diagram respectively.*

Further analysis was done to investigate the contribution of the primary and secondary dead space in suppressing α^*(β^*) in a given *w*. GaAs α' in Table 5.1 was taken while setting β' =0 and electron threshold energy of 3.0 eV was assumed. α_s in a 1.0 µm PIN at electric field of 250 and 400 kV/cm were calculated as shown in Figure 5.9 in a similar manner as described above while α^* and α_{local} for these electric fields are shown as well. Again, the device α' can be estimated when α_s ($x > d_e$) where α_s remains fairly constant as a function of distance.

At a relatively low field of 250 kV/cm where near unity gain is obtained as illustrated in Figure 5.9, α' is similar to α^* as opposed to α_{local}. This is because the gain is mostly due to the primary carrier and therefore the contribution of secondary carriers is minimal. However the secondary carrier dead space effect becomes more dominant when the

feedback ionisation results in a higher gain at field of 400 kV/cm. Also, increasing the electric field strength decreases the primary carrier dead space distance in a given device and this explains α_{local} converges to α'. Therefore, the assumption of α' (β') $\approx \alpha_{MC}$ (β_{MC}) due to the absence of α_{MC} (β_{MC}) in [118] can lead to erroneous estimation of breakdown voltage.

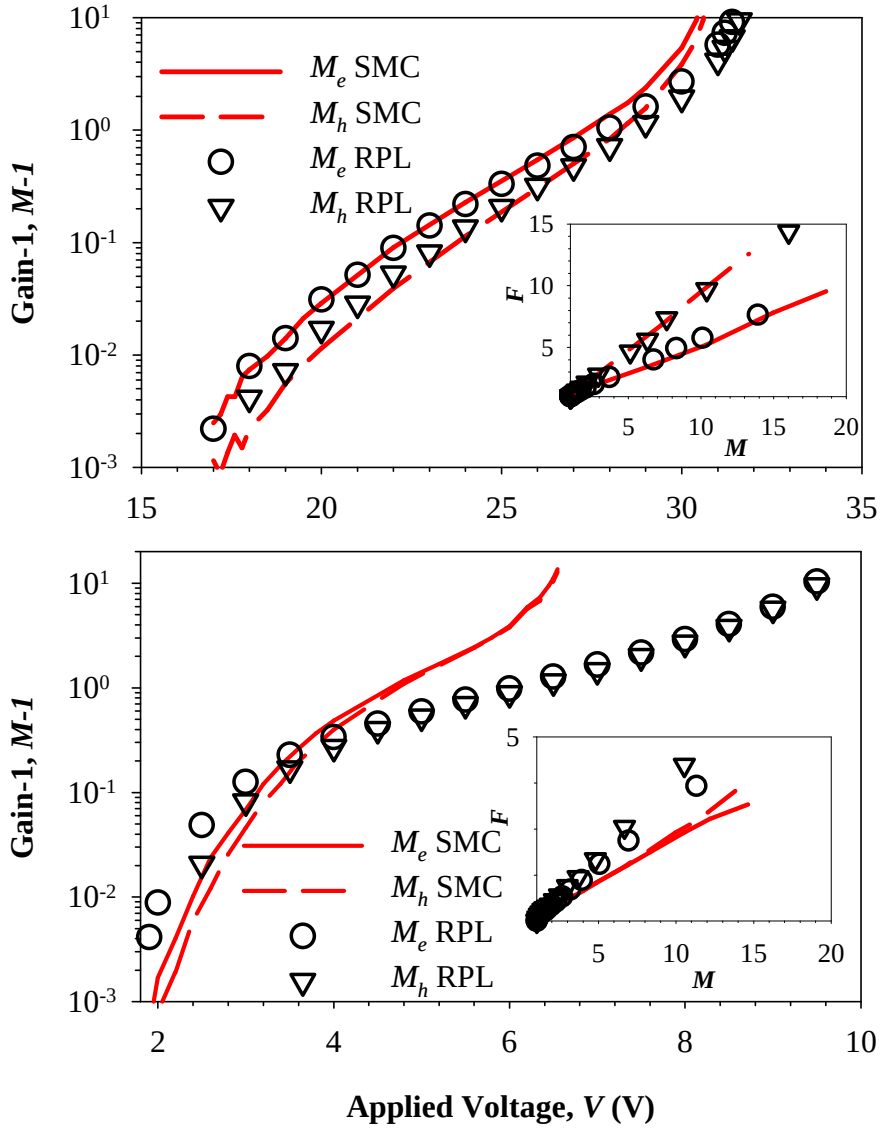

Figure 5.10 *Simulated M_e (M_h) obtained from SMC and RPL model in a 1.0 (top) and 0.1 µm (bottom) PINs showed by solid (dashed) lines and circles (triangles) respectively. α^* (β^*) used in RPL* model was taken from α' assuming α'^{-1} (β'^{-1})$\approx \alpha^{*-1}$ (β^{*-1}) + $d_e(d_h)$. *Insets show the excess noise vs. multiplication obtained from these PINs.*

To show this clearly, GaAs α' (β') in Table 5.1 was corrected for α^* (β^*) using α'^{-1} (β'^{-1}) $\approx \alpha^{*-1}$ (β^{*-1}) + $d_e(d_h)$ and the simulated M and F in 1.0 and 0.1 µm PINs were compared with that of SMC model, as shown in Figure 5.10. Similar to section 5.3, it was assumed the results from the SMC model are "true" experimental data. Although the excess noise

and low *M*-1 values simulated in both models agrees fairly well, there are noticeable discrepancies in breakdown voltages, especially in the 0.1 μm PIN.

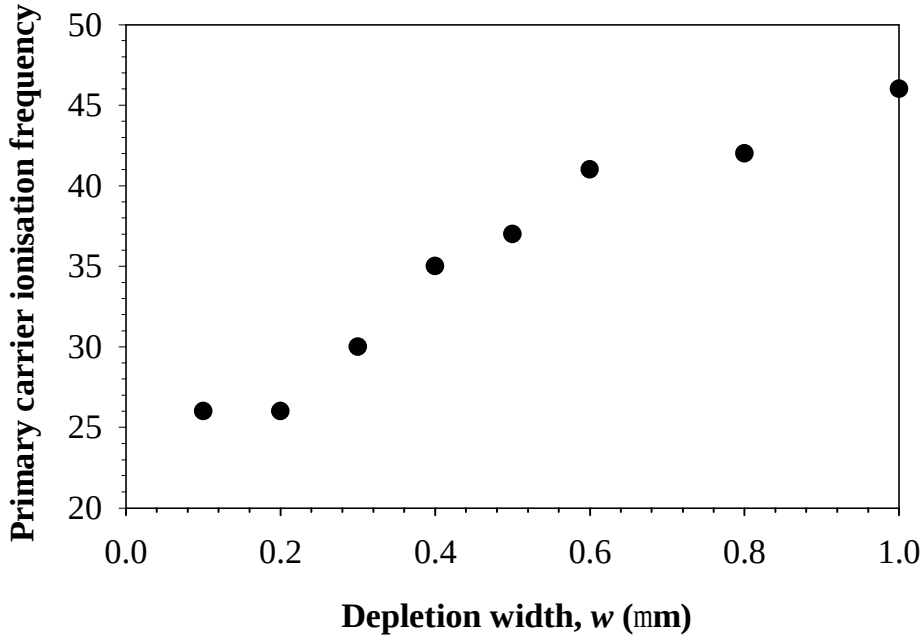

Figure 5.11 *The primary carrier ionisation frequency as a function of depletion width thickness using 50,000 trials at M = 20.*

To understand the increasing discrepancy in breakdown voltage with decreasing *w*, the ionising frequency of the primary carrier at a fix gain of 20 was obtained in PINs with depletion width from 0.1 – 1.0 μm as shown in Figure 5.11. It becomes obvious that the contribution of the primary carrier to the multiplication is decreasing with depletion width and therefore the suppression of the ionisation coefficient is mostly due to the secondary carriers dead spaces. The accuracy of the RPL modelled excess noise however, is not relying on the carriers mean ionisation lengths, but rather their respective threshold energies and hence the results agree with SMC's data.

5.5 Conclusion

Given the ionisation threshold energies, the enabled α^* (β^*) required by the DSMT model can be recovered from experimentally determined α' (β') derived from multiplication measurements only in a range of PINs and NIPs of different width by using the simple relationship, $a' = \frac{1}{\frac{1}{a^*} + 2d_e}$. This can then be used in the DSMT model to predict not only the mean multiplication, but the excess noise, the breakdown probability and breakdown voltage in structures with an arbitrary electric-field profile. With the consideration of slightly different threshold energies for primary and secondary carriers, multiplication and noise data calculated from the DSMT model fits well with the SMC results, even for a 0.05 μm thick PIN with a hard dead-space ionisation PDF.

Chapter 6 DESIGN AND CHARACTERISATION IN ALINP SAM-APD

6.1 Introduction

A narrow spectral full-width- half-maximum (FWHM) in a photodetector can be achieved by utilizing the band discontinuities at the $Ga_{0.52}In_{0.48}P$-$Al_{0.52}In_{0.48}P$ interface [189], as discussed in section 1.3. An alternative way of removing the carriers created by short wavelength light is to ensure that they recombine before they reach the depletion region. This requires materials with short minority carriers' diffusion lengths. Potential materials are aluminium-based alloy semiconductors such as AlGaAs and AlGaInP, which high-quality wafer growth can be challenging due to the strong affinity between aluminum and oxygen. Residual oxygen during growth introduces deep-level traps and reduces the minority carrier lifetime in aluminium containing alloys [190, 191]. This reduces the diffusion length significantly and thereby potentially allows a material to have a narrow spectral FWHM intrinsically without having a hetero-junction interface. Unfortunately, the narrow spectral response also results in a decrease in the peak responsivity, as shown in section 4.3. Avalanche photodiodes (APDs) utilize the impact ionisation process to provide a gain mechanism and can provide an increase in sensitivity, compensating for any reduction in responsivity. Ong ***et al.*** [111] showed that homo-junction AlInP PINs retain a low dark current density of < 6 $nA \cdot cm^{-2}$ even at high reverse bias up to 95% of breakdown voltage and therefore the material may be used in an APD to improve the signal-to-noise ratio of a photodiode. Since the electron device-independent ionisation coefficient (α') is larger than the hole ionisation coefficient (β'), electrons should initiate the multiplication process for optimum noise performance.

The design of AlInP APD is now feasible after both absorption and ionisation coefficients were extracted, as shown in Chapter 4 and 5 respectively. In this chapter, a homo-junction AlInP based APD that provides an inherently narrow FWHM centred at around 480 nm and is capable of high gain is demonstrated.

6.2 Design

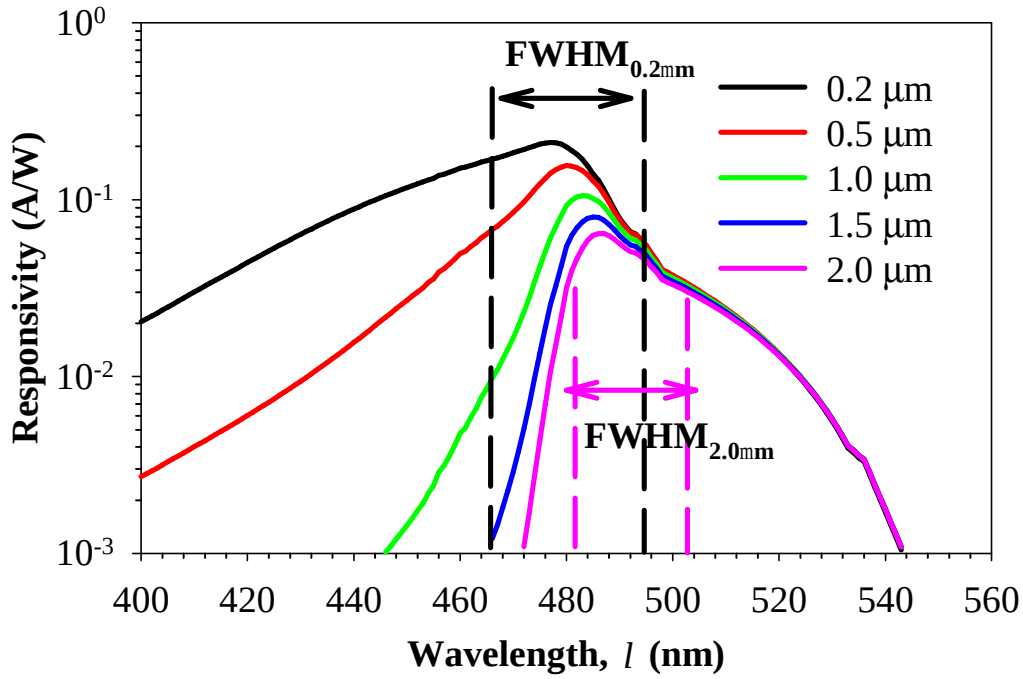

Figure 6.1 *Simulated spectral responses of fully depleted AlInP SAM-APD with p^+ cladding thicknesses of 0.2, 0.5, 1.0, 1.5 and 2.0 µm. The spectral FWHM with p^+ cladding thicknesses of 0.2 and 2.0 µm are shown.*

A simple AlInP PIN diode with a thick absorption region will make a poor APD as besides having a large operating voltage, it may suffer from poor noise performance due to both electrons and holes with distinctive ionisation ratio (k) initiating the multiplication process, as discussed in section 2.6. To overcome these problems, we propose an AlInP homo-junction Separate-Absorption-Multiplication Avalanche Photodiode (SAM-APD) in which the device electric field profile can be tailored as shown in Appendix A, Figure A.1. Photo-generated carriers ideally are created in the absorber region ($w2$) and subsequently multiplied in the avalanche region ($w3$). A SAM-APD typically has a thin multiplication region at high field and a thick absorption region at low field, ensuring a relatively low operating voltage and high quantum efficiency respectively. A 0.2 µm thick avalanche region AlInP PIN diode has been reported with negligible tunnelling current up to breakdown voltage [111] so this was chosen as the multiplication region thickness. A 1.0 µm thick un-doped absorption region provides reasonable quantum efficiency at the desired peak response wavelength of 480 nm and the electric fields in these two regions are bridged by a 0.175 µm thick charge sheet layer with doping density of 3×10^{17} cm^{-3} such that the electric field in the multiplication region does not breakdown before punch-through while ensuring a low

electric field of ~ 100 kV/cm across the absorption region. As the electric field profile in the high field region of the SAM-APD is similar to that of a 0.2 μm PIN [111], the SAM-APD breakdown voltage should be ~ -40 V (summation of the breakdown voltage of the 0.2 μm PIN and the voltage drop in the absorption region).

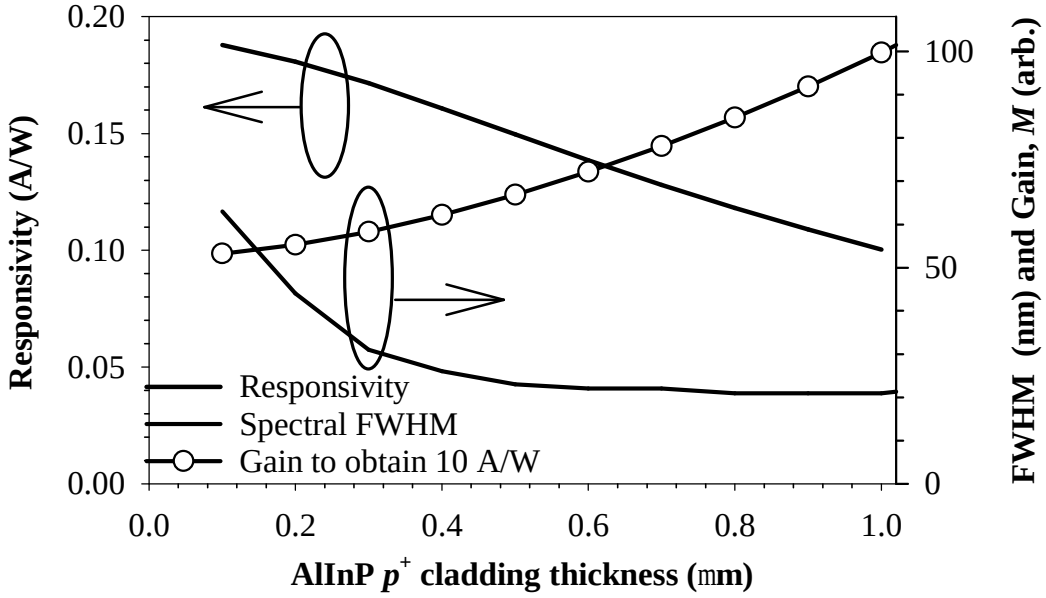

Figure 6.2 *The responsivities at 480 nm and spectral FWHM of AlInP SAM-APD (solid lines) with increasing p^+ cladding thickness. Also shown the multiplication required to achieve responsivity of 10 A/W (symbol with line).*

Using the absorption coefficient obtained from AlInP PINs as illustrated in Figure 4.12, the spectral responses of SAM-APD with varying p^+ cladding thicknesses were simulated using the quantum efficiency model as discussed in section 2.3. The modelling result in Figure 6.1 shows that a narrow spectral FWHM of 21 nm can be achieved from a homo-junction AlInP SAM-APD with an active region thickness of 1.4 μm (the total thickness of absorption region, charge sheet and multiplication region) by increasing the p^+ cladding thickness albeit at the expense of device responsivity. The peak response wavelength also shifts slightly to longer wavelength with increasing cladding thickness since more carriers created at shorter wavelengths recombine and are unable to contribute to the photocurrent. Figure 6.1 shows the responsivity roll-off at shorter wavelengths improves with p^+ cladding thickness and the FWHM saturates at 21 nm for a 1 μm thickness as illustrated in Figure 6.2. However this also results in reduced peak responsivity and consequently a higher multiplication gain is therefore required to achieve a given responsivity, arbitrarily chosen to be 10 A/W in Figure 6.2. To have the narrowest FWHM of 21 nm, 1.0 μm p^+ cladding was determined as the

optimum thickness with peak response wavelength at 480 nm in addition of ensuring > 97 % of electrons generated in the p^+ and absorption region at such wavelength. The designed SAM-APD has the structure as shown in Figure 6.8. A highly doped, thin GaAs cap was deposited on top of the p^+-cladding to ensure a good ohmic contact. The summary of the structure can be found in Table *6.1*.

Table 6.1 *Structure details of AlInP SAM-APD*

Purpose	**Material**	**Type**	**Nominal/Extracted Doping (´ 10^{17} cm^{-3})**	**Nominal/Extracted Thickness (nm)**
Cladding	GaAs	p^+	20/–	50/–
	$Al_{0.52}In_{0.48}P$	p^+	20/3.5	1000/1000
Absorber	$Al_{0.52}In_{0.48}P$	i	–/0.015	1000/460
Charge	$Al_{0.52}In_{0.48}P$	p^-	3.0/0.57	175/770
Avalanche	$Al_{0.52}In_{0.48}P$	i	–/0.70	200/200
Cladding	$Al_{0.52}In_{0.48}P$	n^+	20/20	300/300
Buffer	GaAs	n^+	20/–	500/–
Substrate	GaAs	n^+	---	---

To model the multiplication and noise for the non-uniform electric field profile in the SAM-APD, the electron ionisation probability density, $h_e(x_0,x)$ which describes the ionising probability of an electron at x_0 after travelling a distance x can be expressed as [192]

$$h_e(x \mid x_0) = \begin{cases} 0 & , x - x_0 \le d_e(x_0) \\ a^*(x + x_0)\exp\left[- \int_{d_e(x_0)}^{x} a^*(z + x_0)dz \right] & , x - x_0 > d_e(x_0) \end{cases} \tag{6.1}$$

In equation (6.1), $d_e(x_0)$ is the distance of the dead-space, which is derived from the threshold energy, E_{the} and electric field, x given by

$$E_{the} = \int_{d_e(x_0)}^{x} x(x)dx \tag{6.2}$$

By integrating equation (6.1), the probability of an electron not ionising after travelling a distance x from x_0, r is expressed as

$$\ln(r) = -\int_{d_e(x_0)}^{x} a^{*}(z + x_0)dz \tag{6.3}$$

where $0 < r < 1$ determines the electron (hole) ionising length. The multiplication can be easily computed after all the carriers exit the depletion width. The expressions for holes are easily obtained by replacing α^*, d_e and E_{the} with β^*, d_h and E_{thh} respectively. The depletion width was discretized into a suitable mesh to calculate d_e (d_h) and $\alpha^*(\beta^*)$. The simulation was repeated until the multiplication value converges.

The enabled ionisation coefficients $\alpha^*(\beta^*)$, were obtained from the local parameterized ionisation coefficients, $\alpha'(\beta')$ using a simple correction $\frac{1}{a^*} = \frac{1}{a'} - 2d_e$ and $\frac{1}{b^*} = \frac{1}{b'} - 2d_h$ as discussed in section 5.2, where both $\alpha'(\beta')$ and $d_e(d_h)$ can be found in Table 5.1. The simulations were done assuming a pure electron (hole) initiated multiplication.

The excess noise of the designed SAM-APD shown in Table 6.1 was simulated as shown in Figure 6.3, where k of 0.2 can be achieved. The multiplication region can be narrower to further exploit the dead space effect, where k of less than 0.1 can be achieved in multiplication region of 0.07 µm. However, the narrowing of the avalanche region of < 0.2 µm will result in higher electric fields of > 1.2 MV/cm as shown in Figure 6.3 where tunnelling current could be pronounced. Unfortunately, *I-V* measurements in PINs which correspond to electric fields > 1.2 MV/cm were not reported. To ensure the SAM-APD have the lowest possible dark current, multiplication region of 0.2 µm was chosen.

Excess noise in perfect PINs with avalanche width of 1, 0.5, 0.2, 0.1 and 0.07 µm was simulated as well in Figure 6.3. The excess noise in PINs is higher than that of SAM-APD with the same avalanche thickness, where the discrepancy is most pronounce in w = 0.2 µm. This is primarily due to a more deterministic ionisation in electrons, where they gain energy by first drifting in the absorber region and the charge sheet before ionise in the avalanche region.

The SAM-APD was grown and fabricated using the same growth and fabrication technique as that of the PIN diode. To ensure the incident light is only absorbed by the AlInP p^+ cladding layer, the thin GaAs cap is etched off in the central window region, similar to those PINs as discussed in section 4.4 before forming mesa diodes.

.

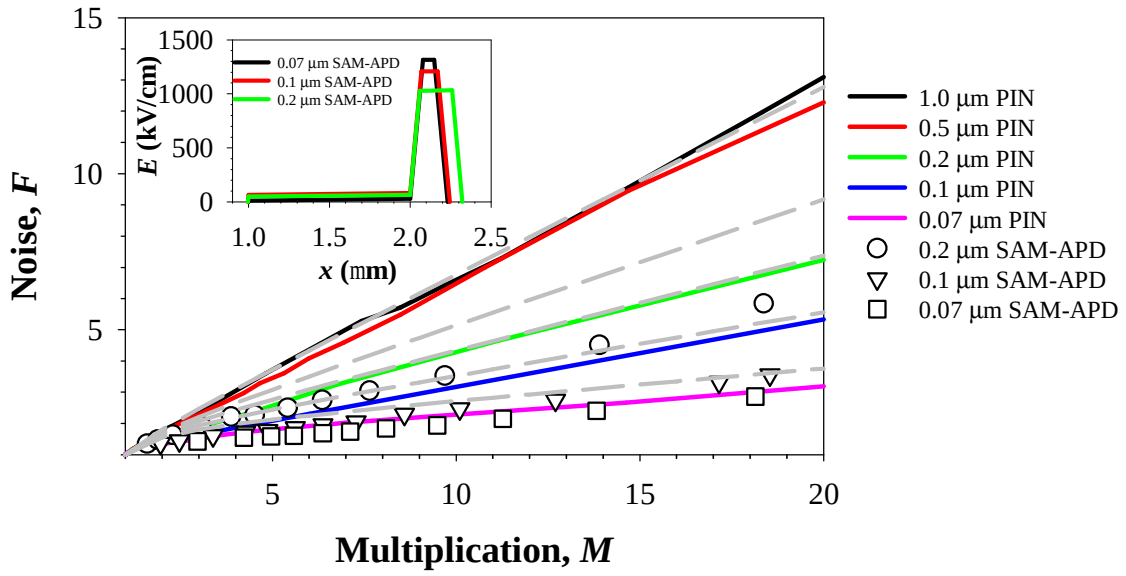

Figure 6.3 *Simulated noise in PINs with w = 1.0, 0.5, 0.2, 0.1 and 0.07 µm as black, red, green, blue and pink solid lines. The simulated results in SAM-APD with the avalanche thicknesses of w = 0.2, 0.1 and 0.07 µm as ○, ▽ and □ and their corresponding electric field profiles are in the inset shown as black, red and green solid lines.*

6.3 Fabrication and Electrical Characterisation

The SAM-APD was fabricated using the same method as discussed in section 4.4, where the devices were passivated with SU-8 photoresist and gold shown in Figure 4.5. This was done to prevent side wall illumination which gives rise to abnormal optical behaviour in these AlInP devices in the presence of avalanche gain. Due to the un-optimised bevel structure, field crowding can occur in these devices with significantly higher gain at the surface of the devices compared to the bulk [53] resulting in non-uniform avalanche multiplication. The spectral responses measured in a nominal 1 µm unpassivated AlInP PIN illustrated in Figure 6.4 shows an enhanced short-wavelength response due to avalanche multiplication.

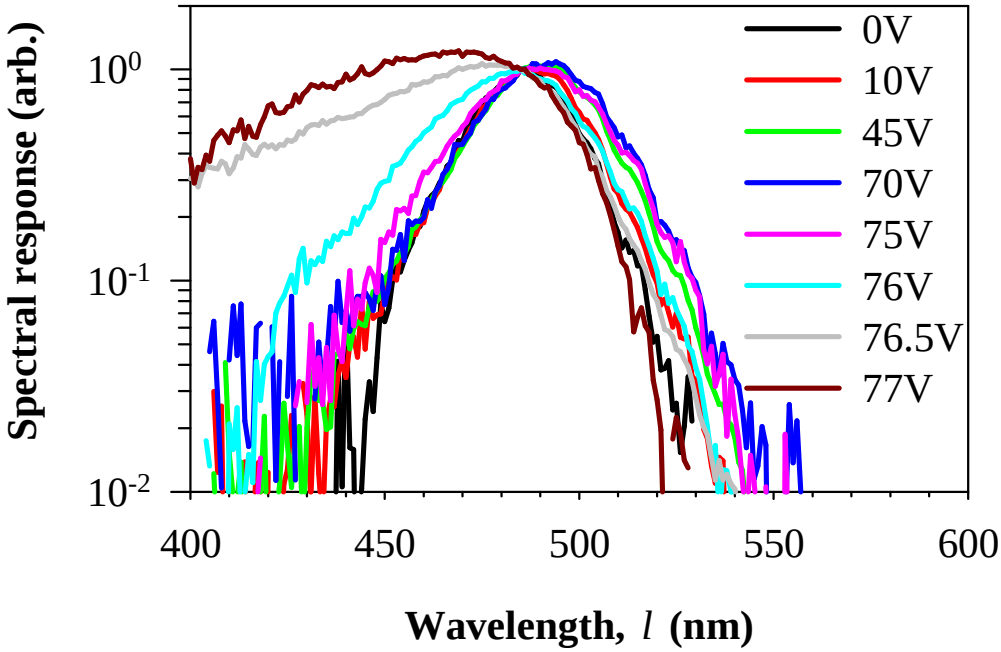

Figure 6.4 *Spectral responses obtained from an un-passivated 1 μm PIN with increasing reverse bias voltage*

To confirm that the abnormality in the spectral response is primarily due to the edges, a 2-D photocurrent scan was performed. This was done by focusing the laser beam to a small spot and scanning it across the top cladding layer to check the gain uniformity of a device at gains of 2 and 10. Via this technique, the edge breakdown mechanism can be easily observed around the device perimeter, indicated by sharp peaks illustrated in Figure 6.5 even at low gains of 2 and becoming more significant at a higher gain of 10 where the gain due to the edge is 100 (10 times higher than that of the bulk).

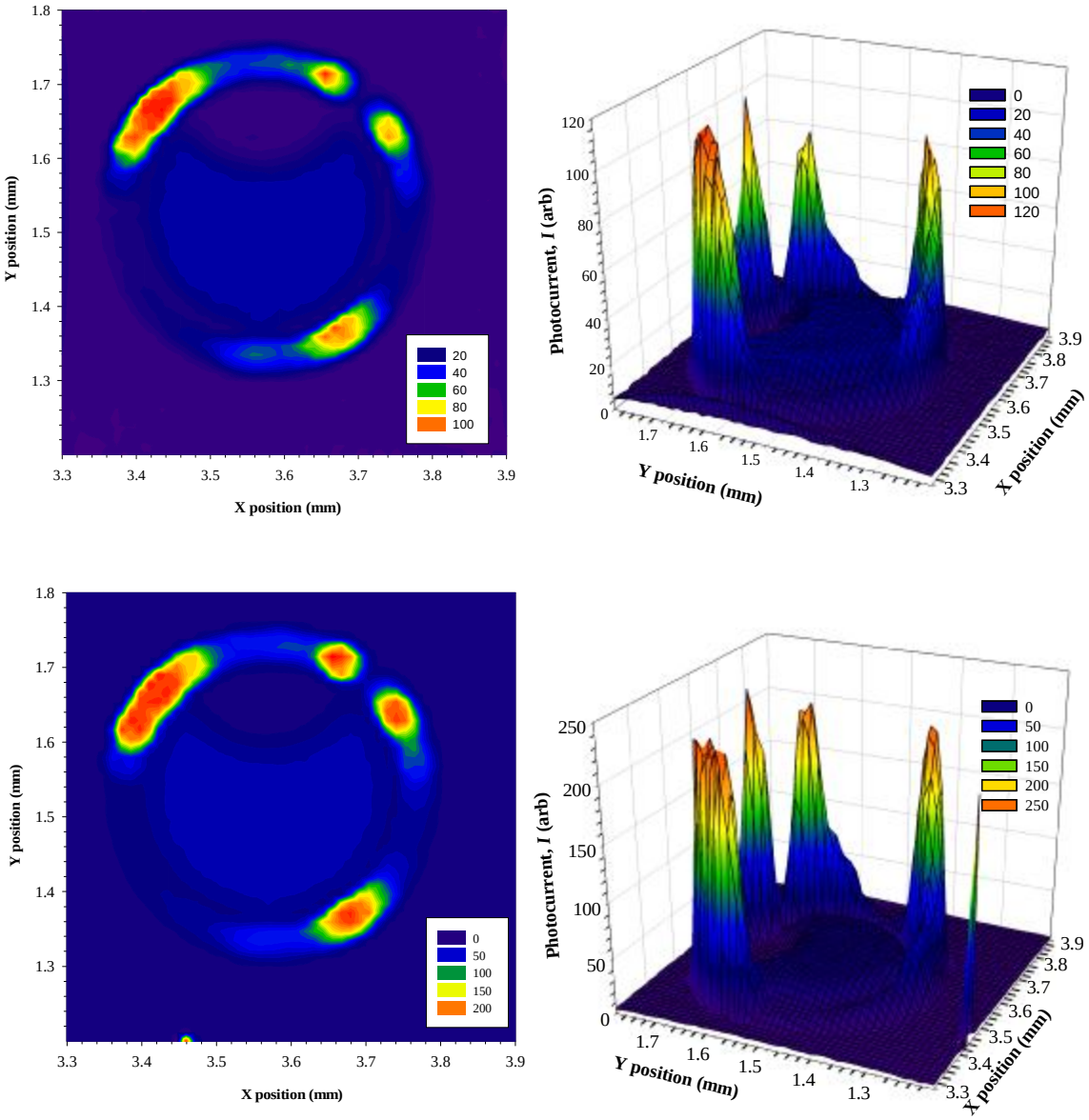

Figure 6.5 *2-D photocurrent scan on 200 µm radii devices in contour (left) and 3-D mesh (right) plots at gain of 2 (top) and 10 (bottom) at reverse bias voltages of -65 V and -70 V respectively.*

These anomalous photocurrents can have major impact on determining the multiplication in AlInP. Similar measurement was performed on the same device after SU-8 and gold passivation and uniform photocurrent profile was obtained at a gain of 10 as illustrated in Figure 6.6.

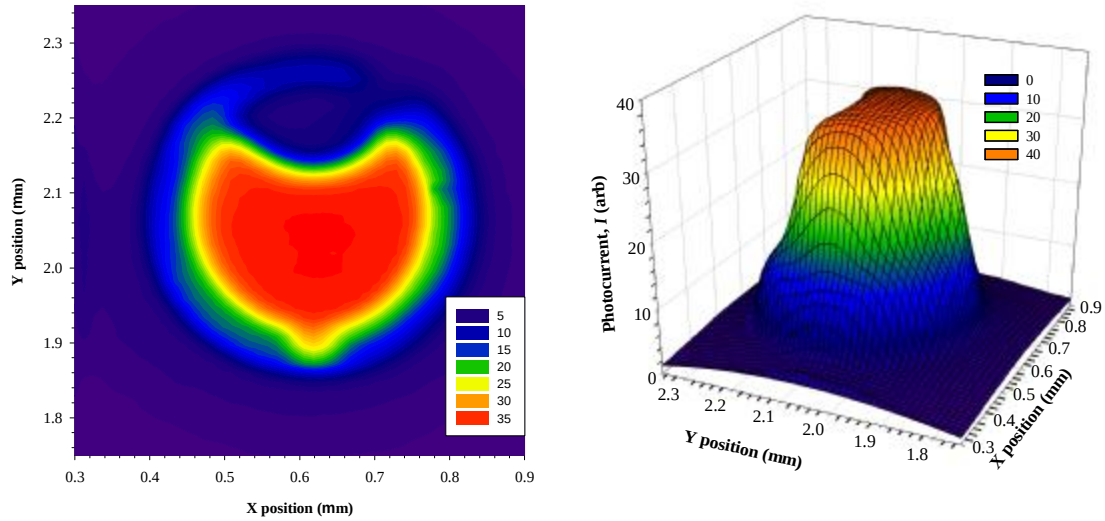

Figure 6.6 *2-D photocurrent scan on 210 µm radii devices in contour (left) and 3-D mesh (right) plots at gain of 10 at reverse bias voltages of -65 V and -70 V respectively.*

Capacitance-voltage (*C-V*) measurements were performed to obtain the doping densities and thicknesses of the absorption region, charge sheet and multiplication region. This information was subsequently corroborated by Secondary Ion Mass Spectroscopy (SIMS) measurements. Using the doping profile obtained from *C-V*, good agreement was obtained between experimental *C-V* and modelling results of the structure using the values tabulated in Table 6.1 as shown in Figure 6.7. The discrepancies of the *p* doping densities in cladding and charge sheet have been discussed in section 4.4.1. Due to the dopant diffusion from the charge sheet, the absorption region width is reduced to 0.47 µm with a ~ 1.0 µm almost uniformly doped charge sheet and multiplication region of ~ 6×10^{16} cm^{-3} which results in a higher punch-through and breakdown voltage. The simulated electric field profiles of the diode at breakdown voltage (-66.5 V) illustrated in Figure 6.8 using the extracted parameters is similar to that of a one-sided *p-n* junction. The departure of the doping profile from the intended design due to dopant diffusion however, should not alter the primary spectral response since the active regions thicknesses are similar.

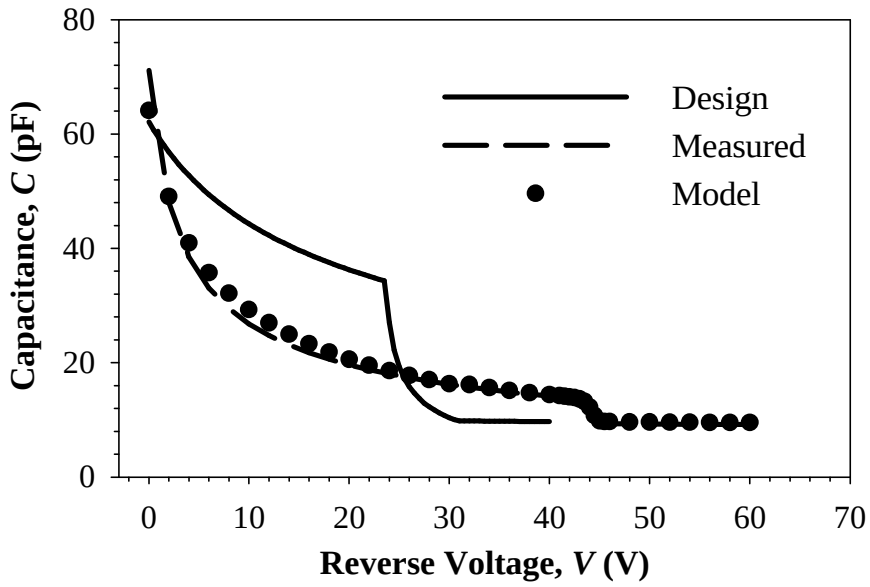

Figure 6.7 *Modelled C-V of designed (solid line) and grown (dashed line) 210 µm devices. Symbols are experimental obtained data, assuming uniform doping densities in all regions.*

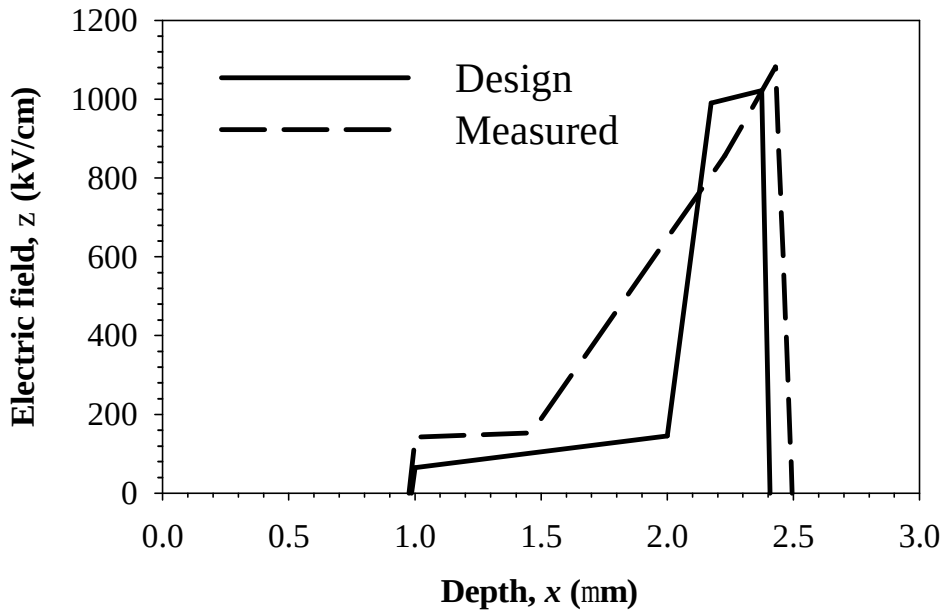

Figure 6.8 *Simulated electric field profiles of design (solid line) and grown (dashed line) structures at breakdown voltage.*

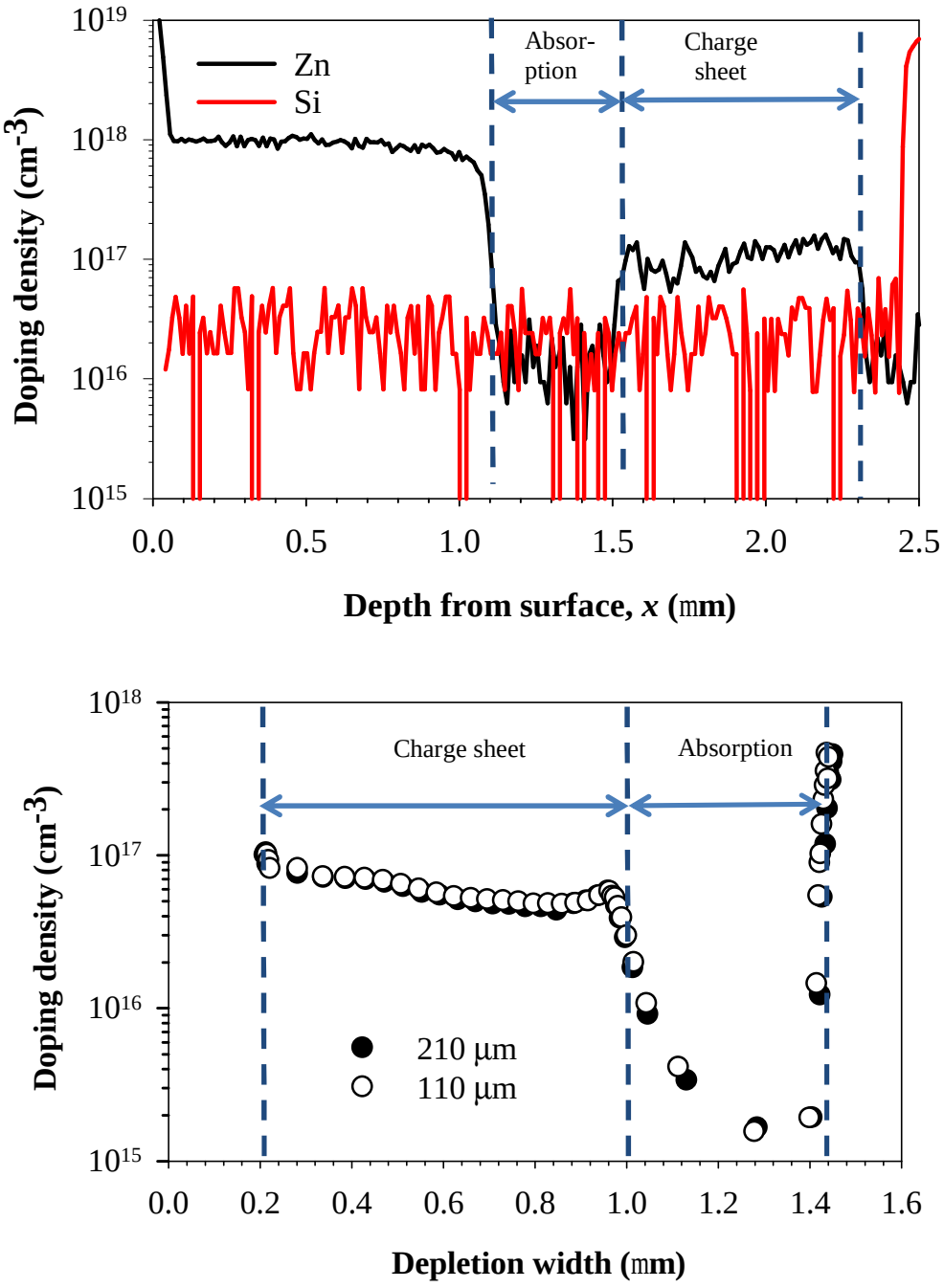

Figure 6.9 *Top*: *Doping profile of AlInP SAM-APD obtained from SIMs. Zinc and silicon dopant concentrations are shown in black and red lines respectively. Bottom: Doping profile of AlInP SAM-APD obtained from C-V measurements in 210 µm and 110 µm radii devices shown in closed and opened symbols respectively.*

I-V measurements were performed on the devices in dark condition. The reverse *I-V* in Figure 6.12 shows an abrupt breakdown voltage of -66.5 V without the presence of tunnelling current despite a peak breakdown electric field exceeding 1000 kV/cm.

The successful growth of the SAM-APD depends crucially on the charge sheet thickness and the corresponding doping density. A thicker or higher doping concentration in the charge sheet might cause the device fail to punch-through before the breakdown voltage. The simulated electric field at the device breakdown voltage obtained from the *C-V* measurement is similar to that of a *p-n* junction as shown in Figure 6.10. Another extreme case is to have a lower doping concentration or narrower charge sheet layer. This results in an electric field profile similar to that of a PIN. *I-V* measurement illustrated in Figure 6.21 shows qualitative agreement in breakdown voltages, where the sample which has a higher doping concentration gives a lower breakdown voltage. The sample also showed a higher dark current due to a higher peak field of 1.2 MV/cm. The following text will now based on the best grown SAM-APD which the electric field profile is shown in Figure 6.8.

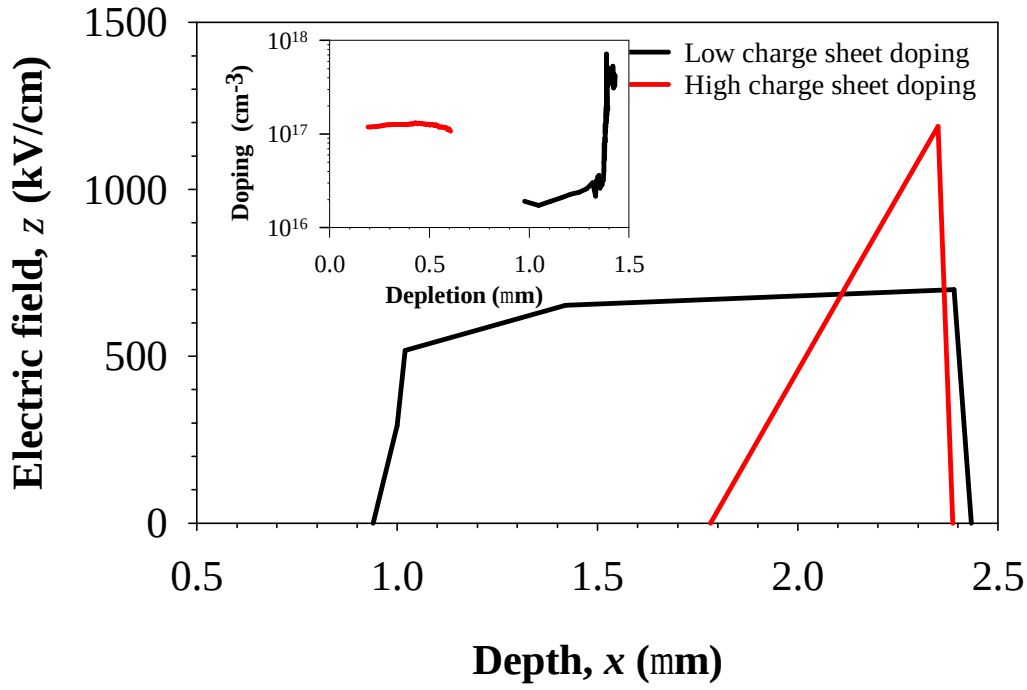

Figure 6.10 *The calculated electric field profiles resultant from a lower and higher charge sheet doping in AlInP SAM-APDs showed as black and red lines respectively. Their corresponding doping profiles are shown in the inset.*

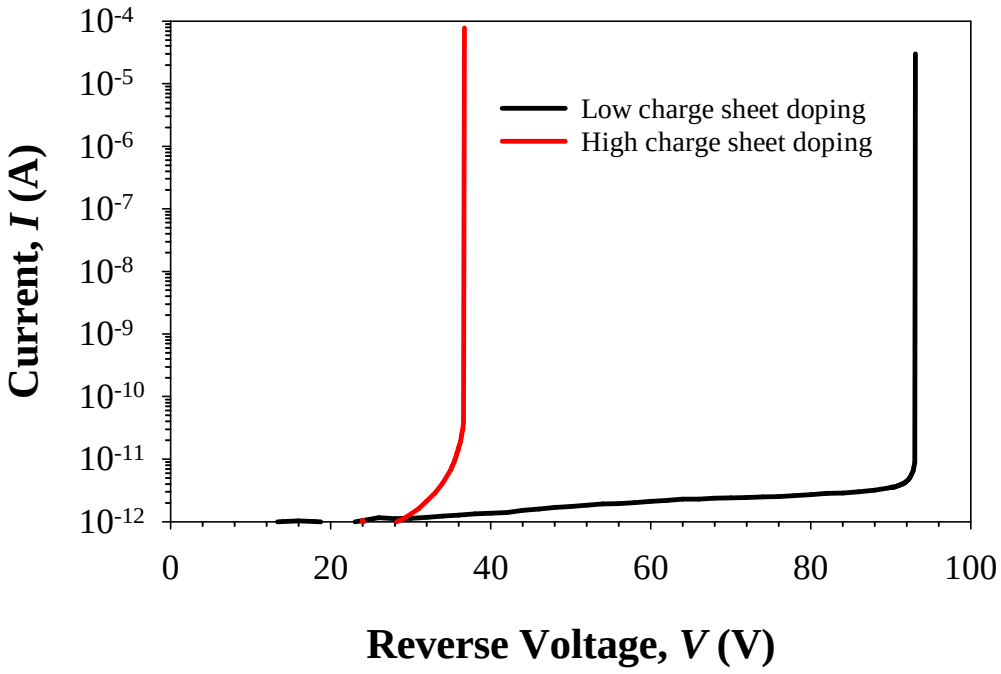

Figure 6.11 The measured dark current *I-V*s in unsuccessful growths of AlInP SAM-APDs which the charge sheet dopings were lower and higher than the desired values shown in black and red lines respectively.

It is important to estimate the primary photocurrent to calculate the quantum efficiency at unity gain and also the gain of the APD. Although local model is criticised of being not able to simulate the low multiplication values ($M < 2$), Plimmer *et al*. [107] showed the model is capable to give accurate high gain ($M > 2$)and breakdown voltages of a rapidly varying electric field. Using the reported ionisation coefficients [111], the gain (M) of the SAM-APD was simulated in Figure 6.13. The predicted breakdown voltage obtained by extrapolating $1/M(V)$ to zero agrees well with the experimental breakdown voltage value.

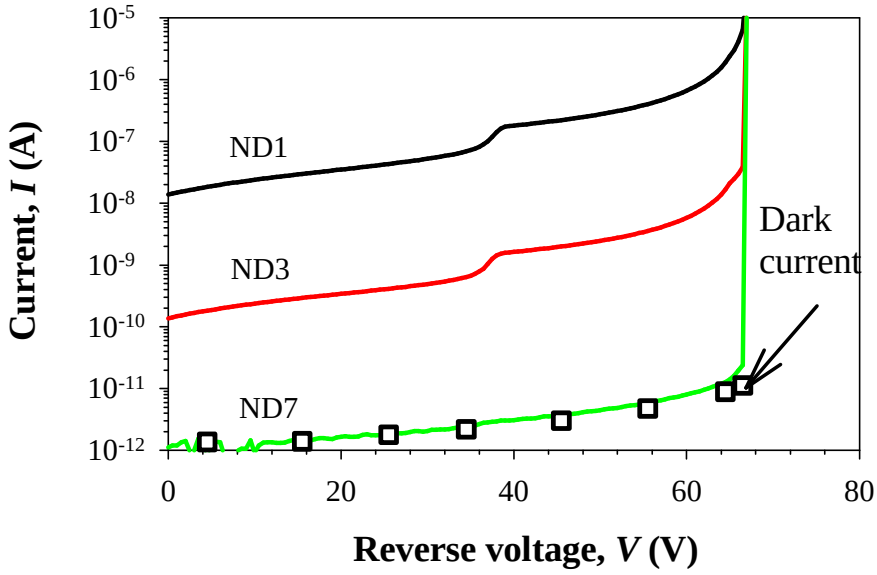

Figure 6.12 *Dark current of an AlInP SAM-APD device and the measured photocurrent illuminated with 480 nm of light.*

Such a low dark current obtained in the SAM-APD allows a direct extraction of photocurrent due to 480 nm illumination attenuated by 10^7 using neutral density filter down to 10 pW shown in Figure 6.12. The calculated responsivity of the same device with 480 nm illumination as a function of reverse bias is shown in Figure 6.13. Using the gain predicted by the local model, the modelled responsivity-voltage (*R*-*V*) curve shows good agreement with the experimental results and a simulated gain of 167 was obtained at -65.9 V. The dark current density of 5 nA cm^{-2} in our devices at a gain of 100 was limited by the measurement system noise floor and compares very favourably with the performance of previously grown AlInP PIN [48] at low bias, an AlInP PIN (95% of breakdown voltage) [111], a commercial gallium phosphide photodiode (< 70 nA cm^{-2} at 95% of breakdown voltage) [193] and a good commercial silicon APD (28 nA cm^{-2} at a gain of 100) [194].

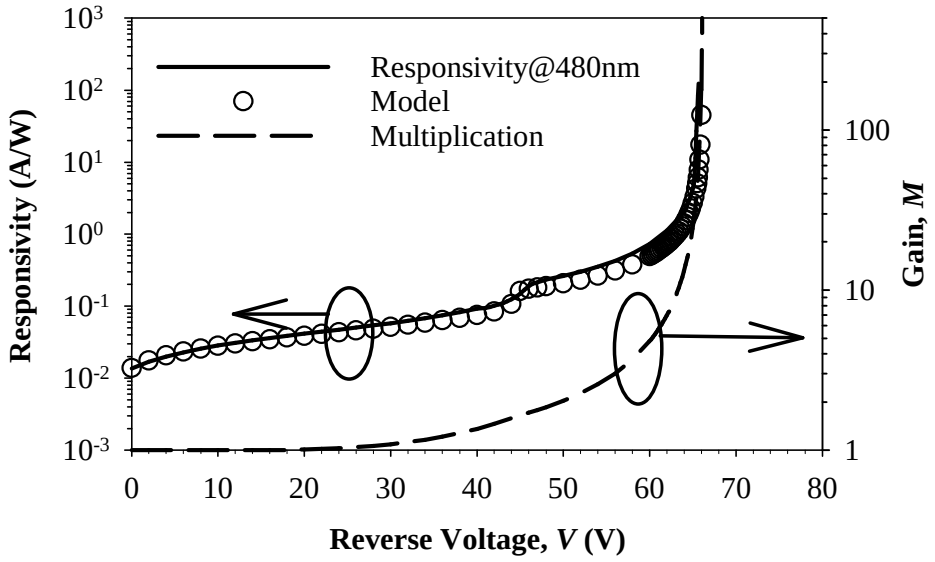

Figure 6.13 *Responsivity versus voltage (solid line) of an AlInP SAM-APD illuminated with 480 nm of light together with simulated responsivity (circle) using the gain obtained from local model (dashed line).*

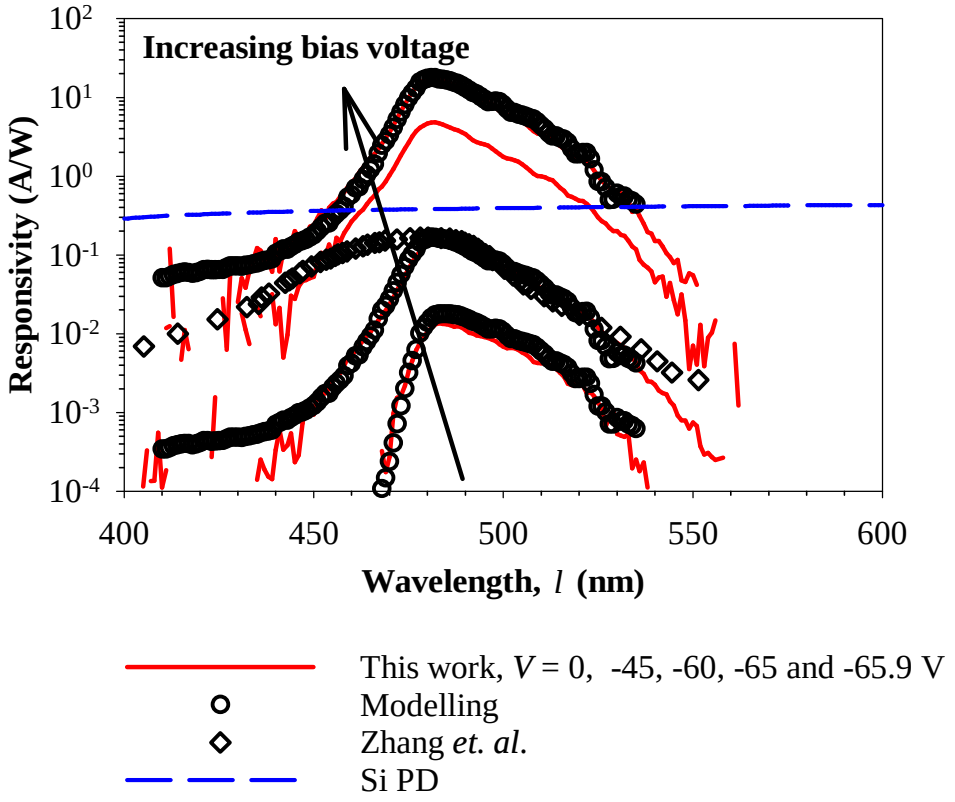

Figure 6.14 *Spectral responses (solid line) of AlInP SAM-APD at reverse bias voltages of 0, -45, -60, -65 and -65.9 V along with the simulated results (circle symbol). S5973-02 Hamamatsu silicon photodiode (dashed line) [19], and the reported AlInP PIN responsivity (diamond symbol) [3] are shown as well.*

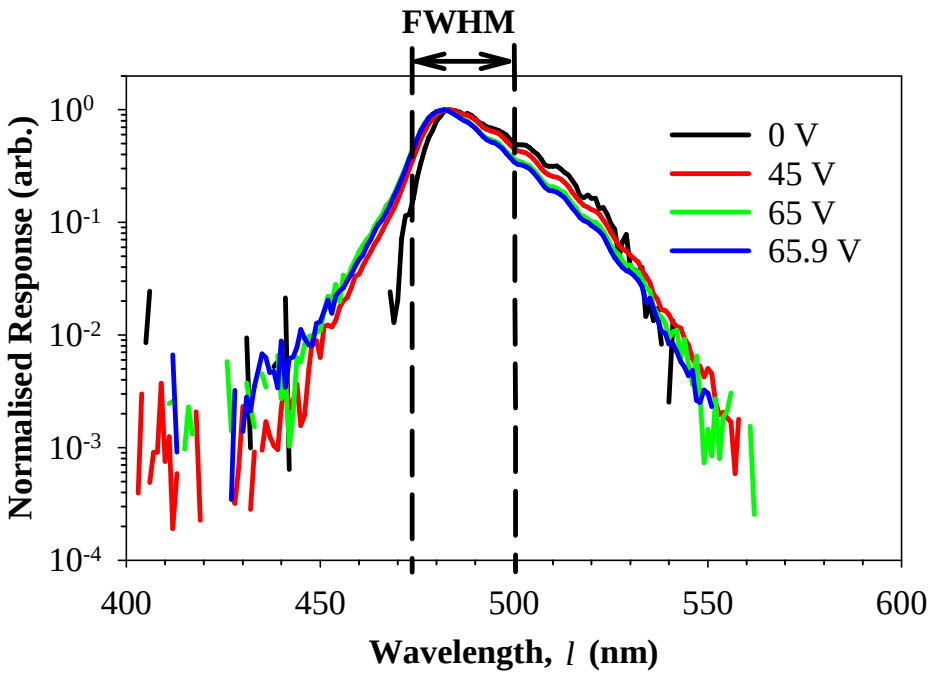

Figure 6.15 *Normalised spectral response obtained from Figure 6.14.*

Figure 6.14 shows that the spectral response of the SAM-APD obtained in the same manner as for the PIN diodes (the details can be found in section 4.4) is independent of applied voltage up to near breakdown, giving a peak response wavelength at 482 nm with a FWHM of ~ 22 nm, which is narrower than that of previous work [48] and a Hamamatsu S5973-02 silicon photodiode. Using the doping densities and thicknesses extracted from the earlier *C-V* measurements, the simulated spectral response has a good agreement with experimental data at 0V. Excellent agreement at higher biases up to -65.9 V can also be obtained by including the effect of avalanche multiplication as shown in Figure 6.14. The measured responsivity and external quantum efficiency at 483 nm is 0.15 A/W and 38 % respectively at the device punch-through voltage of -45 V. This relatively low value of responsivity is partly due to the lack of an anti-reflection coating but primarily due to the poor diffusion length of minority carriers in the p^+ AlInP layer. A peak responsivity of 18.0 A/W is achieved at -65.9 V without affecting the FWHM and it is two orders of magnitude higher than the previous work [48] due to the presence of avalanche gain.

Experiment results obtained in different bias voltages in Figure 6.9 were then normalised to their respective peaks to inspect the Franz-Keldysh effect. As expected, the FWHMs obtained from spectral responses which measured at bias voltages above the punch-through voltage are very similar. Since AlInP is an indirect- bandgap material, the spectral response FWHM is bias-voltage independent as discussed in section 4.5.

Narrowest FWHM is obtained at 0 V due to un-depleted absorber region. The peak response wavelength blue shifted with increasing bias voltage due to the depletion in the p^+ cladding layer.

6.4 Device performance under ambient light

In order to have a higher power at 480 nm, the tungsten light bulb was replaced by a Thorlabs 470 nm blue LED [195], which is the closest source to 480 nm that could be obtained commercially. Using this LED and the monochromator set to 480 nm, the photocurrent was measured in both AlInP and commercial Si APD S2381 [194] as a function of reverse bias voltage as shown in Figure 6.16. The illumination power on both APDs was 1.8 µW. This was reduced using neutral density filters to ensure the photocurrent linearity. In the silicon APD the gain was determined in a similar manner to Woods *et al*. [114] by normalising the photocurrent characteristic to the un-multiplied photocurrent.

To demonstrate the feasibility in these detectors to operate in strong ambient light, a tungsten light bulb was used to provide a broad band DC background illumination of ~1 kW m^{-2}, mimicking the solar irradiation on a sunny day. The AlInP APD was mounted on the TO-5 header. The photocurrent due to the white light source in both APDs is shown in Figure 6.16. Due to the detrimental effect of the colour band-pass filter to the device responsivity shown in Figure 1.7, both APDs were operated without any filters. The photocurrent due to this background illumination was found to be below the LED illumination level, even after the 480 nm light is attenuated using ND2 in the AlInP APD because of the inherent narrow spectral FWHM. Results obtained from the Si APD showed indistinguishable photocurrent levels due to these light sources as the APD was dominated by the ambient light.

The LED was then pulsed with a square wave of 180 Hz, which well below the cut-off frequency of the LED of 80 kHz. The peak incident light power was remained at 1.8 µW. The resulting photocurrent from the detectors was amplified with a gain of 5100 by a trans-impedance amplifier (TIA) which has an operational bandwidth of 25 MHz and subsequently the signal was read by an oscilloscope. Due to the superior responsivity of the Si APD, the modulated signal could be retrieved as shown in Figure 6.17 at near unity gain. Nevertheless, AlInP APD clearly has an advantage over the Si APD at high multiplication of ~20 where the signal was retrieved successfully as demonstrated in Figure 6.17.

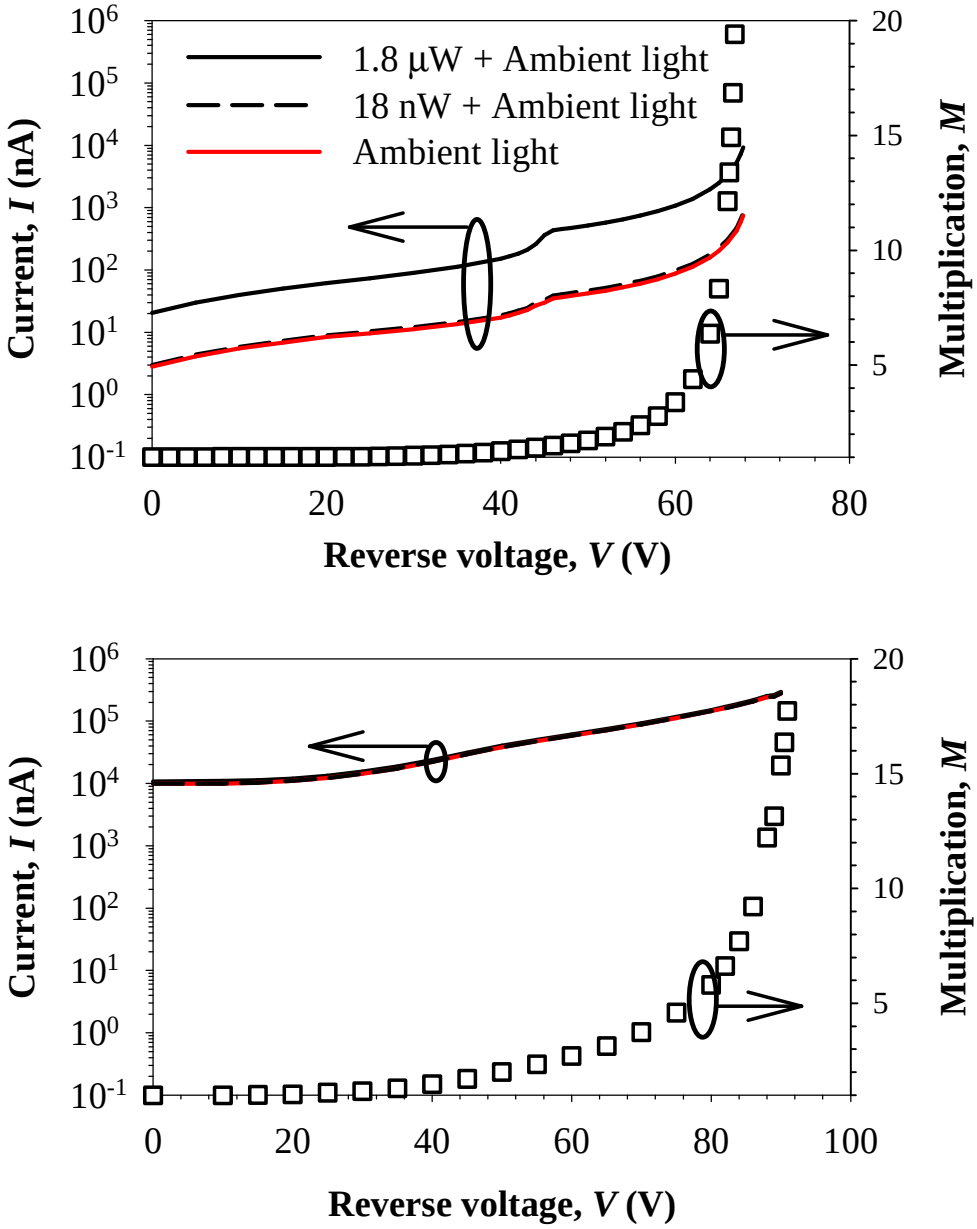

Figure 6.16 *Photocurrent vs reverse bias voltage under presence of white light source (red lines), in addition to 480 nm with illumination power of 1.8 µW and 18 nW (black solid and dashed lines respectively) measured in AlInP APD (top) and S2381 (bottom). Also shown the calculated multiplication in both APDs (symbols).*

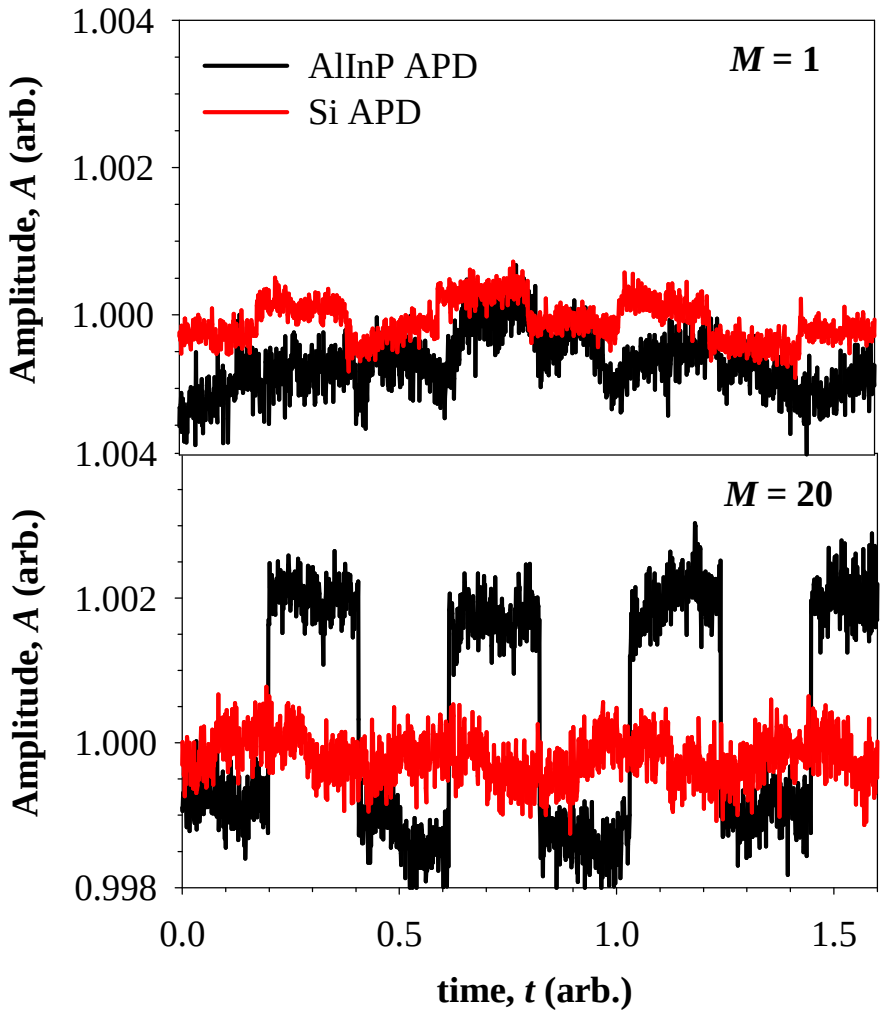

Figure 6.17 *Waveform retrieved by AlInP APD (black) and S2381 (red) at an avalanche gain of ~2 (top) and ~20 (bottom) at reverse bias voltages of -66.8 V and -91 V respectively under illumination of 18 nW 480 nm signal and background irradiance of 1 kW* m^{-2}

6.5 Excess noise modelling

To validate the model as described in section 6.2, the modelled results were compared against experimental excess noise results reported by Qiao *et al.* [196]. The measured results consist of AlInP SAM-APD used in this work, as well as AlInP PINs with nominal (measured) thickness of 1.0 (0.95) and 0.04 (0.06) µm. The doping concentrations in p^+ and n^+ cladding layers are 3×10^{17} cm^{-3} and 4×10^{18} cm^{-3} respectively [196]. The excess noise in the PINs was obtained by 442 nm to ensure the electron initiates the multiplication to give the lowest possible noise, considering $\alpha' > \beta'$ in this material. The absorption profile was calculated and is plotted in Figure 6.18 using the absorption coefficient obtained at 442 nm (~ 10^6 cm^{-1}) mentioned in section 4.4. From the graph below, it is clear that > 99.99 % of the photon is absorbed in the cladding. Therefore, the obtained photocurrent is contributed by the p^+ claddings only. This is confirmed in Figure 6.19 where the measured photocurrent was fully contributed by the p^+ cladding layer.

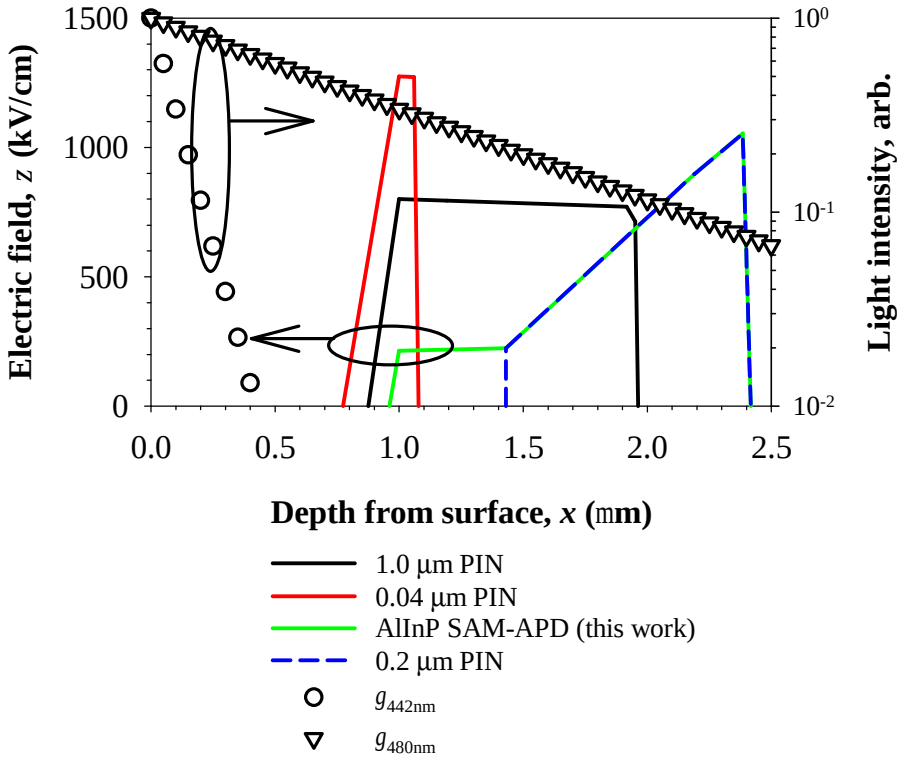

Figure 6.18 *Simulated electric field profiles in nominal 1.0 and 0.04 µm PIN, as well as the SAM-APD shown in black, red and green lines using the results obtained from capacitance-voltage measurement. The electric field profile similar to that of the SAM-APD shown in blue dashed line was used for excess noise simulation. Also shown the absorption profiles of 442 and 480 nm, i.e. the light attenuation vs distance, as circles and triangles respectively.*

The excess noise in the SAM-APD was measured by using a 460 nm LED. In order to determine the dominant wavelength, a spectral response of the AlInP SAM-APD was taken using a monochromator and the 460 nm LED as the light source. As illustrated in Figure 6.20, the dominant wavelength is 480 nm due to the narrow spectral response in the SAM-APD shown in Figure 6.14. Although the absorption coefficient at 480 nm is relatively lower (~ 10^4 cm^{-1}) compared to 442 nm, only a fraction of the photons (< 5 %) are absorbed in the high field region (ζ > 800 kV/cm) as shown in Figure 6.18, it can be assumed that the measured multiplication is initiated by electron. Moreover, most of the multiplication occurs in the peak electric field, where *k* ratio is ~ 1 and therefore, excess noise induced by single or both carriers is indistinguishable.

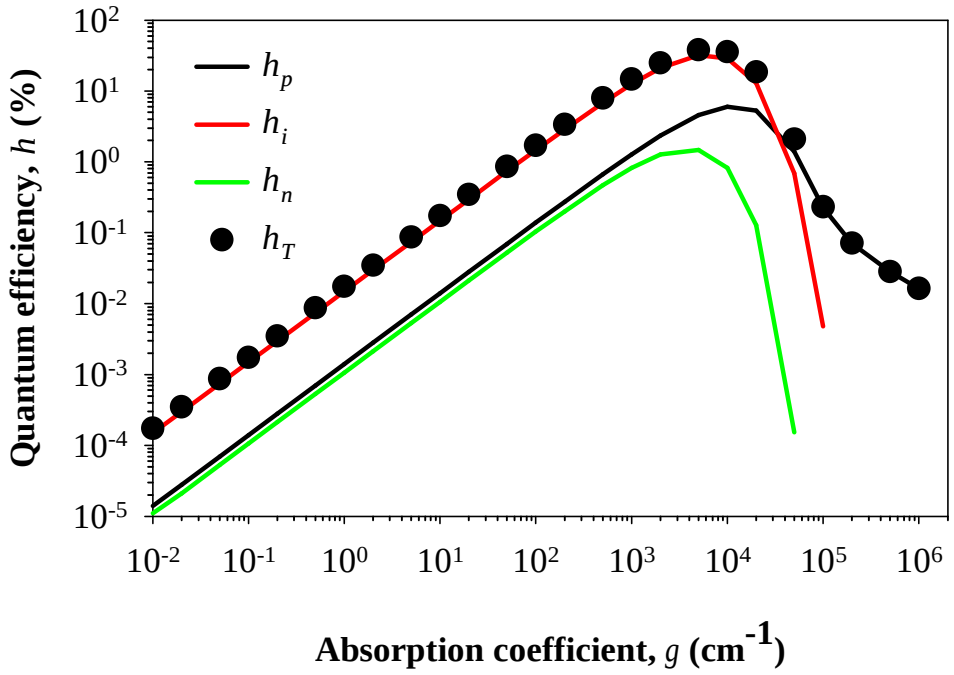

Figure 6.19 *Quantum efficiency contributed by p, i and n layer shown as black, red and green lines. Symbols show the total quantum efficiency in these layers.*

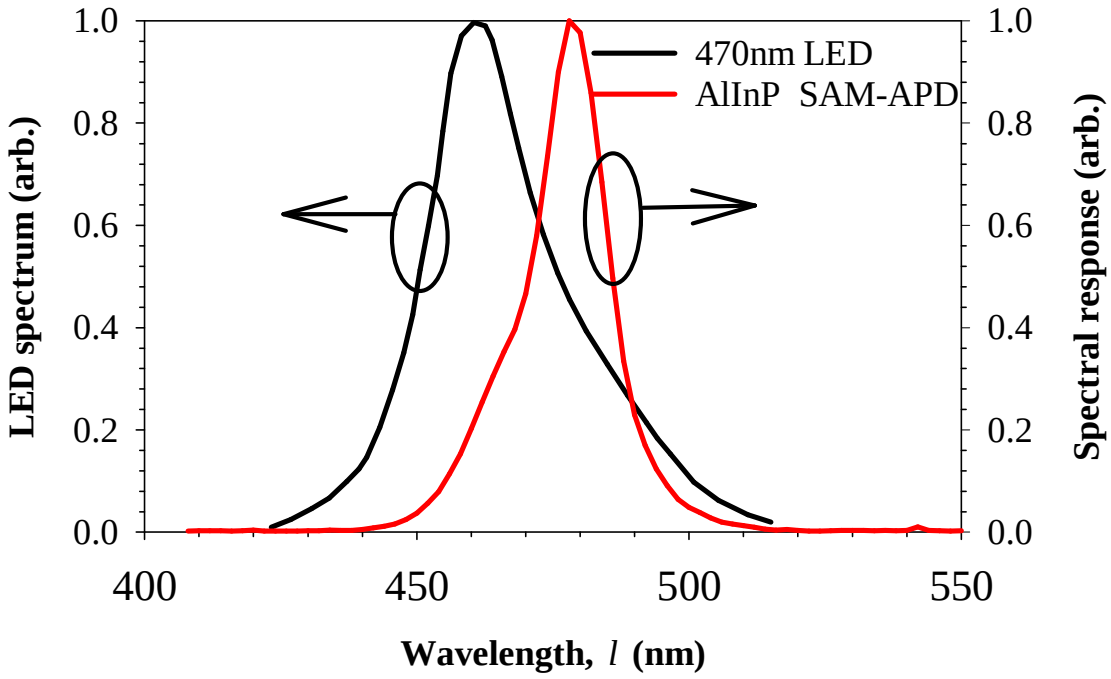

Figure 6.20 *The spectral response of the AlInP SAM-APD, shown as red line was obtained using a monochromator and the 460 nm LED as the light source. The LED light source spectrum is shown as black line.*

Good agreement between experimental and modelled results is shown in Figure 6.21, including the results obtained in the SAM-APD, using the electric field profile illustrated in Figure 6.18. The simulated results also show excess noise obtained from a 0.2 µm PIN, with the electric field profile similar with that of SAM-APD shown in Figure 6.18. The simulated excess noise of this 0.2 µm PIN is similar to that of SAM-APD as shown in Figure 6.21, which indicates that the effective multiplication region in SAM-APD is ~ 0.2 µm.

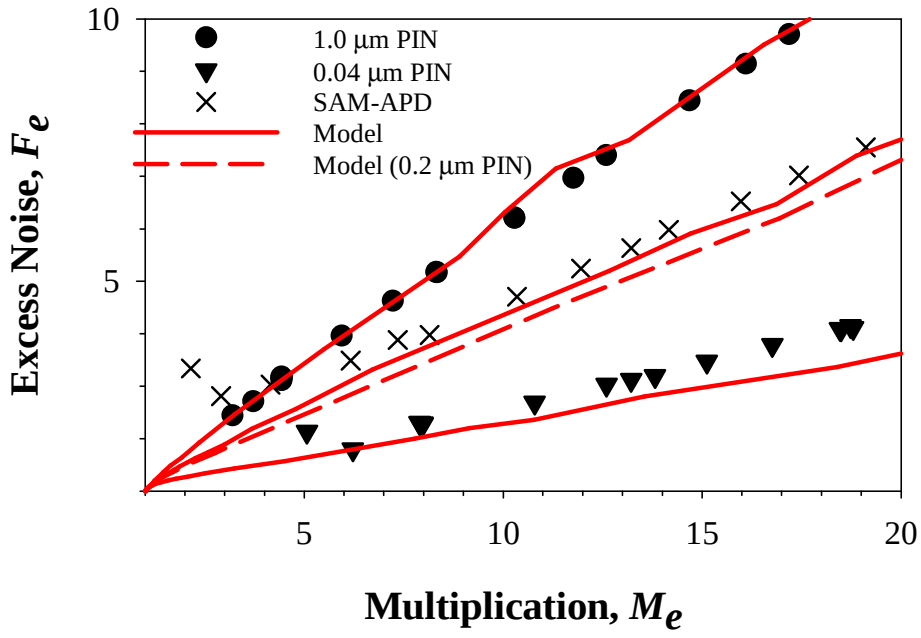

Figure 6.21 *The measured excess noise in 1.0 and 0.04 µm PIN using 442 nm light shown as ● and ▼ whereas the result measured in SAM-APD was obtained using 460 nm illumination (×). The corresponding modelled results are shown as solid lines. The broken line is the modelled result of a 0.2 µm PIN.*

6.6 Conclusion

We have demonstrated the successful growth of a highly sensitive homo-junction AlInP SAM-APD with extremely low dark current, narrow spectral response FWHM and peak response near to the desired wavelength of 480 nm. Although the charge sheet thickness widens due to the dopant diffusion, the responsivity and dark current of the devices are not affected. Using the absorption coefficients and ionisation coefficients derived from the PINs, the spectral response and multiplication of the APD is accurately predicted. This material system therefore may form the basis of detectors for underwater communication systems.

Chapter 7 CONCLUSION AND FUTURE WORK

7.1 Summary of results

The photo-response of AlInP has been studied in detail using a series of PINs and NIPs with the top cladding and intrinsic region thicknesses of 0.2 – 1.0 μm, where the peak response wavelength is ~ 480 nm in these samples. Due to the large band gap in this material, the measured dark currents are very low limited by the instruments to 10^{-12} A, and therefore this allows extremely weak photocurrents to be measured. By measuring the increase in photocurrent as a function of bias voltage, the minority carrier diffusion lengths can be extracted. From the photoresponse, the absorption coefficients in AlInP were successfully deduced over a wide dynamic range from 10^{6} down to 10^{0} cm^{-1} using a simplified model, and this was found to be consistent in all samples. Using the calculated absorption coefficients, the simulated quantum efficiencies replicate the experiment data well, and have good agreement with the results from samples where the top cladding layers were etched down to 0.2 μm. From the absorption coefficients, the energy gaps in Γ and X valleys were extracted and they are consistent with the values from the literature.

A narrow spectral full-width-half-maximum (FWHM) is one of the requirements to achieve a good signal-to-noise ratio in AlInP photodetectors as a receiver in underwater optical communication systems. Spectral responses in AlInP PINs were measured up to the device breakdown voltage to understand the electro-absorption process (Franz-Keldysh effect) in this material. By utilising the local ionisation coefficients, the improvement in responsivity with increasing reverse bias voltages can be determined whether it is due to the depletion into the cladding layer, avalanche multiplication or Franz-Keldysh electro-absorption. The absorption coefficients extracted at near breakdown voltages were showed to be composed of the intrinsic bulk absorption and electro-absorption. Unlike direct band-gap materials such as GaAs, AlInP showed almost bias-independent spectral response due to a relatively stronger absorption contributed by the X valley. Therefore, a narrow FWHM of 22 nm was achieved even if the device was operated under high bias voltages in order to have avalanche multiplication for better photodetector sensitivity. This property makes the AlInP APD less susceptible to the background radiation, while improving the sensitivity of the APD using avalanche gain at high electric fields.

A narrow avalanche width APD is used to exploit the dead space effect to achieve low avalanche noise. However, avalanche excess noise and tunnelling current essentially limit the maximum useful gain of an APD. Due to AlInP's large band-gap, negligibly low tunnelling current was found up to an electric field of 1.2 MV/cm and therefore allows a thinner APD structure. Due to the neglect of the dead spaces, the simulated excess noise using the published local ionisation coefficients (α' and β') in AlInP is inaccurate. The random-path-length (RPL) model is capable of simulating both multiplication and noise accurately, but this requires the enabled ionisation coefficients (α* and β*) and their respective threshold energies, which is not available in the literature. By equating the mean ionising lengths obtained in both primary and secondary carriers with and without dead-spaces, a simple relationship between α'(β') and α*(β*) in terms of dead space was obtained and the expression is nearly independent of the k ratio, allowing good fits of both simulated multiplication and excess noise data to the experiment results in several semiconductor materials. The relationship enables α*(β*) to be obtained from α'(β') unambiguously in all semiconductor materials.

In the absence of published threshold energies for AlInP, the parameters were extracted from single-carrier-initiated multiplication (M_e and M_h). Due to the relatively long mean ionising lengths in the primary carrier at low bias voltages which give low multiplication values (M < 2), there is negligible contribution to the gain by the feedback carriers and therefore the suppression of the low multiplication values was assumed to be associated with the primary carrier threshold energy. A range of threshold energies ranging from the band-gap, E_g (the minimum possible threshold energies) to ~ 3× of that E_g were used for the fitting process where only a unique pair of threshold energies (E_{the} and E_{thh}) gave good agreement in both low multiplication values and breakdown voltages. It was shown that the E_{the} and E_{thh} determined in this way gave good agreement to multiplication and noise data in a series of PINs and NIP in AlInP. This method allows extraction of E_{the} and E_{thh} without the need for separate experimental noise data and thus simplifies the conventional fitting procedures as proposed in the literature.

To have a high quantum efficiency at ~ 480 nm, narrow FWHM, low avalanche excess noise and operating voltage, a homo-junction AlInP APD was designed and grown. By utilising the absorption coefficient obtained in the PINs and NIP, the p^+ cladding thickness in the APD was optimised to obtain a narrow FWHM with central wavelength

of 480 nm without overly compromising the quantum efficiency. The thin avalanche region ensures a low avalanche noise and operating voltage. The absorption thickness is sufficiently thick to give 97% pure electron injection. By knowing accurately the doping densities and thicknesses in the SAM-APD, the modelled spectral responses as a function of wavelength with various bias voltages have good agreement with the measured data. Using both ionisation and absorption coefficients, responsivity at 480 nm as a function of bias voltages was simulated and the results fit the experimental data well. From the simulation data, the highest achievable gain was 180. The experimental excess noise measurement was consistent with the simulation results, which assumes a pure electron initiated multiplication. Due to a low dark current density of 5 nA cm^{-2} at bias voltage of 0.999 V_{bd} direct measurements of photocurrent down to an optical power of 10 pW was possible. With an inherently narrow FWHM of 22 nm and a central wavelength which is independent of incident light angle, the APD was relatively insensitive to ambient light up to an irradiance of 1 kW m^{-2}. This material system therefore may form the basis of detectors for free-space optical communication systems.

7.2 Future work

1. A detector response speed is one of the crucial factors in realising high-speed communication systems. The AlInP SAM-APD cut-off frequency was not able to be measured as this was limited by the bandwidth of the commercial blue LED of ~80 kHz. The results were confirmed by repeating the same measurement on a commercial Si APD S2381 which has a cut-off frequency of 1 GHz. As illustrated in Figure 7.1, both APDs showed identical 3dB response where the square wave response has noticeably rounded rising edge when the LED was pulsed at such frequency. A fast pulsed laser maybe required to measure the bandwidth of AlInP as a function of avalanche gain by measuring the square signal rise time. Prior to the high speed measurement, it may be beneficial to grow AlInP epilayers on semi-insulating GaAs substrates to further reduce the parasitic capacitance. Optimisation of the device sensitivity based on avalanche gain, avalanche noise and bandwidth can therefore be determined as demonstrated in [197].

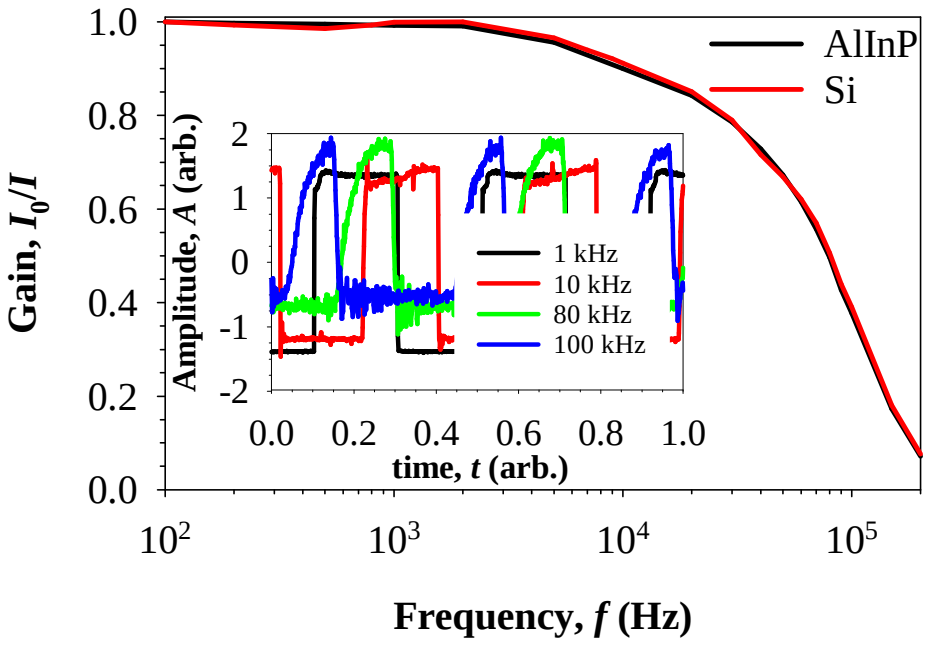

Figure 7.1 *The frequency response obtained in AlInP and Si APD shown by black and red lines respectively. Inset shows AlInP photocurrent response when the LED was pulsed at 1, 10 and 80 kHz.*

2. There is an emerging interest in filter-less narrow band visible light detectors [198, 199] for imaging and Light-Fidelity applications. By reducing the aluminium composition in $(Al_xGa_{1-x})_{0.52}In_{0.48}P$, spectral response of the receiver can be tuneable due to a narrower bandgap. However, as Al% reduces, the quaternary alloy spectral response FWHM is more likely to be broader than AlInP due to a longer carrier diffusion length [200]. Also, the quarternary alloy becomes a more direct band-gap material and therefore the spectral FWHMs broaden when the device is operated in high bias voltages due to the Franz-Keldysh effect. Moreover, unlike AlGaAs where the ionisation k ratio decreases with increasing Al%, avalanche excess noise in AlGaInP alloys will most probably give $k \sim 1$ due to the crossover of hole and electron ionisation coefficients as Al% increases from 0 (GaInP) to 1 (AlInP), which the ionisation coefficients are reported as $\beta' > \alpha'$ and $\alpha' > \beta'$ respectively. To minimise these detrimental effects, hetero-junction SAM-APD can be grown with similar structure as shown in Table *6.1* where both p^+ and absorber region are comprised of AlGaInP while AlInP is used as the charge sheet and avalanche region. It will be useful to grow initially a series of $(Al_xGa_{1-x})_{0.52}In_{0.48}P$ to extract the absorption coefficients to optimise the design of the SAM-APD as discussed in

section 6.2. Another attractive design of SAM-APD is to have InGaN (~18 % of In to have decent absorption at ~ 480 nm [42]) as an absorber region, while utilises 4H-SiC as multiplication layer similar to the structure proposed in [201] since the latter were shown to be solar blind, have low dark current density besides exhibiting low avalanche excess noise, k ~ 0.1 [181].

3. Since AlInP is a wide band-gap semiconductor, the dark current density and breakdown voltage theoretically should be more temperature insensitive compared to narrower band-gap materials such as GaAs and Si. It was reported that AlInP has a very low breakdown voltage temperature coefficient of 15 mV/K even in the thick 1 μm PIN for a temperature range of 77 – 300 K [55]. The work can be expanded by measuring the dark currents and spectral responses in both AlInP PINs and SAM-APD as a function of temperature and bias voltage to extract both ionisation and absorption coefficients up to 500 K. This potentially allows AlInP APD to be operated at extreme temperature environment such as in aerospace or oil well drilling electronic systems without any cooling mechanism.

BIBLIOGRAPHY

[1] Underwater Acoustic Sensor Networks (UW-ASN) [Online]. Available: http://www2.ece.gatech.edu/research/labs/bwn/UWASN/

[2] I. F. Akyildiz, D. Pompili, and T. Melodia, "Underwater acoustic sensor networks: research challenges," *Ad Hoc Networks,* vol. 3, pp. 257-279, 2005.

[3] I. S. Bogie, "Conduction and magnetic signalling in the sea a background review," *Radio and Electronic Engineer,* vol. 42, pp. 447-452, 1972.

[4] P. Lacovara, "High-Bandwidth Underwater Communications," *Marine Technology Society Journal,* vol. 42, pp. 93-102, 2008.

[5] M. Stojanovic, J. Catipovic, and J. G. Proakis, "Adaptive multichannel combining and equalization for underwater acoustic communications," *The Journal of the Acoustical Society of America,* vol. 94, pp. 1621-1631, 1993.

[6] L. Lanbo, Z. Shengli, and C. Jun-Hong, "Prospects and problems of wireless communication for underwater sensor networks," *Wireless Communications and Mobile Computing,* vol. 8, pp. 977-994, 2008.

[7] N. G. Jerlov, *Marine Optics*: Elsevier Science, 1976.

[8] J. Barrett and J. H. Baxendale, "The photolysis of liquid water," *Transactions of the Faraday Society,* vol. 56, pp. 37-43, 1960.

[9] J. A. Curcio and C. C. Petty, "The Near Infrared Absorption Spectrum of Liquid Water," *Journal of the Optical Society of America,* vol. 41, pp. 302-304, 1951.

[10] K. S. Shifrin, *Physical Optics of Ocean Water*: American Inst. of Physics, 1998.

[11] S. Sugihara and R. Tsuda, "Light scattering and size distribution of particles in the surface waters of the North Pacific Ocean," *Journal of the Oceanographical Society of Japan,* vol. 35, pp. 82-90, 1979.

[12] B. Wozniak and J. Dera, *Light Absorption in Sea Water*: Springer New York, 2007.

[13] R. Hollins, A. Rudge, and S. Bennett, "Technologies for blue-green underwater optical communications," in *Proceedings of SPIE*, Toulouse, 2013, pp. 88990F-88990F-7.

[14] O. H. Nestor and C. Y. Huang, "Bismuth Germanate: A High-Z Gamma-Ray and Charged Particle Detector," *Nuclear Science, IEEE Transactions on,* vol. 22, pp. 68-71, 1975.

[15] D. M. Drake, L. R. Nilsson, and J. Faucett, "Bismuth germanate scintillators as detectors for high-energy gamma radiation," *Nuclear Instruments and Methods in Physics Research,* vol. 188, pp. 313-317, 1981.

[16] W. E. Schultz, H. D. Smith, and P. F. McKinlay, "Combination of epithermal and inelastic neutron scattering methods to locate coal and oil shale zones," ed: Google Patents, 1976.

[17] A. M. Srivastava, H. A. Comanzo, and C. D. Greskovich, "Ultraviolet emitting scintillators for oil detection," ed: Google Patents, 2006.

[18] G. E. Stillman and C. M. Wolfe, *Avalanche photodiodes, Semiconductors and Semimetals* vol. 12: New York: Academic, 1977.

[19] Y. Yu, Y. Jiang, K. Zheng, Z. Zhu, X. Lan, Y. Zhang, *et al.*, "Ultralow-voltage and high gain photoconductor based on ZnS:Ga nanoribbons for the detection of low-intensity ultraviolet light," *Journal of Materials Chemistry C,* vol. 2, pp. 3583-3588, 2014.

[20] "CdS Light Dependent Photoresistors for Sensor Applications," Token Electronics Industry Co. Ltd.2010.

[21] X. Li, J. E. Carey, J. W. Sickler, M. U. Pralle, C. Palsule, and C. J. Vineis, "Silicon photodiodes with high photoconductive gain at room temperature," *Optics Express,* vol. 20, pp. 5518-5523, 2012.
[22] "Photomultiplier Tubes : Basics and Application Third Edition," Hamamatsu Photonics K. K.
[23] W. Yang, T. Nohava, S. Krishnankutty, R. Torreano, S. McPherson, and H. Marsh, "High gain GaN/AlGaN heterojunction phototransistor," *Applied Physics Letters,* vol. 73, pp. 978-980, 1998.
[24] Z. H. Zaidi and P. A. Houston, "Highly Sensitive UV Detection Mechanism in AlGaN/GaN HEMTs," *Electron Devices, IEEE Transactions on,* vol. 60, pp. 2776-2781, 2013.
[25] E. F. Zalewski and C. R. Duda, "Silicon photodiode device with 100% external quantum efficiency," *Applied Optics,* vol. 22, pp. 2867-2873, 1983/09/15 1983.
[26] J. Bowers and C. Burrus, "Ultrawide-band long-wavelength p-i-n photodetectors," *Journal of Lightwave Technology,* vol. 5, pp. 1339-1350, 1987.
[27] M. S. Unlu, B. M. Onat, and Y. Leblebici, "Transient simulation of heterojunction photodiodes-part II: analysis of resonant cavity enhanced photodetectors," *Journal of Lightwave Technology,* vol. 13, pp. 406-415, 1995.
[28] R. B. Emmons, "Avalanche - Photodiode Frequency Response," *Journal of Applied Physics,* vol. 38, pp. 3705-3714, 1967.
[29] F. Capasso, T. Won-Tien, and G. F. Williams, "Staircase solid-state photomultipliers and avalanche photodiodes with enhanced ionization rates ratio," *Electron Devices, IEEE Transactions on,* vol. 30, pp. 381-390, 1983.
[30] A. R. J. Marshall, P. J. Ker, A. Krysa, J. P. R. David, and C. H. Tan, "High speed InAs electron avalanche photodiodes overcome the conventional gain-bandwidth product limit," *Optics Express,* vol. 19, pp. 23341-23349, 2011.
[31] G. M. Williams, M. Compton, D. A. Ramirez, M. M. Hayat, and A. S. Huntington, "Multi-Gain-Stage InGaAs Avalanche Photodiode With Enhanced Gain and Reduced Excess Noise," *Electron Devices Society, IEEE Journal of the,* vol. 1, pp. 54-65, 2013.
[32] G. M. Williams, M. A. Compton, and A. S. Huntington, "High-speed photon counting with linear-mode APD receivers," in *Proceedings of SPIE*, Orlando, 2009, pp. 732012-732012-9.
[33] J. Xie, S. Xie, R. C. Tozer, and C. H. Tan, "Excess Noise Characteristics of Thin AlAsSb APDs," *IEEE Transactions on Electron Devices,* vol. 59, pp. 1475-1479, 2012.
[34] L. Tein-Pei, C. A. Burrus, Jr., and A. G. Dentai, "InGaAs/InP p-i-n photodiodes for lightwave communications at the 0.95-1.65 μm wavelength," *Quantum Electronics, IEEE Journal of,* vol. 17, pp. 232-238, 1981.
[35] G. Masini, L. Calace, G. Assanto, H.-C. Luan, and L. C. Kimerling, "High-performance p-i-n Ge on Si photodetectors for the near infrared: from model to demonstration," *Electron Devices, IEEE Transactions on,* vol. 48, pp. 1092-1096, 2001.
[36] S. Adachi, "Optical properties of $In_{1-x}Ga_xAs_yP_{1-y}$ alloys," *Physical Review B,* vol. 39, pp. 12612-12621, 1989.
[37] D. E. Aspnes and A. A. Studna, "Dielectric functions and optical parameters of Si, Ge, GaP, GaAs, GaSb, InP, InAs, and InSb from 1.5 to 6.0 eV," *Physical Review B,* vol. 27, pp. 985-1009, 01/15/ 1983.
[38] T. Takizawa, "Wavelength Modulated Reflectivities of the Direct Exciton Edge in GaP," *Journal of the Physical Society of Japan,* vol. 52, pp. 1057-1063, 1983.
[39] D. McIntosh, Q. Zhou, Y. Chen, and J. C. Campbell, "High quantum efficiency GaP avalanche photodiodes," *Optics Express,* vol. 19, pp. 19607-19612, 2011.

[40] J. Bai, B. Xu, F. G. Guzman, K. Xing, Y. Gong, Y. Hou, *et al.*, "(11-22) semipolar InGaN emitters from green to amber on overgrown GaN on micro-rod templates," *Applied Physics Letters,* vol. 107, p. 261103, 2015.
[41] A. Masahiro, Y. Yusuke, E. Yohei, K. Takashi, S. Takamichi, T. Shinji, *et al.*, "Low Threshold Current Density InGaN Based 520–530 nm Green Laser Diodes on Semi-Polar {2021} Free-Standing GaN Substrates," *Applied Physics Express,* vol. 3, p. 121001, 2010.
[42] R. Singh, D. Doppalapudi, T. D. Moustakas, and L. T. Romano, "Phase separation in InGaN thick films and formation of InGaN/GaN double heterostructures in the entire alloy composition," *Applied Physics Letters,* vol. 70, pp. 1089-1091, 1997.
[43] H. R. Philipp and E. A. Taft, "Optical Constants of Silicon in the Region 1 to 10 ev," *Physical Review,* vol. 120, pp. 37-38, 1960.
[44] "Low bias operation, for 800 nm band," Hamamatsu Photonics K. K.2014.
[45] R. E. Bird, R. L. Hulstrom, and L. J. Lewis, "Terrestrial solar spectral data sets," *Solar Energy,* vol. 30, pp. 563-573, 1983.
[46] I. Vasilescu, K. Kotay, D. Rus, M. Dunbabin, and P. Corke, "Data collection, storage, and retrieval with an underwater sensor network," in *Proceedings of the 3rd international conference on Embedded networked sensor systems*, 2005, pp. 154-165.
[47] B. K. Ng, "Impact Ionization in Wide Band-Gap Semiconductors: AlxGa1-xAs and 4H-SiC," PhD, Electronic and Electrical Department, University of Sheffield, 2002.
[48] Z. Yonggang, L. Cheng, G. Yi, W. Kai, L. Haosibaiyin, S. XiuMei, *et al.*, "GaInP-AlInP-GaAs Blue Photovoltaic Detectors With Narrow Response Wavelength Width," *Photonics Technology Letters, IEEE,* vol. 22, pp. 944-946, 2010.
[49] J. S. Cheong, J. S. Ng, A. B. Krysa, J. S. L. Ong, and J. P. R. David, "Determination of absorption coefficients in AlInP lattice matched to GaAs," *Journal of Physics D: Applied Physics,* vol. 48, p. 405101, 2015.
[50] J. S. Cheong, A. Auckloo, J. S. Ng, A. B. Krysa, and J. P. R. David, "A high sensitivity detector for underwater communication systems," 2015, pp. 96470O-96470O-6.
[51] R. D. Dupuis, J.-H. Ryou, S.-C. Shen, P. D. Yoder, Y. Zhang, H. J. Kim, *et al.*, "Growth and fabrication of high-performance GaN-based ultraviolet avalanche photodiodes," *Journal of Crystal Growth,* vol. 310, pp. 5217-5222, 2008.
[52] J. B. Limb, D. Yoo, J. H. Ryou, W. Lee, S. C. Shen, R. D. Dupuis, *et al.*, "GaN ultraviolet avalanche photodiodes with optical gain greater than 1000 grown on GaN substrates by metal-organic chemical vapor deposition," *Applied Physics Letters,* vol. 89, p. 011112, 2006.
[53] A. L. Beck, Y. Bo, X. Guo, and J. C. Campbell, "Edge breakdown in 4H-SiC avalanche photodiodes," *Quantum Electronics, IEEE Journal of,* vol. 40, pp. 321-324, 2004.
[54] X. Guo, A. L. Beck, X. Li, J. C. Campbell, D. Emerson, and J. Sumakeris, "Study of reverse dark current in 4H-SiC avalanche photodiodes," *Quantum Electronics, IEEE Journal of,* vol. 41, pp. 562-567, 2005.
[55] J. S. L. Ong, J. S. Ng, A. B. Krysa, and J. P. R. David, "Temperature dependence of avalanche multiplication and breakdown voltage in $Al_{0.52}In_{0.48}P$," *Journal of Applied Physics,* vol. 115, p. 064507, 2014.
[56] W. Shockley, "The Theory of p-n Junctions in Semiconductors and p-n Junction Transistors," *Bell System Technical Journal,* vol. 28, pp. 435-489, 1949.

[57] J. M. Shah, Y.-L. Li, T. Gessmann, and E. F. Schubert, "Experimental analysis and theoretical model for anomalously high ideality factors (n≫2.0) in AlGaN/GaN p-n junction diodes," *Journal of Applied Physics,* vol. 94, pp. 2627-2630, 2003.
[58] W. Shockley and W. T. Read, "Statistics of the Recombinations of Holes and Electrons," *Physical Review,* vol. 87, pp. 835-842, 1952.
[59] C. T. Sah, R. N. Noyce, and W. Shockley, "Carrier Generation and Recombination in P-N Junctions and P-N Junction Characteristics," *Proceedings of the IRE,* vol. 45, pp. 1228-1243, 1957.
[60] R. A. Smith, *Semiconductors*: University Press, 1961.
[61] L. Hall, J. Bardeen, and F. Blatt, "Infrared absorption spectrum of germanium," *Physical Review,* vol. 95, p. 559, 1954.
[62] H. C. Casey, D. D. Sell, and K. W. Wecht, "Concentration dependence of the absorption coefficient for n− and p−type GaAs between 1.3 and 1.6 eV," *Journal of Applied Physics,* vol. 46, pp. 250-257, 1975.
[63] H. Burkhard, H. W. Dinges, and E. Kuphal, "Optical properties of $In_{1-x}GaxP_{1-y}As_y$, InP, GaAs, and GaP determined by ellipsometry," *Journal of Applied Physics,* vol. 53, pp. 655-662, 1982.
[64] G. G. Macfarlane and V. Roberts, "Infrared Absorption of Germanium near the Lattice Edge," *Physical Review,* vol. 97, pp. 1714-1716, 1955.
[65] G. G. Macfarlane and V. Roberts, "Infrared Absorption of Silicon Near the Lattice Edge," *Physical Review,* vol. 98, pp. 1865-1866, 1955.
[66] W. F. Z. Naturforsch, "Influence of an electric field on an optical absorption edge," *Journal of Experimental and Theoretical Physics,* vol. 13a, p. 484, 1958.
[67] L. V. Keldysh, "Behaviour of Non-Metallic Crystals in Strong Electric Fields," *Journal of Experimental and Theoretical Physics,* vol. 33, 1957.
[68] B. R. Bennett and R. A. Soref, "Electrorefraction and electroabsorption in InP, GaAs, GaSb, InAs, and InSb," *Quantum Electronics, IEEE Journal of,* vol. 23, pp. 2159-2166, 1987.
[69] A. Frova, P. Handler, F. A. Germano, and D. E. Aspnes, "Electro-Absorption Effects at the Band Edges of Silicon and Germanium," *Physical Review,* vol. 145, pp. 575-583, 1966.
[70] J. Callaway, "Optical Absorption in an Electric Field," *Physical Review,* vol. 134, pp. A998-A1000, 1964.
[71] K. Tharmalingam, "Optical Absorption in the Presence of a Uniform Field," *Physical Review,* vol. 130, pp. 2204-2206, 06/15/ 1963.
[72] J. P. Zheng, L. Shi, F. S. Choa, P. L. Liu, and H. S. Kwok, "Intensity‐dependent photoluminescence spectra of semiconductor‐doped glasses," *Applied Physics Letters,* vol. 53, pp. 643-645, 1988.
[73] G. Allan, C. Delerue, and M. Lannoo, "Nature of Luminescent Surface States of Semiconductor Nanocrystallites," *Physical Review Letters,* vol. 76, pp. 2961-2964, 1996.
[74] C. H. Henry and D. V. Lang, "Nonradiative capture and recombination by multiphonon emission in GaAs and GaP," *Physical Review B,* vol. 15, pp. 989-1016, 1977.
[75] D. E. Aspnes, "Recombination at semiconductor surfaces and interfaces," *Surface Science,* vol. 132, pp. 406-421, 1983.
[76] R. J. Nelson and R. G. Sobers, "Interfacial recombination velocity in GaAlAs/GaAs heterostructures," *Applied Physics Letters,* vol. 32, pp. 761-763, 1978.

[77] J. S. Rimmer, J. M. Langer, M. Missous, J. H. Evans, I. Poole, A. R. Peaker, *et al.*, "Minority-carrier confinement by doping barriers," *Materials Science and Engineering: B,* vol. 9, pp. 375-378, 1991.
[78] D. K. Schroder, "Carrier lifetimes in silicon," *Electron Devices, IEEE Transactions on,* vol. 44, pp. 160-170, 1997.
[79] S. S. Li and W. R. Thurber, "The dopant density and temperature dependence of electron mobility and resistivity in n-type silicon," *Solid-State Electronics,* vol. 20, pp. 609-616, 1977.
[80] H. A. Zarem, J. A. Lebens, K. B. Nordstrom, P. C. Sercel, S. Sanders, L. E. Eng, *et al.*, "Effect of Al mole fraction on carrier diffusion lengths and lifetimes in AlxGa1−xAs," *Applied Physics Letters,* vol. 55, pp. 2622-2624, 1989.
[81] M. I. Yernaux, C. Battochio, P. Verlinden, and F. Van De Wiele, "A one-dimensional model for the quantum efficiency of front-surface-field solar cells," *Solar Cells,* vol. 13, pp. 83-97, 1984.
[82] M. Becker and H. Fan, "Optical properties of semiconductors. III. Infra-red transmission of silicon," *Physical Review,* vol. 76, p. 1531, 1949.
[83] M. Becker and H. Y. Fan, "Optical Properties of Semiconductors. II. Infra-Red Transmission of Germanium," *Physical Review,* vol. 76, pp. 1530-1531, 1949.
[84] W. Brattain and H. Briggs, "The optical constants of germanium in the infra-red and visible," *Physical Review,* vol. 75, p. 1705, 1949.
[85] R. B. Barnes and M. Czerny, "Concerning the Reflection Power of Metals in Thin Layers for the Infrared," *Physical Review,* vol. 38, pp. 338-345, 1931.
[86] H. Levinstein, "The Growth and Structure of Thin Metallic Films," *Journal of Applied Physics,* vol. 20, pp. 306-315, 1949.
[87] K. Lark-Horovitz and K. W. Meissner, "The Optical Properties of Semiconductors. I. The Reflectivity of Germanium Semiconductors," *Physical Review,* vol. 76, pp. 1530-1530, 1949.
[88] K. Gurtler, K. Bange, W. Wagner, F. Rauch, and H. Hantsche, "Characterization of Ta_2O_5 layers by electron spectroscopy for chemical analysis rutherford backscattering spectrometry, nuclear reaction analysis and optical methods," *Thin Solid Films,* vol. 175, pp. 185-189, 1989.
[89] P. Drude, C. R. Mann, and R. A. Millikan, *The Theory of Optics*: Longmans, Green, and Company, 1901.
[90] L. Ingersoll and J. Littleton Jr, "A New Method of Determining the Optical Constants of Metals, and the Optical Constants of Silicon," *Physical Review (Series I),* vol. 31, p. 489, 1910.
[91] K. Hirokazu, S. Adachi, N. H., and O. K., "Optical Properties of $(Al_xGa_{1-x})0.5In_{0.5}P$ Quaternary Alloys " *Japanese Journal of Applied Physics,* vol. 33, pp. 186-192, 1994.
[92] R. W. Collins, I. An, H. Fujiwara, J. Lee, Y. Lu, J. Koh, *et al.*, "Advances in multichannel spectroscopic ellipsometry," *Thin Solid Films,* vol. 313–314, pp. 18-32, 1998.
[93] K. G. McKay and K. B. McAfee, "Electron Multiplication in Silicon and Germanium," *Physical Review,* vol. 91, pp. 1079-1084, 1953.
[94] C. L. Anderson and C. R. Crowell, "Threshold Energies for Electron-Hole Pair Production by Impact Ionization in Semiconductors," *Physical Review B,* vol. 5, pp. 2267-2272, 1972.
[95] S. Ahmad and W. S. Khokley, "Transition probability of impact ionization in silicon," *Journal of Physics and Chemistry of Solids,* vol. 28, pp. 2499-2507, 1967.

[96] R. A. Ballinger, K. G. Major, and J. R. Mallinson, "Impact ionization thresholds in semiconductors," *Journal of Physics C: Solid State Physics,* vol. 6, p. 2573, 1973.
[97] J. R. Hauser, "Threshold Energy for Avalanche Multiplication in Semiconductors," *Journal of Applied Physics,* vol. 37, pp. 507-509, 1966.
[98] J. Bude and K. Hess, "Thresholds of impact ionization in semiconductors," *Journal of Applied Physics,* vol. 72, pp. 3554-3561, 1992.
[99] T. P. Pearsall, R. E. Nahory, and J. R. Chelikowsky, "Orientation Dependence of Free-Carrier Impact Ionization in Semiconductors: GaAs," *Physical Review Letters,* vol. 39, pp. 295-298, 1977.
[100] J. Bude, K. Hess, and G. J. Iafrate, "Impact ionization in semiconductors: Effects of high electric fields and high scattering rates," *Physical Review B,* vol. 45, pp. 10958-10964, 1992.
[101] W. Shockley, "Problems related to p-n junctions in silicon," *Solid-State Electronics,* vol. 2, pp. 35-67, 1961.
[102] M. V. Fischetti and S. E. Laux, "Monte carlo analysis of electron transport in small semiconductor devices including band-structure and space-charge effects," *Physical Review B,* vol. 38, pp. 9721-9745, 1988.
[103] A. Spinelli, A. Pacelli, and A. L. Lacaita, "Dead space approximation for impact ionization in silicon," *Applied Physics Letters,* vol. 69, pp. 3707-3709, 1996.
[104] R. J. McIntyre, "Multiplication noise in uniform avalanche diodes," *Electron Devices, IEEE Transactions on,* vol. ED-13, pp. 164-168, 1966.
[105] G. Meurant, *Semiconductors & Semimetals V21B*: Elsevier Science, 1984.
[106] W. N. Grant, "Electron and hole ionization rates in epitaxial silicon at high electric fields," *Solid-State Electronics,* vol. 16, pp. 1189-1203, 1973.
[107] S. A. Plimmer, J. P. R. David, G. J. Rees, and P. N. Robson, "Ionization coefficients in Al x Ga 1- x As (x = 0 - 0.60)," *Semiconductor Science and Technology,* vol. 15, p. 692, 2000.
[108] R. Van Overstraeten and H. De Man, "Measurement of the ionization rates in diffused silicon p-n junctions," *Solid-State Electronics,* vol. 13, pp. 583-608, 1970.
[109] L. W. Cook, G. E. Bulman, and G. E. Stillman, "Electron and hole impact ionization coefficients in InP determined by photomultiplication measurements," *Applied Physics Letters,* vol. 40, pp. 589-591, 1982.
[110] B. K. Ng, J. P. R. David, S. A. Plimmer, G. J. Rees, R. C. Tozer, M. Hopkinson, *et al.*, "Avalanche multiplication characteristics of $Al_{0.8}Ga_{0.2}As$ diodes," *Electron Devices, IEEE Transactions on,* vol. 48, pp. 2198-2204, 2001.
[111] J. S. L. Ong, J. S. Ng, A. B. Krysa, and J. P. R. David, "Impact Ionization Coefficients in $Al_{0.52}In_{0.48}P$," *Electron Device Letters, IEEE,* vol. 32, pp. 1528-1530, 2011.
[112] J. S. Cheong, M. M. Hayat, Z. Xinxin, and J. P. R. David, "Relating the Experimental Ionization Coefficients in Semiconductors to the Nonlocal Ionization Coefficients," *Electron Devices, IEEE Transactions on,* vol. 62, pp. 1946-1952, 2015.
[113] G. E. Bulman, V. M. Robbins, G. E. Stillman, and G. E. Stillman, "The determination of impact ionization coefficients in (100) Gallium Arsenide using avalanche noise and photocurrent multiplication measurements," *Electron Devices, IEEE Transactions on,* vol. 32, pp. 2454-2466, 1985.
[114] M. H. Woods, W. C. Johnson, and M. A. Lampert, "Use of a Schottky barrier to measure impact ionization coefficients in semiconductors," *Solid-State Electronics,* vol. 16, pp. 381-394, 1973.

[115] Y. Okuto and C. R. Crowell, "Ionization coefficients in semiconductors: A nonlocalized property," *Physical Review B,* vol. 10, pp. 4284-4296, 1974.
[116] R. M. Flitcroft, J. P. R. David, P. A. Houston, and C. C. Button, "Avalanche multiplication in GaInP/GaAs single heterojunction bipolar transistors," *Electron Devices, IEEE Transactions on,* vol. 45, pp. 1207-1212, 1998.
[117] C. Hu, K. A. Anselm, B. G. Streetman, and J. C. Campbell, "Noise characteristics of thin multiplication region GaAs avalanche photodiodes," *Applied Physics Letters,* vol. 69, pp. 3734-3736, 1996.
[118] K. F. Li, D. S. Ong, J. P. R. David, G. J. Rees, R. C. Tozer, P. N. Robson, *et al.*, "Avalanche multiplication noise characteristics in thin GaAs p^+-i-n^+ diodes," *Electron Devices, IEEE Transactions on,* vol. 45, pp. 2102-2107, 1998.
[119] D. S. Ong, K. F. Li, S. A. Plimmer, G. J. Rees, J. P. R. David, and P. N. Robson, "Full band Monte Carlo modeling of impact ionization, avalanche multiplication, and noise in submicron GaAs p+-i-n+ diodes," *Journal of Applied Physics,* vol. 87, pp. 7885-7891, 2000.
[120] M. M. Hayat, B. E. A. Saleh, and M. C. Teich, "Effect of dead space on gain and noise of double-carrier-multiplication avalanche photodiodes," *Electron Devices, IEEE Transactions on,* vol. 39, pp. 546-552, 1992.
[121] K. B. Athreya and P. E. Ney, *Branching Processes*: Springer Berlin Heidelberg, 2012.
[122] D. S. Ong, K. F. Li, G. J. Rees, J. P. R. David, and P. N. Robson, "A simple model to determine multiplication and noise in avalanche photodiodes," *Journal of Applied Physics,* vol. 83, pp. 3426-3428, 1998.
[123] M. A. Saleh, M. M. Hayat, O.-H. Kwon, A. L. Holmes, J. C. Campbell, B. E. A. Saleh, *et al.*, "Breakdown voltage in thin III–V avalanche photodiodes," *Applied Physics Letters,* vol. 79, pp. 4037-4039, 2001.
[124] C. H. Tan, J. C. Clark, J. P. R. David, G. J. Rees, S. A. Plimmer, R. C. Tozer, *et al.*, "Avalanche noise measurement in thin Si p+-i-n+ diodes," *Applied Physics Letters,* vol. 76, pp. 3926-3928, 2000.
[125] K. Brennan and K. Hess, "High field transport in GaAs, InP and InAs," *Solid-State Electronics,* vol. 27, pp. 347-357, 1984.
[126] C. Jacoboni, C. Canali, G. Ottaviani, and A. Alberigi Quaranta, "A review of some charge transport properties of silicon," *Solid-State Electronics,* vol. 20, pp. 77-89, 1977.
[127] H. Shichijo and K. Hess, "Band-structure-dependent transport and impact ionization in GaAs," *Physical Review B,* vol. 23, pp. 4197-4207, 1981.
[128] M. Feng, L. Ning, and J. C. Campbell, "Monte Carlo simulations of the bandwidth of InAlAs avalanche photodiodes," *Electron Devices, IEEE Transactions on,* vol. 50, pp. 2291-2294, 2003.
[129] S. Wenlu, X. Zheng, L. Zhiwen, and J. C. Campbell, "Monte Carlo Simulation of InAlAs/InAlGaAs Tandem Avalanche Photodiodes," *Quantum Electronics, IEEE Journal of,* vol. 48, pp. 528-532, 2012.
[130] S. Wenlu, X. Zheng, L. Zhiwen, and J. C. Campbell, "Monte Carlo Simulation of $Al_xGa_{1-x}As$ (x > 0.6) Avalanche Photodiodes," *Quantum Electronics, IEEE Journal of,* vol. 47, pp. 1531-1536, 2011.
[131] S. A. Plimmer, J. P. R. David, D. S. Ong, and K. F. Li, "A simple model for avalanche multiplication including deadspace effects," *Electron Devices, IEEE Transactions on,* vol. 46, pp. 769-775, 1999.
[132] S. C. L. T. Mun, C. H. Tan, Y. L. Goh, A. R. J. Marshall, and J. P. R. David, "Modeling of avalanche multiplication and excess noise factor in In0.52Al0.48As avalanche photodiodes using a simple Monte Carlo model," *Journal of Applied Physics,* vol. 104, p. 013114, 2008.

[133] X. Zhou, J. S. Ng, and C. H. Tan, "A simple Monte Carlo model for prediction of avalanche multiplication process in Silicon," *Journal of Instrumentation,* vol. 7, p. P08006, 2012.
[134] L. V. Keldysh, "Kinetic Theory of Impact Ionization in Semiconductors," *J. Exptl. Theoret. Phys,* vol. 10, pp. 509-518, 1959.
[135] H. D. Rees, "Calculation of distribution functions by exploiting the stability of the steady state," *Journal of Physics and Chemistry of Solids,* vol. 30, pp. 643-655, 1969.
[136] D. J. Mowbray, O. P. Kowalski, M. Hopkinson, M. S. Skolnick, and J. P. R. David, "Electronic band structure of AlGaInP grown by solid‐source molecular‐beam epitaxy," *Applied Physics Letters,* vol. 65, pp. 213-215, 1994.
[137] A. Onton and R. J. Chicotka, "Conduction Bands in In1−xAlxP," *Journal of Applied Physics,* vol. 41, pp. 4205-4207, 1970.
[138] "High speed photodiodes (S5973 series: 1 GHz)," Hamamatsu Photonics K. K.1 Sept 2015 2012.
[139] "Model SR830 DSP Lock-in Amplifier," Stanford Research Systems 2006.
[140] M. Yang, M. Yamaguchi, T. Takamoto, E. Ikeda, H. Kurita, and M. Ohmori, "Photoluminescence analysis of InGaP top cells for high-efficiency multi-junction solar cells," *Solar Energy Materials and Solar Cells,* vol. 45, pp. 331-339, 1997.
[141] H. Sugawara, K. Itaya, and G. Hatakoshi, "Characteristics of a distributed Bragg reflector for the visible‐light spectral region using InGaAlP and GaAs: Comparison of transparent‐ and loss‐type structures," *Journal of Applied Physics,* vol. 74, pp. 3189-3193, 1993.
[142] K. Kishino, A. Kikuchi, Y. Kaneko, and I. Nomura, "Enhanced carrier confinement effect by the multiquantum barrier in 660 nm GaInP/AlInP visible lasers," *Applied Physics Letters,* vol. 58, pp. 1822-1824, 1991.
[143] C. N. Atkins, A. B. Krysa, D. G. Revin, K. Kennedy, J. P. Commin, and J. W. Cockburn, "Low threshold room temperature GaAs/AlGaAs quantum cascade laser with InAlP waveguide," *Electronics Letters,* vol. 47, pp. 1193-1194, 2011.
[144] J. S. Cheong, J. S. L. Ong, J. S. Ng, A. B. Krysa, and J. P. R. David, "$Al_{0.52}In_{0.48}P$ SAM-APD as a Blue-Green Detector," *Selected Topics in Quantum Electronics, IEEE Journal of,* vol. 20, pp. 142-146, 2014.
[145] W. C. Dash and R. Newman, "Intrinsic Optical Absorption in Single-Crystal Germanium and Silicon at 77K and 300K," *Physical Review,* vol. 99, pp. 1151-1155, 1955.
[146] H. R. Philipp and E. A. Taft, "Optical Constants of Germanium in the Region 1 to 10 ev," *Physical Review,* vol. 113, pp. 1002-1005, 1959.
[147] S. Adachi, H. Kato, A. Moki, and K. Ohtsuka, "Refractive index of $(Al_xGa_{1-x})_{0.5}In_{0.5}P$ quaternary alloys," *Journal of Applied Physics,* vol. 75, pp. 478-480, 1994.
[148] D. E. Aspnes, S. M. Kelso, R. A. Logan, and R. Bhat, "Optical properties of AlxGa1−x As," *Journal of Applied Physics,* vol. 60, pp. 754-767, 1986.
[149] M. O. Watanabe and Y. Ohba, "Interface properties for GaAs/InGaAlP heterojunctions by the capacitance‐voltage profiling technique," *Applied Physics Letters,* vol. 50, pp. 906-908, 1987.
[150] A. K. Saxena, "Non-Γ Deep Levels and the Conduction Band Structure of Ga1−xAlxAs Alloys," *physica status solidi (b),* vol. 105, pp. 777-787, 1981.
[151] J. S. Cheong, J. S. L. Ong, J. S. Ng, A. B. Krysa, F. Bastiman, and J. P. R. David, "Design of high sensitivity detector for underwater communication system," 2013, pp. 88990G-88990G-9.

[152] D. Bimberg, M. Grundmann, and N. N. Ledentsov, *Quantum Dot Heterostructures*: Wiley, 1999.
[153] A. K. Saxena, "The conduction band structure and deep levels in Ga 1-x Al x As alloys from a high-pressure experiment," *Journal of Physics C: Solid State Physics,* vol. 13, p. 4323, 1980.
[154] L. C. Su, I. H. Ho, and G. B. Stringfellow, "Effects of substrate misorientation and growth rate on ordering in GaInP," *Journal of Applied Physics,* vol. 75, pp. 5135-5141, 1994.
[155] Y. Nishikawa, M. Ishikawa, Y. Tsuburai, and Y. Kokubun, "Lattice constant shift in Zn-doped InGaAIP grown by low-pressure metalorganic chemical vapor deposition," *Journal of Crystal Growth,* vol. 100, pp. 63-67, 1990.
[156] A. L. Holmes, M. R. Islam, R. V. Chelakara, F. J. Ciuba, R. D. Dupuis, M. J. Ries, *et al.*, "High - reflectivity visible - wavelength semiconductor native oxide Bragg reflectors grown by metalorganic chemical vapor deposition," *Applied Physics Letters,* vol. 66, pp. 2831-2833, 1995.
[157] H. Amano, M. Kito, K. Hiramatsu, and I. Akasaki, "P-Type Conduction in Mg-Doped GaN Treated with Low-Energy Electron Beam Irradiation (LEEBI)," *Japanese Journal of Applied Physics,* vol. 28, p. L2112, 1989.
[158] K. A. Bertness, S. R. Kurtz, S. E. Asher, and R. C. Reedy Jr, "AlInP benchmarks for growth of AlGaInP compounds by organometallic vapor-phase epitaxy," *Journal of Crystal Growth,* vol. 196, pp. 13-22, 1999.
[159] Y. Ohba, Y. Nishikawa, C. Nozaki, H. Sugawara, and T. Nakanisi, "A study of p-type doping for AlGaInP grown by low-pressure MOCVD," *Journal of Crystal Growth,* vol. 93, pp. 613-617, 1988.
[160] L. G. Meiners, "Temperature dependence of the dielectric constant of InP," *Journal of Applied Physics,* vol. 59, pp. 1611-1613, 1986.
[161] B. Monemar, "Determination of band gap and refractive index of AIP from optical absorption," *Solid State Communications,* vol. 8, pp. 1295-1298, 1970/08/15 1970.
[162] M. B. Panish and H. C. Casey, "Temperature Dependence of the Energy Gap in GaAs and GaP," *Journal of Applied Physics,* vol. 40, pp. 163-167, 1969.
[163] S. A. Wood, C. H. Molloy, P. M. Smowton, P. Blood, D. J. Somerford, and C. C. Button, "Electron transport in AlGaInP quantum well lasers," *Applied Physics Letters,* vol. 75, pp. 1748-1750, 1999.
[164] J. M. Dishman and M. DiDomenico, "Optical Absorption by Impurities in p-Type Gallium Phosphide," *Physical Review B,* vol. 4, pp. 2621-2634, 10/15/ 1971.
[165] R. Cheung, S. Thoms, M. Watt, M. A. Foad, C. M. Sotomayor-Torres, C. D. W. Wilkinson, *et al.*, "Reactive ion etching induced damage in GaAs and $Al_{0.3}Ga_{0.7}As$ using $SiCl_4$," *Semiconductor Science and Technology,* vol. 7, p. 1189, 1992.
[166] G. E. Stillman, C. M. Wolfe, J. A. Rossi, and J. P. Donnelly, "Electroabsorption avalanche photodiodes," *Applied Physics Letters,* vol. 25, pp. 671-673, 1974.
[167] I. Vurgaftman, J. R. Meyer, and L. R. Ram-Mohan, "Band parameters for III–V compound semiconductors and their alloys," *Journal of Applied Physics,* vol. 89, pp. 5815-5875, 2001.
[168] P. Lawaetz, "Valence-Band Parameters in Cubic Semiconductors," *Physical Review B,* vol. 4, pp. 3460-3467, 1971.
[169] P. Merle, D. Auvergne, H. Mathieu, and J. Chevallier, "Conduction band structure of GaInP," *Physical Review B,* vol. 15, pp. 2032-2047, 02/15/ 1977.

[170] C. H. Seager, P. M. Lenahan, K. L. Brower, and R. E. Mikawa, "Dangling bonds and the Urbach tail in silicon," *Journal of Applied Physics,* vol. 58, pp. 2704-2708, 1985.
[171] S. R. Johnson and T. Tiedje, "Temperature dependence of the Urbach edge in GaAs," *Journal of Applied Physics,* vol. 78, pp. 5609-5613, 1995.
[172] F. Urbach, "The Long-Wavelength Edge of Photographic Sensitivity and of the Electronic Absorption of Solids," *Physical Review,* vol. 92, pp. 1324-1324, 1953.
[173] M. V. Kurik, "Urbach rule," *physica status solidi (a),* vol. 8, pp. 9-45, 1971.
[174] M. A. Saleh, M. M. Hayat, P. P. Sotirelis, A. L. Holmes, J. C. Campbell, B. E. A. Saleh, *et al.*, "Impact-ionization and noise characteristics of thin III-V avalanche photodiodes," *Electron Devices, IEEE Transactions on,* vol. 48, pp. 2722-2731, 2001.
[175] M. M. Hayat, U. Sakoglu, O.-H. Kwon, W. Shuling, J. C. Campbell, B. E. A. Saleh, *et al.*, "Breakdown probabilities for thin heterostructure avalanche photodiodes," *Quantum Electronics, IEEE Journal of,* vol. 39, pp. 179-185, 2003.
[176] C. Groves, C. H. Tan, J. P. R. David, G. J. Rees, and M. M. Hayat, "Exponential time response in analogue and Geiger mode avalanche photodiodes," *Electron Devices, IEEE Transactions on,* vol. 52, pp. 1527-1534, 2005.
[177] M. M. Hayat, O.-H. Kwon, P. Yi, P. Sotirelis, J. C. Campbell, B. E. A. Saleh, *et al.*, "Gain-bandwidth characteristics of thin avalanche photodiodes," *Electron Devices, IEEE Transactions on,* vol. 49, pp. 770-781, 2002.
[178] A. Spinelli and A. L. Lacaita, "Mean gain of avalanche photodiodes in a dead space model," *Electron Devices, IEEE Transactions on,* vol. 43, pp. 23-30, 1996.
[179] J. S. Ng, C. H. Tan, B. K. Ng, P. J. Hambleton, J. P. R. David, G. J. Rees, *et al.*, "Effect of dead space on avalanche speed [APDs]," *Electron Devices, IEEE Transactions on,* vol. 49, pp. 544-549, 2002.
[180] L. J. J. Tan, J. S. Ng, C. H. Tan, and J. P. R. David, "Avalanche Noise Characteristics in Submicron InP Diodes," *Quantum Electronics, IEEE Journal of,* vol. 44, pp. 378-382, 2008.
[181] B. K. Ng, J. P. R. David, R. C. Tozer, G. J. Rees, Y. Feng, J. H. Zhao, *et al.*, "Nonlocal effects in thin 4H-SiC UV avalanche photodiodes," *Electron Devices, IEEE Transactions on,* vol. 50, pp. 1724-1732, 2003.
[182] C. H. Tan, J. P. R. David, S. A. Plimmer, G. J. Rees, R. C. Tozer, and R. Grey, "Low multiplication noise thin $Al_{0.6}Ga_{0.4}As$ avalanche photodiodes," *Electron Devices, IEEE Transactions on,* vol. 48, pp. 1310-1317, 2001.
[183] B. K. Ng, J. P. R. David, R. C. Tozer, M. Hopkinson, G. Hill, and G. J. Rees, "Excess noise characteristics of $Al_{0.8}Ga_{0.2}As$ avalanche photodiodes," *Photonics Technology Letters, IEEE,* vol. 14, pp. 522-524, 2002.
[184] Y. L. Goh, A. R. J. Marshall, D. J. Massey, J. S. Ng, C. H. Tan, M. Hopkinson, *et al.*, "Excess Avalanche Noise in $In_{0.52}Al_{0.48}As$," *Quantum Electronics, IEEE Journal of,* vol. 43, pp. 503-507, 2007.
[185] C. H. Tan, R. Ghin, J. P. R. David, G. J. Rees, and M. Hopkinson, "The effect of dead space on gain and excess noise in $In_{0.48}Ga_{0.52}P$ p+in+ diodes," *Semiconductor Science and Technology,* vol. 18, p. 803, 2003.
[186] F. Capasso, *Physics of avalanche photodiodes* vol. 22. New York, 1977.
[187] Y. L. Goh, D. J. Massey, A. R. J. Marshall, J. S. Ng, C. H. Tan, W. K. Ng, *et al.*, "Avalanche Multiplication in InAlAs," *Electron Devices, IEEE Transactions on,* vol. 54, pp. 11-16, 2007.
[188] R. Ghin, J. P. R. David, S. A. Plimmer, M. Hopkinson, G. J. Rees, D. C. Herbert, *et al.*, "Avalanche multiplication and breakdown in $Ga_{0.52}In_{0.48}P$ diodes," *Electron Devices, IEEE Transactions on,* vol. 45, pp. 2096-2101, 1998.

[189] D. Vignaud and F. Mollot, "Conduction band offset in the $Al_xGa_yIn_{1-x-y}P/Ga_{0.52}In_{0.48}P$ system as studied by luminescence spectroscopy," *Journal of Applied Physics,* vol. 93, pp. 384-389, 2003.
[190] R. K. Ahrenkiel, "Measurement of minority-carrier lifetime by time-resolved photoluminescence," *Solid-State Electronics,* vol. 35, pp. 239-250, 1992.
[191] R. K. Ahrenkiel, D. J. Dunlavy, R. Y. Loo, and G. S. Kamath, "Minority-carrier lifetime in n Al0.38Ga0.62As," *Journal of Applied Physics,* vol. 63, pp. 5174-5176, 1988.
[192] D. A. Ramirez, M. M. Hayat, A. S. Huntington, and G. M. Williams, "Non-Local Model for the Spatial Distribution of Impact Ionization Events in Avalanche Photodiodes," *Photonics Technology Letters, IEEE,* vol. 26, pp. 25-28, 2014.
[193] Thorlabs. GaP Photodiode [Online]. Available: http://www.thorlabs.de/thorcat/12100/FGAP71-SpecSheet.PDF
[194] H. P. K. K. (2 Nov). *Low bias operation, for 800 nm band*. Available: http://www.hamamatsu.com/resources/pdf/ssd/s12023-02_etc_kapd1007e.pdf
[195] Thorlabs. LED with Ball Lens [Online]. Available: http://www.thorlabs.de/thorcat/22300/LED470L-SpecSheet.pdf
[196] L. Qiao, J. S. Cheong, J. S. L. Ong, J. S. Ng, A. B. Krysa, J. E. Green, *et al.*, "Avalanche Noise in $Al_{0.52}In_{0.48}P$ Diodes," *Photonics Technology Letters, IEEE,* vol. 28, pp. 481-484, 2016.
[197] D. S. G. Ong, J. S. Ng, M. M. Hayat, P. Sun, and J. P. R. David, "Optimization of InP APDs for High-Speed Lightwave Systems," *Journal of Lightwave Technology,* vol. 27, pp. 3294-3302, 2009.
[198] A. Armin, R. D. Jansen-van Vuuren, N. Kopidakis, P. L. Burn, and P. Meredith, "Narrowband light detection via internal quantum efficiency manipulation of organic photodiodes," *Nat Commun,* vol. 6, 02/27/online 2015.
[199] Q. Lin, A. Armin, P. L. Burn, and P. Meredith, "Filterless narrowband visible photodetectors," *Nat Photon,* vol. 9, pp. 687-694, 10//print 2015.
[200] G. W. Hooft, C. van Opdorp, H. Veenvliet, and A. T. Vink, "Minority carrier lifetime and luminescence in MOVPE-grown (Al,Ga)As epilayers and DH lasers," *Journal of Crystal Growth,* vol. 55, pp. 173-182, 1981/10/01 1981.
[201] Q. Zhou, D. C. McIntosh, Z. Lu, J. C. Campbell, A. V. Sampath, H. Shen, *et al.*, "GaN/SiC avalanche photodiodes," *Applied Physics Letters,* vol. 99, p. 131110, 2011.

APPENDIX A ELECTRIC FIELD MODELLING

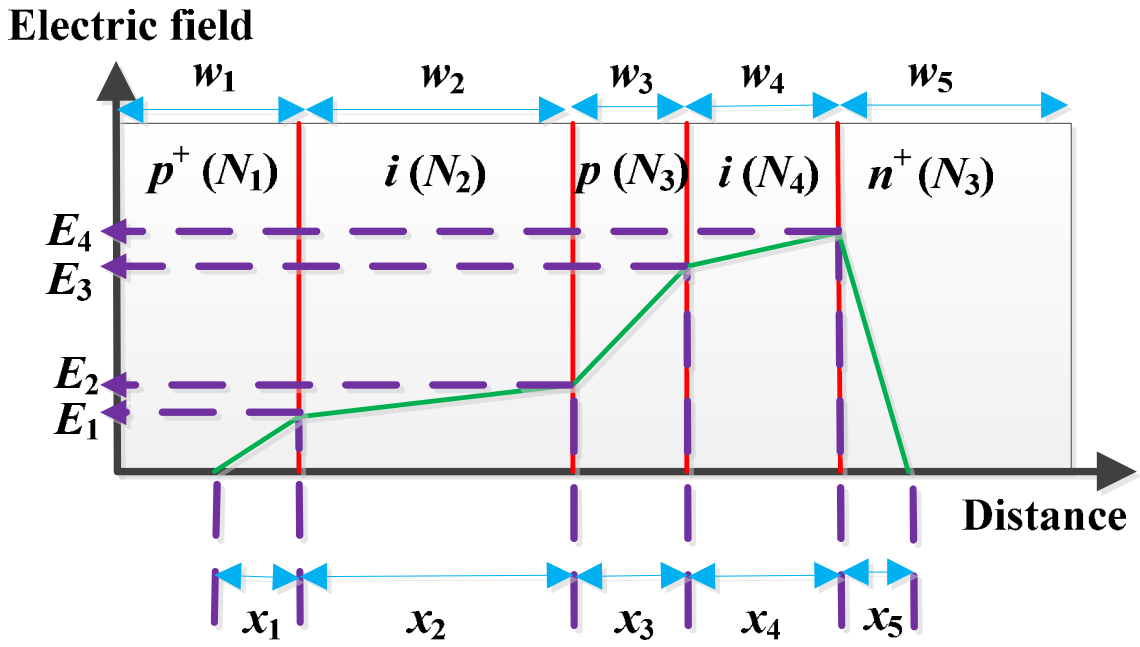

Figure A.1 *Electric field profile of a SAM APD, assuming $p^+p^-pp^-n$ structure with doping of N1, N2, N3, N4 and N5 with thickness of w1, w2, w3, w4 and w5 and dielectric constant of ϵ_1, ϵ_2, ϵ_3, ϵ_4 and ϵ_5 respectively.*

Electric field at E_1, E_2, E_3 and E_4 in Figure A.1 can be expressed as

$$E_1 = \frac{qN_1x_1}{\epsilon_1} E_2 = E_1 + \frac{qN_2x_2}{\epsilon_2} \tag{A.1}$$

$$E_3 = E_2 + \frac{qN_3x_3}{\epsilon_3} E_4 = E_3 + \frac{qN_4x_4}{\epsilon_4} E_4 = \frac{-qN_5x_5}{\epsilon_5}$$

where x_1, x_2, x_3, x_4 and x_5 is the thickness of depletion region in *p*-cladding, absorption region, charge sheet, multiplication region and *n*-cladding respectively. Rearranging equations (A.1) yields

$$x_5 = \frac{-\epsilon_5}{N_5}\left(\frac{N_1x_1}{\epsilon_1} + \frac{N_2x_2}{\epsilon_2} + \frac{N_3x_3}{\epsilon_3} + \frac{N_4x_4}{\epsilon_4}\right) \tag{A.2}$$

Also, the total voltage across the diode, V_T is area under electric field profile such that

$$V_T = \frac{1}{2}[x_1E_1 + x_2(E_1 + E_2) + x_3(E_2 + E_3) + x_4(E_3 + E_4) + x_5E_4] \quad \text{(A.3)}$$

Substitute equation (A.1) and (A.2) into (A.3),

$$\begin{aligned} V_T = \frac{1}{2}[x_1 \frac{qN_1x_1}{\epsilon_1} &+ x_2\left(\frac{2qN_1x_1}{\epsilon_1} + \frac{qN_2x_2}{\epsilon_2}\right) \\ &+ x_3\left(\frac{2qN_1x_1}{\epsilon_1} + \frac{2qN_2x_2}{\epsilon_2} + \frac{qN_3x_3}{\epsilon_3}\right) \\ &+ x_4\left(\frac{2qN_1x_1}{\epsilon_1} + \frac{2qN_2x_2}{\epsilon_2} + \frac{2qN_3x_3}{\epsilon_3} + \frac{qN_4x_4}{\epsilon_4}\right) \\ &+ \frac{-\epsilon_5}{N_5}(\frac{N_1x_1}{\epsilon_1} + \frac{N_2x_2}{\epsilon_2} + \frac{N_3x_3}{\epsilon_3} \\ &+ \frac{N_4x_4}{\epsilon_4})\left(\frac{qN_1x_1}{\epsilon_1} + \frac{qN_2x_2}{\epsilon_2} + \frac{qN_3x_3}{\epsilon_3} + \frac{qN_4x_4}{\epsilon_4}\right)] \end{aligned} \quad \text{(A.4)}$$

Simplify equation (A.4) to $ax_1{}^2 + bx_1 + c = 0$ where a, b and c are

$$a = \frac{N_1}{\epsilon_1}[1 + \frac{-\epsilon_5}{N_5}\left(\frac{N_1}{\epsilon_1}\right)] \quad \text{(A.5)}$$

$$b = 2N_1[\frac{-\epsilon_5}{N_5}(\frac{N_2x_2}{\epsilon_1\epsilon_2} + \frac{N_3x_3}{\epsilon_1\epsilon_3} + \frac{N_4x_4}{\epsilon_1\epsilon_4}) + \frac{x_2}{\epsilon_1} + \frac{x_3}{\epsilon_1} + \frac{x_4}{\epsilon_1}] \quad \text{(A.6)}$$

$$\begin{aligned} c = \frac{-\epsilon_5}{N_5}\Bigg(&\frac{N_2{}^2x_2{}^2}{\epsilon_2{}^2} + \frac{N_3{}^2x_3{}^2}{\epsilon_3{}^2} + \frac{N_4{}^2x_4{}^2}{\epsilon_4{}^2} + \frac{2N_2x_2N_4x_4}{\epsilon_2\epsilon_4} + \frac{2N_2x_2N_3x_3}{\epsilon_2\epsilon_3} \\ &+ \frac{2N_3x_3N_4x_4}{\epsilon_3\epsilon_4}\Bigg) + \left(\frac{N_2x_2{}^2}{\epsilon_2} + \frac{2N_2x_2x_3}{\epsilon_2} + \frac{N_3x_3{}^2}{\epsilon_3}\right) \\ &+ \frac{2N_2x_2x_4}{\epsilon_2} + \frac{2N_3x_3x_4}{\epsilon_3} + \frac{N_4x_4{}^2}{\epsilon_4} - \frac{2V_T}{q} \end{aligned} \quad \text{(A.7)}$$

where $x_2 = w_2, x_3 = w_3$ and $x_4 = w_4.x_1$ can be solved using

$$x_1 = \frac{-b \pm \sqrt{b^2 - 4ac}}{2a} \tag{A.8}$$

Consider V_T is sufficient to fully deplete w3 and w4 such that $x_1 = 0$, it simplifies equation (A.1) to

$$V_T = \frac{1}{2}[x_2\left(\frac{qN_2x_2}{\epsilon_2}\right) + x_3\left(\frac{2qN_2x_2}{\epsilon_2} + \frac{qN_3x_3}{\epsilon_3}\right) + x_4\left(\frac{2qN_2x_2}{\epsilon_2} + \frac{2qN_3x_3}{\epsilon_3} + \frac{qN_4x_4}{\epsilon_4}\right) + \frac{-\epsilon_5}{N_5}(\frac{N_2x_2}{\epsilon_2} + \frac{N_3x_3}{\epsilon_3} + \frac{N_4x_4}{\epsilon_4})\left(\frac{qN_2x_2}{\epsilon_2} + \frac{qN_3x_3}{\epsilon_3} + \frac{qN_4x_4}{\epsilon_4}\right)] \tag{A.9}$$

Quadratic equation $ax_2{}^2 + bx_2 + c = 0$ can be solved with *a*, *b*, *c* coefficients are,

$$a = \frac{N_2}{\epsilon_2}[1 + \frac{-\epsilon_5}{N_5}\left(\frac{N_2}{\epsilon_2}\right)] \tag{A.10}$$

$$b = 2N_2[\frac{-\epsilon_5}{N_5}(\frac{N_3x_3}{\epsilon_2\epsilon_3} + \frac{N_4x_4}{\epsilon_2\epsilon_4}) + \frac{x_3}{\epsilon_2} + \frac{x_4}{\epsilon_2}] \tag{A.11}$$

$$c = \frac{-\epsilon_5}{N_5}\left(\frac{N_3{}^2x_3{}^2}{\epsilon_3{}^2} + \frac{N_4{}^2x_4{}^2}{\epsilon_4{}^2} + \frac{2N_3x_3N_4x_4}{\epsilon_3\epsilon_4}\right) + \left(\frac{N_3x_3{}^2}{\epsilon_3} + \frac{2N_3x_3x_4}{\epsilon_3} + \frac{N_4x_4{}^2}{\epsilon_4}\right) - \frac{2V_T}{q} \tag{A.12}$$

where $x_3 = w_3$ and $x_4 = w_4$. x_5 can be computed by

$$x_5 = \frac{-\epsilon_5}{N_5}(\frac{N_2x_2}{\epsilon_2} + \frac{N_3x_3}{\epsilon_3} + \frac{N_4x_4}{\epsilon_4}) \tag{A.13}$$

A SAM-APD depletion region is identical to a *p-i-n* if $x_1 = x_2 = 0$. V_T can be simplified using similar method,

$$V_T = \frac{1}{2}[x_3\left(\frac{qN_3x_3}{\epsilon_3}\right) + x_4\left(\frac{2qN_3x_3}{\epsilon_3} + \frac{qN_4x_4}{\epsilon_4}\right) + \frac{-\epsilon_5}{N_5}(\frac{N_3x_3}{\epsilon_3} + \frac{N_4x_4}{\epsilon_4})\left(\frac{qN_3x_3}{\epsilon_3} + \frac{qN_4x_4}{\epsilon_4}\right)] \quad \text{(A.14)}$$

Arranging (A.14) into quadratic equation $ax_3{}^2 + bx_3 + c = 0$ where,

$$a = \frac{N_3}{\epsilon_3}[1 + \frac{-\epsilon_5}{N_5}\left(\frac{N_3}{\epsilon_3}\right)] \quad \text{(A.15)}$$

$$b = 2N_3[\frac{-\epsilon_5}{N_5}(\frac{N_4x_4}{\epsilon_3\epsilon_4}) + \frac{x_3}{\epsilon_2}] \quad \text{(A.16)}$$

$$c = \frac{-\epsilon_5}{N_5}\left(\frac{N_4{}^2x_4{}^2}{\epsilon_4{}^2}\right) + \frac{N_4x_4{}^2}{\epsilon_4} - \frac{2V_T}{q} \quad \text{(A.17)}$$

where $x_4 = w_4$. x_5 can be computed by

$$x_5 = \frac{-\epsilon_5}{N_5}(\frac{N_3x_3}{\epsilon_3} + \frac{N_4x_4}{\epsilon_4}) \quad \text{(A.18)}$$

Depletion region of a *p-n* junction can be observed as $x_1 = x_2 = x_3 = 0$. V_T can be expressed as,

$$V_T = \frac{1}{2}[x_4\left(\frac{qN_4x_4}{\epsilon_4}\right) + \frac{-\epsilon_5}{N_5}(\frac{N_4x_4}{\epsilon_4})\left(\frac{qN_4x_4}{\epsilon_4}\right)] \quad \text{(A.19)}$$

$$x_4 = \sqrt{\frac{2V_T\epsilon_4{}^2}{q}\frac{N_5}{N_4(\epsilon_4N_5 - \epsilon_5N_4)}} \quad \text{(A.20)}$$

$$x_5 = \frac{-\epsilon_5}{N_5}(\frac{N_4x_4}{\epsilon_4}) \quad \text{(A.21)}$$

APPENDIX B DEFINITIONS OF VARIOUS IONISATION COEFFICIENTS

There are six α's (β's) used in the thesis, namely α (β), α_{device} (β_{device}), α' (β'), α^* (β^*), α_{MC} (β_{MC}), α_s (β_s). The definitions of these ionisation coefficients are summarised as follows, while the detailed descriptions can be found in section 2.5 and 2.6. To simplify the description in this appendix, a perfect homo-junction PIN structure is assumed where the electric field is constant throughout the avalanche width and the multiplication is initiated by one carrier type only, i.e. M_e (M_h). The notations used in equations below are the same as the main text.

1. McIntyre's ionisation coefficient, α (β)

In the absence of any dead-space, the ionisation probability density function (PDF) has a simple exponential shape as shown in Figure B.0.1, with the mean distance (defined as $1/\alpha$) corresponding to the $1/e$ point of the PDF.

In such a case, M_e (M_h) in a device of a given avalanche width can be calculated using α and β in the local model as,

$$M_e = \frac{1}{1-\frac{a}{b-a}\left[\exp\left(w\left(b-a\right)w\right)-1\right]} \tag{B.1}$$

$$M_h = \frac{1}{1-\frac{b}{a-b}\left[\exp\left(w\left(a-b\right)w\right)-1\right]} \tag{B.2}$$

α and β are solely dependent on the electric field strength, ζ and can be calculated from M_e and M_h using

$$a = \frac{1}{w}\left(\frac{M_e-1}{M_e-M_h}\right)\ln\left(\frac{M_e}{M_h}\right) \tag{B.3}$$

$$b = \frac{1}{w}\left(\frac{M_h-1}{M_e-M_h}\right)\ln\left(\frac{M_e}{M_h}\right) \tag{B.4}$$

Figure B.0.2 shows α obtained in a series of PINs with different avalanche widths (w), assuming that the dead-space is zero. Figure B.0.2 shows that if we use Equation B.3 to obtain α, we get a series of α vs the inverse of electric field, $1/F$ curves which overlap. In devices where the dead space is negligible, all the different definitions of α's are identical, i.e. $\alpha\ (\beta) = \alpha_{device}\ (\beta_{device}) = \alpha'\ (\beta') = \alpha^*\ (\beta^*) = \alpha_{MC}\ (\beta_{MC}) = \alpha_s\ (\beta_s)$.

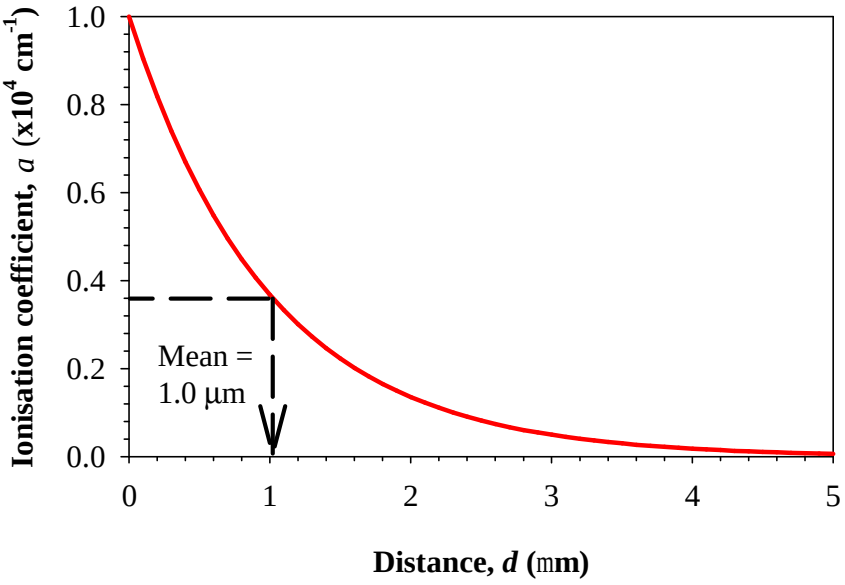

Figure B.0.1 *The electron ionisation PDF which $\alpha = 1 \times 10^4\ cm^{-1}$. Also shown the mean ionising distance of 1.0 µm.*

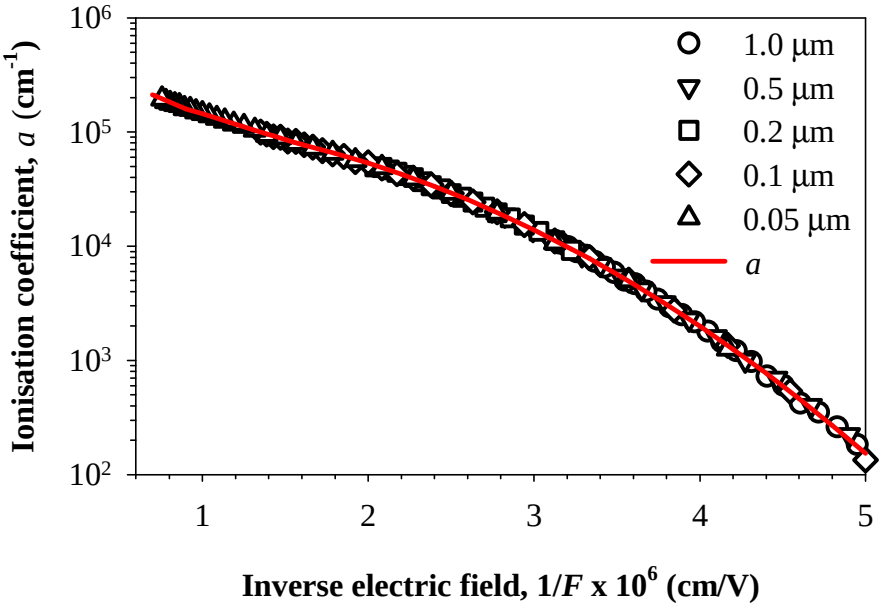

Figure B.0.2 *α extracted from PIN with w=0.05, 0.1, 0.2, 0.5 and 1.0µm without the effect of dead space denoted as △,◇, □, ▽, and ○, respectively. The results overlap and α depends only on the electric field.*

2. Device-width-dependent ionisation coefficient, α_{device} (β_{device})

The presence of dead space complicates the definition of the ionisation coefficients significantly. Figure B.0.3 shows the ionisation coefficient when there is a dead-space, *d*. α obtained from PINs with different *w* will differ slightly from those described in section 1. α calculated from these M_e (M_h) using equation B.3 in various GaAs PINs now do not overlap, especially for the thinner *w* devices at relatively low electric fields which correspond to low multiplications M_e (M_h) << 2, as illustrated in Figure B.3, i.e. α is seen to drop off very rapidly as the electric-field decreases. α obtained now depends on not only the electric field but also the *w*. Note that for thicker *w* devices, this effect can be small and the effect of the dead-space can be ignored and treated as in section 1.

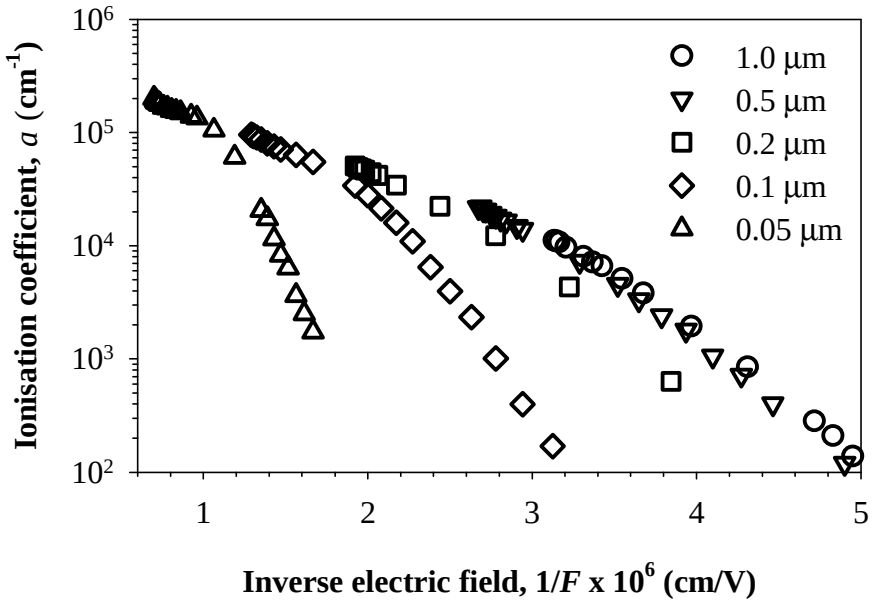

Figure B.0.3 α_{device} *of 0.05, 0.1, 0.2, 0.5 and 1.0µm PINs calculated from equation B.3 denoted as* △, ◇, □, ▽, *and* ○, *respectively.*

From Figure B.0.3, different values of α (β) at a given electric field are required to fit the multiplication values in PINs with different *w* using equations (B.1) and (B.2). As α (β) are device dependent, these ionisation coefficients are now named as α_{device} (β_{device}).

3. Device-independent ionisation coefficient, α' (β')

The red line in Fig. B.4 shows that at any given electric-field, there is a maximum value of α. This ionisation coefficient is now named as α' (β') and can be used with some simple corrections to the limits of the ionisation integrals in the local model to predict

the multiplication approximately even in devices with thin *w*'s. This technique removes the need to deal with varying α at low fields in devices with thin *w*'s.

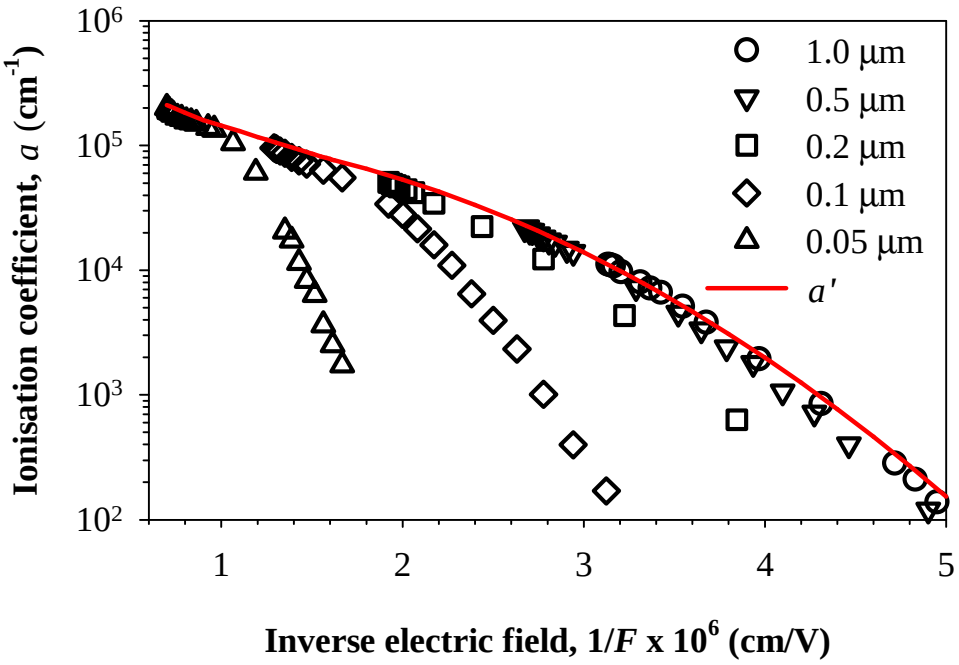

Figure B.0.4 α_{device} *of 0.05, 0.1, 0.2, 0.5 and 1.0µm PINs calculated from equation B.3 denoted as* △, ◇, □, ▽, *and* ○, *respectively.* α' *is shown in solid red line.*

4. Monte-Carlo ionisation coefficient, α_{MC} (β_{MC})

The ionisation coefficient that is defined as α_{MC} (β_{MC}) is different compared to α (β), α_{device} (β_{device}) and α' (β') as it is not obtained from the multiplication characteristics of a PIN. Using a Monte Carlo model [131], we look at the distance a carrier travels in a constant electric-field before it ionises. As the ionisation is a stochastic process this distance can vary between trials, so several thousand trails were averaged to obtain a reliable mean ionisation length. The inverse of the mean ionisation length is then defined as α_{MC} (β_{MC}). The spread in different ionisation lengths can be used to construct the ionising PDF. The dead space d_e (d_h) is defined as the distance where the rising edge of the PDF reached 50% of its peak value as shown in Figure B.4 [103].

As illustrated in Figure B.4 and B.5, $\alpha_{MC} > \alpha'$ at the same electric field due to the latter being obtained from M_e (M_h) in a device and no dead space being considered. The former reflects a more realistic ionisation PDF as shown in Figure B.3 where carriers

have a dead space d_e, where no ionisation is possible until they achieve the threshold energy (E_{th}).

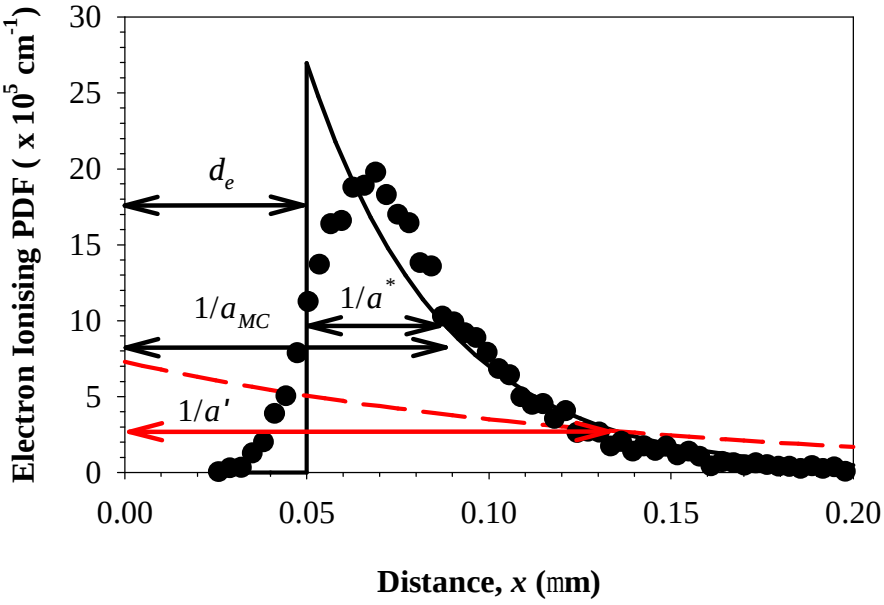

Figure B.4 *The electron ionising PDF of GaAs at 600 kV/cm obtained from the SMC simulations (●). The mean ionising length (x_e=1/α_{MC}) and dead space (d_e) were determined to calculate α* using equation B.6 to generate the PDF (solid line). Also shown is α' which corresponds to the same electric field of 600kV/cm as dashed line.*

5. Enabled ionisation coefficient, α* (β*)

The ionising PDF simulated by the simple MC model shown in Figure B.4 can be approximated by a displaced exponential function as

$$h_e(x \mid x_0) = \begin{cases} 0 & , x - x_0 \le d_e \\ a^* \exp\left[-a^*(x - x_0 - d_e)\right] & , x - x_0 > d_e \end{cases} \qquad \text{(B.5)}$$

Similar expression for holes is shown in equation (2.40). α* can then be calculated using the relationship

$$\frac{1}{a_{MC}} = d_e + \frac{1}{a^*}. \qquad \text{(B.6)}$$

Similar expression for holes can be obtained by replacing α*, α_{MC} and d_e with β*, β_{MC} and d_h. The details of obtaining d_e (d_h) can be found in the previous section in this appendix. From Equation B.6, α* > α_{MC} as shown in Fig. B.5.

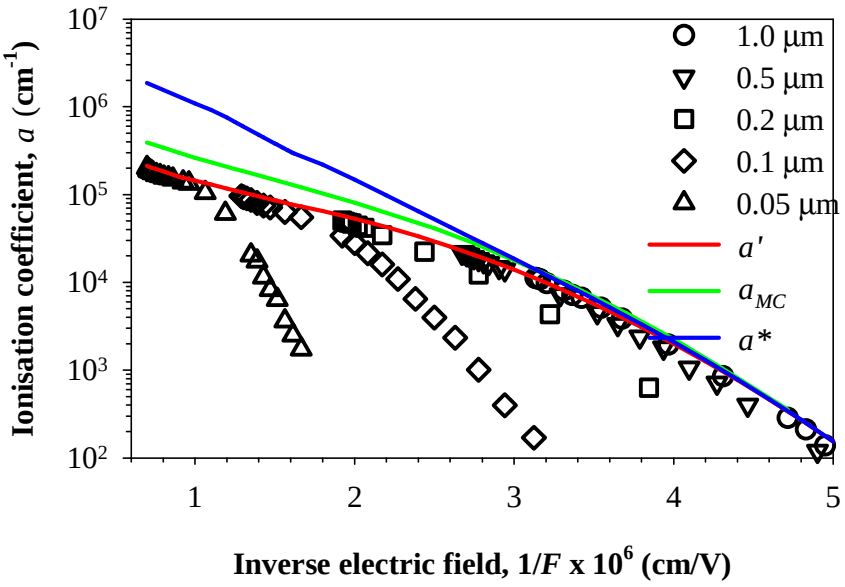

Figure B.5 α_{device} *of 0.05, 0.1, 0.2, 0.5 and 1.0µm PINs calculated from equation B.3 denoted as* △,◇, □, ▽, *and* ○, *respectively.* α', α_{MC} and α^* *are shown in red, green and blue solid lines respectively.*

6. Spatial ionisation coefficient, α_s (β_s)

The spatial ionisation coefficients, α_s (β_s), are yet again a different definition, and are obtained from the rate of change in electron (hole) current with distance in an avalanching structure. In a steady state where a PIN diode is undergoing avalanche multiplication, the electron and hole concentrations are varying with distance across the multiplication region but the sum of electron and hole currents is constant for a given bias voltage. As the electron (hole) current at a position, *x*, is proportional to the number of electrons (holes) present there, these spatial ionisation coefficients can be expressed as

$$a_s(x) = \frac{1}{N}\frac{dn}{dx}, \qquad \text{(B.7)}$$

where *N* is the total number of electrons (holes) and *dn* is the change in the electron concentration in a distance *dx* due to electron initiated ionisation. Equation (B.7) can be implemented easily in numerical models such as RPL and SMC model by meshing the depletion width, *w*, and logging the number of injected electrons, *N* and the frequency of electron ionisation, *dn* in a bin, *dx*. It is a powerful tool to analyse the effect of primary and secondary carriers' dead spaces on α_{device} (β_{device}) as discussed in section 5.4.

APPENDIX C CORRELATION BETWEEN α^* (β^*) and α_{device} (β_{device})

The derivation in this section shows α^* (β^*) can be approximated from α_{device} (β_{device}) provided that a reasonably accurate knowledge of E_{the} (E_{thh}) is known. Equation (5.4) was arrived when local model in equation (2.31) was related to the analytical expression equivalent to RPL model shown in equation (5.4), assuming $\alpha^* = \beta^*$ and $\beta^* = 0$.

Case 1: $\alpha^* = \beta^*$

Equation (5.7) can be simplified to

$$\alpha_{SL} = \frac{1}{d_e + \frac{1}{\alpha^*}} \tag{C.1}$$

α_{SL} is used here instead of α as α_{SL} is the electron mean ionising distance, valid in the range of $d_e < x < w - d_h$.

Substituting (C.1) into equation (5.5),

$$\begin{aligned} M(x) &= \frac{1}{1 - \int_{d_e}^{W-d_e} \alpha_{SL}\, dx} \\ &= \frac{1}{1 - \alpha_{SL}(w - 2d_e)} \end{aligned} \tag{C.2}$$

Pure electron injection, M_e can be approximated using the following equation

$$\begin{aligned} M_e = M(W) &\approx M(W - d_e) \cdot e^{\alpha_{SL} d_e} \\ &= \frac{e^{\alpha_{SL} d_e}}{1 - \alpha_{SL}(w - 2d_e)} \end{aligned} \tag{C.3}$$

as shown in [178]. Provided $d_e \ll 1/\alpha$, $e^{\alpha_{SL} d_e} \approx 1 + \alpha_{SL} d_e$, equation (C.3) can be approximated as

$$M_e \approx \frac{1 + \alpha_{SL} d_e}{1 - \alpha_{SL}(w - 2d_e)} \tag{C.4}$$

As $\alpha_{device} = \beta_{device}$, equation (2.31) can be written as

$$\alpha_{device} = \frac{1}{w}\frac{M_e - 1}{M_e} = \frac{1}{w}(1 - \frac{1}{M_e}) \quad \text{(C.5)}$$

Substitute (C.4) to (C.5),

$$\alpha_{device} = \frac{1}{w}[1 - \frac{1 - \alpha_{SL}(w - 2d_e)}{1 + \alpha_{SL}d_e}] \quad \text{(C.6)}$$

$$= \frac{1}{w}[\frac{1 + \alpha_{SL}d_e - 1 + \alpha_{SL}(w - 2d_e)}{1 + \alpha_{SL}d_e}]$$

$$= \frac{1}{w}[\frac{\alpha_{SL}(w - d_e)}{1 + \alpha_{SL}d_e}]$$

Write α_{SL} in terms of α_{device},

$$\alpha_{SL} = \frac{\alpha_{device}w}{w - d_e - \alpha_{device}wd_e} \quad \text{(C.7)}$$

$$= \frac{\alpha_{device}}{1 - \frac{d_e}{w} - \alpha_{device}d_e}$$

Substitute (C7) to (C1),

$$\frac{\alpha_{device}w}{w - d_e - \alpha_{device}wd_e} = \frac{1}{d_e + \frac{1}{\alpha^*}}$$

$$\alpha_{device}[w\left(d_e + \frac{1}{\alpha^*}\right) + wd_e] = w - d_e$$

$$\alpha_{device} = \frac{1 - \frac{d_e}{w}}{\frac{1}{\alpha^*} + 2d_e}$$

Case 2: $\beta^*=0$, therefore $d_h=0$

Equation (5.7) can be simplified to

$$\alpha_{SL} = \frac{1}{2d_e + \frac{1}{\alpha^*}} \quad \text{(C.8)}$$

Substituting (C.8) into equation (5.5)

$$M(W) = \frac{1}{1 - \int_{d_e}^{W} \alpha_{SL} e^{\int_{x'}^{W} \alpha_{SL} dx'}} \tag{C.9}$$

$$= \frac{1}{e^{-\alpha_{SL}(w-d_e)}} = e^{\alpha_{SL}(w-d_e)}$$

As $\beta_{device} = 0$,

$$\alpha_{device} = \frac{1}{w} \ln(M_e) \tag{C.10}$$

Substitute (C.9) to (C.10)

$$\alpha_{device} = \frac{1}{w} \alpha_{SL}(w - d_e) \tag{C.11}$$

$$\alpha_{SL} = \frac{\alpha_{device}}{1 - \frac{d_e}{w}}$$

Substitute (C.8) to (C.11)

$$\alpha_{device} = \frac{1}{w} \alpha_{SL}(w - d_e) \tag{C.12}$$

$$\frac{1}{2d_e + 1/\alpha^*} = \frac{\alpha_{device}}{1 - \frac{d_e}{w}}$$

$$\alpha_{device}(2d_e + 1/\alpha^*) = 1 - \frac{d_e}{w}$$

$$\alpha_{device} = \frac{1 - \frac{d_e}{w}}{2d_e + \frac{1}{\alpha^*}}$$

APPENDIX D SIMULATION RESULTS (CHAPTER 5)

The following results show both multiplication and excess noise results obtained from RPL model and experiment data, where the published α' (β') tabulated in Table 5.1 were used to calculate α^* (β^*) using equation (5.4).

1. Si

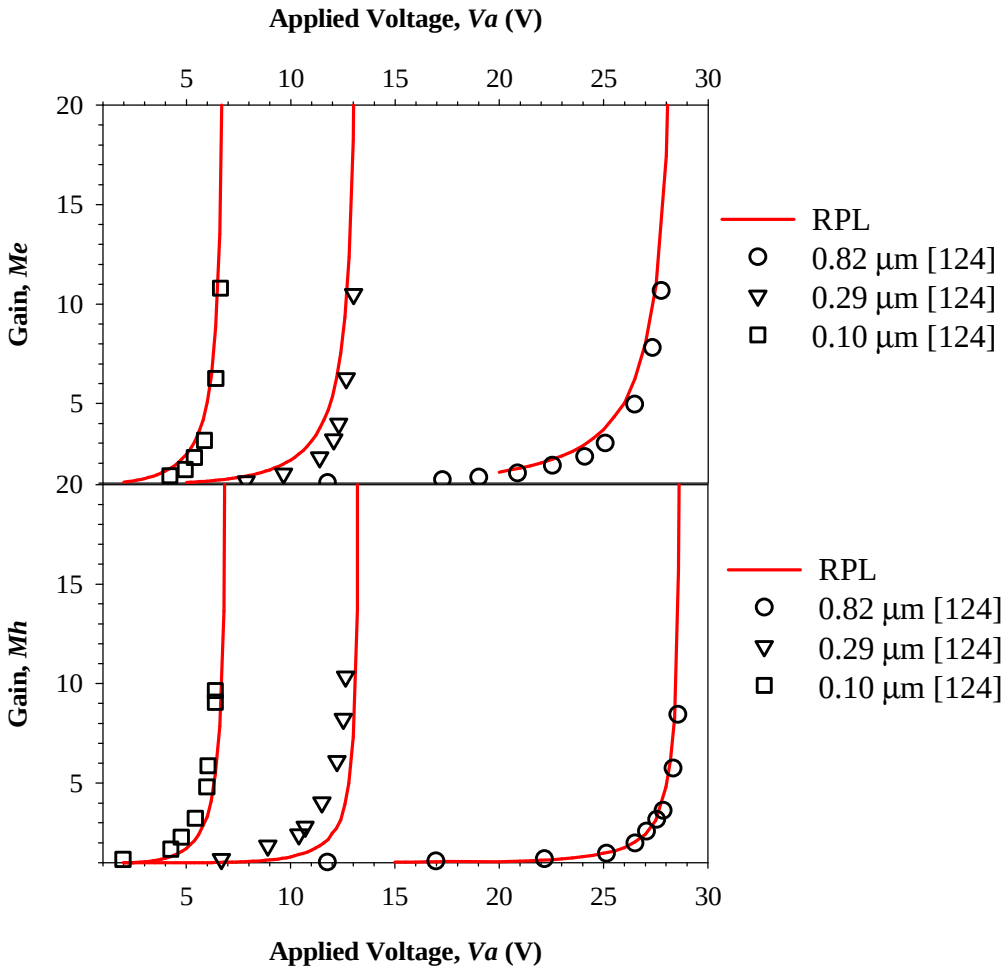

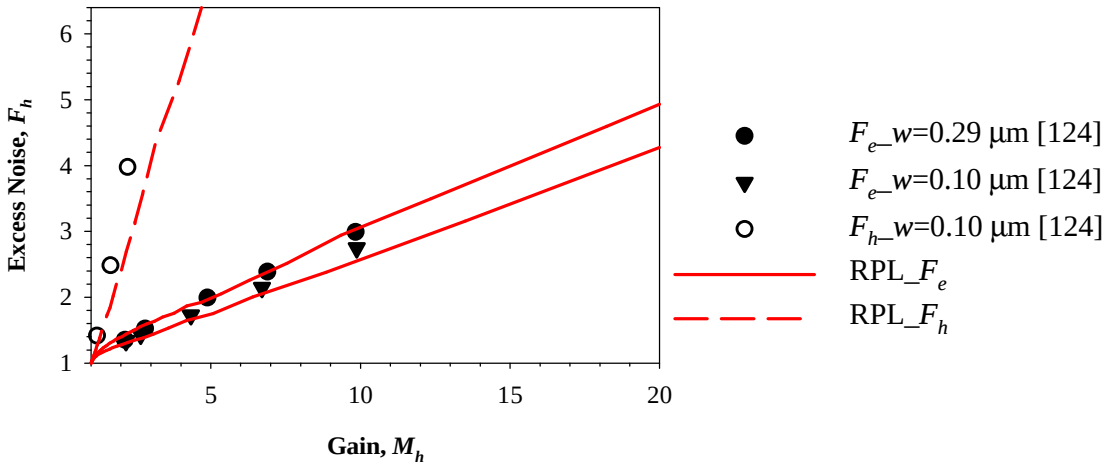
Excess Noise, F_h
Gain, M_h
F_e_w=0.29 μm [124]
F_e_w=0.10 μm [124]
F_h_w=0.10 μm [124]
RPL_F_e
RPL_F_h

2. InP

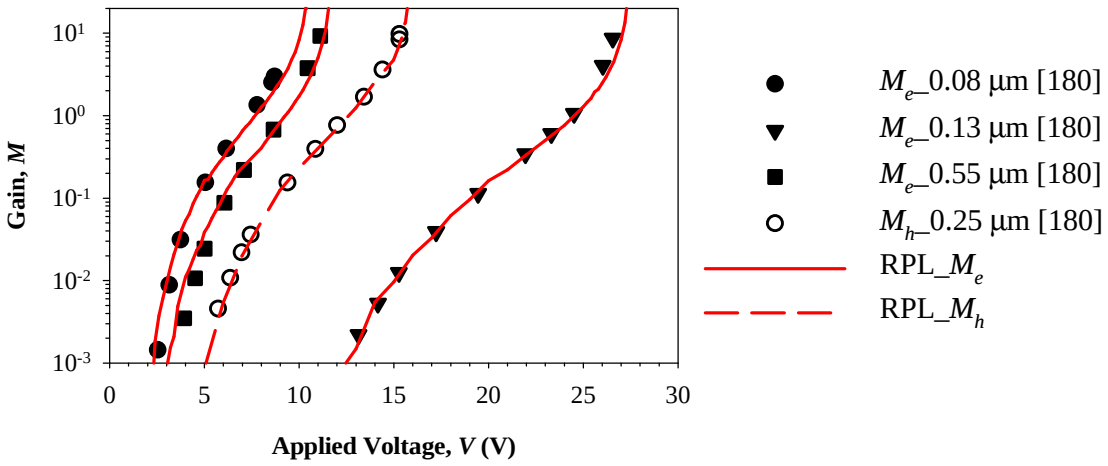
Gain, M
Applied Voltage, V (V)
M_e_0.08 μm [180]
M_e_0.13 μm [180]
M_e_0.55 μm [180]
M_h_0.25 μm [180]
RPL_M_e
RPL_M_h

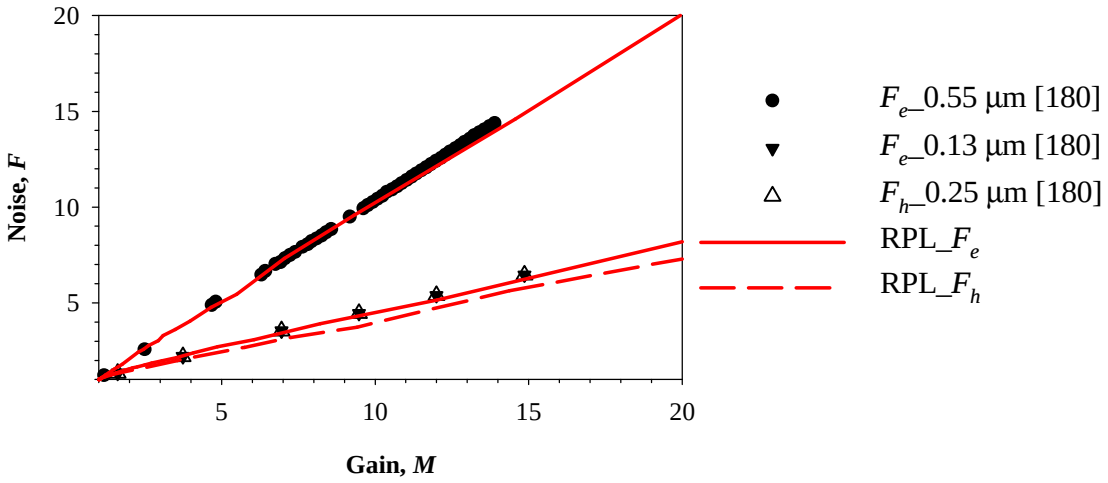
Noise, F
Gain, M
F_e_0.55 μm [180]
F_e_0.13 μm [180]
F_h_0.25 μm [180]
RPL_F_e
RPL_F_h

3. SiC

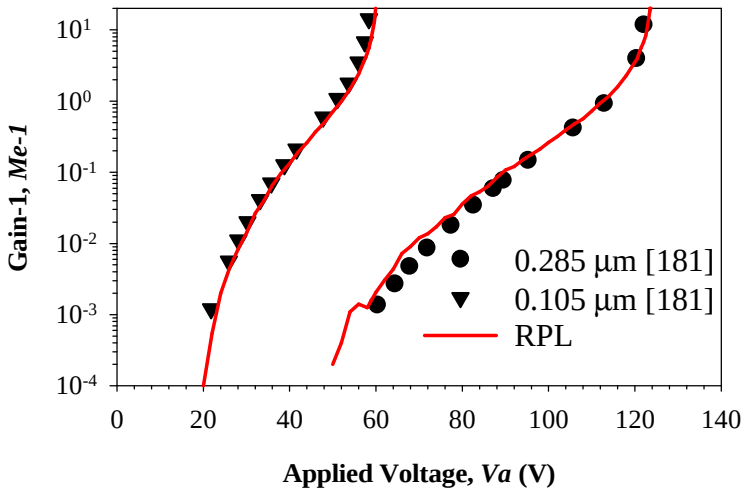
Gain-1, Me-1
Applied Voltage, Va (V)
0.285 µm [181]
0.105 µm [181]
RPL

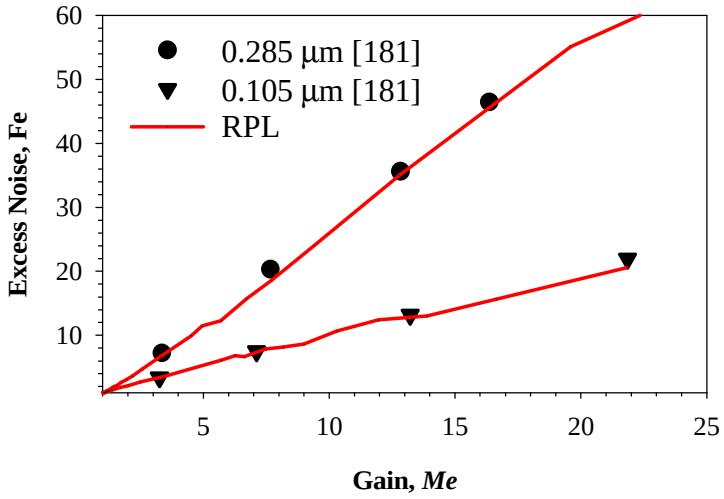
Excess Noise, Fe
Gain, Me
0.285 µm [181]
0.105 µm [181]
RPL

4. $Al_{0.6}Ga_{0.4}As$

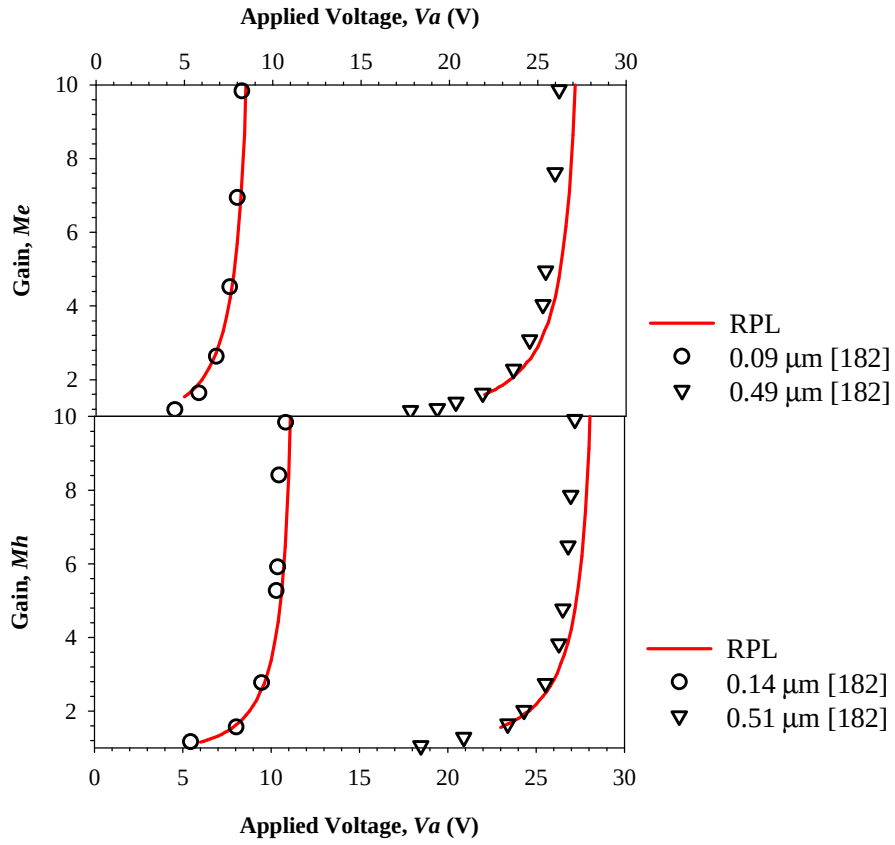

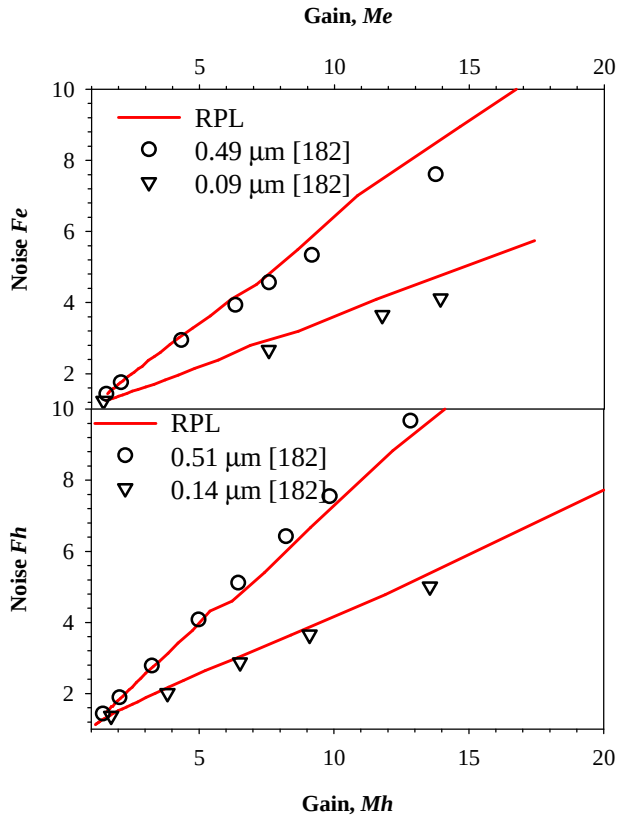

5. $Al_{0.8}Ga_{0.2}As$

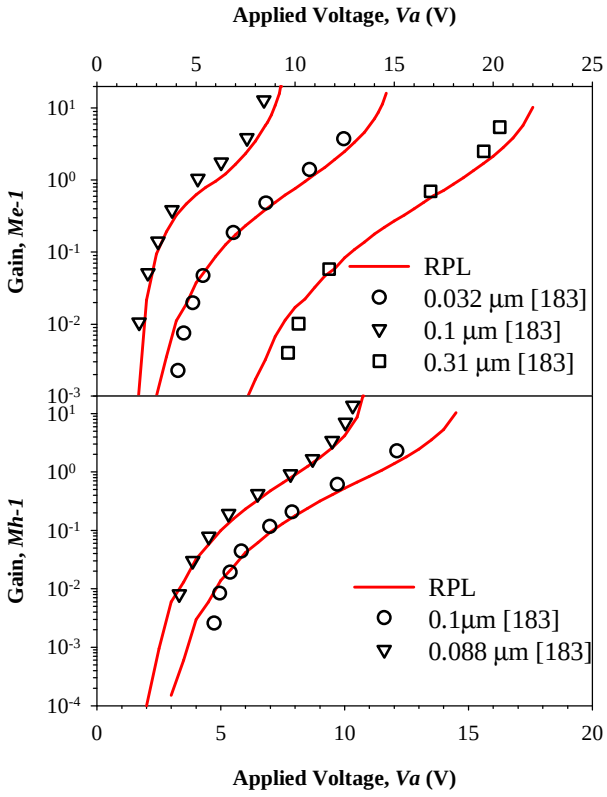

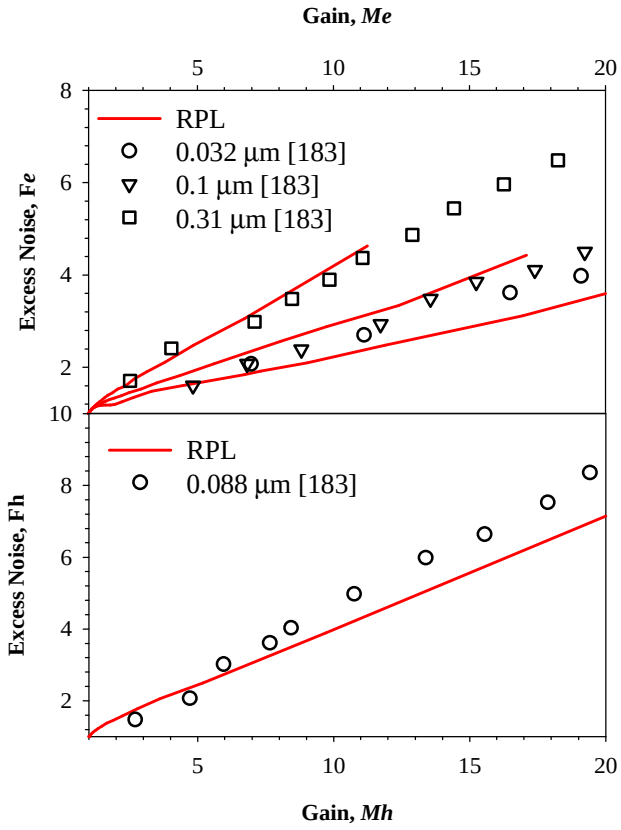

6. $In_{0.52}Al_{0.48}As$

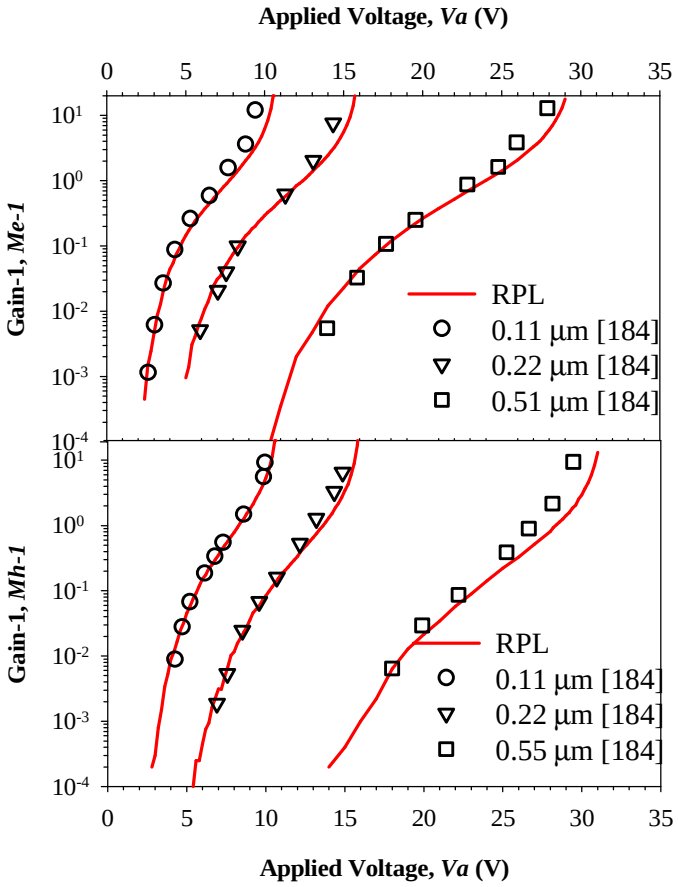

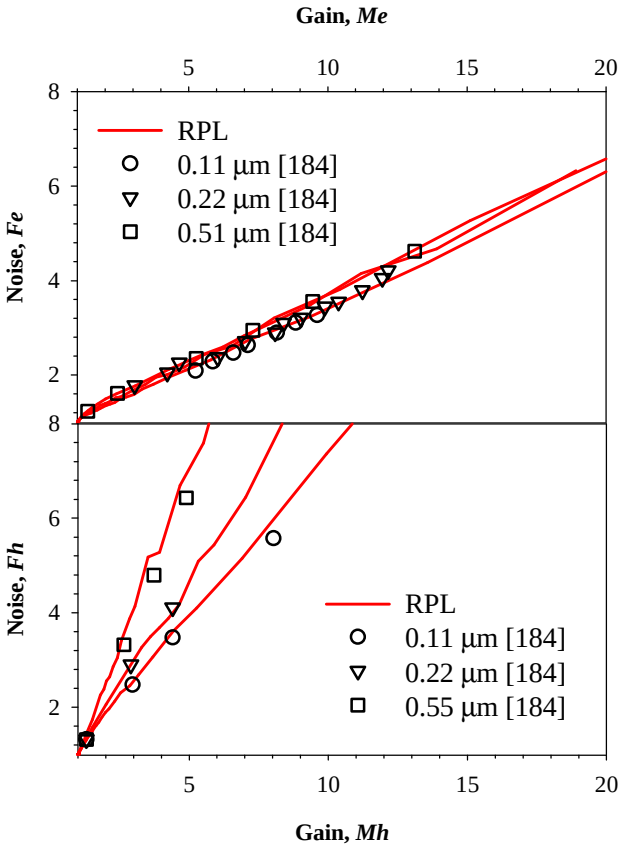

7. $Ga_{0.52}In_{0.48}P$

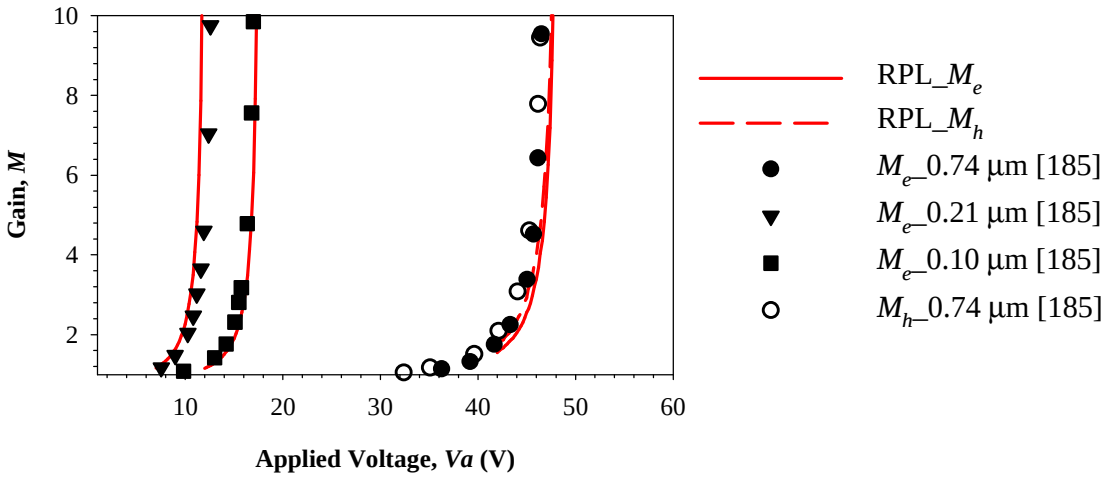

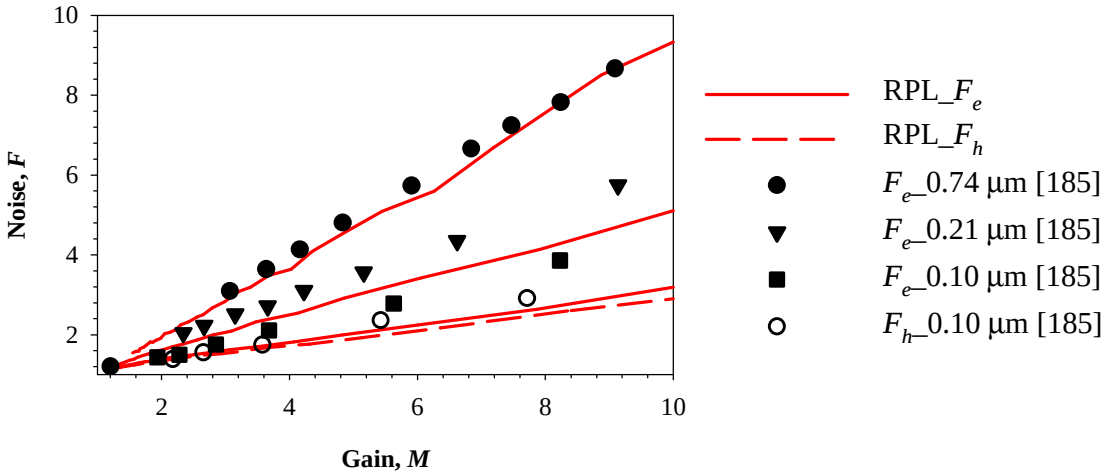

8. $Al_{0.52}In_{0.48}P$

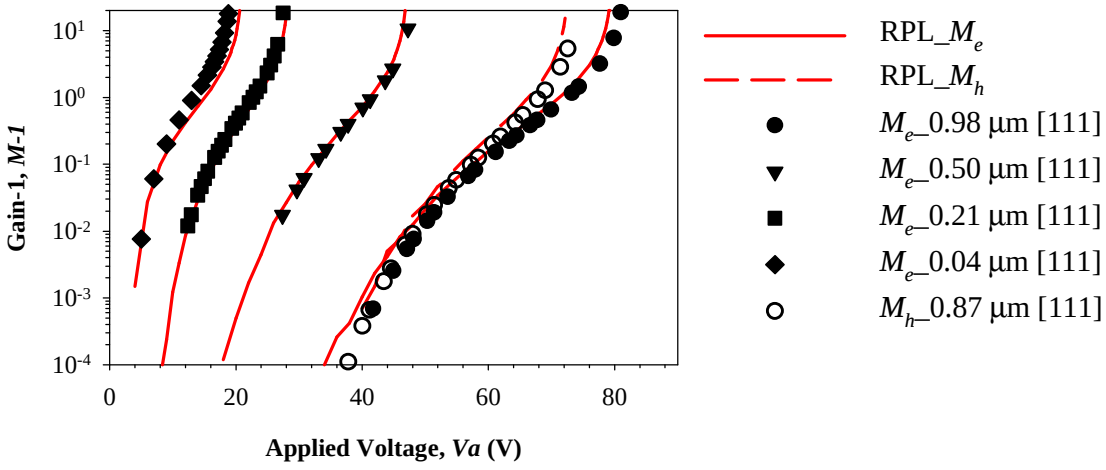

APPENDIX E DERIVATION OF IONISATION THRESHOLD ENERGY

Assuming all carriers have equal masses, ($m_e = m_h$) and three particles are travelling at the same velocity, v ($v_1 = v_2 = v_3$) after ionisation, therefore

$$m_e v = m_e v_1 + m_e v_2 + m_h v_3 \tag{E.1}$$

$$v_1 = v/3 \tag{E.2}$$

to observe the conservation of momentum.

From Equation (E.2), each particle after collision has kinetic energy, E of

$$E = \frac{1}{2} m_e \left(\frac{v}{3} \right)^2 = \frac{p^2}{18 m_e} \tag{E.3}$$

where p is the momentum and therefore the sum of energy of three particles after impact ionisation, E_{total} is

$$E_{total} = \frac{p^2}{6 m_e} \tag{E.4}$$

If the initial energy of the parent carrier is E_{i}, then

$$E_i = \frac{p^2}{2 m_e} \tag{E.5}$$

with E_{i} can be written as

$$E_i = E_g + E_{total} \tag{E.6}$$

since E_{i} is the sum of the minimum energy to create an electron-hole pair, ie. the band gap, E_{g} and excess energy in the three particles after impact ionisation.

By substituting equation (E.4) into (E.5) and thereafter into (E.6),

$$E_i = E_g + \frac{1}{3} E_i \tag{E.7}$$

and therefore,

$$E_g = \frac{3}{2} E_i \tag{E.8}$$

APPENDIX F FABRICATION OF ALINP PINS

The fabrication procedure consists of sample cleaning, back contact, top contact, optical window opening, mesa etch, SU 8 passivation and metallisation. Detailed fabrication steps are listed below.

1. Sample cleaning

1) Cleave a small sample from AlInP wafer.

2) Dip cotton buds into cold n-butyl and roll them over the sample surface to remove dust.

3) 3-step sample cleaning (boiled in n-butyl, acetone and isopropyl alcohol)

4) Blow dry the sample using a nitrogen gun.

2. Back contact

1) Deposit In-Ge/Au (20/200 nm) onto the substrate using evaporator.

2) Anneal sample at 420°C for 30 seconds.

3) 3-stage sample cleaning.

3. Top contact

1) Bake the sample at 100 °C for 1 minute.

2) Coat the sample with BPRS 200 positive photo-resist and spin at 4000 RPM for 30 seconds. Bake the sample again at 100 °C for 1 minute.

3) Align photolithography mask (Top contact mask) on the sample using UV400 mask aligner and expose for 8.0 seconds.

4) Develop the sample using MF26A: H_2O = 1:0.7 for 1 minute, and then rinse the sample in DIW.

5) Blow dry the sample and inspect the developed pattern under a microscope.

6) Clean the sample surface using an Asher for 1-2 minute (Optional)

7) Deposit Au/Zn/Au (5/10/200 nm) on the sample

8) Lift off. Leave the sample in acetone for several minutes and squirt acetone onto the sample to remove the excess metals.

9) 3-stage sample cleaning.

10) Anneal sample at 350°C for 1 minute and finally perform 3-stage cleaning.

4. Optical window opening

1) Dip the sample into piranha solution, H_2SO_4: H_2O_2: H2O (ratio of 1: 8: 80) for ~ 30 seconds to etch the 50nm-thick GaAs cap.

5. Mesa etch

1) Bake the sample at 100 °C for 1 minute.

2) Coat the sample with BPRS 200 positive photo-resist and spin at 4000 RPM for 30 seconds. Bake the sample again at 100 °C for 1 minute.

3) Align photolithography mask (Deep mesa etch mask) on the sample (using UV400 mask aligner) and expose for 8.0 seconds.

4) Develop the sample using MF26A: H_2O = 1:0.7 for 1 minute, and then rinse the sample in DIW.

5) Blow dry the sample and inspect the developed pattern under a microscope.

6) Measure the photo-resist thickness using DEKTEK.

7) Dip the sample into universal etchant solution, HBr: CH_3COOH: $K_2Cr_2O_7$ (ratio of 1: 1: 1). Etch rate is ~ 2 - 3 µm/min.

5. SU 8 passivation

1) Bake the sample at 100 °C for 1 minute.

2) Coat the sample with SU 8 negative photoresist at 4000 RPM for 30 seconds. Bake the sample at 65 °C for 1 minute and subsequently at 95 °C for 3 minutes.

3) Using UV400 mask aligner to exposure (Mesa etch mask) the sample for 50 seconds.

4) Bake the sample at 65 °C for 1 minute and subsequently at 95 °C for 3 minutes.

5) Develop the sample in EC solvent for 1 minute and subsequently into isopropyl alcohol for 1 minute. Blow dry the sample.

6. Metallisation

1) Bake the sample at 100 °C for 1 minute.

2) Coat the sample with BPRS 200 positive photo-resist and spin at 4000 RPM for 30 seconds. Bake the sample again at 100 °C for 1 minute.

3) Align photolithography mask (Mesa etch mask) on the sample (using UV400 mask aligner) and expose for 8.0 seconds.

4) Develop the sample using MF26A: H_2O = 1:0.7 for 1 minute, and then rinse the sample in DIW.

5) Blow dry the sample and inspect the developed pattern under a microscope.

7) Deposit Au/Zn/Au (5/10/200 nm) on the sample.

8) Lift off.